University of Nottingham
UK | CHINA | MALAYSIA

Efficient organic solar cells based on thiophene [3,2-b] pyrrole non-fullerene acceptors

Jintao ZHU

Thesis submitted to University of Nottingham for the degree of Doctor of Philosophy

10th May 2023

Contents

Acknowledgments

Firstly, I wish to express my genuine appreciation and deepest gratitude to my supervisors, Dr. Hainam Do and Dr. Fei Chen, for their kind support. During my research, they have provided patient guidance and valuable suggestions from perspectives of computational chemistry and organic optoelectronics. If they had not discovered my talent, I am probably still doing synthesis work in the company day by day. It is a great pleasure to work with you both. The same goes for my co-supervisor, Dr. Yong Ren. Besides, I would also thank my internal accessor, Dr. Chengheng Pang, who has paid efforts to review my work and provided valuable comments on my research. In addition, I also appreciate the kind support from my PGR director, Dr. Nicholas Hamm.

Secondly, I would like to thank my co-workers, Zeyu Guo, Run Pan, Zhuohan Zhang, Shanshan Jiang, Zixuan Qin, Ai Lan, Yifan Lv, and Hong Lu, who gave me valuable suggestions on my research work. It has been a great pleasure working with them for the past three years. I wish to thank all my colleagues and friends, including Li Lv, Xinyi Mao, Zijun Yan, Chenrui Xie, and Huiwen Zhu. Without their inspiration, I may quit halfway because of intense stress and depression.

At the same time, I wish to thank all my collaborators in other institutes, including those from the National Center for Nanoscience in Beijing, Ningbo Institute of Materials, Ningbo Institute of Northwestern Polytechnical University, the University of Nottingham High-Performance Computing Facility in Ningbo for their help in tests and corporations. I thank New Material Institute at the University of Nottingham Ningbo China for a PhD scholarship.

Finally and significantly, I would like to give my love and appreciation to my family. Their endless love always supports and encourages me.

List of Publications

The following peer-reviewed journal articles have been published or are in preparation to be published as a result of the work undertaken as part of this thesis:

1. **Zhu, J.**, Zhang, Z., Lv, Y., Lan, A., Lu, H., Do, H., & Chen, F. (2022). "Organic solar cells based on non-fullerene acceptors containing thiophene [3,2-b] pyrrole." *Organic electronics*, 103, 106461.

2. **Zhu, J.**, Zhang, Z., Lv, Y., Lan, A., Zhou, J., Lv, Y., Lu, H., Zhou, E., Do, H., Chen, Z., & Chen, F. (2023). "Conformation flipping of asymmetric nonfullerene acceptors enabling high performance organic solar cells with 77% fill factors." *Solar rrl*, 7, 2300171.

3. **Zhu, J.**, Qin, Z., Lan, A., Jiang, S., Mou, J., Ren, Y., Do, H., Chen, Z., & Chen, F. (2023). "A-D-A type nonfullerene acceptors synthesized by core segmentation and isomerization for realizing organic solar cells with low nonradiative energy loss." *Small*, Under review.

4. **Zhu, J.**, Guo, Z., Lan, A., Jiang, S., Lv, Y., Zhang, Z., Lv, Y., Lu, H., Pan, R., Do, H., Chen, Z., & Chen, F. (2023). "Side-chain engineering in ITIC skeleton enabling over 14% efficiency as-cast organic solar cells" *Journal of Material Chemistry C*, In preparation.

The following peer-reviewed journal articles have been published or are in preparation to be published, but not as part of this thesis:

5. Zhang, Z., **Zhu, J.**, Lv, Y., Lan, A., Lu, H., Chen, F. & Huang, W. (2021). "Explore fused-ring core incorporated A-π-D-π-A type acceptors and their application in organic solar cells: Insight into molecular conformation, optical and electrochemical properties, film morphology, and energy loss." *Dye and pigments*, 196, 109572.

6. Lan, A., Lv, Y., **Zhu, J.**, Lu, H., Do, H., Chen, Z., Zhou, J., Wang, H., Chen, F. & Zhou, E. (2022). "High-Performance Ternary Organic Solar Cells through Incorporation of a Series of A2-A1-D-A1-A2 Type Nonfullerene Acceptors with Different Terminal Groups." *ACS Energy letters*, 7, 8, 2845–2855.

7. Lan, A., Li, Y., Zhu, H., **Zhu, J.**, Lu, H., Do, H. Lv, Y., Chen, Y., Chen, Z., Chen, F. & Huang, W. (2023). "Improved Efficiency and Stability of Organic Solar Cells by Interface Modification Using Atomic Layer Deposition of Ultrathin Aluminum Oxide." *Energy & Environmental Materials*, DOI: 10.1002/eem2.12620.

8. Liu, H., Chen, Z., Peng, R., Qiu, Y., **Zhu, J.**, Shi, J., Tang, Z., Zhang, J., Chen, F. & Ge, Z. (2023). "Quinoxaline-based Non-fullerene Acceptor Guest Enables Ternary Organic Solar Cells Achieving 18.9% Efficiency via Reducing Energy Loss and Balancing Charge Mobility." Solar RRL, Under review.

9. Chen, Z., **Zhu, J.**, Yang, D., Song, W., Shi, J., Ge, J., Guo, Y., Tong, X., Chen, F. & Ge, Z. (2023). "Isomerization Strategy on Non-fullerene Guest Acceptor Enables Stable Organic Solar Cells over 19% Efficiency." *Energy & Environmental Science*, DOI: 10.1039/D3EE01164J.

10. Guo, Y., Chen, Z., Ge, J., **Zhu, J.**, Zhang, J., Meng, Y., Ye, Q., Chen, F., Ma, W., Ge, Z. (2023). "Fine-tuning alkyl chains on quinoxaline non-fullerene acceptors enables high-efficiency ternary organic solar cells with optimizing molecular stacking and reducing energy loss." *Advanced Functional Materials*, Under review.

11. Lan, A., **Zhu, J.**, Zhang, Z., Lv, Y., Lu, H., Zhao, N., Do, H., Chen, Z. & Chen, F. (2023) "Asymmetric ITIC derivatives incorporated ternary organic solar cells." *ACS Applied Materials & Interfaces*, Under review.

12. Ye, Q., Chen, Z., Yang, D., Song, W., **Zhu, J.**, Yang, S., Ge, J., Chen, F. & Ge, Z. (2023) "Ductile Oligomeric Acceptor Enables Approaching 18% Efficiency Flexible Organic Solar Cells with Excellent Mechanical Robustness." *Advanced Materials*, Under review.

List of Figures

List of Tables

List of Abbreviations

A	Acceptor
AFM	Atomic force microscopy
AQx-1	2,2'-((2Z,2'Z)-((13,14-bis(2-ethylhexyl)-6,7-dimethyl-3,10-diundecyl-13,14-dihydrothieno[2",3":4',5']thieno[2',3':4,5]pyrrolo[3,2-f]thieno[2",3":4',5']thieno[2',3':4,5]pyrrolo[2,3-h]quinoxaline-2,11-diyl)bis(methanylylidene))bis(5,6-difluoro-3-oxo-2,3-dihydro-1H-indene-2,1-diylidene))dimalononitrile
AQx-2	2,2'-((2Z,2'Z)-((13,14-bis(2-ethylhexyl)-3,10-diundecyl-13,14-dihydrothieno[2",3":4',5']thieno[2',3':4,5]pyrrolo[3,2-f]thieno[2",3":4',5']thieno[2',3':4,5]pyrrolo[2,3-h]quinoxaline-2,11-diyl)bis(methanylylidene))bis(5,6-difluoro-3-oxo-2,3-dihydro-1H-indene-2,1-diylidene))dimalononitrile
BHJ	Bulk heterojunction
BDD	Benzo[1,2-c:4,5-c′]dithiophene-4,8-dione
BDT	Benzo[1,2- b:4,5-b’]dithiophene
Br-ITIC	Replacing the end group of ITIC with IC-Br
BT	Benzo[1,2,5]thiadiazole
BTA	Benzotriazole
BT-LIC	2,2'-((2Z,2'Z)-((12,13-bis(2-ethylhexyl)-3,9-diundecyl-12,13-dihydro-[1,2,5]thiadiazolo[3,4-e]thieno[2",3":4',5']thieno[2',3':4,5]pyrrolo[3,2-g]thieno[2',3':4,5]thieno[3,2-b]indole-2,10-diyl)bis(methanylylidene))bis(3-oxo-2,3-dihydro-1H-cyclopenta[b]naphthalene-2,1-diylidene))dimalononitrile
BT-BIC	2,2'-((2Z,2'Z)-((12,13-bis(2-ethylhexyl)-3,9-diundecyl-12,13-dihydro-[1,2,5]thiadiazolo[3,4-e]thieno[2",3":4',5']thieno[2',3':4,5]pyrrolo[3,2-g]thieno[2',3':4,5]thieno[3,2-b]indole-2,10-

	diyl)bis(methanylylidene))bis(1-oxo-1,2-dihydro-3H-cyclopenta[a]naphthalene-2,3-diylidene))dimalononitrile
BT-L4F	2,2'-((2Z,2'Z)-((12,13-bis(2-ethylhexyl)-3,9-diundecyl-12,13-dihydro-[1,2,5]thiadiazolo[3,4-e]thieno[2",3":4',5']thieno[2',3':4,5]pyrrolo[3,2-g]thieno[2',3':4,5]thieno[3,2-b]indole-2,10-diyl)bis(methanylylidene))bis(6,7-difluoro-3-oxo-2,3-dihydro-1H-cyclopenta[b]naphthalene-2,1-diylidene))dimalononitrile
BT-BO-L4F	2,2'-((2Z,2'Z)-((12,13-bis(2-butyloctyl)-3,9-diundecyl-12,13-dihydro-[1,2,5]thiadiazolo[3,4-e]thieno[2",3":4',5']thieno[2',3':4,5]pyrrolo[3,2-g]thieno[2',3':4,5]thieno[3,2-b]indole-2,10-diyl)bis(methanylylidene))bis(6,7-difluoro-3-oxo-2,3-dihydro-1H-cyclopenta[b]naphthalene-2,1-diylidene))dimalononitrile
BTP	dithienothiophen[3,2b]-pyrrolobenzothiadiazole
BTP-4Cl-8	2,2'-((2Z,2'Z)-((12,13-bis(2-ethylhexyl)-3,9-diundecyl-12,13-dihydro-[1,2,5]thiadiazolo[3,4-e]thieno[2",3":4',5']thieno[2',3':4,5]pyrrolo[3,2-g]thieno[2',3':4,5]thieno[3,2-b]indole-2,10-diyl)bis(methanylylidene))bis(5,6-dichloro-3-oxo-2,3-dihydro-1H-indene-2,1-diylidene))dimalononitrile
BTP-4Cl-12/BTP-eC11	2,2'-((2Z,2'Z)-((12,13-bis(2-butyloctyl)-3,9-diundecyl-12,13-dihydro-[1,2,5]thiadiazolo[3,4-e]thieno[2",3":4',5']thieno[2',3':4,5]pyrrolo[3,2-g]thieno[2',3':4,5]thieno[3,2-b]indole-2,10-diyl)bis(methanylylidene))bis(5,6-dichloro-3-oxo-2,3-dihydro-1H-indene-2,1-diylidene))dimalononitrile
BTP-4Cl-16	2,2'-((2Z,2'Z)-((12,13-bis(2-hexyldecyl)-3,9-diundecyl-12,13-dihydro-[1,2,5]thiadiazolo[3,4-e]thieno[2",3":4',5']thieno[2',3':4,5]pyrrolo[3,2-g]thieno[2',3':4,5]thieno[3,2-b]indole-2,10-diyl)bis(methanylylidene))bis(5,6-dichloro-3-oxo-2,3-dihydro-1H-indene-2,1-diylidene))dimalononitrile
BTP-eC7	2,2'-((2Z,2'Z)-((12,13-bis(2-butyloctyl)-3,9-diheptyl-12,13-dihydro-[1,2,5]thiadiazolo[3,4-e]thieno[2",3":4',5']thieno[2',3':4,5]pyrrolo[3,2-g]thieno[2',3':4,5]thieno[3,2-b]indole-2,10-diyl)bis(methanylylidene))bis(5,6-dichloro-3-oxo-2,3-dihydro-1H-indene-2,1-diylidene))dimalononitrile

BTP-eC9	2,2'- [[12,13-Bis(2-butyloctyl)-12,13-dihydro-3,9-dinonylbisthieno[2",3":4',5']thieno[2',3':4,5]pyrrolo[3,2-e:2',3'-g][2,1,3]benzothiadiazole-2,10-diyl]bis[methylene(5,6-chloro-3-oxo-1H -indene-2,1(3H)-dimethylene)]]bis[malononitrile
BTP-4F-8	2,2'-((2Z,2'Z)-((12,13-bis(2-ethylhexyl)-3,9-diundecyl-12,13-dihydro-[1,2,5]thiadiazolo[3,4-e]thieno[2",3":4',5']thieno[2',3':4,5]pyrrolo[3,2-g]thieno[2',3':4,5]thieno[3,2-b]indole-2,10-diyl)bis(methanylylidene))bis(5,6-difluoro-3-oxo-2,3-dihydro-1H-indene-2,1-diylidene))dimalononitrile
BTP-4F-12	2,2'-((2Z,2'Z)-((12,13-bis(2-butyloctyl)-3,9-diundecyl-12,13-dihydro-[1,2,5]thiadiazolo[3,4-e]thieno[2",3":4',5']thieno[2',3':4,5]pyrrolo[3,2-g]thieno[2',3':4,5]thieno[3,2-b]indole-2,10-diyl)bis(methanylylidene))bis(5,6-difluoro-3-oxo-2,3-dihydro-1H-indene-2,1-diylidene))dimalononitrile
BTP-H2	Replacing the end groups with IC-Br of L8BO
BTP-M	Replacing the end groups with IC-M of Y6
C_{60}	Buckminsterfullerene
CA	Contact angle
CB	Chlorobenzene
CCL	Crystal coherence lengths
CdTe	Cadmium telluride
CF	Chloroform
CH1007	2,2'-((2Z,2'Z)-((12,13-bis(2-ethylhexyl)-3,9-diundecyl-12,13-dihydroselenopheno[2",3":4',5']thieno[2',3':4,5]pyrrolo[3,2-g]selenopheno[2',3':4,5]thieno[3,2-b][1,2,5]thiadiazolo[3,4-e]indole-2,10-diyl)bis(methanylylidene))bis(5,6-difluoro-3-oxo-2,3-dihydro-1H-indene-2,1-diylidene))dimalononitrile
C8-ITIC	Replacing the *p*-hexylphenyl in ITIC with octyl.
Cl-ITIC	Replacing the end group of ITIC with IC-Cl
CN	1-chloronaphthalene
COi8DFIC	2,2′-[[4,4,11,11-tetrakis(4-hexylphenyl)-4,11-dihydrothieno[2′,3′:4,5]thieno[2,3-

	d]thieno[2′′′′,3′′′′:4′′′,5′′′]thieno[2′′′,3′′′:4′′,5′′]pyrano[2′′,3′′:4′,5′]thieno[2′,3′:4,5]thieno[3,2-b]pyran-2,9-diyl]bis[methylidyne(5,6-difluoro
CV	Cyclic voltammetry
D	Donor
D18	5-(5-(4,8-bis(5-(2-ethylhexyl)-4-fluorothiophen-2-yl)-6-methylbenzo[1,2-b:4,5-b']dithiophen-2-yl)-4-(2-butyloctyl)thiophen-2-yl)-8-(4-(2-butyloctyl)-5-methylthiophen-2-yl)dithieno[3',2':3,4;2",3":5,6]benzo[1,2-c][1,2,5]thiadiazole
DFT	Density-functional theory
DIO	1,8-diiodooctane
DPP	Diketopyrrolopyrrole
DTP	Dithieno[3,2-b:2',3'-d] pyrrole
DTTC-4Cl	Dithieno[3,2-b]thiophenecyclopentacarbazole (DTTC) based NFA with IC-2Cl end groups
E_g	Optical bandgap
EL	Electroluminescence
E_{Loss}	Energy loss
E_{nonrad}	Non-radiative energy loss
EQE	External quantum efficiency
EQE_{EL}	External quantum efficiency of the electroluminescence
ESP	Electrostatic potential
ETL	Electron transport layer
E_U	Urbach energy
FF	Fill factor
F5IC	2,2'-((2Z,2'Z)-((4,4,9,9-tetrakis(4-hexylphenyl)-4,9-dihydro-s-indaceno[1,2-b:5,6-b']dithiophene-2,7-diyl)bis(methanylylidene))bis(5,6-difluoro-3-oxo-2,3-dihydro-1H-indene-2,1-diylidene))dimalononitrile

F6IC	Replacing the central benzene core with the TT unit in F5IC
F8IC	Replacing the central benzene core with the TT unit in F7IC
F9IC	Adjusting the number of fused rings in the backbone of ITIC, based on dithieno[3,2-b:2’,3’-d]thiophene (TTT)
F10IC	Replacing the central benzene core with the TT unit in F9IC
F-ITIC	Replacing the end group of ITIC with IC-F
FPIC	The benzene core was replaced with pyrene in the IDT backbone with IC-2F end groups
FREA	Fused-ring electron acceptor
FRET	Förster resonance energy transfer
FTAZ	Fluorobenzotriazole
FTPS-EQE	Fourier-transform photocurrent spectroscopy external quantum efficiency
GaAs	Gallium arsenide
GIWAXS	Grazing incidence wide-angle X-ray scattering
GL	Glycerol
HOMO	Highest occupied molecular orbital
HTL	Hole transport layer
IC	3-(Dicyanomethylidene)indan-1-one
IC-Br	2-[5(6)-Bromo-3-oxo-2,3-dihydro-1H-inden-1-ylidene]malononitrile
IC-Cl	2-(5,6-Chloro-3-oxo-2,3-dihydro-1H-inden-1-ylidene)malononitrile
IC-2Cl	2-(5,6-Dichloro-3-oxo-2,3-dihydro-1H-inden-1-ylidene)malononitrile
IC-F	2-[5(6)-Fluoro-3-oxo-2,3-dihydro-1H-inden-1-ylidene]malononitrile
IC-2F	2-(5,6-Difluoro-3-oxo-2,3-dihydro-1H-inden-1-ylidene)malononitrile

IC-I	2-[5(6)-Iodo-3-oxo-2,3-dihydro-1H-inden-1-ylidene]malononitrile
$IC_{60}BA$	Indene-C60 bisadduct
$IC_{70}BA$	Indene-C70 bisadduct
IC-M	2-(6-methyl-3-oxo-2,3-dihydro-1H-inden-1-ylidene)malononitrile
ICT	Intramolecular charge transfer
IDIC	2,7-bis(2-methylene-(3-(1,1-dicyanomethylene)-indanone))- 4,4,9,9-tetrahexyl-sindaceno[1,2-b:5,6-b']dithiophene
IDT	Indacenodithiophene
IDT6CN-M	By reducing one thiophene ring in one side of ITIC-M
IDT8CN-M	By adding one thiophene ring in one side of ITIC-M
IDTIC	Indacenodithiophene (IDT) backbone with 3-(Dicyanomethylidene)indan-1-one (IC) end groups
IDTT	indacenodithieno[3,2-b] thiophene
IHIC1	The benzene core was replaced with naphthalene in indacenodithiophene (IDT) backbone with 3-(Dicyanomethylidene)indan-1-one (IC) end groups
IM-4F	Replacing the hydrogen in the central benzene ring of IT-4F with two methyl groups
IMC6-4F	Replacing the hydrogen in the central benzene ring of ITC6-4F with two methyl groups
IP	In plane
IPS	Ionisation Potential Spectroscopy
ITCF	Replacing the fluorine atom of IT-4F with a methyl group
IT-2Cl	3,9-bis(2-methylene-((3-(1,1-dicyanomethylene)-6,7-chloro)-indanone))-5,5,11,11-tetrakis(4-hexylphenyl)-dithieno[2,3-d:2',3'-d']-s-indaceno[1,2-b:5,6-b']dithiophene
IT-4Cl	3,9-bis(2-methylene-((3-(1,1-dicyanomethylene)-6,7-dichloro)-indanone))-5,5,11,11-tetrakis(4-

	hexylphenyl)-dithieno[2,3-d:2',3'-d']-s-indaceno[1,2-b:5,6-b']dithiophene
IT-4F/F7IC	3,9-bis(2-methylene-((3-(1,1-dicyanomethylene)-6,7-difluoro)-indanone))-5,5,11,11-tetrakis(4-hexylphenyl)-dithieno[2,3-d:2′,3′-d′]-s-indaceno[1,2-b:5,6-b′]dithiophene
INPIC-4F	5,5,12,12-tetrakis(4-hexylphenyl)-indacenobis-(dithieno[3,2-b:2′,3′-d]pyrrol) with IC-2F end groups
IPT-4F	Replacing the DTP block at one side of the INPIC-4F backbone with a thiophene ring
IPTBO-4Cl	Replacing the IC-2F groups and the hexylphenyl side chain of IPT-4F with IC-2Cl end groups and butyloctyl group, respectively.
ITC6-IC	Hexyl side chains are introduced into the TT block in the backbone of ITIC
ITCT-DM	Replacing the hydrogen atoms in ITTC with methyl groups
ITIC	2,2'-[[6,6,12,12-tetrakis(4-hexylphenyl)-s-indacenodithieno[3,2-b]thiophene]methylidyne(3-oxo-1H-indene-2,1(3H)-diylidene)]]bis(propanedinitrile)
ITIC-M/IT-M	3,9-bis(2-methylene-(3-(1,1-dicyanomethylene)indanone-methyl))-5,5,11,11-tetrakis(4-*n*-hexylphenyl)-dithieno[2,3d:2′,3′d′]-s-indaceno[1,2b:5,6b’]dithiophene
ITIC-Th	Replacing the phenyl side chains in ITIC with hexylthienyl side chains
IT-1O	ITIC-based acceptors with methoxy end groups
IT-2O	ITIC-based acceptors with ethoxy end groups
IT-3O	ITIC-based acceptors with propoxy end groups
IT-4O	ITIC-based acceptors with butoxy end groups
ITO	Indium tin oxide
ITTC	Replacing the benzene in ITIC with thiophene
J52	Poly[[5,6-difluoro-2-(2-hexyldecyl)-2H-benzotriazole-4,7-diyl]-2,5-thiophenediyl[4,8-bis[5-

	(2-ethylhexyl)-2-thienyl]benzo[1,2-b:4,5-b']dithiophene-2,6-diyl]-2,5-thiophenediyl]
J71	A medium bandgap 2D-conjugated D-A copolymers based on bithienyl-benzodithiophene (BDTT) donor unit and fluorine-substituted benzotriazole (FBTA) acceptor unit
J_{ph}	Photocurrent density
J_{sat}	Photocurrent when all of the photogenerated excitons are dissociated into free charges and collected by the electrodes at a high effective voltage
J_{SC}	Short-circuit current density
***J-V* curve**	Current-voltage curve
L8-BO	2,2'-((2Z,2'Z)-((12,13-bis(2-ethylhexyl)-3,9-(2-butyloctyl)-12,13-dihydro- [1,2,5]thiadiazolo[3,4-e]thieno[2",3'':4',5']thieno[2',3':4,5]pyrrolo[3,2-g]thieno[2',3':4,5]thieno[3,2-b]indole-2,10-diyl)bis(methanylylidene))bis(5,6- difluoro-3-oxo-2,3-dihydro-1H-indene-2,1-diylidene))dimalononitrile
L8-HD	2,2'-((2Z,2'Z)-((12,13-bis(2-ethylhexyl)-3,9-bis(2-hexyldecyl)-12,13-dihydro-[1,2,5]thiadiazolo[3,4-e]thieno[2",3":4',5']thieno[2',3':4,5]pyrrolo[3,2-g]thieno[2',3':4,5]thieno[3,2-b]indole-2,10-diyl)bis(methanylylidene))bis(5,6-difluoro-3-oxo-2,3-dihydro-1H-indene-2,1-diylidene))dimalononitrile
L8-OD	2,2'-((2Z,2'Z)-((12,13-bis(2-ethylhexyl)-3,9-bis(2-octyldodecyl)-12,13-dihydro-[1,2,5]thiadiazolo[3,4-e]thieno[2",3":4',5']thieno[2',3':4,5]pyrrolo[3,2-g]thieno[2',3':4,5]thieno[3,2-b]indole-2,10-diyl)bis(methanylylidene))bis(5,6-difluoro-3-oxo-2,3-dihydro-1H-indene-2,1-diylidene))dimalononitrile
LE	Local exciton
LUMO	Lowest unoccupied molecular orbital
MALDI-TOF-MS	Matrix-assisted laser desorption/ionization time of flight mass spectrometry
MeIC	Replacing the hydrogen in the end groups of ITTC

m-ITIC	Changing the position of hexyl at the *p*-hexylphenyl chains of ITIC
MoO_3	Molybdenum trioxide
N3	2,2′-((2Z,2’Z)-((12,13-bis(3-ethylheptyl)-3,9-diundecyl12,13-dihydro[1,2,5]thiadiazolo[3,4-e]thieno[2″,3″:4’,5’]thieno[2′,3′:4,5]pyrrolo[3,2-g]thieno [2′,3′:4,5]thieno[3,2-b]indole-2,10-diyl)bis(methanylylidene))bis(5,6-difluoro-3-oxo-2,3- 16 dihydro-1H-indene-2,1-diylidene))dimalononitrile
N4	2,2'-((2Z,2'Z)-((12,13-bis(4-ethyloctyl)-3,9-diundecyl-12,13-dihydro-[1,2,5]thiadiazolo[3,4-e]thieno[2",3":4',5']thieno[2',3':4,5]pyrrolo[3,2-g]thieno[2',3':4,5]thieno[3,2-b]indole-2,10-diyl)bis(methanylylidene))bis(5,6-difluoro-3-oxo-2,3-dihydro-1H-indene-2,1-diylidene))dimalononitrile
NFA	Nonfullerene acceptor
NFBDT	Isomerized ITIC based on BDT core
NIR	Near-infrared
NMR	Nuclear magnetic resonance
NOE	Nuclear Overhauser effect
NOESY	Nuclear Overhauser effect spectroscopy
OOP	Out of plane
OSCs	Organic solar cells
P3HT	Poly(3-hexylthiophene)
PBDB-T	Poly[[4,8-bis[5-(2-ethylhexyl)-2-thienyl]benzo[1,2-b:45-b]dithiophene-2,6-diy]-2,5-thiophenediyl[5,7-bis(2-ethylhexyl)-4,8-dioxo-4H8H-benzo[12-c:4.5-c1dithiophene-1,3-diyl]]
PBDB-T-SF	Poly[(2,6-(4,8-bis(5-(2-ethylhexylthio)-4-fluorothiophen-2-yl)-benzo[1,2-b:4,5-b’]dithiophene))-alt-(5,5-(1’,3’-di-2-thienyl-5’,7’-bis(2-ethylhexyl)benzo[1’,2’-c:4’,5’-c’]dithiophene-4,8-dione)]
PBQ-0F	Poly[5-(5-(4,8-bis(5-(2-ethylhexyl)thiophen-2-yl)-6-methylbenzo[1,2-b:4,5-b']dithiophen-2-yl)thiophen-

	2-yl)-8-(5-methylthiophen-2-yl)-2,3-bis(3-(octyloxy)phenyl)quinoxaline]
PBQ-QF	Poly[5-(5-(4,8-bis(5-(2-ethylhexyl)thiophen-2-yl)-6-methylbenzo[1,2-b:4,5-b']dithiophen-2-yl)thiophen-2-yl)-6,7-difluoro-8-(5-methylthiophen-2-yl)-2,3-bis(3-(octyloxy)phenyl)quinoxaline]
PBQ-4F	Poly[5-(5-(4,8-bis(5-(2-ethylhexyl)-4-fluorothiophen-2-yl)-6-methylbenzo[1,2-b:4,5-b']dithiophen-2-yl)thiophen-2-yl)-6,7-difluoro-8-(5-methylthiophen-2-yl)-2,3-bis(3-(octyloxy)phenyl)quinoxaline]
$PC_{61}BM$	[6,6]-phenyl-C_{61}-butyric acid methyl ester
$PC_{71}BM$	[6,6]-Phenyl-C_{71}-butyric acid methyl ester
PCE	Power conversion efficiency
$\boldsymbol{P_{coll}}$	Charge collection efficiency
PDBT-T1	Poly[[5,10-bis(5-octyl-2-thienyl)dithieno[2,3-d:2′,3′-d′]benzo[1,2-b:4,5-b′]dithiophene-2,7-diyl]-2,5-thiophenediyl[5,7-bis(2-ethylhexyl)-4,8-dioxo-4H,8H-benzo[1,2-c:4,5-c′]dithiophene-1,3-diyl]-2,5-thiophenediyl]
PDCBT	Poly[5,5'-bis(2-butyloctyl)-(2,2'-bithiophene)-4,4'-dicarboxylate-alt-5,5'-2,2'- bithiophene]
PDI	Perylene diimide
PDINN	N,N'-bis[7-(dimethylamino)-4-azaheptyl]-3,4,9,10-perylene tetracarboxylic diimide
$\boldsymbol{P_{diss}}$	Exciton dissociation efficiency
PEDOT:PSS	Poly(3,4-ethylenedioxythiophene):polystyrene sulfonate
PFBDB-T	Poly[(2,6-(4,8-bis(5-(2-ethylhexyl) thiophen-2-yl)-benzo[1,2-b:4,5-b′]dithiophene))-alt-(5,5-(1′,3′-bis(4-fluorothiophen-2-yl)-5′,7′-bis(2-ethylhexyl)benzo[1′,2′-c:4′,5′-c′]dithiophene-4,8-dione)]
PffBT4T	Poly(Naphtho[1,2-c:5,6-c']bis[1,2,5]Thiadiazole)

PffBT4T-2OD	Poly[(5,6-difluoro-2,1,3-benzothiadiazole-4,7-diyl)[3,3'''-bis(2-decyltetradecyl)[2,2':5',2'':5'',2'''-quaterthiophene]-5,5'''-diyl]]
PffBT4T-C_9H_{19}	Poly[(5,6-difluoro-2,1,3-benzothiadiazole-4,7-diyl)[3,3'''-bis(2-octyldodecyl)[2,2':5',2'':5'',2'''-quaterthiophene]-5,5'''-diyl]]
PL	Photoluminescence
P_{light}	Light intensity
P_{in}	Input power
P_m	Maximum output power
PM6/PBDB-TF	Poly[1-(5-(4,8-bis(4-fluoro-5-(2-ethylhexyl)thiophen-2-yl)benzo[1,2-b:4,5-b′]dithiophen-2-yl)thiophe n-2-yl)-5,7-bis(2-ethylhexyl)-3-(thiophen-2-yl)-4H,8H-benzo[1,2-c:4,5-c′]dithiophene-4,8-dione]
PM7	poly[(2,6-(4,8-bis(5-(2-ethylhexyl-3-chloro)thiophen-2-yl)-benzo[1,2-b:4,5-b′]dithiophene))-alt-(5,5-(1′,3′-di-2-thienyl-5′,7′-bis(2-ethylhexyl)benzo[1′,2′-c:4′,5′-c′]dithiophene-4,8-dione)]
PTB1	Poly[dodecyl 6-(4,8-bis(octyloxy)benzo[1,2-b:4,5-b']dithiophen-2-yl)thieno[3,4-b]thiophene-2-carboxylate]
PTB7	Poly([4,8-bis[(2-ethylhexyl)oxy]benzo[1,2-b:4,5-b']dithiophene-2,6-diyl][3-fluoro-2-[(2-ethylhexyl)carbonyl]thieno[3,4-b]thiophenediyl])
PTB7-Th	Poly[(4,8-bis(5-(2-ethylhexyl)-4-fluorothiophen-2-yl)benzo[1,2-b:4,5-b']dithiophene-2,6-diyl)-alt-(3-fluoro-2-[(2-ethylhexyl)carbonyl]thieno[3,4-b]thiophene-)-2,6-diyl)]
PTPDBDT	A thieno[3,4-c]pyrrole-4,6-dione-based conjugated polymer
PTQ10	Poly[(thiophene)-alt-(6,7-difluoro-2-(2-hexyldecyloxy)quinoxaline)]
PTQ11	Poly[(thiophene)-alt-(6,7-difluoro-2-(2-hexyldecyloxy)-3-methylquinoxaline]

PTVT-T	Poly(bis(2-butyloctyl) [2,2′ : 5′,2″-terthiophene]-4,4″-dicarboxylate-5,5′-diyl-vinylene)
PVSCs	perovskite solar cells
Qx	2,3-diphenyl-quinoxaline
RMS	Root-mean-square
RT	Room temperature
S	Sulfur
S_0	Ground state
S_1	The first excited state
SCLC	Space charge limited current
Se	Selenium
SRID-4F	Se-substituted IT-4F
T	Thiophene
TDDFT	Time-dependent density functional theory
TEM	Transmission electron microscopy
TGA	Thermal gravimetric analysis
6TIC	Propanedinitrile,2,2'-[[6,6,12,12-tetrakis(4-hexylphenyl)-6,12-dihydrothieno[2",3":4',5']thieno[3',2':4,5]cyclopenta[1,2-b]thieno[2"',3"ChemicChemicalbookalbook':4",5"]thieno[2",3":3',4']cyclopenta[1',2':4,5]thieno[2,3-d]thiophene-2,8-diyl]bis[methylidyne(3-oxo-1H-indene-2,1(3H)-diylidene)]]bis-
TP	Thiophene[3,2-b] pyrrole
TPTT-2F	Replacing the TT block of ITIC-2F with a thiophene ring
TPTTT-2F	Replacing the TTT block of F9IC with a thiophene ring
TRID-4F	isomerized SRID-4F
TT	Thiophene[3,2-b] thiophene

TTT	Dithieno[3,2-b:2′,3′-d]thiophene
UV-Vis	Ultraviolet–visible spectroscopy
V_{eff}	Effective voltage
VMD	Visual molecular dynamics
V_{OC}	Open-circuit voltage
Y5	2,2'-((2Z,2'Z)-((12,13-bis(2-ethylhexyl)-3,9-diundecyl-12,13-dihydro-[1,2,5]thiadiazolo[3,4-e]thieno[2",3":4',5']thieno[2',3':4,5]pyrrolo[3,2-g]thieno[2',3':4,5]thieno[3,2-b]indole-2,10-diyl)bis(methanylylidene))bis(3-oxo-2,3-dihydro-1H-indene-2,1-diylidene))dimalononitrile
Y6	2,2'-(((12,13-Bis(2-ethylhexyl)-3,9-diundecyl-12,13-dihydro-[1,2,5]thiadiazolo[3,4-e]thieno[2",3":4',5']thieno[2',3':4,5]pyrrolo[3,2-g]thieno[2',3':4,5]thieno[3,2-b]indole-2,10-diyl)bis(methaneylylidene))bis(5,6-difluoro-3-oxo-2,3-dihydro-1H-indene-2,1-diylidene))dimalononitrile
Y6-Se	2,2'-((2Z,2'Z)-((12,13-bis(2-ethylhexyl)-3,9-diundecyl-12,13-dihydro-[1,2,5]selenadiazolo[3,4-e]thieno[2",3":4',5']thieno[2',3':4,5]pyrrolo[3,2-g]thieno[2',3':4,5]thieno[3,2-b]indole-2,10-diyl)bis(methanylylidene))bis(5,6-difluoro-3-oxo-2,3-dihydro-1H-indene-2,1-diylidene))dimalononitrile
ZnO	Zinc oxide
γ	Surface energy
χ	Flory-Huggins interaction parameter

Abstract

Organic solar cells (OSCs) have received wide research attention for their unique properties such as semi-transparency, light weight, low cost, flexibility, and easy to fabricate. The development of bulk heterojunction (BHJ) OSCs has been surging ahead accompanying with the rapid development of multifarious non-fullerene acceptors (NFAs). At present, the well-known NFAs such as ITIC and Y6 series, have replaced fullerene derivatives in fabricating highly efficient BHJ OSCs due to their simple synthesis and purification, tunable spectral absorption, and modulable frontier energy levels in comparison with fullerene acceptors, NFAs based OSCs have achieved a very promising power conversion efficiency (*PCE*) of approaching 19% recently.

N-heteroarene based NFAs, as one of the main kinds of NFAs, exhibited great potential in fabricating high-performance OSCs for their unique features, such as higher energy levels facilitated by the strong electron-donating nitrogen atom, red-shifted absorption, and an extra reaction site for side chain modification. Chapter 1 demonstrates the superiorities of these *N*-heteroarene based NFAs in fabricating high performance OSCs. Hence, Chapter 2 provides a comprehensive overview of *N*-heteroarene based NFAs. The development of *N*-heteroarene based NFAs and their construction are reviewed and discussed in this chapter. Subsequently, Chapter 3 presents the essential methodologies and analysis techniques employed in this thesis to characterize NFAs and the devices.

First of all, thiophene[3,2-b] pyrrole (TP) building block was introduced to construct two fused-ring conjugated NFAs, named as PTBTP-2F and PTBTP-4F (Chapter 4). When blending with donor PBDB-T, the PTBTP-4F fabricated devices afforded a *PCE* of 12.33% with a V_{OC} of 0.86 V, a J_{SC} of 20.74 mA cm^{-2} and a *FF* of 69.02%.

Core engineering has been demonstrated effective to achieve high performance NFAs, as molecular conjugation and intramolecular charge transfer can be readily realized through introducing or removing the aromatic rings on the backbone of NFAs. Additionally, the asymmetric strategy was adopted for molecule modification, which could precisely regulate the intrinsic optoelectronic properties of NFAs. Therefore, asymmetric molecular design strategy was employed to optimize PTBTP-4F and improve the photovoltaic performance (Chapter 5). TP block and thiophene[3,2-b] thiophene (TT) block were utilized to construct asymmetric acceptors, PTBTT-4F/4Cl. Ascribed to the great miscibility between PBDB-TF and PTBTT-4F and thus exquisite phase separation, an outstanding *FF* of 76.73% was achieved. Eventually, the PBDB-TF: PTBTT-4F based devices afforded a maximum *PCE* of 14.49%.

To further optimize the PTBTT backbone, we divided the PTBTT backbone into three segments and reconstructed the TPBTT backbone (Chapter 6). After the isomerization of TP block, the ICT properties improved a lot, owing to the inner placement of the pyrrole ring.. By alternating the position of pyrrole ring, the isomerized TPBTT backbone obtained improved molecular stacking, leading to higher crystallinity and amended energy disorder. Ascribed to improved charge mobility and suppressed E_{Loss}, an impressive *PCE* of 15.72% was achieved in TPBTT-4F based devices, along with a reduced non-radiative energy loss ($\Delta E_{\mathrm{nonrad}}$) of 0.276 eV and a significant improvement in J_{SC}.

In conclusion, this thesis proposes a commercial organic building block, TP block. Based on TP block, PTBTP series were created with suppressed E_{Loss}. Asymmetric design strategy was adopted in PTBTP backbone modification, and constructed PTBTT series with improved device performance. Eventually, TPBTT series were obtained through isomerization, which further achieved more ordered molecular stacking and an improved *PCE*.

Chapter 1

Introduction

1.1 Synopsis

This chapter begins with a background introduction to organic solar cells (OSCs), which work as an available method to facilitate solar energy. It gives an overview of donor and acceptor materials used in OSCs, as well as their unique properties, including energy levels, absorption, and their photovoltaic performance in binary OSCs. Afterward, the chapter briefly introduces the design principles of acceptor materials, especially non-fullerene acceptors (NFAs), followed by highlighting the challenges in developing NFAs. In the end, the aims and objectives as well as an outline of the thesis are provided.

1.2 Organic Solar Cells

OSC is one of the emerging photovoltaic technologies featuring solution-processability and feasibility in performance tuned by the molecular design of key organic photovoltaic materials. OSCs have received wide research attention for their unique properties such as semi-transparency, light weight, low cost, flexibility, and easy to fabricate. However, to go beyond perovskite solar cells (PVSCs), they are still facing some challenges and issues.

1.2.1 Introduction of OSCs

Solar cell technology has evolved through several developmental phases, which can be categorized into four generations. The first generation of monocrystalline silicon and polysilicon solar cells (Yan et al., 2021) have been commercialized for decades, but their applications are limited by the constraints of preparation technology and cost, as well as the environmental pollution during the preparation process. Subsequently, the second generation of inorganic solar cells based on cadmium telluride (CdTe) and gallium arsenide (GaAs) exhibited high photoelectric conversion efficiency. However, due to their limited resources and high cost, their wide application is restricted. OSC is one of the third-generation solar cell technologies, along with perovskite and dye-sensitized solar cells (Rong et al., 2018;Chen et al., 2019). The third generation of solar cells, represented by organic solar cells and perovskite cells, can be manufactured on a large scale through printing and spraying due to their light weight, low cost, and solution processing characteristics (Zhao et al., 2023). Additionally, OSCs have shown great potential in preparing flexible and transparent cells which further broadens their application range. Therefore, OSC is currently a hot research spot in solar energy conversion.

Bulk-heterojunction (BHJ) OSCs have attracted significant attention since 1995 (Yu et al., 1995), with an active layer that consists of a p-type polymer as an electron donor and a fullerene derivative as an electron acceptor. The BHJ structure created more transport channels and donor/acceptor (D/A) interpenetrating networks in blend films. And such a spatial network enhanced the efficiency of exciton separation and charge carrier transport. In the beginning, fullerene derivatives were the commonly used electron acceptors in OSCs. For instance, derivatives of Buckminsterfullerene (C_{60}) molecule, such as [6,6]-phenyl-C_{61}-butyric acid methyl ester ($PC_{61}BM$) and [6,6]-phenyl-C_{71}-butyric acid methyl ester ($PC_{71}BM$), were often chosen as electron acceptors in OSCs (Zhang et al., 2016). However, fullerene derivatives suffer from several limitations such as weak absorption, challenging chemical synthesis, strong aggregation, and unstable morphology. As a result, fullerene-based OSCs have high energy loss and low external quantum efficiency (EQE).

Hence, researchers are continuously exploring novel molecular structures as substitutes for fullerene. In the early stages of research, certain groups investigated new NFAs to pair with the classic p-type polymer, poly(3-hexylthiophene) (P3HT). Although the reported *PCE*s were relatively low, these studies have demonstrated that fullerenes are not the sole option as electron acceptors. Since the emergence of ITIC in 2015 (Lin et al., 2015), non-fullerene OSCs have become a highly researched area due to their advantages in mechanical flexibility, lightweight nature, solution processability, portability, and semitransparency (Koo et al., 2020;Yin et al., 2020;Shen et al., 2023). The success of NFAs stems from their tunable structures, which not only enables the creation of superior energy level alignment and reduction of energy loss but also provides the potential to modify molecular orientation for enhanced molecular stacking and film morphology (Zhao, Wang and Zhan, 2018;Zou et al., 2022). Fullerene molecules are renowned for their spherical geometry, which is distinctly observable in contrast to the planar-like structure of donor polymers in bulk medium. In comparison, NFAs exhibit a 2D plane-like structure that complicates film morphology studies. As a result, NFAs have a tendency to self-aggregate in solution-processed BHJ blend films, leading to reduced electron mobility than fullerene-based OSCs. However, this issue can be partially addressed by incorporating an appropriate amount of fullerene molecules to reduce self-aggregation and enhance electron mobility. Furthermore, NFAs offer several advantages over the C_{60} derivatives in terms of cost of synthesis, tunable structures, and possible use of molecular engineering to control the film morphology. Over the past few years, non-fullerene OSCs have witnessed rapid advancements and achieved remarkable *PCE*s of over 19% (Liang et al., 2022), exhibiting great potential for commercial applications.

Currently, the most promising NFAs primarily include A-D-A and A-DA'D-A types. In 2015, Zhan et al. developed the classic A-D-A type NFA called ITIC, which exhibited impressive properties such as appropriate electronic energy levels, high electron mobility, and favorable morphology. After blending with the donor materials, the devices based on the ITIC derivative (IT-4F) achieved the maximum *PCE* of 13.7% (Li et al., 2018). However, the development of A-D-A type NFAs has reached a bottleneck due to two main reasons. Firstly, A-

D-A type molecules commonly have a large bandgap; secondly, most of them suffer from high energy loss (E_{Loss}). These issues limited the improvement of J_{SC} and V_{OC}. However, the studies of ITIC and its derivatives have enabled the development of various polymer donors, while providing a deeper understanding of the relationship between molecular structure, photophysical properties, and device performance. To break through this efficiency bottleneck, novel NFAs should be developed to realize the milestones for high-performance OSCs. In 2019, Zou et al. reported a novel NFA called Y6 (Yuan et al., 2019b), which features an A-DA'D-A type backbone and a ladder-type fused-ring central core of dithienothiophen[3,2b]-pyrrolobenzothiadiazole (BTP). This NFA achieved an optimal *PCE* of 15.7% after blending with the classic donor PBDB-TF through careful regulation of its absorption and molecular orbital energy levels. Specifically, Y6 possessed a unique C-shaped backbone, which facilitated improved morphology between donors and acceptors, promoted inter/intramolecular interactions, and increased charge carrier mobility and molecular crystallinity. Additionally, alkyl side chains attached to the nitrogen atom of two pyrrole rings enhanced the molecule's solubility and prevented over-aggregation caused by the rigid conjugated skeleton through steric hindrance. At the same time, neoteric A-DA'D-A type-based acceptors commonly present high EQE response, effectively suppressing $\Delta E_{\mathrm{nonrad}}$. Then, hundreds of A-DA'D-A type NFAs originated from Y6 were synthesized, contributing to the development of NFAs.

Since then, the Y series molecules have been the mainstream, and the underlying logic of molecular design is still based on the contribution of electron-deficient core to the whole backbone. However, the electron push-pull effects of A-DA'D-A type molecules can be adapted to A-D-A type molecules and to adjust ICT. To break the record of *PCE*, novel A-D-A NFAs still need to be developed instead of Y series. The role of structural alteration of NFA molecules should be discussed in terms of changes in film morphology and reducing energy loss for improving device performances.

1.2.2 Working Mechanism for OSCs

Currently, most device structures for OSCs are based on BHJ device structures.

According to the transmission direction of electrons or holes, it can be divided into standard configuration, ITO/hole transport layer (HTL)/Active layer/electron transport layer (ETL)/Electrode, and inverted configuration, ITO/ETL/Active layer/HTL/Electrode. As shown in **Figure 1.1**, OSCs have a typical sandwich structure with the active layer in the middle of ETL and HTL. The active layer is mainly composed of donor and acceptor materials to absorb photons. At the same time, Indium tin oxides (ITO) and the metal electrode are used to collect the generated electrons and holes.

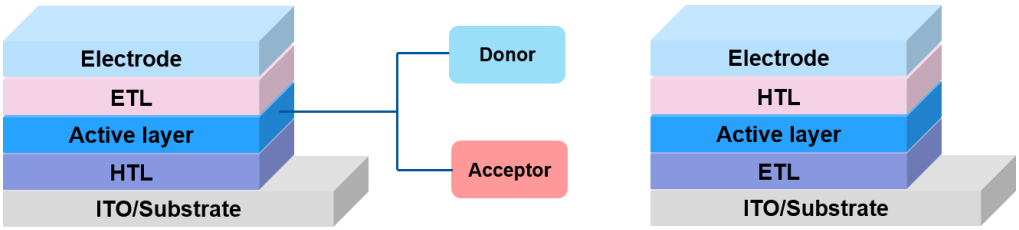

Figure 1.1 The diagram of the standard (left) and inverted (right) structure of OSC devices.

The general working mechanism of organic solar cells is shown in **Figure 1.2** below, which is mainly divided into the following four physical stages (Dou et al., 2013;Heeger, 2014;Huang et al., 2014). First, photoexcitation of the donor generates a Coulomb-correlated electron–hole pair, known as an exciton. The exciton then diffuses to the D/A interface, where the exciton dissociates to form a geminate pair. The free charges are then transported and collected at the respective electrodes. The process of acceptor excitation is similar and, especially for NFAs, can be of comparable importance for generating current.

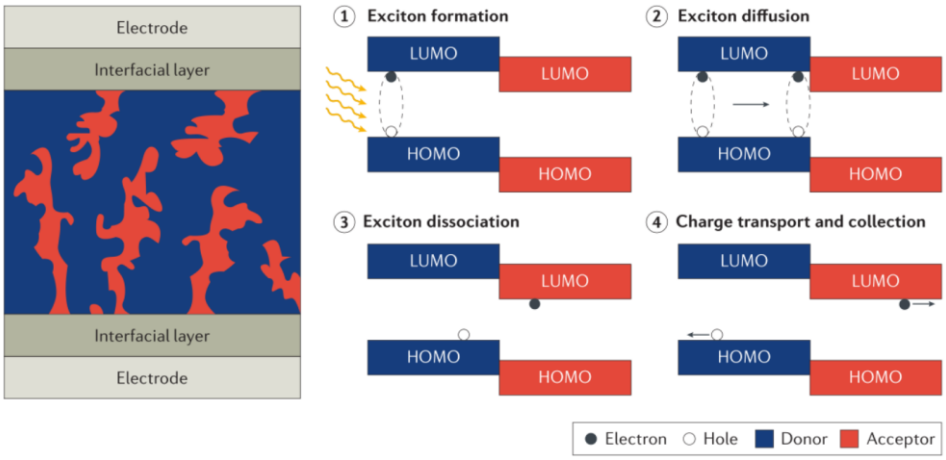

Figure 1.2 The structure and working mechanism of a bulk-heterojunction organic solar cell (Yan et al., 2018a).

1.2.3 Parameters to Evaluate OSCs

Generally, the fundamental parameters of OSCs are evaluated through current-voltage (*J-V*) curves. The device performance is measured through separate tests in darkness and under illumination. As illustrated in **Figure 1.3**, key performance parameters of OSCs, including V_{OC}, J_{SC}, *FF* and *PCE* can be obtained.

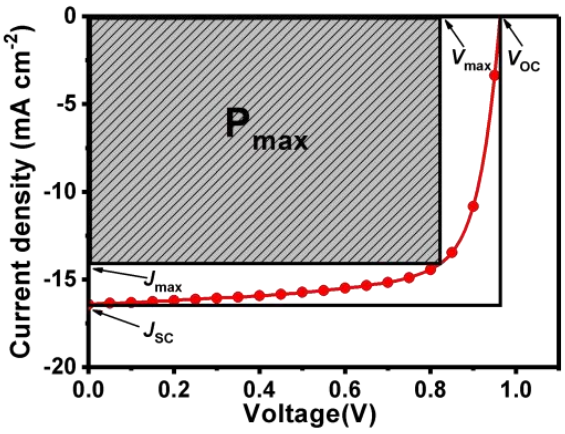

Figure 1.3 The typical *J-V* curve for an OSC device

1) Open-Circuit Voltage (V_{OC})

V_{OC} is defined as the output voltage of the solar cell under open-circuit condition (when the output current is zero). As is shown in **Figure 1.4** and the following equation, V_{OC} of the devices can be estimated by the energy level difference between the HOMO energy levels of the donors and the LUMO energy levels of the acceptors (Potscavage, Sharma and Kippelen, 2009;Elumalai and Uddin, 2016).

$$V_{OC} = (E_{LUMO}^{Acceptor} - E_{HOMO}^{Donor} - 0.3\ eV)/e \quad (1\text{-}1)$$

Besides, V_{OC} is associated with the thickness of the active layer, carrier mobility, D/A ratio, contact between the active layer, transport layer, and electrode.

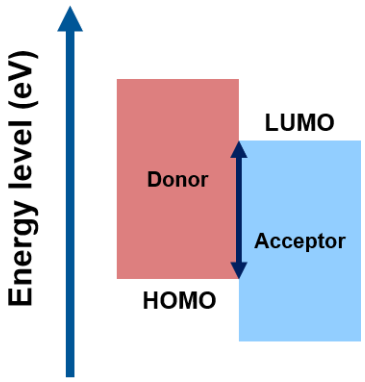

Figure 1.4 The diagram of V_{OC} in OSC devices.

2) Short-Circuit Current Density (J_{SC})

J_{SC} is defined as the current density of the device under short circuit condition (when the output voltage is zero). Commonly, J_{SC} is related to the absorption region and intensity of the active layer, charge dissociation, and charge transport efficiency. At the same time, J_{SC} is associated with molecular stacking in the blend films. The closer stacking of the fabricated films can lead to better crystallinity, and thus higher J_{SC}.

3) Fill Factor (*FF*)

As is shown in **Figure 1.3**, *FF* can be obtained by the following equation:

$$FF = \frac{P_m}{J_{SC} \times V_{OC}} \times 100\% \quad (1\text{-}2)$$

where P_m is the maximum output power. *FF* of the OSC device is predominantly influenced by the collection and recombination of charge carriers. Low *FF* is always caused by the recombination of charge carriers present within the active layer. In order to enhance *FF*, optimizing the miscibility between the donors and acceptors and phase separation is beneficial for forming a 2D interpenetrating network structure. By tuning the D/A ratio, additives, and annealing, phase separation can be optimized, leading to higher *FF*.

4) Power Conversion Efficiency (*PCE*)

PCE is defined as the ratio of the P_m per unit effective area of the solar cell to the input power (P_{in}), which can be calculated by the following equation:

$$PCE = \frac{P_m}{P_{in}} \times 100\% = \frac{J_{SC} \times V_{OC} \times FF}{P_{in}} \times 100\% \quad (1\text{-}3)$$

1.2.3 Development and Challenges of Acceptors in OSCs

As the most promising A-D-A type NFAs at that time, ITIC and its derivatives have distinctive and important molecular structures, leading to a great superiority in photophysical and photovoltaic performance (Gao et al., 2018a;Zhang et al., 2018a). The important features from the chemical structure point of view are: (1) ITIC and its derivatives consist of two electron-deficient end groups and one electron-rich central core. A strong push-pull electronic effect was generated by the electron-deficient and electron-rich units, allowing for the regulation of photoelectric properties such as absorption and energy levels. Besides, the rigid and planar backbone, combined with strong inter/intramolecular interactions, facilitated efficient charge transfer. (2) The attached side chains could adjust molecular solubility and compatibility with the donors, resulting in a favorable nanometer-scale blend with an ideal interpenetrated network. (3) The A-D-A molecules offered multiple reaction sites for the introduction of functional atoms and groups to tune molecular structure and thus the molecular properties. Therefore, NFAs are commonly optimized by core engineering, side-chain engineering and end group engineering.

Rather than conventional molecular modification, designing NFAs through suppressing E_{Loss} is a new method. Compared to silicon and PVSCs, the OSCs usually suffer from larger E_{Loss} and inferior charge mobility, restricting their further performance improvement. The reduction of E_{Loss} in the OSCs using NFAs was generally over 0.5 V (Zhang et al., 2021), considerably higher than that of high-efficiency inorganic or perovskite solar cells (< 0.4 V) (Mahesh et al., 2020). This was primarily due to the high $\Delta E_{\mathrm{nonrad}}$, a result of low electroluminescence external quantum efficiency (EQE_{EL}). The low EQE_{EL} in OSCs could be associated with more disordered internal structure (Huang et al., 2023). Hence, tuning the interfacial bias through molecular engineering and molecular packing would now be critical to squeezing more voltage out of NFA systems that are already nearly perfect at converting light into photocurrent. Furthermore, the characterization of E_{Loss} can provide insights into the nature of binary OSCs and further suggestions for material design.

Chapter 2

Literature Review

2.1 Synopsis

Despite the remarkable achievements in OSCs, there arises an increasing demand for enhancing our elementary comprehension of the interdependent relationships between the structure and properties of the state-of-the-art donor and acceptor materials. These interconnections initiate from the structures and molecular stacking of the organic semiconductors, proceed to the blend morphology and resultant photophysical characteristics. The chemical structures of the donor-acceptor light harvesting materials can dictate the efficiency of the photon-to-electron conversion process, culminating in the specific performance of the devised OSC devices, such as charge generation, transfer, separation efficiency, and E_{Loss} during these processes. The device performance data, in combination with intrinsic material properties obtained through device processing, can generate a feedback loop, facilitating the exploration of material design and device fabrication. This chapter starts with a brief introduction of polymer donors that have been used in constructing binary OSC devices. Then, a comprehensive discussion is provided of the recent progress in NFAs, especially high-performance A−D−A type and A−DA'D−A type NFAs, and the corresponding highly efficient binary OSC systems.

2.2 Conjugated Donor Materials for OSCs

Organic optoelectronic functional materials initially focused on the design and development of donor materials, and various organic optoelectronic donor materials were rapidly developed and reported. Donor materials can be roughly divided into two categories: small-molecular donors and polymer donors. The vigorous development and in-depth research of donor materials have greatly benefited the NFAs and OSCs in recent years, so it is necessary to summarize the donor materials.

2.2.1 Conjugated Polymer Donor Materials

Up to now, several series of conjugated polymer donors have been constructed by the combination of D and A building blocks. Among the polymer donors, some building blocks have exhibited impressive performance in constructing high-performance polymer donors, including benzo[1,2-b:4,5-b']dithiophene (BDT) (Yao et al., 2016), benzo[d][1,2,3]triazole (BTA) (Cui and Li, 2019), quinoxaline (Qx) (Liu et al., 2017a), benzo[1,2-c:4,5-c′]dithiophene-4,8-dione (BDD) (Zheng et al., 2020b). In this part, the progress of some famous polymer donors for application in OSCs is summarized. The chemical structures of the previous polymer donors are presented in **Figure 2.1**.

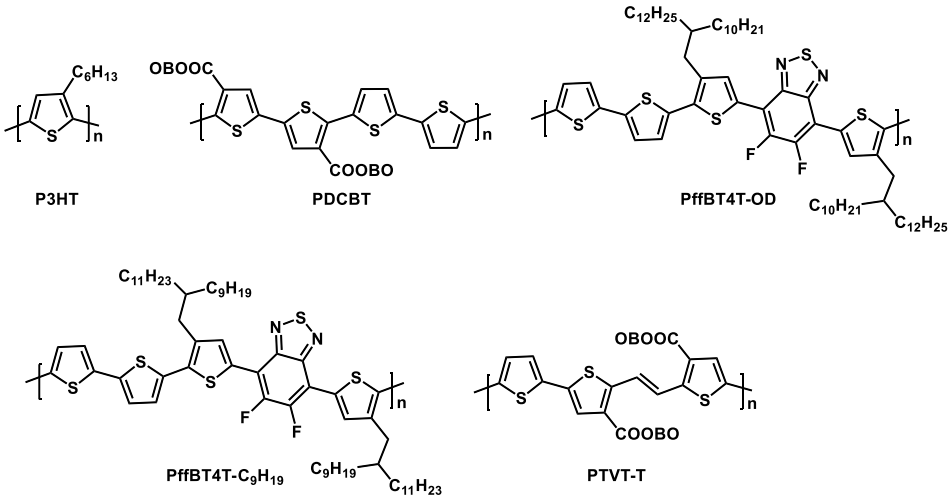

Figure 2.1 The chemical structures of previous polymer donors

In 1986, since P3HT (Haugeneder et al., 1999) was applied in OSCs by Jen et al., polythiophene derivatives have been widely used in the field and have been

used ever since (Li et al., 2005;Kim et al., 2006), owing to their good stability and strong crystallization. Heeger *et al.* optimized the morphology of P3HT/$PC_{61}BM$ blend film through thermal annealing, achieving a *PCE* over 5% in 2005 (Ma et al., 2005). Since then, with the development of fullerene derivatives with higher LUMO levels ($IC_{60}BA$, $IC_{70}BA$, etc.), P3HT-based devices achieved an efficiency of 7% (Xu et al., 2016;Cao et al., 2017). Hou *et al.* (Zhang et al., 2014) introduced ester groups into polythiophene fragment units and successfully synthesized PDCBT, which exhibited closer π-π stacking. The enhanced stacking was beneficial for efficient charge transport. Hence, the PDCBT/$PC_{70}BM$ based devices realized a *PCE* of 7.2% together with improved V_{OC} and *FF*, simultaneously. As the low bandgap NFA of ITIC was designed to fabricate OSCs, the PDCBT based devices achieved a *PCE* of 10.16%, owing to the broadening of the absorption region of the blend films. Subsequently, Yan *et al.* (Liu et al., 2014) prepared a series of polythiophene derivative donor materials named as PffBT4T series, by inserting difluoro-benzothiadiazole (BT) into polythiophene fragments. Owing to the excellent crystallinity and temperature-sensitive molecular aggregation, the morphology of PffBT4T-series based films can be effectively regulated by hot substrate and hot solvent spin-coating. Eventually, the device based on PffBT4T-2OD/$PC_{70}BM$ realized a *PCE* of 10.8% with an *FF* of 75%. After side chain engineering, PffBT4T-C_9H_{19} based devices achieved an efficiency of 11.7% by modulating the active layer morphology with a two-solvent strategy (Zhao et al., 2016a). Recently, Hou *et al.* (Ren et al., 2021) reported a more readily prepared polymer PTVT-T with low cost and strong aggregation behavior, forming nanoscale aggregations and face-on orientation. After blending with the electron acceptor of BTP-eC9, this polymer-based device showed a maximum *PCE* of 16.2%.

BTA, as a weak electron-withdrawing unit, can be employed to construct polymer donors with either wide or medium bandgaps. (**Figure 2.2**) You et al. (Price et al., 2011) successfully designed and prepared two BTA-contained polymer donors, one with fluorine atoms and one without. In contrast to the BTA-based donor, the fluorinated BTA-based donor (denoted as FTAZ) possessed comparable optical and aggregation characteristics, while featuring a significantly deeper HOMO energy level and enhanced hole mobility. After

casting with $PC_{61}BM$, the FTAZ-based devices yielded a higher *PCE* (7.1%) than the BTA-based counterpart (4.3%). Then, Li *et al.* (Bin et al., 2016b) employed a fluorinated BTA-based polymer donor (J52) to fabricate binary devices by combining with a low bandgap acceptor of ITIC and obtained a *PCE* of 5.51%. To realize a 2D structure, the alkylthiophene side chain in J52 was replaced by trialkylsilylthiophene to yield J71 (Bin et al., 2016a). After side-chain engineering, J71 realized a deeper HOMO energy level of −5.40 eV, and formed a favorable BHJ morphology, through the combination with ITIC. The corresponding devices achieved a higher *PCE* of 11.41% compared with the J52-based device. Recently, Ding *et al.* (Liu et al., 2020a) designed a wide bandgap polymer called D18 by combining it with BDT, BTA, and thiophene bridge. After blending with Y6, the D18:Y6 based devices showed an outstanding *PCE* of 18.22%, owing to more delayed exciton lifetime of D18. Therefore, D18 is commonly used as the ternary compound to break through the efficiency record.

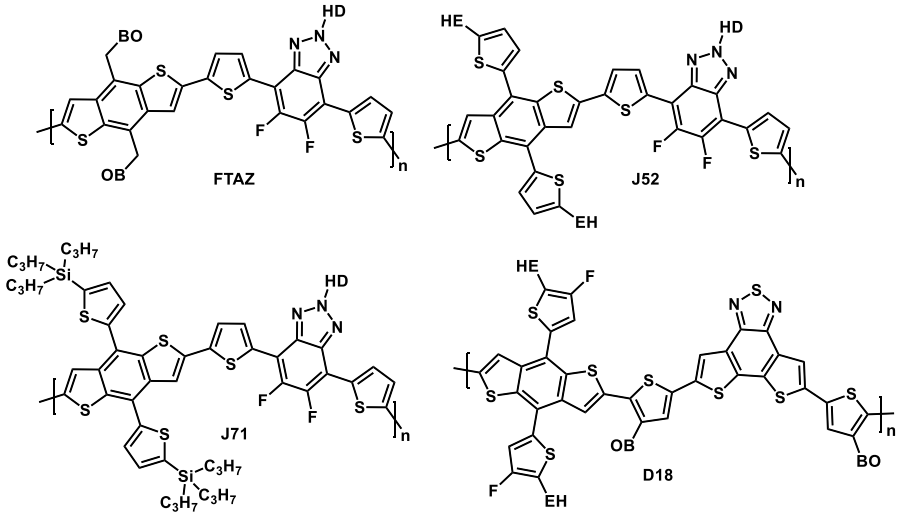

Figure 2.2 The chemical structures of BT based polymer donors

Qx is another popular electron-withdrawing building block in exploring high-performance polymer donors. As exhibited in **Figure 2.3**, many latest Qx-based polymer donors have been designed and applied in OSCs. Hou *et al.* (Liu et al., 2015) successfully prepared three polymer donors, PBQ-0F, PBQ-QF, and PBQ-4F, with different numbers of fluorine atoms on the conjugated skeleton. Among the three polymers, PBQ-4F obtained the deepest HOMO level of −5.05 eV, because of the introduction of fluorine atoms. PBQ-4F based devices

realized a *PCE* of 8.55% by casting with $PC_{71}BM$. Despite the slight deviation of ΔE_{HOMO} by 0.04 eV and ΔE_{LUMO} by 0.24 eV between PBQ-4F and ITIC, the PBQ-4F: ITIC based device exhibited a maximum *PCE* of 11.34% owing to more sufficient charge separation and suppressed bimolecular recombination (Zheng et al., 2018). Compared to fullerene-based devices, devices based on NFAs require less driving force between donors and acceptors, thus demonstrating their great potential for superior device performance. Recently, PTQ10 was developed with a simple structure and low cost, which was regarded as a promising donor material for industrialization (Sun et al., 2018a). The PTQ10: IDIC blend films exhibited a favorable morphology, with strong face-on stacking, thus achieving a *PCE* of 12.7%. Subsequently, PTQ11 was developed by introducing methyl groups onto PTQ10 to realize an up-shifted HOMO level. In addition, PTQ11 obtained enhanced hole mobility and stronger crystallization than PTQ10, leading to an impressive *PCE* of 16.32% eventually (Sun et al., 2020).

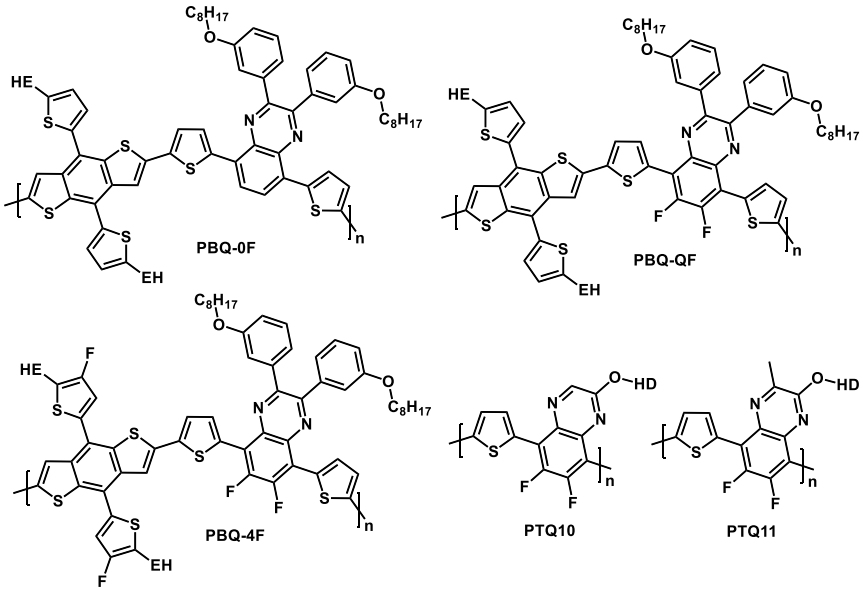

Figure 2.3 The chemical structures of Qx-containing polymer donors

TT is a quinoid structure heterocycle with remarkable stability. Recently, TT has been always used to construct low-bandgap polymers. (**Figure 2.4**) Yu *et al.* synthesized PTB1 in 2009 with complementary absorption with $PC_{61}BM$ and a bandgap of 1.6 eV. Although the PTB1:$PC_{61}BM$ based devices exhibited a higher J_{SC} of 12.5 mA cm^{-2}, the shallow HOMO level of PTB1 led to a quite low V_{OC} of 0.58 eV (Liang et al., 2009). To further improve the morphology and

downshift the HOMO energy level, a series of polymer donors based on PTB1 were developed by incorporating fluorine atoms and tuning the side chains. These efforts ultimately led to the success of PTB7 (Lu and Yu, 2014) and PTB7-Th (Sun et al., 2018c). The versatility and effectiveness of PTB7-Th derivatives have been widely used in semitransparent organic solar cells as well as in tandem solar cells as the rear-cell material (Hu et al., 2020).

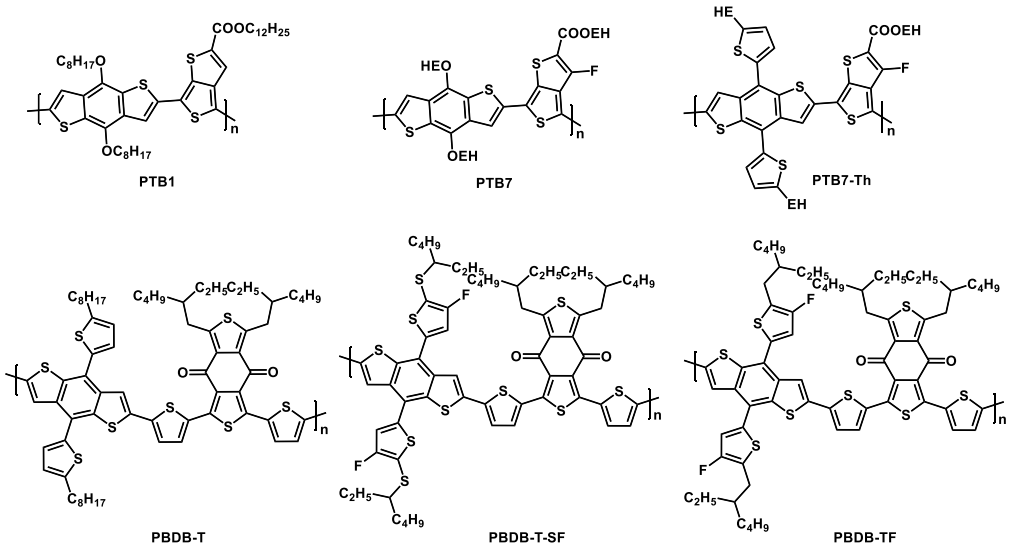

Figure 2.4 The chemical structures of TT and BDD-containing polymer donors

Recently, BDD was regarded as the famous building block to construct high-performance polymer donors. (**Figure 2.4**) Hou *et al.* (Qian et al., 2012) synthesized the first BDD-based polymer donor, PBDB-T, which exhibited a robust temperature-dependent aggregation property and excellent interpenetrating network morphology in the neat films. In 2016, PBDB-T was combined with ITIC to fabricate the active layer with matched energy levels and complementary absorption, resulting in enhanced light harvesting and suppressed E_{Loss}. The blend films also realized a favorable nanoscale phase-separation morphology, leading to an outstanding *PCE* of 11.21% (Zhao et al., 2016b). After fluorination, Hou *et al.* developed PBDB-T-SF based on PBDB-T and IT-4F based on ITIC. The resulting PBDB-T-SF: IT-4F based films exhibited significantly redshifted absorption, and thus a higher efficiency of 13.1% (Zhao et al., 2017), together with an enhanced J_{SC} of 20.5 mA cm^{-2} and maintained V_{OC} of 0.88 V. PBDB-TF, also known as PM6, exhibited better phase-separation morphology when blending with IT-4F, resulting in higher charge mobilities and a *PCE* of 13.7% (Li et al., 2018). Recently, a PBDB-TF-

based device achieved a *PCE* of over 17% by using BTP-eC9 as the acceptor material (Cui et al., 2020c). Currently, the PBDB-T family has been widely used as donor materials to fabricate OSCs with novel NFAs.

2.2.2 The Challenges in Designing Polymer Donors for High-performance OSCs

Conjugated polymer donors have been considered as promising BHJ materials for achieving highly efficient OSCs. In addition, their functions in tandem, ternary, semitransparent, and indoor OSCs have been explored for applications. However, there are several obstacles that must be addressed to further improve device efficiency. One of the challenges involves designing and synthesizing novel conjugated polymers with optimized hole mobilities. Most high-performance polymer donors exhibit low hole mobilities, which is detrimental to enhancing charge collection efficiency, suppressing E_{Loss} and further fabricating thick film devices. Additionally, controlling the morphology of the active layer is critical for enhancing device performance, as it influences exciton generation, charge separation, and collection processes. However, the underlying mechanism of the interplay between the polymer donors and NFAs remains unclear. For instance, although some building blocks, such as diketopyrrolopyrrole (DPP) (Song et al., 2019b;Pan et al., 2020), demonstrated high hole mobilities, their photovoltaic efficiencies were underwhelming after casting with NFAs. Consequently, understanding the molecular interactions between the donors and acceptors is crucial in guiding the design of polymer donors. Once the aforementioned challenges are addressed, the advancement of OSCs will be greatly accelerated.

2.3 Recent Progress on NFAs for OSCs

Electron acceptor materials, as a crucial part of the active layer in OSCs, have attracted increasing attention due to their tunable photophysical properties in recent years. In terms of the development of electron acceptor materials, fused-ring electron acceptor (FREA) materials, particularly fused aromatic diimide

derivatives (such as perylene diimides and naphthalene diimides) (Sun, Chen and Chen, 2019), fullerene acceptors, A-D-A type fused-ring electron acceptors, and A-DA'D-A type FREA, have made significant contributions to the advancement of OSCs. Originally, fullerene derivatives and fused aromatic diimide acceptors were widely used as electron acceptors, but these two types of acceptors have inherent drawbacks. Fullerene acceptors have weak absorption in the visible and near-infrared region, unstable morphology, and difficulties in molecular modification and purification, while fused aromatic diimide acceptors have a narrower absorption range and difficulty in adjusting energy levels. Consequently, these two types of acceptors limit the *PCE* to a moderate level of no more than 13%. However, with the invention of A-D-A type fused-ring electron acceptors in 2015 by Zhan *et al.* and A-DA'D-A type fused-ring electron acceptors in 2017 by Zou *et al.*, the *PCE* of OSCs swiftly increased to 19%. In this chapter, it reviews the existing materials utilized in OSCs regarding structural properties and photophysical modifications. Based on the existing donor materials, this chapter also focuses on the design rules of NFAs, especially A-D-A type and A-DA'D-A type fused-ring electron acceptors, and examines the relationship between molecular structure and device performance.

2.3.1 A-D-A type NFAs

As is shown in **Figure 2.5**, the emergence of ITIC, featuring the typical A-D-A structure, led the exploration and boost of OSCs (Lin et al., 2015). As the most promising acceptor at that time, ITIC and its derivatives possess a distinctive molecular structure, leading to great superiority in photophysical and photovoltaic properties. The molecular structure of ITIC and its derivatives had several notable features: (1) ITIC and its derivatives consist of two electron-deficient end groups (A) and one electron-rich central core (D, fused backbone). The strong push-pull electronic effect resulting from these A and D units can easily regulate the photophysical properties such as absorption and energy levels. Besides, the rigid and planar backbone as well as strong inter/intramolecular interactions was beneficial for charge transfer. (2) The molecular solubility and the miscibility with the donors can be modulated by

side-chain engineering to form a favorable blend and interpenetrated 3D network for sufficient charge transfer tunnels. (3) There are several reaction positions in A-D-A type molecules, enabling the introduction of functional atoms and groups to finely tune the molecular structure and thus the molecular properties. In this section, the development of A-D-A type acceptors based on ITIC would be summarized, focusing on the modification of fused-ring core, end groups, and side chains.

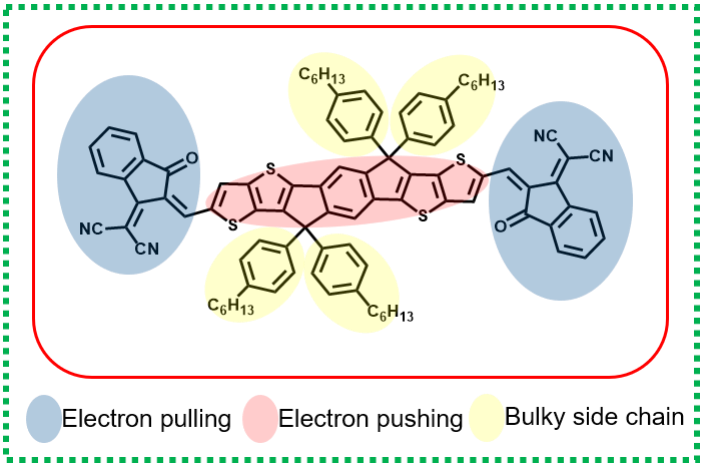

Figure 2.5 The structure of the representative A-D-A type acceptor ITIC

1) Backbone engineering

The backbone of ITIC consists of a central benzene and two flanking thieno[3,2-b] thiophene (TT) blocks that are bridged by two cyclopentadiene groups. Modifications to the fused-ring backbone involve replacing the fused rings, as well as introducing heteroatoms, isomerization, and asymmetry strategy, constructing expanded conjugated backbones.

As is shown in **Figure 2.6**, the benzene-centered IDTIC was firstly reported by Zhan *et al*. (Lin et al., 2016a), constructing pentacyclic indaceno[1,2-b:5,6-b'] dithiophene (IDT) backbone. After blending with the polymer donor PDBT-T1, the PDBT-T1: IDTIC based devices realized a *PCE* of 7.39% and a high V_{OC} of 0.9 V. To optimize IDTIC, the central benzene was replaced with naphthalene to create IHIC1 with a more co-planar backbone, expanded conjugation, thus boosting the electron mobility for IHIC1. Owing to the elevated LUMO energy level, the FTAZ: IHIC1 based devices obtained an enhanced V_{OC}, and a higher *PCE* of 9.21%. Furthermore, FPIC was developed by replacing the naphthalene

core and 3-(Dicyanomethylidene)indan-1-one (IC) end group in IHIC1 with pyrene core and 2-(5,6-Difluoro-3-oxo-2,3-dihydro-1H-inden-1-ylidene)malononitrile (IC-2F), respectively, to expand the conjugation length (Cai et al., 2019). The optimized PTB7-Th: FPIC based devices achieved an efficiency of 8.45%. The enlarged π plane in the center resulted in a blue-shifted absorption and a broader bandgap, but unmatched absorption region with the donor materials. BDT central core was introduced owing to its high planarity, together with enhanced absorption and great charge transfer performance. Based on BDT core, ITIC was isomerized to the novel NFBDT (Kan et al., 2017), which exhibited strong absorption among the range of 600-800 nm and a narrowed E_g of 1.56 eV. After blending with PBDB-T, an impressive *PCE* of 10.42% was achieved. In addition, TT unit is also considered as a promising central core to construct NFAs. By introducing TT unit in the backbone, enhanced ICT and intermolecular interaction can be realized. Based on TT central core and ITIC major structure, Jen *et al.* successfully designed and synthesized 6TIC (Shi et al., 2018). 6TIC exhibited a red-shifted of around 150 nm absorption compared to ITIC. And the PTB7-Th:6TIC based devices realized a *PCE* of 11.07% eventually, owing to the suitable absorption region.

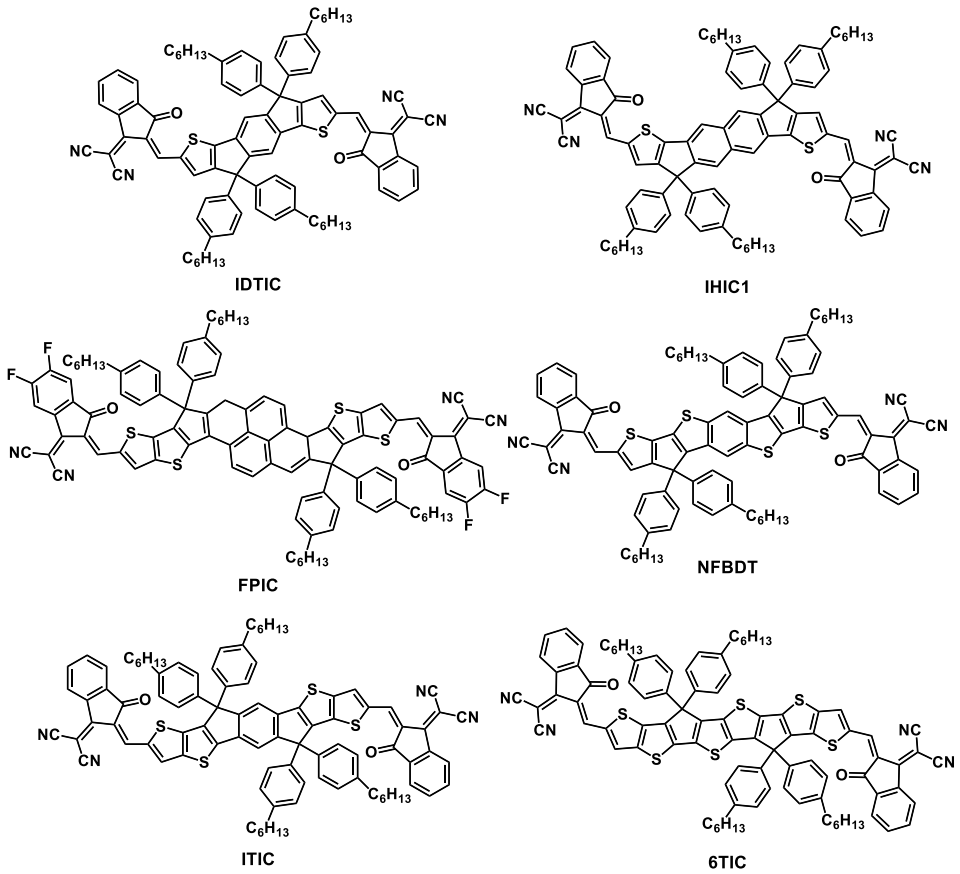

Figure 2.6 Replacement of the central benzene with the fused-ring core

Altering the conjugation length is regarded as another common method to tune the photophysical properties of NFAs. (**Figure 2.7**) Through adjusting the number of fused-rings in the backbone of ITIC, F5IC, F7IC, and F9IC were synthesized based on thiophene (T), TT, and dithieno[3,2-b:2',3'-d]thiophene (TTT) (Dai et al., 2018b). Narrowed bandgaps and elevated energy levels were obtained as the increasing number of rings. Along with the enhancement of intermolecular interaction, the electron mobilities of the blend films led to increased *PCE*s from 5.6% to 11.7% for F5IC, F7IC and F9IC, respectively. Zhan *et al.* (Dai et al., 2018a) replaced the central benzene core with TT unit in F5IC, F7IC and F9IC, constructing F6IC, F8IC and F10IC. Three optimized NFAs exhibited similar property patterns like F5IC, F7IC and F9IC, while stressing the importance of extending molecular conjugation. Based on the symmetric backbones, asymmetric strategy was used to fine-tune the photophysical properties and enhance the dipole moments, for achieving higher carrier mobility and better blend morphology. Then, Yang *et al.* (Gao et al., 2018b;Gao et al., 2018c) employed asymmetric strategy and synthesized asymmetric IDT6CN-M and IDT8CN-M, based on T, TT and TTT units and

methylated IC (IC-M) end groups. The asymmetric acceptors realized high *FF*s of 77% and 79% after casting with PBDB-T.

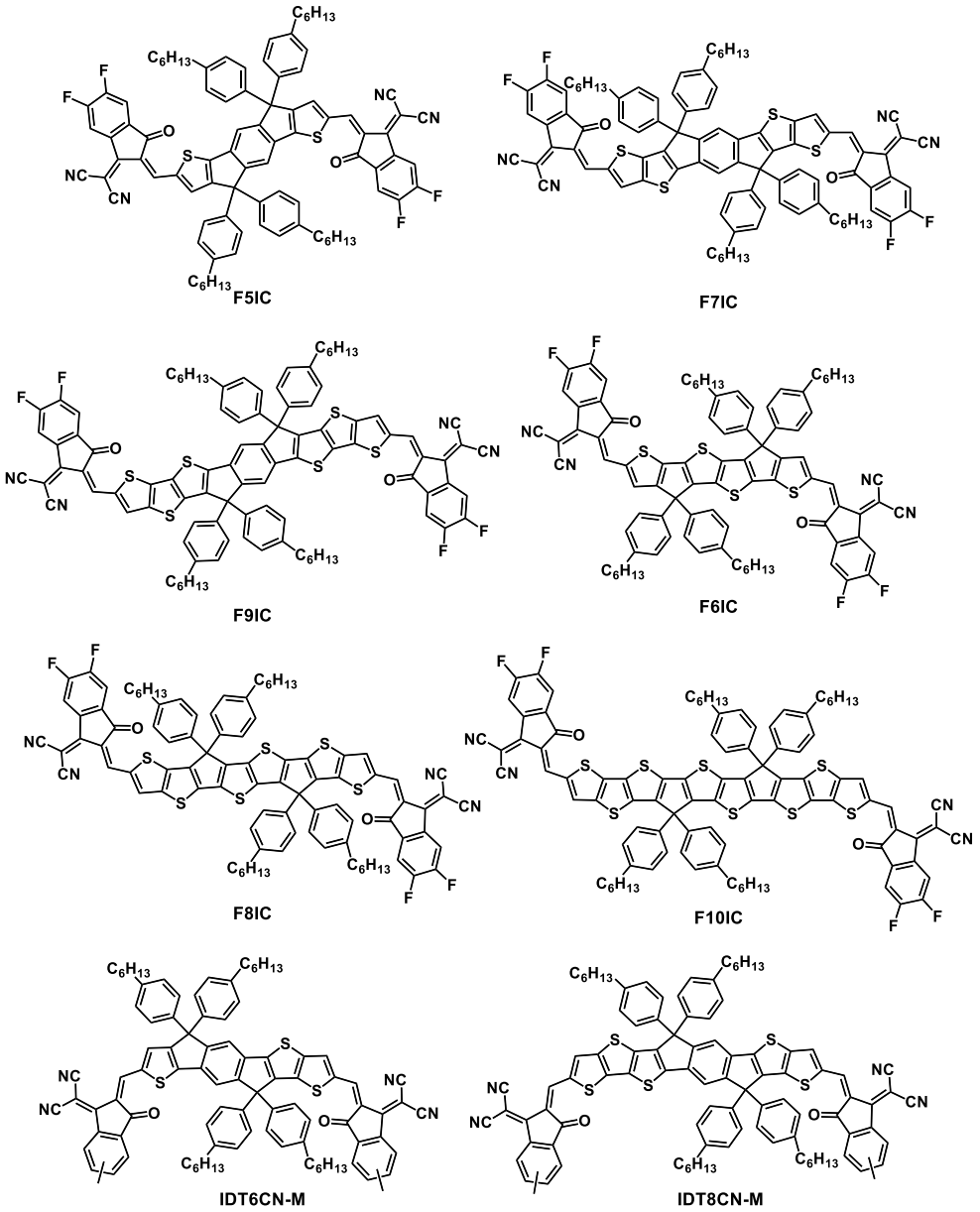

Figure 2.7 Conjugated length expansion of the backbone

Heteroatom substitution, including oxygen, nitrogen, silicon, and selenium, also has gained popularity in designing novel NFAs. (**Figure 2.8**) For instance, Ding *et al.* (Xiao et al., 2017) incorporated oxygen atoms into the bridging group of cyclopentadiene and explored carbon-oxygen-bridged A-D-A type NFAs. In contrast with F8IC, the carbon-oxygen-bridged COi8DFIC exhibited red-shifted absorption and elevated energy levels, leading to improved device performance. The Selenium (Se) atom in selenophene is more polarizable compared to the Sulphur (S) atom in thiophene, resulting in lower electron

density around it. This characteristic gives rise to stronger intermolecular interaction for Se-substituted backbone, leading to better charge transport properties. Subsequently, the Se-substituted NFAs, SRID-4F and TRID-4F, exhibited higher J_{SC} values and lower energy loss than the Se-free IT-4F, highlighting the superior properties of Se.

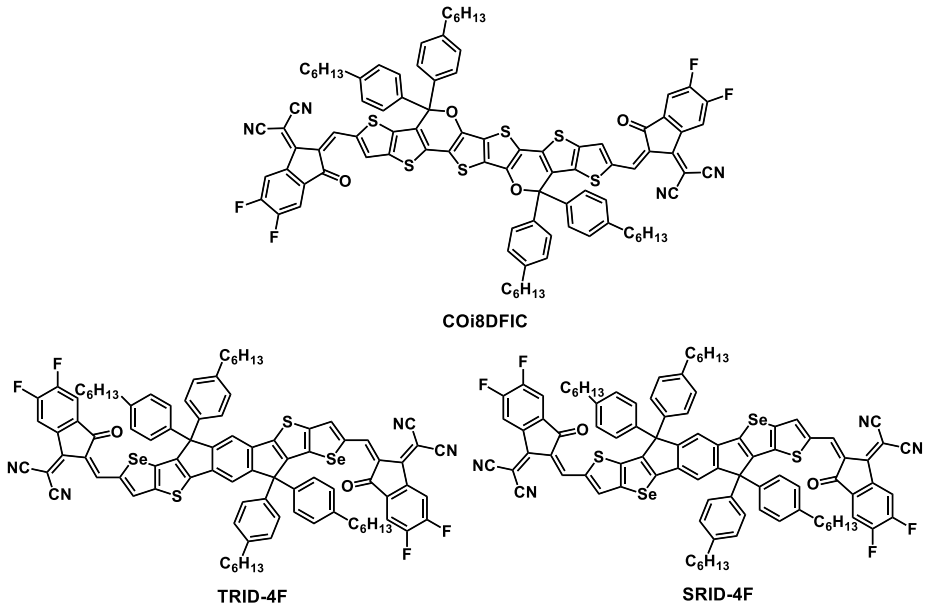

Figure 2.8 Introduction of asymmetric backbone and heteroatoms

2) End group engineering

End group engineering is an effective method to adjust the ICT and intermolecular interactions, owing to the strong electron-deficient properties. IC and its derivatives are the most famous among the end-capping groups. By substitution of the halide groups or alkyl groups with the hydrogen in IC, the stacking inside the blend films can be affected a lot. Herein, end group engineering based on IDTT core is displayed in **Figure 2.9** and reviewed.

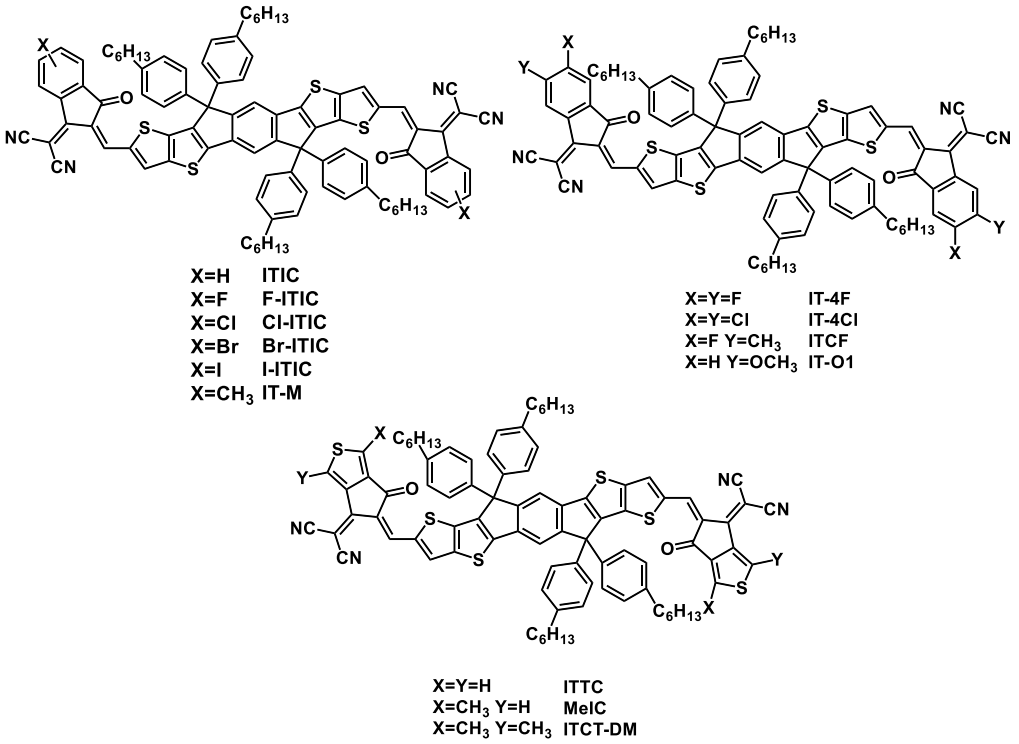

Figure 2.9 End group engineering on A-D-A type NFAs

To explore the impact of halogenation on A-D-A type NFAs, four ITIC based NFAs named as F-ITIC, Cl-ITIC, Br-ITIC, I-ITIC were synthesized (Yang et al., 2017). The halogenated NFAs realized red-shifted absorption and down-shifted energy levels, because of the heavy atom effect of Se and its stronger electron-deficient ability. After blending with PTPDBDT donor, these ITIC derivatives achieved higher *PCE*s than ITIC-based devices. Furthermore, IC-2F and IC-2Cl were introduced to construct IT-4F (Zhao et al., 2017) and IT-4Cl (Zhang et al., 2018a). Compared to IT-2F/2Cl, IT-4F/4Cl exhibited red-shifted absorption and deeper energy levels, causing a lower V_{OC} but increased J_{SC} and *FF*. Eventually, the devices based on PBDB-TF and IT-4Cl/4F achieved *PCE*s over 13%. Additionally, methyl and methoxy groups were always introduced into end-capping groups. Methyl-substituted IT-M was developed by Hou *et al.* with a blue-shifted absorption and up-shifted energy levels. Subsequently, the *PCE* of PBDB-T:IT-M devices achieved 12.05%, along with an enhanced V_{OC} (Li et al., 2016). In another work, Yang *et al.* introduced F atom together with methyl group to the end groups and prepared ITCF (Hao et al., 2019), realizing a high *PCE* over 13% with an impressive *FF* approaching 79%. Hou et al. utilized a range of alkoxyl groups with different lengths to construct IT-O1 to IT-O4 (Zhu et al., 2017). The NFAs with longer alkoxyl chains exhibited larger

domain size, thus resulting in limited J_{SC} and *FF*. Hence, IT-O1 realized better device performance of 11.6% among this series. After replacing benzene in IC by thiophene, a novel end group and its derivatives were explored. Zou *et al.* (Zhang et al., 2017) developed a novel terminal group with thiophene group, and synthesized a novel NFA called ITTC, by connecting the end group with the IDTT core. Owing to its narrowed E_g and higher energy levels, the ITTC-based devices obtained a higher *PCE* of 10.4% compared to ITIC. In addition, Yang *et al.* (Luo et al., 2018) and Zhan *et al.* (Yan et al., 2018b) introduced methyl groups onto the thiophene ring and successfully synthesized two new acceptors, MeIC and ITCT-DM, with higher energy levels. As a result, the J71:MeIC and PBDB-T:ITCT-DM devices showed impressive efficiencies of 12.54% and 10.56%, respectively.

3) Side-chain engineering

The manipulation of side chains is pivotal in regulating both the solubility and photophysical properties. Modification on the side chains (R_1 in central benzene ring, R_2 in cyclopentadiene, R_3 in TT unit) in the backbones can be an effective method of trimming molecular structures, as depicted in **Figure 2.10**. Herein, side-chain engineering based on IDTT core would be reviewed on behalf of A-D-A type NFAs.

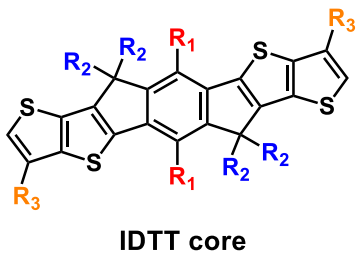

Figure 2.10 Side-chain engineering on IDTT core

Significant efforts were invested in modifying the side chains (R_2) on IDTT backbone. (**Figure 2.11**) Among various side-chain engineering, the common approach involved attaching side chains to the sp^3-hybridized carbon of the bridged cyclopentadiene. Owing to the paired sp^3-hybridized carbons, which were centrosymmetric and located diametrically in the backbone, four hexylphenyl chains heading to different directions were resulted. Li *et al.* (Yang et al., 2016) altered the position of hexyl in the side chains of ITIC and

synthesized m-ITIC, leading to enhanced absorption coefficients and better crystallinity. As a consequence, the J61:m-ITIC devices displayed a superior *PCE* of 11.7% compared to ITIC-based devices. At the same time, Zhan *et al.* (Lin et al., 2016b) introduced thiophene ring instead of benzene in the side chains to construct ITIC-Th. The thienyl side chains were beneficial for improved intermolecular stacking and more sufficient charge transfer. Consequently, the PDBT-T1:ITIC-Th based device achieved a *PCE* of 9.6%. Besides, alkyl chains were also commonly utilized in NFAs. For instance, Heeney *et al.* (Fei et al., 2018) reported C8-ITIC with octyl side chains, leading to a decreased optical bandgap and enhanced crystallinity. This modification eventually resulted in an impressive *PCE* of 13.2% when blended with PFBDB-T.

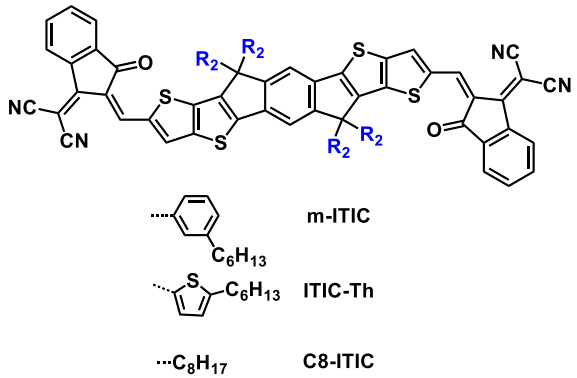

Figure 2.11 Side-chain engineering on R_2 side-chain

Compared to the modification in R_2, side-chain engineering based on R_1 and R_3 in IDTT-based NFAs were seldom explored. In 2018, hexyl side chains were firstly introduced into the TT block in the backbone of ITIC to lock the conformation and develop a novel SMA named as ITC6-IC (as shown in **Figure 2.12**) (Zhang et al., 2018b). According to the calculations of torsion angles, the hexyl substituted TT unit in ITC6-IC with stronger steric hindrance, was beneficial to form a more planar molecular structure. Different from ITIC, ITC6-IC obtained slightly blue-shifted absorption and elevated LUMO energy level, leading to enhanced V_{OC} of 0.97 V and thus a promising *PCE* of 11.61%, after casting with PBDB-T. Furthermore, a novel NFA, named as IM-4F (Zhang et al., 2020d), was successfully designed and synthesized by replacing the hydrogen in R_1 with methyl groups. Consequently, IM-4F exhibited red-shifted absorption compared to IT-4F, owing to the electron-donating property of

methoxy and methyl groups. Benefitting from the enhanced ICT, IM-4F obtained elevated energy levels. Therefore, the PBDB-TF:IM-4F based devices realized improved J_{SC} and V_{OC}, together with a *PCE* of 14.17%, respectively. Based on IM-4F and ITC6-4F, IMC6-4F was designed combined with conformation lock and methyl substitution in the central core, delivering an impressive *PCE* of 15.57%, with an outstanding *FF* of 77% (Zhang et al., 2020b).

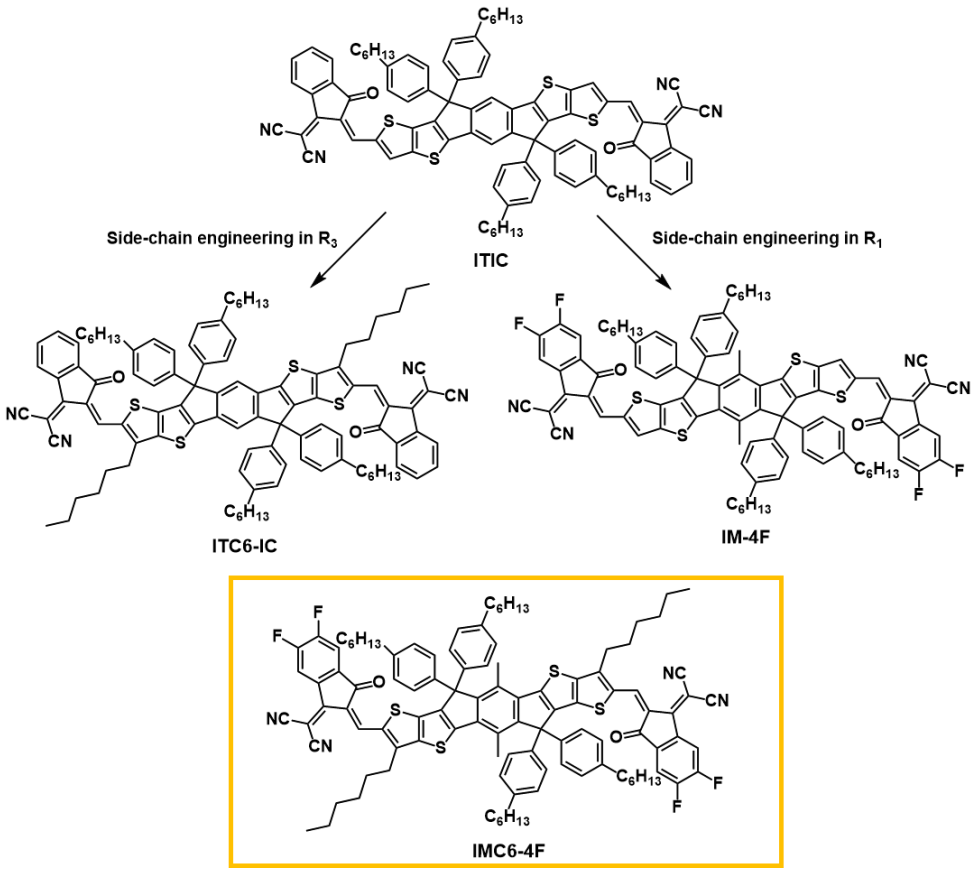

Figure 2.12 Structure design for IMC6-4F

2.3.2 A-DA'D-A type NFAs

As Y6 was reported by Zou *et al.* (Yuan et al., 2019b) in 2019, the inception of a new era in NFAs was started. The peculiar molecular structure of Y6 and its derivatives induced exceptional absorption and photophysical properties. Moreover, the energy levels of these molecules can facilitate efficient electron-hole transfer between NFAs and donors like PBDB-TF, D18 and PTQ-10. Compared to A-D-A type NFAs, the A-DA'D-A configuration and C-shaped conformation enable sufficient properties in the molecules. Similar molecular

engineering methods to optimize the A-D-A type NFAs, can be applied to A-DA'D-A type NFAs as well. Recently, the *PCE* of single junction OSCs has risen from 15.7% to 19.6%, accompanying with the innovation of Y series NFAs. It is crucial to conduct careful structural modifications on A-DA'D-A type NFAs, as the slight modifications can affect the performance a lot. At the same time, the C-shaped structure of Y-series NFAs should be maintained to keep a large dipole moment. Consequently, there was seldom work on backbone modification. And this thesis will focus on core engineering instead of backbone engineering.

1) Core engineering

Modifying the D and A' moieties can tune the ICT strength and photophysical properties of the Y-series NFAs. Until now, the BT core in Y6 has been replaced by Qx and 2-alkylbenzotriazole (BTz) to reconstruct the central core. (**Figure 2.13**) The modification on the D moiety would influence the properties of Y series to a large extend, thus only Se substitution was reported. (**Figure 2.14**)

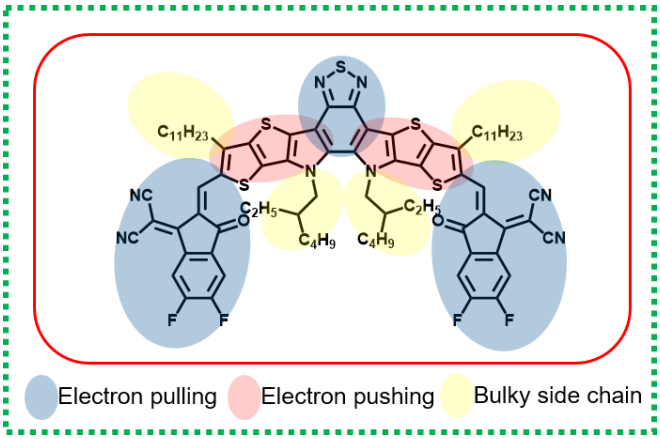

Figure 2.13 The structure of the representative A-DA'D-A type acceptor Y6

Zhu *et al.* first introduced Qx cores into Y series and reported 2,3-dimethyl-substituted AQx-1 and AQx-2 without substitution (Zhou et al., 2020b). Owing to the slightly electron-donating methyl group, AQx-1 obtained red-shifted absorption in chloroform solution compared to AQx-2. While the absorption of neat films exhibited different trend, because the steric hindrance of the methyl groups in AQx-1 caused weaker intermolecular stacking and blue-shifted absorption. Hence, the PBDB-TF: AQx-2 based devices achieved a higher *PCE* (16.6%) than that of the PBDB-TF: AQx-2 based devices (13.3%), owing to the

stronger stacking in PBDB-TF: AQx-2 blend films. Later, Lin *et al.* and Yan *et al.* independently reported NFAs based on Se-substituted BT core, denoted as Y6Se and Y6-Se (Yu et al., 2020), with the same chemical structures. After Se-substitution, red-shifted absorption was realized from Y6Se, which accounted for the increased J_{SC} and thus an impressive *PCE* of 17.7% from the D18: Y6Se based devices (Zhang et al., 2020c). Based on Y6, the S atom in D moiety was replaced with Se atoms by Jen *et al.* (Lin et al., 2020), and constructed CH1007 with varied ICT. Consequently, CH1007 realized closer stacking with a shorter π-π distance (~3.3 Å) compared to Y6 (~3.7 Å), that was observed from in the single crystal characterization. The ternary devices based on PBDB-TF: CH1007: $PC_{71}BM$ achieved a *PCE* of 17.08% with an impressive J_{SC} of 27.48 mA cm^{-2}, benefiting from the broad absorption and higher charge mobilities than that of Y6 counterparts. The innovation of Y-series NFAs was attributed to the implementation of various molecular engineering originated from A-D-A type acceptors. It is evident that introducing a stronger D unit or a weaker A' unit into the DA'D core resulted in enhanced ICT. For further optimizing the A-DA'D-A type NFAs, enhancing the ICT effect is a feasible method to obtain more red-shifted absorption. However, setting up suitable energy levels is particularly challenging with compressed E_g induced by stronger ICT.

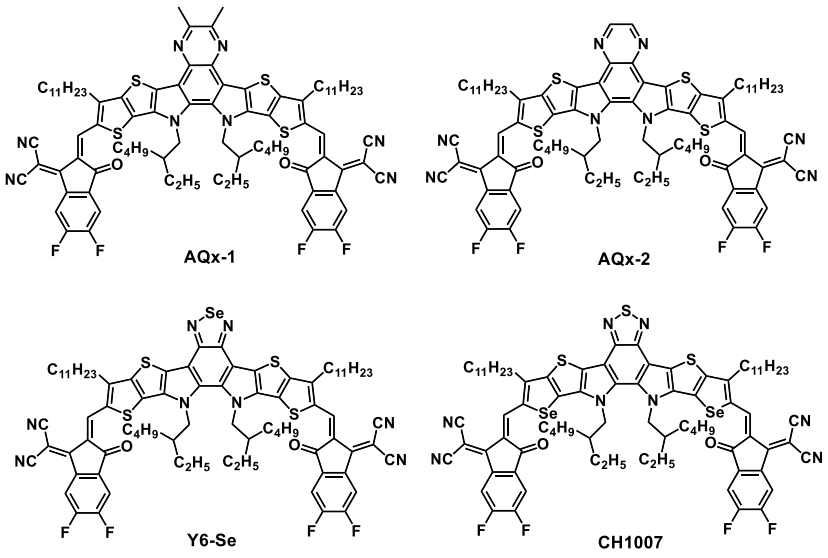

Figure 2.14 Core engineering on A-DA'D-A type NFAs

2) End group engineering

The end group engineering in A-DA'D-A type NFAs is similar to A-D-A type NFAs mentioned above. IC-2F and IC-2Cl have been the most popular end groups used for end-capping. Hou *et al.* suggested that IC-2Cl based NFAs tend to exhibit more suppressed E_{Loss} than other species. Therefore, more NFAs with IC-2Cl end groups emerged in the past three years. Moreover, there are also some successful examples of end group engineering in reinforcing ICT and absorptions. (**Figure 2.15**)

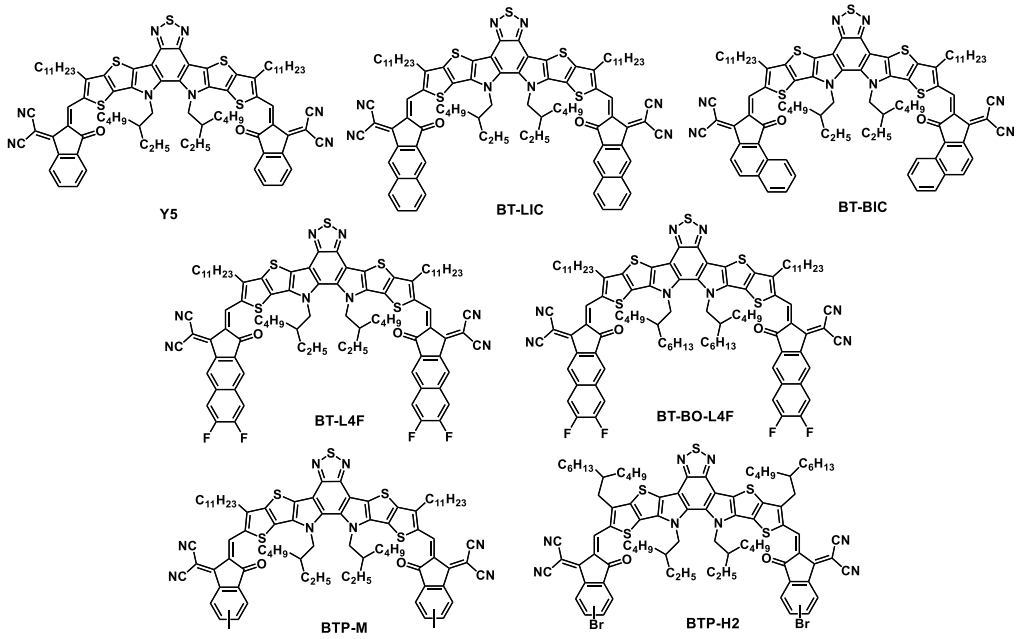

Figure 2.15 End group engineering on A-DA'D-A type NFAs

Zou *et al.* (Yuan et al., 2019a) utilized original IC group and prepared Y5, which showed a blue-shifted absorption edge compared to Y6. Y5 was compatible with many donor polymers. Among them, the PBDB-T: Y5 based devices achieved the highest *PCE* of 14.1%. Later, a series of NFAs based on benzoindanone end group was reported by Marks *et al.* (Li et al., 2021b) called BT-LIC, BT-BIC, BT-L4F, and BT-BO-L4F. Benefitting from more extended conjugation structure, BT-BO-L4F obtained a narrower E_g and a red-shifted absorption edge. Subsequently, the PBDB-TF: BT-BO-L4F based devices achieved a high *PCE* of 16.6% with an outstanding J_{SC} of 27.8 mA cm^{-2}. In addition, mono-substituted IC can act as potential end groups due to their moderate electron-deficient properties. For instance, Chen *et al.* (Zhan et al., 2020) designed the BTP-M with mid band gap for ternary OSC devices. By incorporating methyl group into the IC end group in BTP-M, the absorption of

BTP-M blue-shifted slightly. And the *PCE* of PM6: Y6: BTP-M ternary system increased from 15.61% to 17.03%, with suppressed energy loss and enhanced J_{SC}. Recently, Chen *et al.* (He et al., 2022b) presented an NFA, BTP-H2, with single brominated end group, which obtained remarkable OSC performance of 19.2% in *PCE* (a V_{OC} of 0.89 V, a J_{SC} of 26.68 mA cm^{-2}, and an *FF* of 80.7%) after being integrated as the third component in the PM6: L8-BO blends. As the introduction of IC-Br group, the BTP-H2 based films exhibited more ordered molecular packing, together with a slightly blue-shifted absorption edge. After adding BTP-H2, the ΔE_{nonrad} of the ternary devices was significantly suppressed, thus promoting sufficient charge generation. The design rules of the end groups for Y-series NFAs were similar to A-D-A type NFAs. However, the goal of end group engineering was still limited to promoting the molecular stacking and chasing for higher *PCE*s instead of stability. To further improve the stability of devices, next generation of end groups should possess more robust structures.

3) Side-chain engineering

The solubilities, crystallinities, morphologies, and photophysical properties of Y-series NFAs can be altered through side-chain engineering, which also affects the packing of NFA molecules.

As is shown in **Figure 2.16**, the *N*-alkyl chains in Y series (BTP-4F/4Cl-8, BTP-4F/4Cl-12, and BTP-4Cl-16) with varied lengths (2-ethylhexyl, 2-butyloctyl, and 2-hexyldecyl) were synthesized to explore the designing rules of side-chain engineering (Hong et al., 2019;Cui et al., 2020a). Consequently, the 2-butyloctyl substituted BTP-4F/4Cl-12 exhibited balanced solubility and crystallinity for decent film morphology. And the *PCE*s of PBDB-TF:BTP-4F/4Cl-12 based devices realized 16.4% and 17.0%, respectively. Another successful side-chain engineering was reported by Yan *et al.* (Jiang et al., 2019), with different side chains in the pyrrole ring. The alkyl chains in N3 and N4 were beneficial for enhancing aggregation and crystallinity. In addition, N3 (3-ethylheptyl) and N4 (4-ethyloctyl) with extended alkyl chains would alleviate the steric interactions between the core and branches. Eventually, N3-based

OPV devices (PM6:N3 and PM6:N3:$PC_{71}BM$) showed exceptional *PCE*s of 15.98% and 16.74%, respectively.

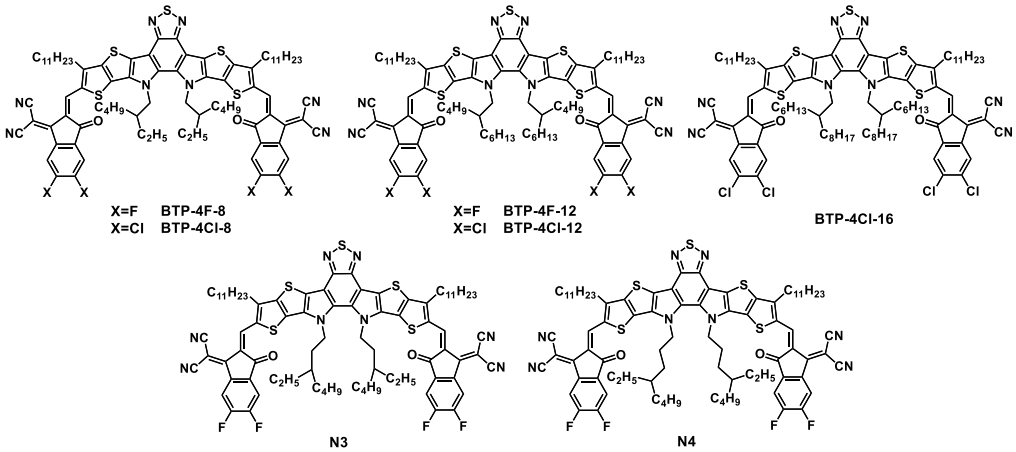

Figure 2.16 Side-chain engineering on the *N*-alkyl chains in A-DA'D-A type NFAs

There was also many successful side-chain engineering in outer alkyl chains. (**Figure 2.17**) Hou *et al.* investigated the impact of outer side chains with different lengths and synthesized BTP-eC7, BTP-eC9, and BTP-eC11 (BTP-4Cl-12) (Cui et al., 2020b). They chose 2-butyloctyl as the *N*-substituting side chain, and *n*-heptyl, *n*-nonyl, and *n*-undecyl as outer side chains in BTP-eC7, BTP-eC9, and BTP-eC11, respectively. After optimization, BTP-eC9 exhibited more balanced crystallinity and solubility. Owing to more ordered stacking indicated from the lower Urbach energy in BTP-eC9 blend films, the PBDB-TF: BTP-eC9 based devices achieved a promising *PCE* of 17.8%. Another remarkable work on tuning the outer side chains was reported by Sun *et al.* (Li et al., 2021a). L8-BO, L8-HD, and L8-OD were synthesized with modified side chains of 2-butyloctyl, 2- hexyldecyl, and 2-octyldodecyl. The blue-shifted absorptions of these NFAs were attributed to their distinct molecular packing patterns compared to Y6, as demonstrated in single-crystal characterization. Benefitting from the elevated LUMO energy levels, three molecules exhibited enhanced V_{OC} and maintained J_{SC}. At the same time, the PBDB-TF: L8-BO based devices realized a remarkable *PCE* of 18.32% with an outstanding *FF* of 81.5%. Not only solubility and processability, the modification of inner and outer side chains also impacts the photophysical characteristics of Y series NFAs by tuning the aggregation in the blend films. The employment of these bulky side chains (such as branching side chains) can improve the LUMO

energy levels and thus obtained higher V_{OC} and maintained absorption and J_{SC}, making them ideal third components for energy levels with ladder pattern and alloyed morphology in high-performance ternary OSCs.

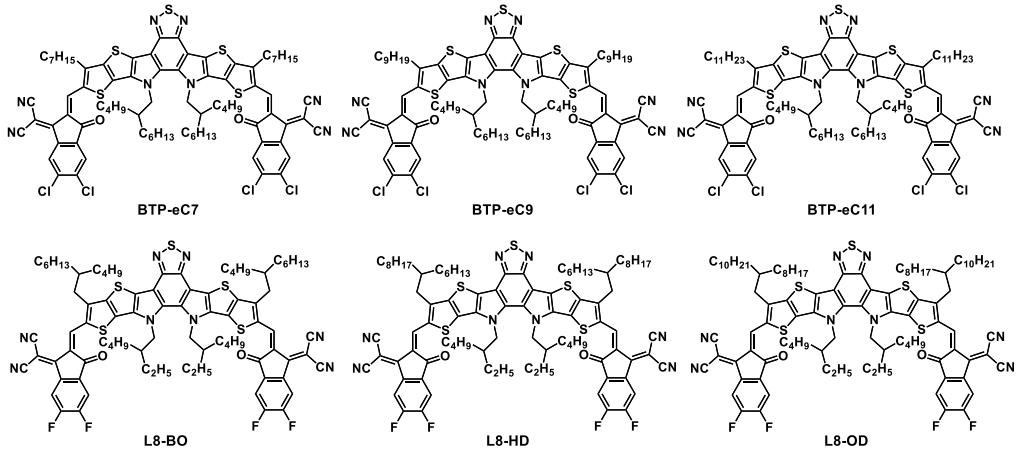

Figure 2.17 Side-chain engineering on the outer chains in A-DA'D-A type NFAs

2.3.3 The Challenges in Designing NFAs for High-performance OSCs

This chapter reviews the progress on polymer donors and NFAs in OSCs. The following conclusions can be drawn based on the above discussion.

(1) Though the efficiency of OSCs has achieved 19%, the material innovation has arrived at bottleneck. The NFAs used in the active layer reported, hardly leave without BTP-eC9, L8-BO, Y6, and N3. It can be reckoned that there has been seldom substantively meaningful progress on NFAs. And BTP-eC9, L8-BO, Y6, and N3 are A-DA'D-A type NFAs based on the similar BTP core. Therefore, it is necessary to design novel cores instead of BTP derivatives.

(2) The underlying logic of molecular design is still based on the contribution of electron-deficient core to the whole backbone. Actually, the electron push-pull effect of A-DA'D-A type molecules can be adapted to A-D-A type molecules and to adjust the ICT.

(3) As reviewed about A-DA'D-A type molecules, the construction of pyrrole rings relies on the ring-closure reaction, which is challenging for molecular design and synthesis. Additionally, the pyrrole-contained building blocks

utilized in NFAs were limited. Therefore, it is essential to explore novel building blocks in NFAs.

(4) The energy loss mechanism in OSCs is still unclear. Until now, seldom works regarding materials in OSCs focus on suppressing energy loss. In addition, only when the devices were characterized and a high V_{OC} was obtained, the energy loss was considered to be analyzed in these works, which is unreasonable and illogical. Hence, it is challenging but essential to design molecules with suppressed energy loss before synthesis and device fabrication.

2.4 Aims and Objectives

In this thesis, a novel TP block was introduced in backbones to construct new NFAs and to investigate the design rules for highly efficient binary OSCs. It aims to provide a more comprehensive understanding of the molecular design of novel backbones, to give insights into better material design of NFAs and the corresponding devices. The main objectives of this thesis include:

(1) Designing novel NFAs based on TP block and the reliable reaction routes to obtain these molecules. These NFAs would be prepared by multi-step organic synthesis, and each intermediate should be characterized by nuclear magnetic resonance (NMR) and matrix-assisted laser desorption/ionization time of flight mass spectrometry (MALDI-TOF-MS).

(2) Photophysical property analysis. Once obtaining the goal NFAs, the photophysical characterizations, including Ultraviolet-visible spectroscopy (UV-Vis) and Ionisation potential spectroscopy (IPS), should be conducted to learn the absorption, energy levels, and structural-property relationships. The electrochemistry and photophysical properties of NFAs are essential to help choose appropriate donor materials, when constructing binary solar cells.

(3) After choosing proper donor and acceptor materials, OSC devices will be fabricated and optimized by manipulating donor/acceptor blend ratios, introducing various additives, and varying annealing temperatures.

Subsequently, the photovoltaic properties of the corresponding devices will be tested to evaluate the binary devices and the synthesized NFAs.

(4) To explain the photovoltaic differences in the devices, the surface morphology of the different blend films should be characterized by atomic force microscopy (AFM) and transmission electron microscope (TEM) to check the surface roughness and phase separation. The morphology of D/A blend films can be illustrated to compare different NFAs after blending with the same donor material. The results can provide guidance for further structural optimization.

(5) The stacking in the blends can be detected to evaluate the intermolecular interaction. Commonly, more ordered π-π stacking in the blends tends to facilitate enhanced crystallinity and lower energetic disorder in the blend films. Therefore, the molecular stacking properties will be used to compare the energetic disorder, $\Delta E_{\mathrm{nonrad}}$, and electron mobilities. Around the stacking properties, NFAs can be optimized through molecular engineering.

Based on the introduction of the TP block, it is expected to obtain highly efficient NFAs with suppressed E_{Loss}, which will benefit the understanding and design of NFAs and the corresponding devices.

2.5 Outline of Thesis

This thesis is organized into the following seven chapters:

Chapter 1 provides a concise overview for the evolution of OSCs. The working mechanism and device architectures for OSCs are also introduced. Additionally, this chapter highlights the development and challenges for acceptors in OSCs.

Chapter 2 reviews the existing materials utilized in OSCs regarding structural properties and photophysical modifications. Based on the existing donor materials, this chapter also reviews the design rules of A-D-A type and A-DA’D-A type NFAs, followed by the introduction of challenges and barriers in designing high-efficient NFAs.

Chapter 3 describes the methodology and characterizations utilized in this thesis. It starts from the characterization of the organic intermediates and final products. It then specifies the characterization methods of nano-morphology of the active layer, including AFM, TEM, and grazing incidence wide-angle X-ray scattering (GIWAXS), etc. Moreover, the device physics, including interfacial electronic structures and E_{Loss}, is important for understanding the working mechanism of OSCs. Therefore, the characterization methods for device physics are illustrated to seek new approaches to further improve the photovoltaic performance of OSCs.

Chapter 4 demonstrates the novel TP building block and exhibits its potential for constructing highly efficient NFAs. The TP unit was firstly introduced as a building block to construct pyrrole-containing conjugated backbones for synthesizing NFAs. Two novel acceptors, namely, PTBTP-2F and PTBTP-4F, were designed and synthesized successfully. The photophysical and electrochemical properties, device performance, E_{Loss}, and morphology of the blend films were investigated to evaluate the performance of the novel acceptors. The end-group capping effects on the acceptors and the performance of the TP unit were also investigated through evaluating the performance of the acceptors.

Chapter 5 demonstrates that asymmetric design strategy would be a promising method for finely regulating the molecular structure and synthesizing high performance NFAs for fabricating OSCs with high *FF*s and low E_{Loss}. Two asymmetric acceptors PTBTT-4F/4Cl were designed and synthesized, derived from IT-4F/4Cl and PTBTP-4F/4Cl. The photophysical and photovoltaic properties of IT-4F/4Cl, PTBTT-4F/4Cl, and PTBTP-4F/4Cl were investigated to address the influence of molecular backbone engineering of acceptors on the device performance of OSCs. Three chlorinated acceptors were synthesized and compared with fluorinated acceptors as a check experiment to verify the asymmetric design strategy in this work.

Chapter 6 further optimized the PTBTT backbone through core segmentation and isomerization. The chapter provides a rational method of further suppressing V_{OC} loss and improving the ultimate device performance. The isomerized TPBTT-4F/4Cl obtained stronger ICT, thus leading to elevated

HOMO energy level and reduced bandgap (E_g). According to $E_{Loss} = E_g - qV_{OC}$, the reduced E_g and enhanced V_{OC} indicated E_{Loss} was suppressed in the TPBTT-4F/4Cl based devices. Furthermore, compared to PTBTT derivatives, the isomeric TPBTT derivatives exhibited planar molecular structure and closer intermolecular stacking, affording higher crystallinity of neat films relative to PTBTT derivatives. Therefore, the reduced energy disorder and corresponding lower Urbach energy (E_u) in TPBTT-4F/4Cl based devices exhibited low E_{Loss} and high charge-carrier mobility in OSCs. Benefitting from synergetic control of molecular stacking and energetic offsets, a maximum *PCE* of 15.72% was realized in TPBTT-4F based devices, along with a reduced ΔE_{nonrad} of 0.276 eV.

Eventually, Chapter 7 summarises the main findings in NFAs based on TP. The principal contributions of this thesis are emphasized, followed by the exploration of potential extensions and future research directions.

Chapter 3

Methodology

3.1 Synopsis

The chapter would first review the device fabrication methods for OSCs, and introduce a more detailed fabrication method used in this thesis. Then, it would move on to the calculation methods for molecular structures, including molecular optimization, energy levels, and electrostatic potential (ESP). Subsequently, the characterization technologies for the organic intermediates and final products are described. It then specifies the characterization methods of nano-morphology of the active layer, including AFM, TEM, and GIWAXS, etc. Moreover, the characterization methods for device physics, such as E_{Loss} and space charge limited current measurements, are introduced. The specific characterization procedures are discussed in each chapter.

3.2 Fabrication Methods of OSC Devices

Not only the device performance but also the material utilization and cost relate closely to the fabrication method. The fabrication methods even affect surface roughness and molecule arrangement.

Numerous researches reported about the deposition methods like thermal annealing (Guo et al.), and sputtering (Jeon et al., 2016). The vacuum deposition

method has been widely used to fabricate organic semiconductors, especially for small molecules, multilayer devices, and controlling the thickness (Wang and Zhan, 2016). The organic materials squeezed by point injection were evaporated at high temperatures under high pressure on the ITO source plate. This method always leads to poor film uniformity, and the point source sometimes results in material wasting which is one of the main problems in the process. Additionally, large area-size panels, as well as large-scale production (Chatterjee, Jinnai and Ie, 2021), demand a larger vacuum environment. Therefore, the original vacuum technique is unrealistic for applications in digital displays owing to the high manufacturing cost and waste.

Compared to the relatively high cost of vacuum deposition methods, solution processing methods like spin-coating is simpler, with higher resource utilization, and easier to scale up. Spin-coating is commonly chosen to fabricate OSC devices (Li et al., 2022b). The whole process is shown below (**Figure 3.1**). The solution containing organic molecules is coated on the ITO layer. Then the layer with high viscosity is rotated at high speed and dried with airflow. When the film preliminarily forms, it is then heated to remove the solvent further and obtain the final film. The spin speed controls the thickness of the film. It has to be noticed that the film roughness is related to fabrication methods. From the AFM images, it is found that the spin-coated device is much smoother.

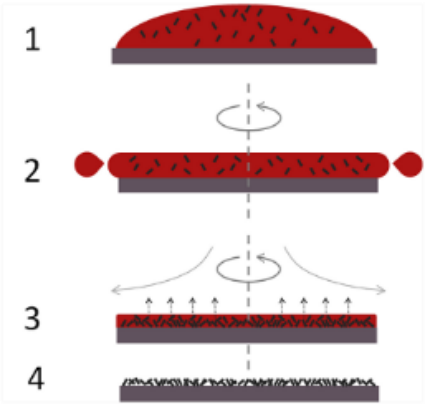

Figure 3.1 Procedures of spin-coating for preparing OSCs

Eventually, the devices were fabricated with a standard architecture of indium tin oxide (ITO) /PEDOT:PSS/active layer/PDINN/Ag. The ITO substrates were first cleaned by sequential sonication in soap-deionized water, deionized water, and ethyl alcohol for 15 min, respectively. Then, the substrates were dried with

high pure nitrogen gas and treated with oxygen plasma for 3 min to improve their work function and clearance. The poly-(3,4-ethylenedioxythiophene): poly-(styrenesulphonicacid) (PEDOT: PSS) (clevios P VPAl 4083, purchased from H. C. Starck co. Ltd.) solution was spin-coated to fabricate thin films on the cleaned ITO substrates at 4500 rpm for 30 s and annealed at 150 °C for 30 min in air. All of the solutions in chloroform were at a total concentration of 16 mg/mL, with different D/A ratios and volume ratios of 1,8-diiodooctane (DIO) or 1-chloronaphthalene (Fei et al.) as the additive. The solutions were stirred for 14 hours at RT and then spin-coated at 2500 rpm~3500 rpm for 30s on top of the PEDOT: PSS layer in high purity nitrogen-filled glove box. The active layer was then thermally annealed for 5 min at various temperatures. Afterward, a PDINN cathode interlayer was spin-coated onto the active layer at 2500 rpm for 30s. Finally, 100 nm Ag was deposited by thermal evaporation with a shadow mask.

3.3 Quantum Chemical Calculations

To make quantum chemical calculations tractable, the long-chain alkyl side group was replaced by a methyl group for all the molecules, which speeded up excited state calculation without altering the nature of frontier molecular orbitals. The molecular geometries of all the molecules were firstly optimized using density functional theory (DFT) at the B3LYP/6-31G (d,p) level. Time-dependent density functional theory (TDDFT) was employed to characterize the electronic excitations of the acceptors. The long-range corrected ωB97XD functional in conjunction with the 6-31G (d,p) basis set was employed to compute the lowest five singlet states, as this functional could capture both short- and long-range interactions and describe charge transfer states accurately. The effects of the size of the basis set and the number of electronic states on the excited states calculation results have been discussed in our recent work. All quantum chemical calculations were performed with the Gaussian 09 program package (Frisch et al., 2009), while the electronic structure-property analysis was completed using the Multiwfn codes(Lu and Chen, 2012;Zhang and Lu, 2021). The ESP was computed to characterize the electron distribution between

different structures, which was presented and painted by Visual Molecular Dynamics (VMD) (Humphrey, Dalke and Schulten, 1996) to obtain the final results.

3.4 Characterisation Technologies for OSCs

3.4.1 Characterisation of molecular Structures

1) Nuclear Magnetic Resonance (NMR)

NMR spectroscopy is a method commonly used to characterize the structures of organic molecules. The technique relies on the detection of electromagnetic radiation absorption within a frequency range, typically between 400 to 900 MHz. When waves are absorbed in a magnetic field, a unique type of nuclear transition occurs. This absorption occurs at specific frequencies which correspond to the energy difference between the spin states of the nuclei. The frequency of the radiation needed to cause a transition depends on the chemical environment of the nuclei, such as the presence of neighboring atoms. Therefore, the NMR spectrum can provide the details of molecular structure and functional groups. Because the chemical shifts and coupling in the NMR spectrum for every organic compound are unique, NMR has been the most important method to identify organic compounds. The most common types of NMR spectrum are ^{1}H NMR and ^{13}C NMR. Under certain situations, ^{19}F NMR was also used to characterize the fluorinated molecules in OSCs. Correlation spectroscopy is developed from one-dimensional NMR, which can identify the neighboring substituents of a functional group and precisely recognize the resonances. Correlation spectroscopy utilizes nucleus-centered emission. It detects response on the correlated nucleus frequency if it is coupled through-bond or through-space with another nucleus. Since the Nuclear Overhauser effect (NOE) depends on the distance of the nuclei, quantifying the NOE for each nucleus allows more information in structural analysis and identification achievable.

Herein, ^{1}H NMR and ^{13}C NMR spectra are used to characterize the structures of organic intermediates in Chapter 4-6, and Nuclear Overhauser effect

spectroscopy (NOESY) is utilized to judge the molecular conformation in Chapter 5.

2) Matrix-assisted laser desorption/ionization time of flight mass spectrometry (MALDI-TOF-MS)

During the mass spectra measurements, some organic molecules or polymers with large molecular weights are difficult to form molecular ions under normal ionization techniques. Among the ionization techniques, MALDI is a simple and fast method to give the results. With the matrix method, protons would be transferred to the sample molecules first, which would charge the molecules for forming charged ions. Then, the charged ions of the fragments can be detected from the mass spectrum to give the molecular weight. All the NFAs in the thesis were characterized by MALDI-TOF-MS together with the NMR spectrum to identify the chemical structures accurately.

3.4.2 Characterization of Intrinsic Properties of NFAs

1) Ultraviolet-visible Absorption Spectra (UV-Vis)

UV-Vis absorption spectroscopy is a method utilized for detecting the absorption of light by molecules in the ultraviolet and visible regions. When the light with varied wavelengths transmits through the sample, part of the light would be soaked up by the substance at each wavelength. Commonly, the absorption spectrum can provide structural information of the substance, and the absorption coefficient of different materials.

In this thesis, the UV-Vis absorption spectroscopy is used to characterize the parameters, including absorption regions, the highest absorption peaks, absorption onset, and absorption coefficient. The optical bandgap of the NFAs can be calculated by the absorption onset observed from the films. And the absorption coefficient measured from the solution state is an essential parameter to evaluate the absorption strength of an NFA. As is shown in **Figure 3.2**, an idea NFA should possess broad and strong absorption, and complementary absorption region with donor materials. Herein, the UV-Vis absorption spectra were recorded on a UV-Vis instrument (UV-1800, SHIMADZU).

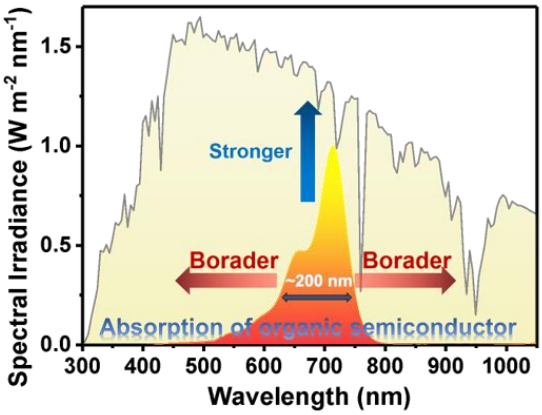

Figure 3.2 Absorption design rules of organic semiconductors

2) Photoluminescence Spectroscopy (PL)

PL is a methodology utilized to investigate the light-emitting characteristics of materials. The sample is excited by the light source with a certain wavelength, and the emission spectrum of the sample can be measured. From the PL spectra, the energy band structure and wavelength of highest emission peak can be obtained. In Chapter 6, the PL spectra were measured to detect the quenching efficiency. The higher quenching of the PL spectra implies an efficient transition from local energy states to charge transfer states of the blend films, associated with sufficient energy offset. At the same time, the energy gap can be obtained accurately from the intersection point between the absorption spectra of the film state and the PL spectra. In this thesis, the PL spectra of the films were measured by HORIBA (FL3-111) fluorescence spectroscopy in Ningbo Institute of Materials Technology and Engineering.

3) Ionisation Potential Spectroscopy (IPS) Measurements

Different from Cyclic Voltammetry (CV), IPS is an infrequent technique utilized for measuring the HOMO energy levels of various materials. Under inert gas atmosphere, the neat films were ionized through exposure to either photons or electrons. Subsequently, the energy distribution of the emitted electrons is measured. Through fitting the measured curves, the ionization potential can be obtained accurately as the HOMO energy levels.

In the following chapters, the HOMO energy levels of all the molecules were measured by the ionization energy measurement system (Model IPS-4, Nanjing Sunny Tech Ltd., China) from 4 eV to 7.3 eV under N_2 atmosphere.

4) Thermal Gravimetric Analysis (TGA)

TGA is a common technique used in thermal analysis by measuring the mass of a sample over time under varying temperatures. A typical thermal gravimetric equipment entails a precise balance positioned in a temperature control system. In this thesis, TGA was conducted to evaluate the thermal stability of the NFAs at a heating rate of 50 °C min^{-1} from 45 °C to 800 °C under N_2 atmosphere. The instrument type was TGA/SDTA851E (Mettler Toledo). The decomposition temperatures (Td, 5% weight loss) can be obtained directly from the TGA curves.

3.4.3 Characterization of Photovoltaic Properties

1) Current Density-Voltage (J-V) Measurements

To evaluate the performance of OSC devices, the *J-V* measurements are used to obtain the most important parameters, such as V_{OC}, J_{SC}, and *FF*. The simulated sunlight is converted into electricity during the test to give these parameters. The parameters can not only help understand the performance of OSC devices, but also provide a reference for further optimization of device structure and material design. Commonly, *J-V* measurements are conducted under standardized conditions, with a certain strength of illumination and maintained temperature.

In chapter 4-6, the *J-V* curves were measured in a nitrogen glove box and were conducted on a computer-controlled Keithley 2400 source measure unit under AM 1.5G illumination at 100 mW cm^{-2} using an SS-F5-3A Solar Simulator (Enlitech) and calibrated with a NREL standard silicon photodiode together with a protective KG5 filter.

2) External Quantum Efficiency (EQE)

EQE measurement is a technique utilized to evaluate the light response intensity of OSC devices, specifically their photon-to-electricity conversion properties.

The measurement involves determining the current density generated by the solar cell in response to the incident light. Hence, the *EQE* depends on both the absorption of light and the collection of charges. The fabricated OSC devices are expected to realize a strong and broad *EQE* response for a high J_{SC} value.

As a result, the *EQE* spectra were measured by a Solar Cell Spectral Response Measurement System QE-R3011 (Enlitech Co., Ltd.). The *EQE* curves are presented together with integrated current curves in the following chapters.

3) Space Charge Limited Current (SCLC) Measurements

The SCLC method was conducted to evaluate charge transport properties of the blend films. The hole and electron mobilities (μ_{h} and μ_{e}) of the devices can be determined and used to evaluate the molecular packing of the corresponding blend films. Herein, electron-only devices were fabricated in a structure of ITO/ZnO/Active Layer/PDINN/Ag, whereas hole-only devices were fabricated utilizing a structure of ITO/PEDOT:PSS/Active Layer/MoO_3/Ag. The fabrication conditions of the active layers followed the same procedure described above. The charge mobilities were determined by fitting the dark current measurement curves according to the following equation:

$$J = \frac{9}{8}\mu\varepsilon_{\mathrm{r}}\varepsilon_0(V^2/L^3) \tag{3-1}$$

where J is the dark current density (mA cm^{-2}), ε_0 is the permittivity of free space, ε_r is the dielectric constant of the blend materials, V is the effective voltage and L is the thickness of the active layer. According to the formula above, the electron and hole mobilities were calculated in the following chapters.

4) Energy loss (E_{Loss}) Measurements

Electroluminescence (EL) measurement is a unique technique to quantify energy loss in OSC devices. By applying an electric field to the OSC sample, photons would be generated due to the recombination of electron-hole pairs. These photons can then be detected and analyzed, providing information about the energy loss processes occurring within the devices. The light emission efficiency under the varied voltages is denoted as EQE_{EL}, causing $\Delta E_{\mathrm{nonrad}}$.

Hence, $\Delta E_{\mathrm{nonrad}}$ of the device can be calculated from EQE_{EL}. Combined with Fourier-transform photocurrent spectroscopy external quantum efficiency (FTPS-EQE) measurements and device parameters, three sections of E_{Loss} could be quantified. The detailed calculation procedures of E_{Loss} are plotted in Chapter 4-6. (The FTPS-EQE can also be called highly sensitive *EQE*, with a similar testing mechanism to the original *EQE* spectra but higher precision. FTPS-EQE has been always used to evaluate the energy loss and defect density of the OSC devices.)

In this thesis, FTPS-EQE spectra were measured with an FTPS-EQE measurement system (Enlitech PECT-600). The EL spectra were collected with an Enlitech REPS system, which consists of a monochromator in combination with a Si-CCD detector.

3.4.4 Morphology Characterization

1) Contact Angle (CA) Measurements

CA measurement is a method used to evaluate the ability of a liquid to wet a solid surface. The contact angle is the angle between the liquid-solid interface and the tangent to the liquid drop. To evaluate the miscibility between the donor and the acceptor, CA is commonly used to characterize the wetting properties. The miscibility between the blend components can affect morphology and phase separation to a large extent. Hence, the CA measurements are always used to investigate side-chain engineering effects on material performance in OSCs. The surface energy parameters can be calculated by the following equations:

$$(1 + cos\theta_1)\gamma_1 = 4(\frac{\gamma_1^{\mathrm{d}}\gamma_{\mathrm{s}}^{\mathrm{d}}}{\gamma_1^{\mathrm{d}}+\gamma_{\mathrm{s}}^{\mathrm{d}}} + \frac{\gamma_1^{\mathrm{p}}\gamma_{\mathrm{s}}^{\mathrm{p}}}{\gamma_1^{\mathrm{p}}+\gamma_{\mathrm{s}}^{\mathrm{p}}})$$

$$(1 + cos\theta_2)\gamma_2 = 4(\frac{\gamma_2^{\mathrm{d}}\gamma_{\mathrm{s}}^{\mathrm{d}}}{\gamma_2^{\mathrm{d}}+\gamma_{\mathrm{s}}^{\mathrm{d}}} + \frac{\gamma_2^{\mathrm{p}}\gamma_{\mathrm{s}}^{\mathrm{p}}}{\gamma_2^{\mathrm{p}}+\gamma_{\mathrm{s}}^{\mathrm{p}}})$$

$$\gamma_{\mathrm{s}} = \gamma_{\mathrm{s}}^{\mathrm{d}} + \gamma_{\mathrm{s}}^{\mathrm{p}} \quad (3\text{-}2)$$

where $\gamma_{\mathrm{s}}^{\mathrm{d}}$ represents the dispersive components, $\gamma_{\mathrm{s}}^{\mathrm{p}}$ is the polar component. θ_1 and θ_2 are the contact angles of water and glycerol, respectively. In this thesis, contact angles were measured for the neat films on the PEDOT:PSS coated substrates.

2) Atomic Force Microscopy (AFM)

AFM has been an essential technique due to its ability to produce high-resolution images and to provide valuable information on both surface topography and physical properties of materials on a nanoscale level. It utilizes a sharp tip to scan over the surface of a sample, generating an accurate and high-resolution image. More importantly, AFM can provide surface features and physical properties of a material without destroying it. In OSCs, AFM tests are commonly conducted to observe the surface morphology of the organic layers, and to provide the parameters such as roughness. As a general rule, the surface of the layers should be smooth for good device performance.

The samples were fabricated on PEDOT:PSS layer above the substrates. AFM measurements were carried out on the tapping mode (3100 SPM, VEECO).

3) Transmission Electron Microscopy (TEM) Measurements

In TEM measurements, a beam of electrons is transmitted through the fabricated sample. The resulting images are formed by the electrons that pass through the sample and are detected on a fluorescent screen. To succeed in forming the images, the thickness of the sample should be extremely thin to allow the electrons to pass through. At the same time, the copper grids with carbon membranes were used in the following TEM tests to enhance the electrical

conductivity. In OSCs, TEM is frequently used to characterize the nanostructures and inner morphology of the blend films. From the TEM images, the phase separation and domain size can be observed directly. The phase separation of the blend films is related to the miscibility between the donors and acceptors, the fabrication details of the active layer, and the annealing procedure. Hence, the resulting TEM images can give feedback on the optimisation of materials and device fabrication.

In the following chapters, TEM measurements were conducted on Thermo Fisher (Talos F200X). The samples for TEM tests were prepared by dissolving the PEDOT:PSS layer with deionized water and picking up the active layer with 400-mesh copper TEM grids.

4) Grazing Incidence Wide-Angle X-Ray Scattering (GIWAXS) Measurements

GIWAXS provides unique insights to explore the inner morphology of the blend films at nanoscale level. The molecular stacking, crystal alignment, and crystallinity in the films can be probed by a beam of X-ray under grazing incidence (Muller-Buschbaum, 2014). The examples of diffraction patterns are exhibited in **Figure 3.3**, the GIWAXS pattern in **Figure 3.3** (a&c) suggests more ordered stacking compared to the pattern in **Figure 3.3** (b&d). Length scales from nanometers to several hundred nanometers are sensitive in GIWAXS measurements. Therefore, the organic layers in OSCs can be detected by GIWAXS to examine the molecular packing and crystallinity. By analyzing the crystallographic orientation and alignment of the organic materials, GIWAXS can provide valuable insights into the charge carrier transport and recombination properties in OSC devices.

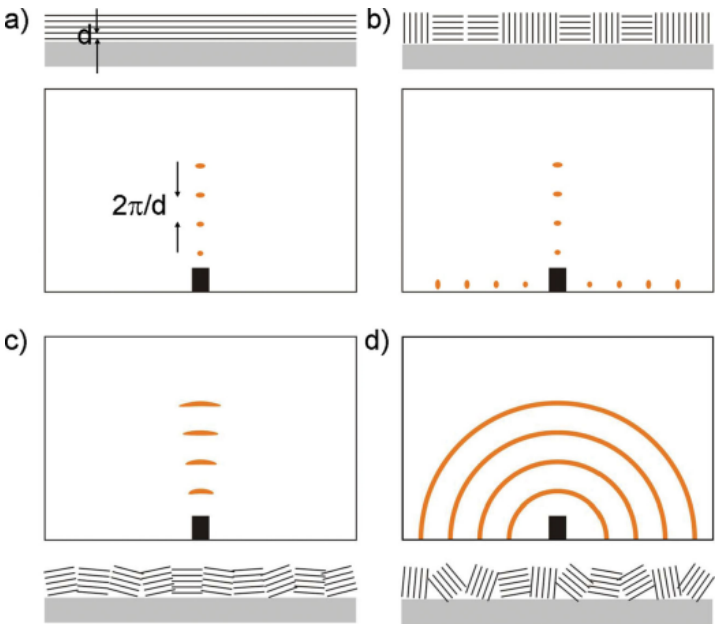

Figure 3.3 Sketch of film crystallinity and the corresponding 2D GIWAXS data in case of (a) vertical lamellar stacking, (b) crystallites with vertical and horizontal orientations, (c) oriented domains and (d) full rotational disorder of crystallites (Muller-Buschbaum, 2014).

In Chapter 4, GIWAXS measurements were carried out on the XEUSS SAXS/WAXS system (XENOCS, France) at the National Center for Nanoscience and Technology (NCNST, Beijing). GIWAXS measurements in Chapter 5 were conducted with the BL14B1 beamline of the Shanghai Synchrotron Radiation Facility (SSRF), under an X-ray with a wavelength of 1.2398 Å and an energy of 10 keV. The GIWAXS tests shown in Chapter 6 were measured at 13A beam line of National Synchrotron Radiation Research Center (NSRRC, Taiwan). These samples for GIWAXS were radiated at 12 keV X-ray with an incident angle of 0.2°. All the samples for GIWAXS measurements were spin-coated on the PEDOT:PSS layer above silicon substrates.

3.5 Concluding Remarks

In this chapter, NMR and MALDI-TOF-MS are first introduced to characterize the molecular structures of intermediates and NFAs. Secondly, this chapter involves some Gaussian calculations for molecular optimization, and ESP, which shall be used in the following works. Afterward, the conventional

characterizations for detecting the photophysical and photovoltaic properties are described. Subsequently, the morphology characterization methods of the blend films are illustrated and discussed. In the following chapters, the above methods will be employed to characterize NFAs and the corresponding devices to investigate the structural-properties relationships in order to construct highly efficient NFAs.

Chapter 4

Organic solar cells based on non-fullerene acceptors containing thiophene [3,2-b] pyrrole*

4.1 Synopsis

Thiophene[3,2-b] pyrrole (TP) was introduced to construct two novel fused-ring conjugated NFAs, named as PTBTP-2F and PTBTP-4F. By fusing two pyrrole rings on both sides of an indacenodithiophene (IDT) unit, a brand-new central core based on TP block (denoted as PTBTP) was achieved to serve as the D core to construct an A-D-A type NFA together with two accepting units (IC-F and IC-2F). Benefitting from the nitrogen atom in the pyrrole ring, both PTBTP-2F and PTBTP-4F exhibited great film forming property as well as high LUMO energy levels of -4.09 eV and -4.11 eV for PTBTP-2F and PTBTP-4F,

* The work in this chapter was published in:

Zhu, J., Zhang, Z., Lv, Y., Lan, A., Lu, H., Do, H., & Chen, F. (2022). "Organic solar cells based on non-fullerene acceptors containing thiophene [3,2-b] pyrrole." *Organic electronics*, 103, 106461.

respectively. Since IC-2F presents stronger electron-withdrawing capability than IC-F, PTBTP-4F demonstrated red-shifted absorptions in solution/film in comparison with PTBTP-2F. When blending with donor PBDB-T, the PTBTP-2F fabricated devices achieved an average *PCE* of 11.14% with a V_{OC} of 0.91 V, a J_{SC} of 17.89 mA cm^{-2} and an *FF* of 68.66%, while the PTBTP-4F fabricated devices afforded a *PCE* of 12.33% with a V_{OC} of 0.86 V, a J_{SC} of 20.74 mA cm^{-2} and an *FF* of 69.02%.

4.2 Introduction

OSCs have received wide research attention for their unique properties such as semi-transparency, light weight, low cost, flexibility, and easy to fabricate, etc (Li et al., 2017b;Liu et al., 2017b;Peng et al., 2017;Dai and Zhan, 2018;Zhang et al., 2019;Ji et al., 2020). The development of OSCs has been surging ahead accompanying with the rapid development of multifarious NFAs. At present, the well-known NFAs such as ITIC (Lin and Zhan, 2015;Li et al., 2017a;Hou et al., 2018;Yan et al., 2018a;Song et al., 2019a;Zhao et al., 2020) and Y6 (Yuan et al., 2019b;Chen et al., 2020b;Zhang et al., 2020a;Zhu et al., 2020) series, have replaced fullerene derivatives in fabricating high efficiency BHJ OSCs due to their simple synthesis and purification, tuneable spectral absorption, and modulable frontier energy levels in comparison with fullerene acceptors, NFAs based OSCs have achieved a very promising *PCE* of approaching 19% recently (Bi et al., 2021). To develop narrow bandgap NFAs with appropriately matched energy levels with electron donors has been considered as an effective approach to developing highly efficient OSCs with high J_{SC} and V_{OC} at the same time (Hodgkiss, 2021).

Pyrrole-based NFAs, as the main kind of *N*-heteroarene based NFAs, exhibited great potential in fabricating high performance OSCs for their unique features, (Wetzel et al., 2015;Huang et al., 2018;Li et al., 2020) such as, higher energy levels facilitated by the strong electron-donating nitrogen atom, red-shifted absorption and an extra reaction site for side chain modification. Generally, the pyrrole ring can be introduced by *N* bridge or pyrrole-based building blocks. On

this basis, Jen *et al.* and Chen *et al.* designed and synthesized SN6IC-4F, in which the five-membered carbon ring in F6IC was replaced with a pyrrole ring to enhance the conjugation and to tune the energy levels of the molecule, red-shifted absorption by 83 nm was thus observed from SN6IC-4F, which resulted in better utilization of sunlight, the corresponding OSCs achieved a high *PCE* of 13.2% (Huang et al., 2018). Zou *et al.* took advantage of the extra reaction site in the pyrrole ring and constructed several Y-series acceptors (Y5, Y6, N3) with expanded geometry (Yuan et al., 2019b). These acceptors constructed through *N*-bridging strategy have presented many superiorities in fabricating high performance OSCs. Besides of *N*-bridging strategy, the usage of pyrrole-based building blocks, such as carbazole or dithieno[3,2-b:2',3'-d] pyrrole (DTP), has also been an effective way to develop high performance NFAs. Hou *et al.* introduced a carbazole core to design and construct DTTC-4Cl, which afforded an outstanding *PCE* of 15.42% (Chen et al., 2020a). DTP has also been the most successful building block for constructing NFAs. Tang's group developed several DTP-based NFAs, which obtained promising *PCE*s of over 15% through systematic molecular optimization (Yang et al., 2020). Although DTTC-4Cl or DTP-based acceptors were designed modularly based on pyrrole-based building blocks and realized high *PCE*s, pyrrole-based NFAs still have not been extensively investigated. At the same time, the category of pyrrole-based building blocks was limited when constructing novel pyrrole-based NFAs.

In this work, TP block, which has been used in synthesizing a thieno-pyrrole fused BODIPY photosensitizer (SBDPiR690) for the applications of photodynamic therapy and dye-sensitized solar cells (Watley et al., 2015;Kubota et al., 2019), was introduced as a building block for synthesizing NFAs. IDT unit (Li et al., 2019c) has been one of the typical central cores to construct fused-ring backbones for NFAs. By fusing two pyrrole rings on both sides of the IDT unit, a brand-new central core based on TP block (denoted as PTBTP) can thus be obtained, which can serve as a D core to construct A-D-A type NFAs together with electron-accepting units. Meanwhile, the nitrogen atom of pyrrole was hexyl functionalized to facilitate sufficient solubility of the molecule. IC-F and IC-2F were selected as the end-capping groups (A units) to construct two novel TP-based acceptors, named as PTBTP-2F and PTBTP-4F,

respectively (**Figure 4.1**). In CF solution, both PTBTP-2F and PTBTP-4F exhibited strong absorption among 500 nm-900 nm with a narrow optical bandgap around 1.46 eV, which resulted from effective molecular stacking and ICT, that would be ascribed to the highly conjugated and electron-rich core of the molecules. Compared with IT-4F, both PTBTP-2F and PTBTP-4F showed red-shifted absorption spectra by ~40 nm and enhanced LUMO energy levels by ~0.15 eV, owing to their stronger ICT induced by more conjugated PTBTP backbones. The fluorinated end-capping groups IC-F and IC-2F are expected to enhance inter/intramolecular charge transfer and improve the crystallinity of the films. The impacts of the fluorination effect on the photophysical properties of the molecules were investigated as well. Due to the matchable energy levels and complementary light absorption with PTBTP-2F and PTBTP-4F, PBDB-T (Zheng et al., 2020b) was chosen as the donor to pair with the two acceptors for fabricating OSCs and to evaluate the performance of the novel acceptors. As a result, the PBDB-T: PTBTP-2F based devices achieved an average *PCE* of 11.14%, while the PBDB-T: PTBTP-4F based devices afforded a higher *PCE* of 12.33%. Although the slightly down-shifted energy levels led to a lower V_{OC} for PTBTP-4F based devices, the J_{SC} of them was high up to 20.74 mA cm^{-2} due to better charge extraction and photon collection capability of the devices, which can be validated from the EQE measurements. Furthermore, the E_{Loss} of PBDB-T: IT-4F, PBDB-T: PTBTP-2F, and PBDB-T: PTBTP-4F based devices were determined to be 0.83 eV, 0.62 eV, and 0.66 eV, respectively. Both the PBDB-T: PTBTP-2F and PBDB-T: PTBTP-4F blends showed less non-radiative energy loss and thus lower total energy loss because of their more matched energy levels with PBDB-T. The performance of PTBTP-4F based devices was superior to PTBTP-2F based devices, although the non-radiative energy loss was reduced significantly in the PTBTP-2F based devices, as PTBTP-4F exhibited better compatibility with PBDB-T, which can be verified from film morphology investigation. The fabricated PTBTP-4F devices thus presented a reduced energy loss and afforded higher J_{SC}s and *FF*s.

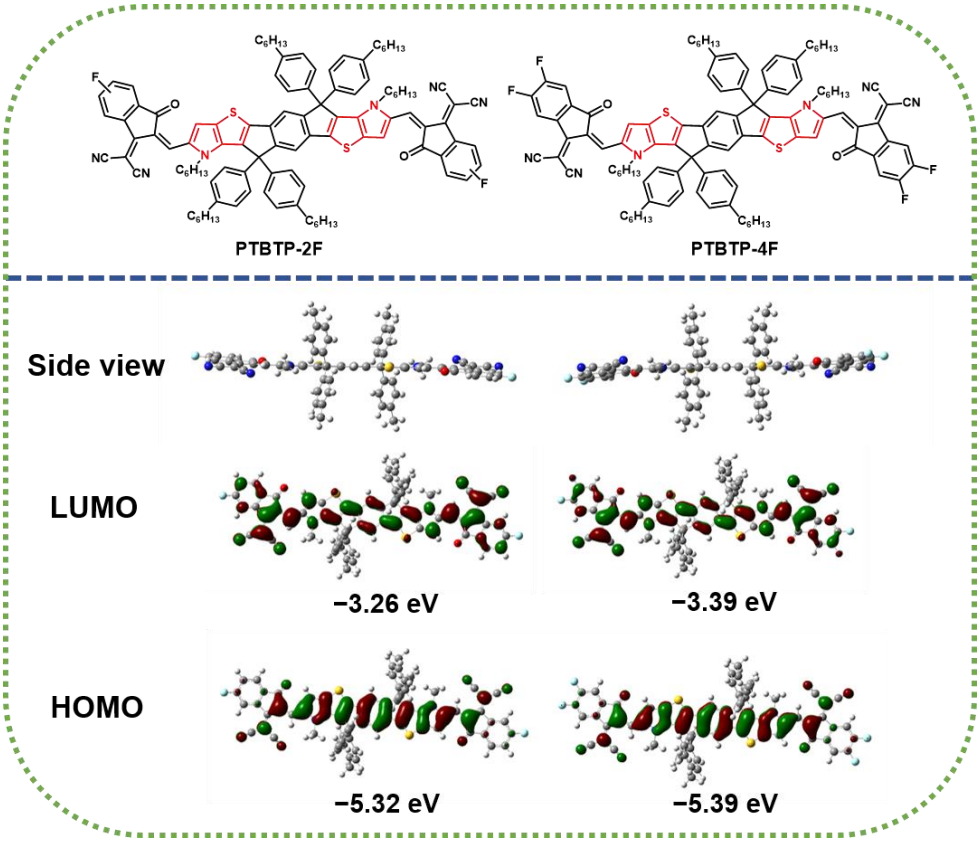

Figure 4.1 The molecular structures, side view geometries and calculated HOMO and LUMO energy levels for PTBTP-2F and PTBTP-4F

4.3 Results and Discussion

4.3.1 Synthesis and Characterization

PTBTP-2F and PTBTP-4F were designed and prepared via modular synthesis strategy successfully. Firstly, the TP block was prepared according to the previous method. The PTBTP central core was then synthesized through Stille coupling and reductive cyclization. Finally, PTBTP-2F and PTBTP-4F were synthesized by Knoevenagel condensation of IC-F and IC-2F respectively with the corresponding dialdehydes. The synthetic routes and details for the target molecules are provided in **Appendix I**. The target molecular structures were characterized by MS-TOF, ^{1}H NMR, and ^{13}C NMR. Benefitting from the extra alkyl chains on the pyrrole ring, PTBTP-2F and PTBTP-4F exhibited great solubility in common solvents, that were 97 mg/mL and 91 mg/mL in CF and 67 mg/mL and 58 mg/mL in chlorobenzene (CB), respectively. At the same time, both acceptors presented high decomposition temperatures (Td, 5%

weight loss) of 354 ℃ for PTBTP-2F and 345 ℃ for PTBTP-4F, respectively (**Figure 4.2**).

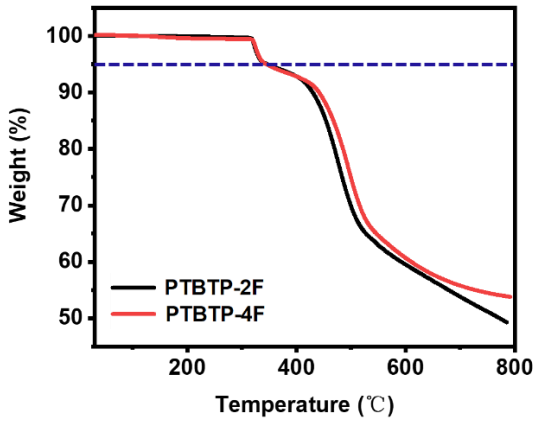

Figure 4.2 TGA curves of **PTBTP-2F** and **PTBTP-4F**

DFT calculations were carried out at the B3LYP/6-31G (d,p) level by Gaussian 09 to optimize the molecular geometry and to determine the energy levels of PTBTP-2F and PTBTP-4F (**Figure 4.1**). The alkyl side chains were replaced with methyl groups to simplify the calculation process. Both of the NFAs show planar structures from the side views, which are attributed to the rigid pyrrole fused-ring structure of the backbone. The highly conjugated backbones with excellent planarity are not only favorable for transporting charge carriers, but also beneficial to improving intermolecular π-π stacking in the photosensitive blend films. As depicted in **Figure 4.1**, the simulated HOMOs of the molecules were predominately located at the central core, while the LUMOs tended to delocalize over the entire backbone but without any contribution from the side chains. The corresponding HOMO/LUMO energy levels for PTBTP-2F and PTBTP-4F were pretty close, which were calculated to be -5.39 eV/-3.31 eV for PTBTP-4F and -5.32/-3.26 eV for PTBTP-2F, respectively. Compared with PTBTP-2F, PTBTP-4F presented relatively down-shifted energy levels, due to the stronger electron-withdrawing end group IC-2F, which complied with the previous studies.

The absorption spectra of PTBTP-2F and PTBTP-4F in chloroform solution and films were measured and shown in **Figure 4.3(a)**. The photophysical properties of IT-4F, PTBTP-2F and PTBTP-4F are summarized in **Table 4.1**. As shown in **Figure 4.3(b)**, PTBTP-2F and PTBTP-4F exhibited almost the same absorption

profiles both in solution and films, since the two molecules possessed similar frameworks and end group structures, thus presenting analogous electron push-pull effects in the molecules. Hence, similar optical bandgaps of PTBTP-2F and PTBTP-4F were measured to be 1.47 eV and 1.46 eV, respectively. The molecules in solutions presented strong absorption bands from the visible to near-infrared (NIR) region (500 nm-800 nm) with a maximum absorption peak at 730 nm. Compared with IT-4F, the absorption spectra of PTBTP-2F and PTBTP-4F red-shifted by ~40 nm, owing to a more conjugated PTBTP backbone. Moreover, with an increasing number of fluorine atoms and stronger conjugation, an enhanced tendency of the maximum extinction coefficients can be observed from IT-4F (2.06×10^5 M^{-1} cm^{-1}), PTBTP-2F (2.43×10^5 M^{-1} cm^{-1}), PTBTP-4F (2.71×10^5 M^{-1} cm^{-1}). Compared with the absorption from solutions, the maximum absorption peaks of the films located at 772 nm with a distinct red-shift by ~40 nm, suggesting that enhanced intermolecular π-π interaction was generated in the films. As validated by the absorption of the blend films (**Figure 4.4**), both acceptors realized complementary light absorption with PBDB-T to harvest photons sufficiently.

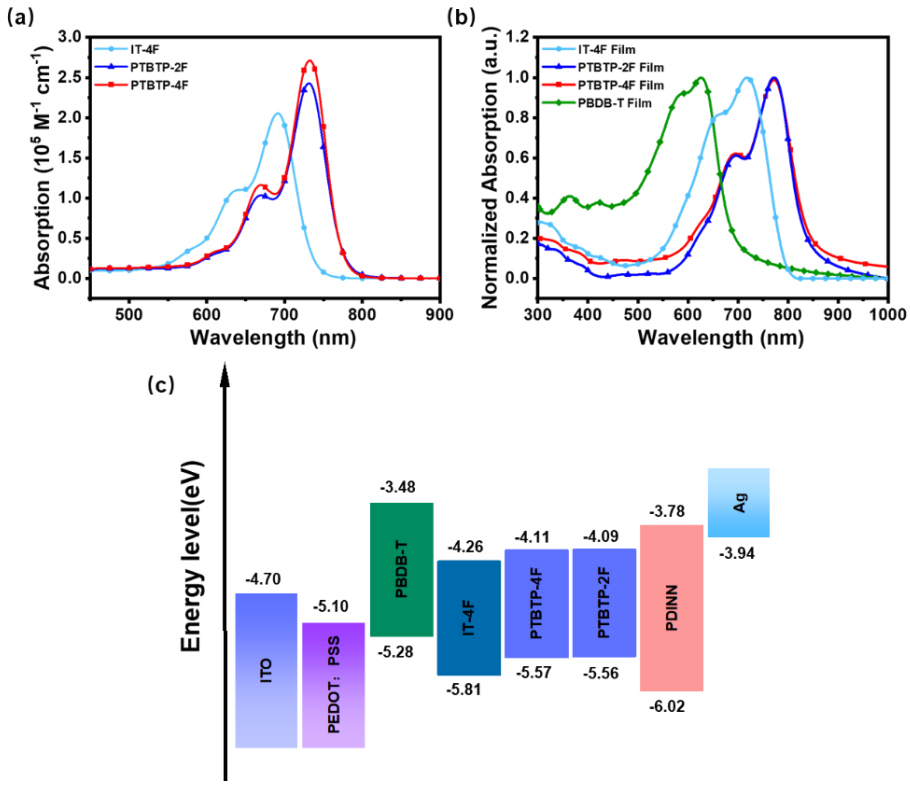

Figure 4.3 (a) Absorption curves of IT-4F, PTBTP-2F and PTBTP-4F in dilute chloroform solutions (10^{-5} M). (b) Normalized absorption spectra of IT-4F, PTBTP-2F and PTBTP-4F in films. (c) Energy levels diagram of the devices.

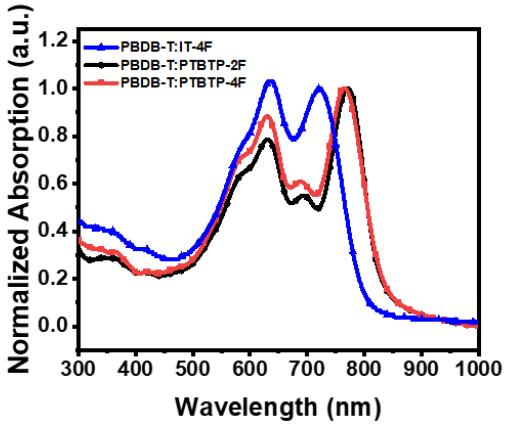

Figure 4.4 UV-vis absorption curves of **PBDB-T: Acceptors** blend films.

The electrochemical properties of IT-4F, PTBTP-2F, and PTBTP-4F were investigated by IPS under N_2 atmosphere. As shown in **Figure 4.5**, the HOMO energy levels were measured to be -5.81 eV for IT-4F, -5.56 eV for PTBTP-2F, and -5.57 eV for PTBTP-4F, respectively. Benefitting from the enhanced conjugation induced by the pyrrole ring of the TP block, the HOMO energy levels of PTBTP-2F and PTBTP-4F up-shifted by ~0.15 eV with narrowed band gaps. Compared with PTBTP-2F, the energy levels of PTBTP-4F were slightly

lower owing to the stronger electron-withdrawing ability of the end-capping group. The LUMO energy levels were calculated from the HOMO energy levels and optical band gaps. The corresponding LUMO energy levels of PTBTP-2F (-4.09 eV) up-shifted in comparison with PTBTP-4F (-4.11 eV) and IT-4F (-4.26 eV), resulting in higher $\boldsymbol{V_{OC}}$ for the devices based on PTBTP-2F. The HOMO energy level offsets between the donor PBDB-T and two acceptors were over 0.28 eV, indicating that both of the blend films supplied ample driving force for charge separation. In all, the two TP block contained acceptors possessed complementary absorptions and matched energy levels with PBDB-T. In addition, fluorination of the molecules induced descending HOMO energy levels which agreed well with the theoretical calculations.

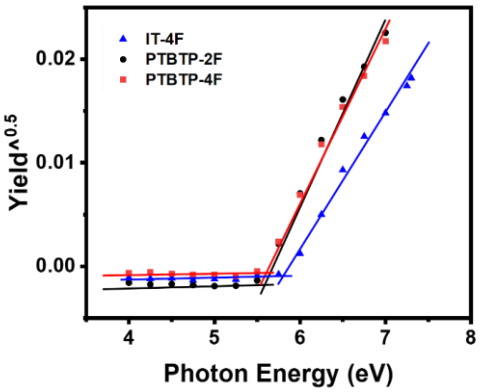

Figure 4.5 IPS curves of **IT-4F**, **PTBTP-2F**, **PTBTP-4F** under N_2.

Table 4.1 The electrochemistry and photophysical properties of IT-4F, PTBTP-2F and PTBTP-4F.

Acceptors	E_{HOMO} [eV]	E_{LUMO} [eV]	$\lambda_{max}^{sol.}$ a) [nm]	$\lambda_{sol.onset}$ a) [nm]	λ_{max}^{film} [nm]	λ_{onset}^{film} [nm]	E_g^{opt} b) [eV]	ε_{max} a) [M^{-1} cm^{-1}]
IT-4F	-5.81	-4.26	691	739	719	798	1.55	2.06×10^5
PTBTP-2F	-5.56	-4.09	735	769	772	843	1.47	2.43×10^5
PTBTP-4F	-5.57	-4.11	732	762	772	849	1.46	2.71×10^5

a)In chloroform solution. b)$E_g^{opt}=1240/\lambda_{onset}^{film}$

4.3.2 Photovoltaic Properties

To characterize photovoltaic performance of the acceptors, OSCs with a conventional device configuration of ITO/PEDOT:PSS/Active layer/PDINN/Ag were fabricated. The blend solutions of PBDB-T: PTBTP-2F or PTBTP-4F (1:0.8, w/w) in chloroform at a total concentration of 15 mg/mL

were spin-coated as the active layer. Similarly, the blend solution of PBDB-T: IT-4F (1:1, w/w) in chloroform at a total concentration of 16 mg/mL was spin-coated to fabricate control devices. The device performance was optimized by manipulating the donor/acceptor blend ratio, type of additives, and annealing temperature, as summarized in **Table 4.2**. As a result, the best-performance device based on PTBTP-4F achieved a *PCE* of 12.33% by operating the blends with the addition of 0.5% DIO and thermal annealing at 100 ℃ for 5 min. Under the same condition, the optimal device based on PTBTP-2F exhibited a lower *PCE* of 11.19%. The detailed photovoltaic parameters are summarized in **Table 4.3**. Benefitting from the more electron-rich backbone, PTBTP-4F presented enhanced energy levels and red-shifted absorption induced by stronger ICT effect compared with IT-4F, leading to a higher $\boldsymbol{V_{OC}}$ by 0.14 eV of the PTBTP-4F devices. Compared with PTBTP-2F, the more electron-deficient end-capping group IC-2F also contributed to the stronger ICT effect and deeper energy levels of PTBTP-4F. As depicted in **Figure 4.6 (a)**, the PBDB-T: PTBTP-2F based devices obtained a higher $\boldsymbol{V_{OC}}$ by 0.05 eV, owing to the slightly elevated energy levels.

Table 4.2 The optimized photovoltaic parameters of devices based on PBDB-T: PTBTP-4F blends

Ratio	Additive	TA [°C]	V_{OC} [V]	J_{SC} [mA cm^{-2}]	*FF* [%]	*PCE* [%]
1:0.7	-	-	0.87	19.36	62.74	10.61
1:0.8	-	-	0.88	18.29	66.33	10.70
1:1	-	-	0.87	17.11	62.66	9.39
1:1.2	-	-	0.87	17.60	60.67	9.35
1:0.8	0.5%DIO	-	0.89	18.39	68.01	11.07
1:0.8	0.5%DIO&CN	-	0.87	17.10	68.26	10.10
1:0.8	0.5%CN	-	0.87	19.51	68.82	10.95
1:0.8	0.5%DIO	-	0.89	18.39	68.01	11.07
1:0.8	0.5%DIO	80	0.86	18.81	64.21	10.39
1:0.8	0.5%DIO	100	0.86	20.74	69.02	12.33
1:0.8	0.5%DIO	120	0.86	19.90	68.62	11.78
1:0.8	0.5%DIO	150	0.83	21.89	67.60	11.68

Table 4.3 Photovoltaic parameters of the optimized OSCs based on two PBDB-T: acceptor blends

Acceptors	V_{OC} [V]	J_{SC} [mAcm^{-2}]	$J_{cal.}$[a)] [mAcm^{-2}]	*FF* [%]	*PCE*[b)] [%]
IT-4F	0.722 (0.720±0.006)	19.16 (18.89±0.27)	18.51	68.93 (68.21±1.52)	9.53
PTBTP-2F	0.907 (0.907±0.003)	17.89 (17.69±0.26)	17.04	68.66 (68.60±1.21)	11.14
PTBTP-4F	0.862 (0.861±0.001)	20.74 (20.65±0.23)	20.68	69.02 (68.63±1.37)	12.33

[a)]Integrated current densities from the EQE curves. [b)]Average *PCE*s from 12 devices.

The EQE spectra of the devices were conducted to understand the photon collection efficiency of the devices (**Figure 4.6b**). The PBDB-T: PTBTP-4F based devices presented broader and more sensitive photon response from 300 nm to 860 nm, while the PBDB-T: IT-4F based devices showed photon response in a wavelength region from 300 nm to 800 nm, which indicated lower photon conversion efficiency. Compared with the PTBTP-2F devices, the PTBTP-4F devices realized much higher average photon response. All of the above explained the higher J_{SC}s of PBDB-T: PTBTP-4F-based devices. The integrated J_{cal}s of PBDB-T: PTBTP-2F and PBDB-T: PTBTP-4F based devices were 17.04 mA cm^{-2} and 20.68 mA cm^{-2}, respectively, which were consistent with those obtained from *J-V* characterizations (within 5% mismatch). In sacrifice with V_{OC}, the PBDB-T: PTBTP-4F based devices exhibited an increase of nearly 3 mA cm^{-2} in J_{SC}, which was mainly due to the higher EQE response of the blend films. Compared with the PTBTP-2F based devices, the PTBTP-4F based devices realized more balanced V_{OC}s and J_{SC}s and thus higher *PCE*s.

The dependence of photocurrent (J_{ph}) on the effective voltage (V_{eff}) was plotted to probe into the charge generation and collection efficiencies in the devices. As shown in **Figure 4.6c**, when J_{ph} reached the saturation (J_{sat}) at high applied voltages, the excitons completely dissociated into free charge carriers, and soon be collected at the corresponding electrodes with minimal charge recombination. J_{sat} indicated the light collecting and exciton generation abilities of the devices, which were 20.7 mA cm^{-2}, 20.1 mA cm^{-2}, and 21.8 mA cm^{-2} for the PBDB-T: IT-4F, PBDB-T: PTBTP-2F and PBDB-T: PTBTP-4F devices, respectively.

The $\boldsymbol{J_{ph}/J_{sat}}$ ratio is an indicator to characterize the exciton dissociation and collection probability. The $\boldsymbol{J_{ph}/J_{sat}}$ values of PBDB-T: PTBTP-4F based devices were calculated to be 94.0% and 83.8% under short-circuit and maximum power output conditions, respectively, which were higher than those of PBDB-T: IT-4F based devices (92.6% and 80.7%) and PBDB-T: PTBTP-2F-based devices (92.7% and 78.2%). The higher $\boldsymbol{J_{ph}/J_{sat}}$ ratio of PBDB-T: PTBTP-4F based devices suggested their better exciton dissociation ability and more efficient charge collection in contrast with those of the other two blends prepared devices, which led to higher *FF*s of PBDB-T: PTBTP-4F devices. Through measuring the *J-V* curves under various light intensities ($\boldsymbol{P_{light}}$), the recombination mechanism can be evaluated from the slopes (α) of linearly fitted $\boldsymbol{ln(J_{SC}) - ln(P_{light})}$ curves which indicates the extent of bimolecular recombination (**Figure 4.6d**). The weaker the bimolecular recombination in the devices, the bigger the α value is closer to 1. The slopes (α) of linearly fitted $\boldsymbol{ln(J_{SC}) - ln(P_{light})}$ curves were 0.996 for PTBTP-4F based OSCs, 1.006 for IT-4F based OSCs and 0.966 for PTBTP-2F based OSCs, respectively. The results suggested that the bimolecular recombination in those devices was extremely suppressed, which facilitated efficient charge extraction, thus resulted in high *FF*s. PTBTP-4F devices showed weaker bimolecular recombination due to enhanced crystallinity caused by the stronger end-group stacking in PTBTP-4F prepared films. Another possibility for enhanced *FF* and $\boldsymbol{J_{SC}}$ could be ascribed to the improved charge transport behavior. To investigate the influence of the end-capping group on the charge-transport behavior, the SCLC method was conducted to measure the hole and electron mobilities ($\boldsymbol{\mu_h}$ and $\boldsymbol{\mu_e}$) (**Figure 4.7**). The PTBTP-4F based films presented a $\boldsymbol{\mu_h}$ of 1.62×10^{-4} $cm^2\ V^{-1}\ s^{-1}$ and a $\boldsymbol{\mu_e}$ of 3.62×10^{-4} $cm^2\ V^{-1}\ s^{-1}$, while the PTBTP-2F based films owned a $\boldsymbol{\mu_h}$ of 2.13×10^{-4} $cm^2\ V^{-1}\ s^{-1}$ and a $\boldsymbol{\mu_e}$ of 2.40×10^{-4} $cm^2\ V^{-1}\ s^{-1}$. With similar hole mobility in comparison with PBDB-T: PTBTP-2F, PBDB-T: PTBTP-4F showed a much higher $\boldsymbol{\mu_e}$ than that of PBDB-T: PTBTP-2F, which was induced by stronger end-group stacking and enhanced crystallinity in PTBTP-4F prepared films. The PBDB-T: IT-4F based films presented a $\boldsymbol{\mu_h}$ of 1.50×10^{-4} $cm^2\ V^{-1}\ s^{-1}$ and a $\boldsymbol{\mu_e}$ of 2.54×10^{-4} $cm^2\ V^{-1}\ s^{-1}$, and $\boldsymbol{\mu_e}$ was also less than that of PBDB-T: PTBTP-4F, which was due to the enhanced electron-rich

core induced intermolecular stacking of PTBTP-4F and thus enhanced electron transportation.

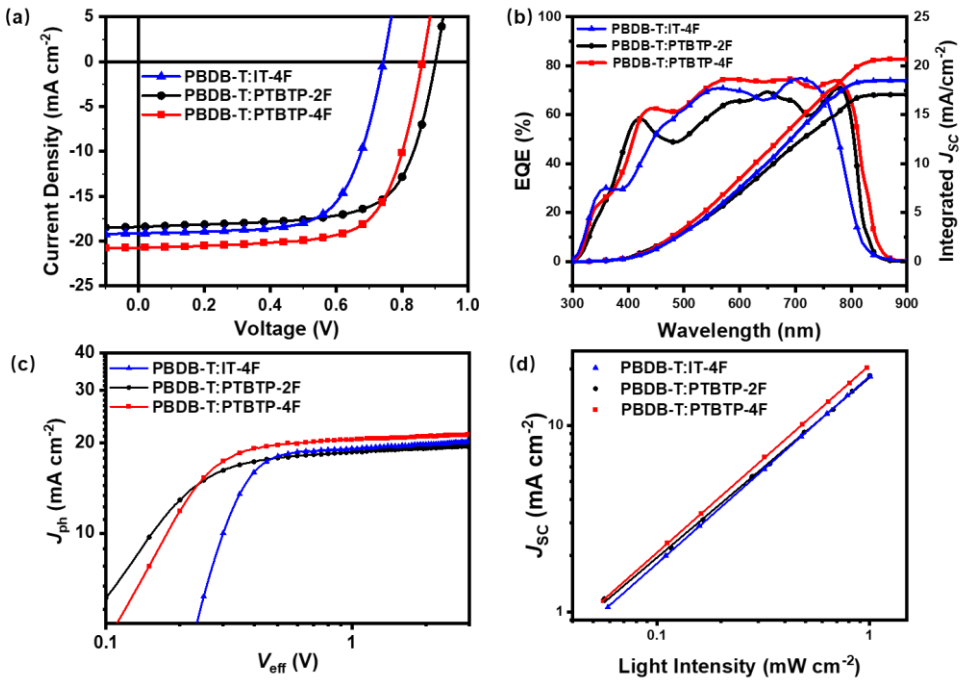

Figure 4.6 (a) J-V characteristics of the optimal OSCs. (b) EQE spectra and integrated J_{cal}s for the IT-4F, PTBTP-2F and PTBTP-4F based OSCs. (c) J_{ph}s versus V_{eff}s. and (d) J_{SC}s versus light intensity of the optimized devices.

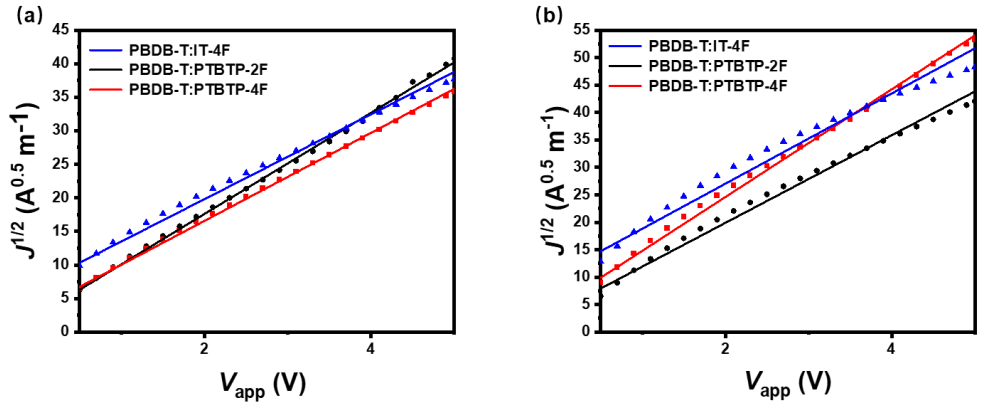

Figure 4.7 (a) Hole and (b) Electron mobilities of the blend films.

4.3.3 Energy Loss

The influence of the end-capping groups of the acceptors on the E_{Loss} of the blends was investigated by FTPS-EQE measurement and EL spectra measurement. The E_{Loss} was calculated according to the following equation: $E_{\mathrm{Loss}} = E_{\mathrm{g}} - qV_{\mathrm{OC}}$, which can also be divided into three parts, i.e., $E_{\mathrm{Loss}} = E_{\mathrm{g}} - qV_{\mathrm{OC}} = \left(E_{\mathrm{g}} - qV_{\mathrm{OC}}^{\mathrm{SQ}}\right) + \left(qV_{\mathrm{OC}}^{\mathrm{SQ}} - qV_{\mathrm{OC}}^{\mathrm{Rad}}\right) + \left(qV_{\mathrm{OC}}^{\mathrm{Rad}} - qV_{\mathrm{OC}}\right) = \Delta E_1 + \Delta E_2 + \Delta E_3$ (Amorim et al., 2012), where ΔE_1 arises from the loss related to the Shockley-Queisser (SQ) limit (Rao and Friend, 2017;Guillemoles et al., 2019), ΔE_2 is induced from radiative recombination, and ΔE_3 is caused by nonradiative recombination. The detailed E_{Loss} data are summarized in **Table 4.4**.

Table 4.4 Detailed E_{Loss} parameters of the OSCs based on PBDB-T: acceptor blends

Acceptors	E_g [eV]	V_{OC}^{SQ} a) [V]	ΔE_1 [eV]	V_{OC}^{rad} b) [V]	ΔE_2 [eV]	ΔE_3 [eV]	E_{Loss} [eV]
IT-4F	1.55	1.293	0.257	1.100	0.193	0.378	0.83
PTBTP-2F	1.53	1.259	0.271	1.229	0.030	0.319	0.62
PTBTP-4F	1.52	1.254	0.266	1.219	0.035	0.359	0.66

a) V_{OC}^{SQ} was calculated according to the Shockley-Queisser (SQ) theory. b) V_{OC}^{rad} was calculated from EL and FTPS measurements.

In general, coulombic binding force between electrons and holes needs to be overcome during the charge separation process. In OSCs, stronger electron-deficient accepting unit in A-D-A type molecules is favorable for intermolecular stacking. Along with the enhanced intermolecular interaction, more hybridized CT states are thus formed, leading to a higher energy offset between CT states and local exciton (LE) states and thus more efficient charge separation. The energy barrier to generate free charges depends on appropriate energetic offsets, ΔE_{CT}, which is the difference between E_{g} and E_{CT} (Faist et al., 2012;Eisner et al., 2019) in **Figure 4.9**. Herein, the study of the CT states was involved to detect the driving force for charge separation. The E_{CT}s were obtained by single-line fitting of the FTPS-EQE measurements in **Figure 4.8**. ΔE_{CT} was achieved as 0.15 eV for IT-4F, 0.08 eV for PTBTP-2F and 0.09 eV for PTBTP-4F, respectively, which suggested more sufficient charge separation occurred in

PBDB-T: PTBTP-4F blend films, and hence the highest J_{SC} was achieved for the corresponding devices.

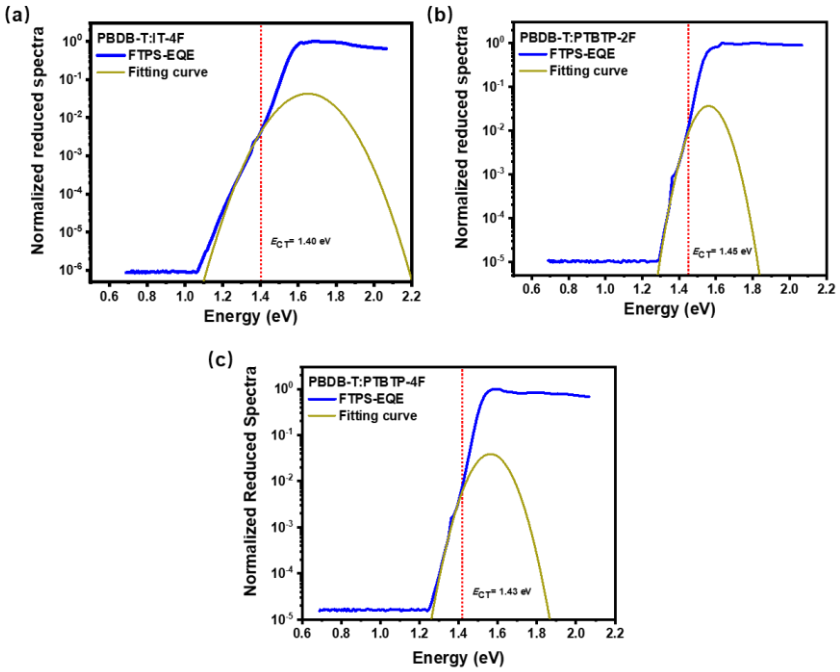

Figure 4.8 FTPS-EQE and single-fitting curves of (a) PBDB-T: IT-4F based devices (b) PBDB-T: PTBTP-2F based devices and (c) PBDB-T: PTBTP-4F based devices.

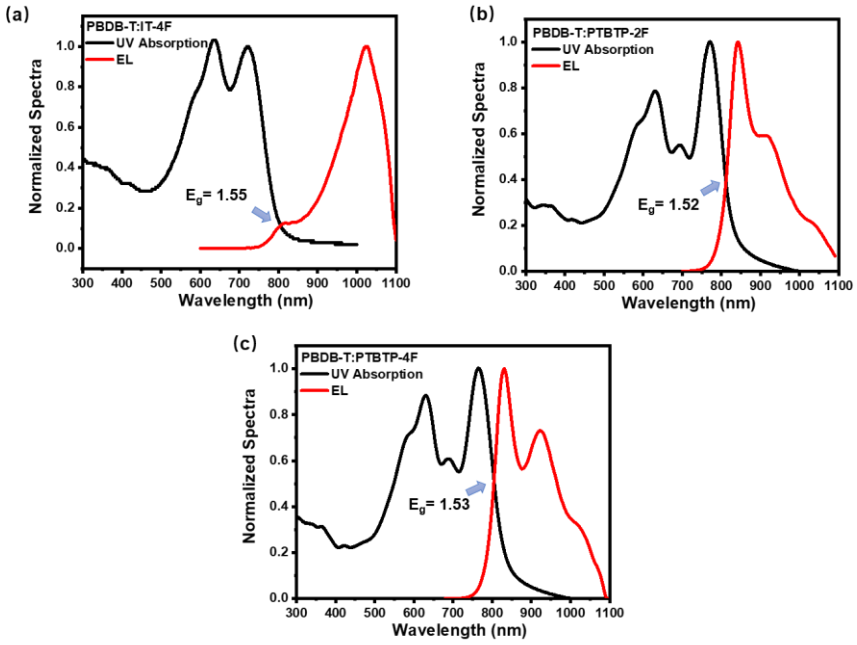

Figure 4.9 Normalized UV-vis absorption and EL emission spectra of the blend films.

As summarized in **Table 4.4**, the red-shifted absorption induced by end-capping group variation of two acceptors led to a lower ΔE_1 (0.266 eV) for PTBTP-4F based devices, while ΔE_2 (0.035 eV) was similar for both blends, and ΔE_3 (0.359 eV) was higher for PTBTP-4F blends. Thus, a total energy loss of 0.66 eV was induced in PTBTP-4F based devices. Meanwhile, the PBDB-T: IT-4F based devices suffered from serious radiative energy loss of 0.193 eV, mainly because of mismatched energy levels between PBDB-T and IT-4F, reflected in lower V_{OC} by ~0.14 V. To further explore the non-radiative energy loss, EQE_{EL} measurement, which was directly related to ΔE_3, was conducted and exhibited in **Figure 4.10**. The EQE_{EL} spectra of the OSCs based on PBDB-T: IT-4F and PBDB-T: PTBTP-4F blends were much lower than that of PTBTP-2F based ones, suggesting more serious non-radiative recombination, leading to higher ΔE_3 of the IT-4F and PTBTP-4F blends. Therefore, accompanying with the improvement of intermolecular interaction in PBDB-T: IT-4F and PBDB-T: PTBTP-4F blend films, sufficient charge separation was induced, which afforded higher J_{SC}s, though it caused enhanced ΔE_3 and thus certain V_{OC} loss.

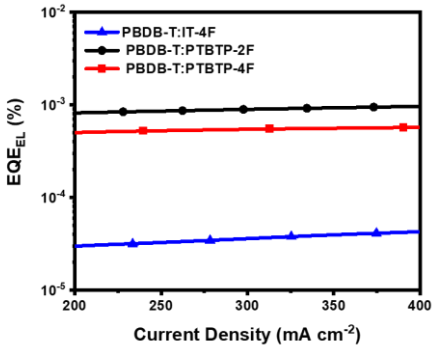

Figure 4.10 EQE_{EL} spectra of the blend films.

4.3.4 Morphology Characterization

To investigate the influence of surface properties and surface morphology of the active layers on the device performance, contact angles between the neat films of PBDB-T, PTBTP-2F, and PTBTP-4F and H_2O/ glycerol (GL) were measured (Goh et al., 2005;Kim et al., 2012). The contact angles (θ) and surface energies (γ) are depicted in **Figure 4.11a and Table 4.5**.

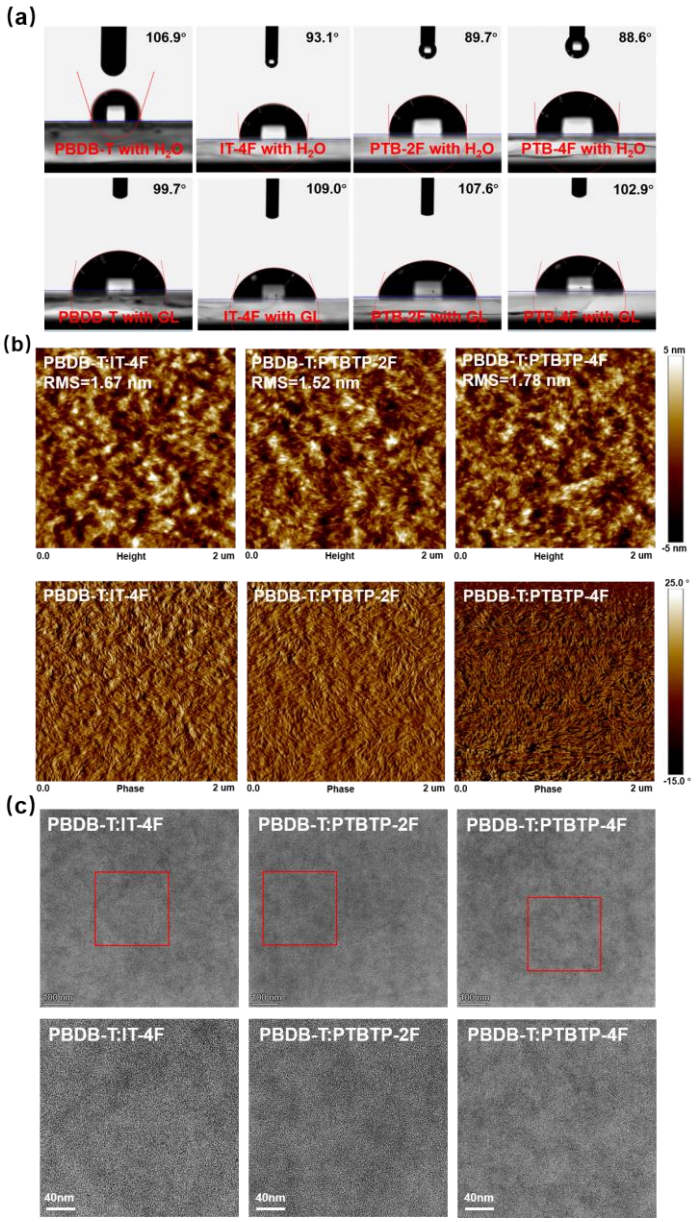

Figure 4.11 (a) Contact angles between the neat films and H_2O/ glycerol (GL). (b) AFM images (c) TEM images of the blend films based on PBDB-T and IT-4F/PTBTP-2F/PTBTP-4F.

Table 4.5 Summarized contact angles and surface free energy parameters of PBDB-T and two acceptors.

Films	θ_{water} [°]	θ_{GL}[°]	γ[mN m^{-1}]	$\chi_{donor\text{-}acceptor}[k]$
PBDB-T	106.9	99.7	16.64	-
IT-4F	93.1	109.2	40.47	5.21
PTBTP-2F	89.7	107.6	45.53	7.11
PTBTP-4F	88.6	102.9	37.26	4.10

Three acceptors exhibited similar contact angles with H_2O and GL. Compared with PBDB-T neat films, smaller contact angles between acceptor films and H_2O and GL suggested enhanced lipophilicity. The corresponding γ values of IT-4F, PTBTP-2F, and PTBTP-4F were 40.47 mN m^{-1}, 45.53 mN m^{-1}, and 37.26 mN m^{-1}, respectively, which was favorable for forming decent vertical phase separation. To evaluate the miscibility between donor and acceptor, $\chi_{donor-acceptor}$ was also calculated (Kim et al., 2012). $\chi_{donor-acceptor}$ of PBDB-T: PTBTP-4F was lower than that of PBDB-T: PTBTP-2F and PBDB-T: IT-4F, suggesting better miscibility between PBDB-T and PTBTP-4F, which may result in higher *FF*s of the PTBTP-4F based devices.

AFM was employed to study the surface morphology of the active layers (**Figure 4.11b**). All three blend films presented quite a smooth surface with the root mean-square-roughness (RMS) of 1.67 nm for IT-4F, 1.78 nm for PTBTP-4F based films, and 1.52 nm for PTBTP-2F based film, respectively. On the same scale, the clearer nano phase images of PBDB-T: PTBTP-4F blended films with higher contrast ratio suggested PBDB-T: PTBTP-4F blended films realized more fibrillar-like phase separation, which resulted in higher exciton dissociation efficiency, thus higher *FF*s of the devices. As depicted in **Figure 4.11c**, TEM was employed to further investigate the inner phase separation of the blend films. As seen from the TEM images, as-cast PBDB-T: PTBTP-4F films exhibited clear and intercalated nanophase separation networks in the zoomed images. The dark area indicated material aggregations, while the brighter area indicated slightly larger phase separation in the PBDB-T: PTBTP-4F blend films. Compared with PBDB-T: PTBTP-4F blend films, PBDB-T: PTBTP-2F and PBDB-T: IT-4F blend films exhibited larger phase domain size,

which resulted in lower interface area and thus lower exciton dissociation efficiency.

To study the molecular packing and crystallinity in the IT-4F, PTBTP-2F, and PTBTP-4F binary blends, GIWAXS measurement was carried out (**Figure 4.12**). The face-on orientational molecular packing of the acceptor molecules in their blended films was verified as the π-π stacking peaks appeared from the out-of-plane linecuts and the lamellar peaks appeared mainly from the in-plane linecuts. The π-π stacking along (010) direction appeared at ~17.5 nm^{-1} for the PTBTP-2F binary films, and ~18 $nm^{-1}$for the IT-4F and PTBTP-4F binary films, which corresponded to a π-π stacking distance of 3.5 Å and 3.6 Å, respectively. The results indicated that all three blend films tended to be face-on stacking orientational rather than edge-on stacking orientation. Meanwhile, the crystalline coherent lengths (CCLs) estimated from the π-π stacking peaks were about 10.61 nm, 10.67 nm, and 11.38 nm for the IT-4F, PTBTP-2F, and PTBTP-4F binary films, respectively. The more compact molecular packing and higher crystallinity can be associated with the more conjugated π-π system and stronger intermolecular interaction induced by the more electron-deficient end-capping group of PTBTP-4F, which also illustrated the larger electron mobility of PTBTP-4F blend films. In addition, all of the (100) peaks of the binary films are located at ~3.1 nm^{-1}. The corresponding CCL values of (100) peaks were calculated to be 6.63 nm, 6.96 nm, and 13.38 nm for the IT-4F, PTBTP-2F, and PTBTP-4F binary films. The enlarged (100) CCL values verified more uniform, finer, and ordered interpenetrating nanofibril-like phase separation network as observed from the AFM phase images of PTBTP-4F, which led to higher *FF*s in comparison to the PTBTP-2F and IT-4F binary films.

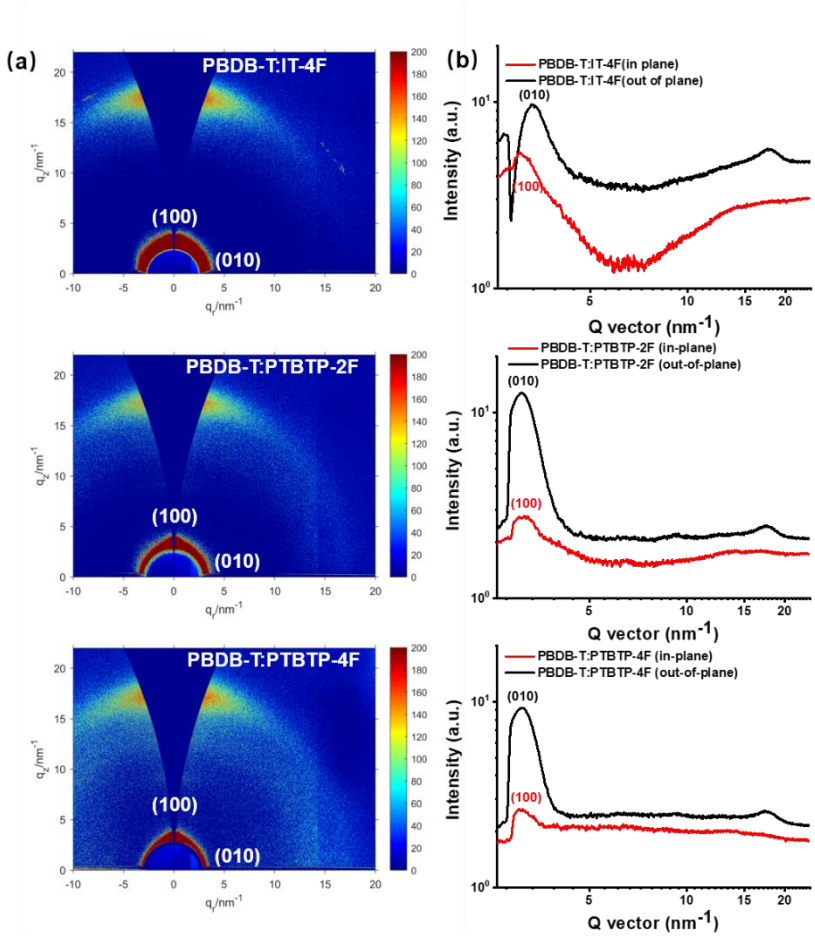

Figure 4.12 (a) 2D GIWAXS patterns of the PBDB-T: acceptors blend films (b) The corresponding in-plane (red lines) and out-of-plane (black lines) line cuts.

4.4 Conclusion

In conclusion, the TP unit was introduced as a building block to construct pyrrole-containing conjugated backbones for synthesizing NFAs. Two novel acceptors, namely, PTBTP-2F and PTBTP-4F, were designed and synthesized successfully. The photophysical and electrochemical properties, device performance, energy loss, and morphology of the blend films have been investigated to evaluate the performance of the novel acceptors. Compared with IT-4F, the introduction of the TP unit onto the central core can enhance the energy levels of the acceptors, thus leading to higher V_{OC}. Meanwhile, the end-group capping effects on the acceptors and the performance of the TP unit were also investigated through evaluating the performance of the acceptors. Benefitting from the well-matched energy levels and complementary light

absorption of donor and acceptors, the devices based on PBDB-T: PTBTP-2F blends achieved an average *PCE* of 11.14%, a V_{OC} of 0.91 V, a J_{SC} of 17.89 mA cm^{-2} and an *FF* of 68.66%. Compared with PTBTP-2F, more fluorinated PTBTP-4F not only exhibited slightly down-shifted energy levels and red-shifted absorption, but also afforded weaker bimolecular recombination and suitable phase separation for efficient charge dissociation. However, more hybridized CT states of PTBTP-4F induced higher non-radiative energy loss. In sacrifice with certain V_{OC}, the PBDB-T: PTBTP-4F based devices exhibited an obvious increase in J_{SC}s, and eventually realized a promising *PCE* of 12.33%, with a V_{OC} of 0.86 V, a J_{SC} of 20.74 mA cm^{-2} and an *FF* of 69.02%. Our work has demonstrated that when molecular backbones are designed or optimized, modular synthesis mode would be an effective method to simplify reaction routes and to obtain the target molecules, if the building blocks were already available. As an example, our work demonstrated one novel building block, thiophene[3,2-b] pyrrole (TP), had shown its potential for constructing highly efficient NFAs.

Chapter 5

Conformation flipping of asymmetric nonfullerene acceptors enabling high performance organic solar cells with 77% fill factors[†]

5.1 Synopsis

Considerable progress on high performance OSCs has been achieved in the past due to the rapid development of NFAs. Typically, two kinds of methods have been employed to manipulate energy levels and aggregation of NFAs, i.e., molecular engineering on alkyl side chains and modification of the heterocyclic rings in the backbone. In this work, a novel asymmetric TP-based NFA with

[†] The work in this chapter was published in:

Zhu, J., Zhang, Z., Lv, Y., Lan, A., Zhou, J., Lv, Y., Lu, H., Zhou, E., Do, H., Chen, Z., & Chen, F. (2023). "Conformation flipping of asymmetric nonfullerene acceptors enabling high performance organic solar cells with 77% fill factors." *Solar rrl*, 7, 2300171.

flipped molecular conformation, named as PTBTT-4F, was designed and synthesized. The introduction of the pyrrole ring in the novel NFA would not only afford extra reaction sites for side chain modification, but also induce substantial ICT, thus leading to elevated energy levels of the NFA and thereby lower energy loss of the OSCs. When pairing with polymer donor PBDB-TF to fabricate OSCs, concurrent improvement in V_{OC}, J_{SC} and *FF* were realized, which delivered an outstanding *PCE* of 14.49%. Benefitting from effective molecular stacking and optimized phase separation induced by molecular conformation variation, asymmetric PTBTT-4F fabricated OSCs exhibited much higher J_{SC}s and *FF*s than the symmetrical PTBTP-4F devices.

5.2 Introduction

The innovation of photovoltaic materials (Wu and Zhu, 2013;Wang et al., 2016;Liu et al., 2022a;Meng et al., 2022;Zhang et al., 2022c), specially NFAs has pioneered many research hot spots of OSCs for in-depth exploration in the past decades. With combinational efforts devoted to molecule evolution and device engineering, the *PCE* of single-junction solar cells has approached up to 19% (Bi et al., 2021;He et al., 2022a;Zhu et al., 2022b). Various NFAs have been developed in recent years, such as DPP or perylene diimide (PDI) contained molecules (Patil and Misra, 2019;Sun, Chen and Chen, 2019;Yu et al., 2022), A-D-A type acceptors, i.e., ITIC (Lin and Zhan, 2015;Yan et al., 2018a), M series (Zheng et al., 2020a) and Y series molecules (Cui et al., 2020b;Zhu et al., 2020;Li et al., 2021a;Liu et al., 2021), typically Y6 (Yuan et al., 2019b).

Core engineering has been demonstrated effective to achieve high performance NFAs, as molecular conjugation and ICT can be readily realized through introducing or removing the aromatic rings on the backbone of NFAs. Additionally, the asymmetric strategy was adopted for molecule modification, which could precisely regulate the intrinsic optoelectronic properties of NFAs. Derived from symmetric NFAs, i.e., ITIC and IT-4F (Zhao et al., 2017), various A-D-A-type asymmetric NFAs have been designed and synthesized (Sun et al.,

2018d;Cai et al., 2021). Sun's group designed asymmetric TPTT-2F and TPTTT-2F through extending molecular conjugation of the IDT core (Song et al., 2018). Along with the enhanced conjugation, red-shifted absorption, up-shifted energy levels and more ordered face-on molecular stacking were realized simultaneously. Tang *et al.* (Sun et al., 2018b) introduced the DTP unit in the backbone and designed an electron-rich central building block and a symmetric acceptor INPIC-4F, which realized a *PCE* of 13.13% and a high *FF* of 71.5% when pairing with polymer donor PBDB-T. IPT-4F and IPTBO-4Cl were then developed through asymmetric optimization of molecular conformation, which facilitated better miscibility and much more balanced aggregation of the donor and acceptor blends, thus leading to higher *FF*s of 74.15% and 72.57%, respectively (Cao et al., 2020;Yang et al., 2020). Fine-tuning of molecular backbone conjugation is favorable for addressing the drawbacks of NFAs, such as uncomplimentary absorption region, mismatched energy levels and ordinary miscibility to a large extent (Li et al., 2019a;Luo et al., 2020). More importantly, asymmetric molecular design strategy can facilitate larger dipole moments, leading to enhanced ICT and stronger intermolecular interaction of NFAs (Yang et al., 2019;Gao et al., 2020). There are mainly two ways for constructing asymmetric molecular backbones for NFAs, i.e., adding or removing fused rings and heteroarene substitution. The former approach can regulate molecular conjugation to a greater extent and flip the conformation for higher dipole moments, while the latter option is suitable for subtly tuning the absorption region or energy levels. Nevertheless, the asymmetric molecule design strategy also features some issues. Excessive molecular conjugation may cause pseudo potential between HOMO energy levels of donor and acceptor, leading to small driving force. On the contrary, lack of conjugation would induce broader energy gaps and eventually blue-shifted absorption onset (Xia et al., 2021). An A-D-A-type acceptor PTBTP-4F we designed previously (**Figure 5.1**) showed similar issues, though it achieved reduced nonradiative energy loss owing to enhanced energy levels when pairing with PBDB-TF, the binary devices suffered from incompatible HOMO energy levels, and thus limited *FF*s and J_{SC}s.

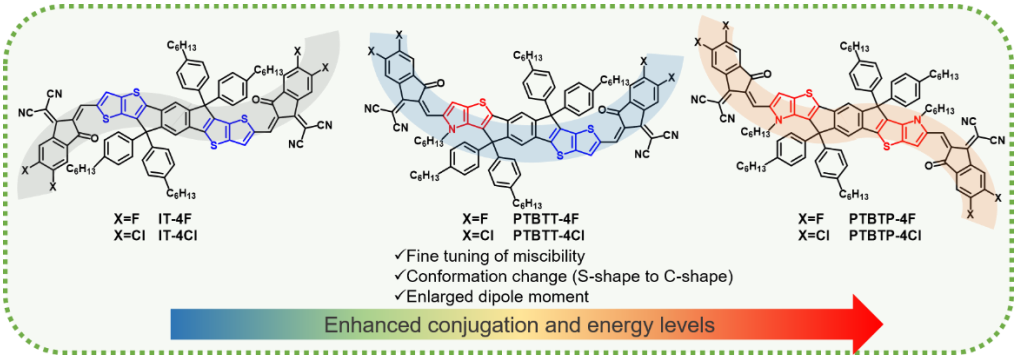

Figure 5.1 Molecular structures of IT-4F/4Cl (left), PTBTT-4F/4Cl (middle) and PTBTP-4F/4Cl (right)

In this work, asymmetric molecular design strategy was employed to optimize PTBTP-4F and improve the photovoltaic performance. TP and TT units were utilized to construct asymmetric acceptors, PTBTT-4F/4Cl. Compared to symmetric IT-4F/4Cl, the external n-hexyl pyrrole would induce flipping of the end-capping groups, and the molecular conformation changed from "S" type to "C" type correspondingly, owing to steric hindrance induced by the hexyl chain, thus larger dipole moments were realized. Moreover, effective ICT and decent miscibility were achieved for the asymmetric acceptors, ascribing to the moderate conjugated backbone and proper side-chain engineering. Benefiting from enhanced LUMO energy levels, the total energy loss of PTBTT-4F/4Cl devices decreased significantly. The performance of PTBTP-4F/4Cl based devices was inferior to asymmetric PTBTT-4F/4Cl based devices, especially in *FF*s. Compared with the IDTT backbone, the introduction of the alkyl chain in the PTBTT backbone resulted in better miscibility with polymer donor, which was also verified from contact angle measurements and film morphology investigations. Ascribed to the great miscibility between PBDB-TF and PTBTT-4F and thus exquisite phase separation, an outstanding *FF* of 76.73% was achieved. Eventually, the PBDB-TF: PTBTT-4F based devices afforded a maximum *PCE* of 14.49%. In all, realized by introducing alkyl-functionalized pyrrole rings, the asymmetric strategy guaranteed low energy loss, thereby squeezing more V_{OC} while maintaining high J_{SC}, as better phase separation and more interfacial area of the blend films were generated. Additionally, the asymmetric molecular conformation and enlarged dipole moments facilitated stronger intermolecular interaction of the acceptor molecules, leading to higher *FF*s.

5.3 Results and Discussion

5.3.1 Materials Synthesis and Photophysical Properties

Two asymmetric TP-contained acceptors named as PTBTT-4F/4Cl were synthesized and compared with symmetric IT-4F/4Cl and PTBTP-4F/4Cl. The hexyl-functionalized TP block was synthesized according to the previous method (Zhu et al., 2022a). The PTBTT central core was synthesized using Stille coupling reaction. The goal products PTBTT-4F/4Cl were obtained as dark blue solids by Knoevenagel condensation between dialdehyde and end-capping groups (IC-2F/2Cl). The molecular structures of PTBTT-4F, PTBTT-4Cl, and PTBTP-4Cl were identified by NMR and high-resolution mass spectrometry, as summarized in **Appendix II**. From the NOSEY NMR measurements, the hydrogen in the end-capping groups exhibited no interaction and thus no space correlation with the hydrogen in the hexyl alkyl chain, which indicated the S-shape conformation of PTBTP-4F/4Cl and C-shape conformation of PTBTT-4F/4Cl. All three acceptors presented high decomposition temperatures (Td, 5% weight loss) of 340 ℃ for PTBTT-4F, 338 ℃ for PTBTT-4Cl, and 348 ℃ for PTBTP-4Cl, respectively (**Figure 5.2**).

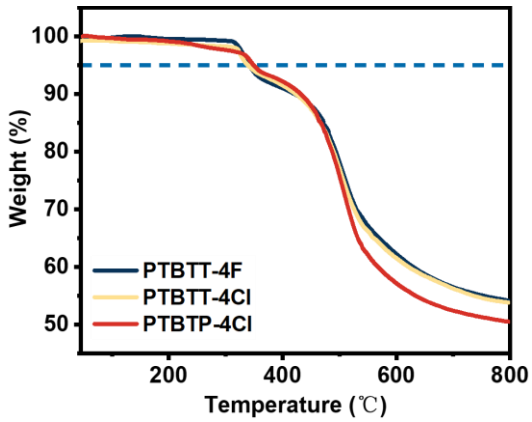

Figure 5.2 TGA curves of PTBTT-4F, PTBTT-4Cl and PTBTP-4Cl

The photophysical properties of IT-4F/4Cl, PTBTT-4F/4Cl and PTBTP-4F/4Cl are summarized in **Table 5.1**. The absorption spectra of six materials in CF solution and films are exhibited in **Figure 5.3a** and **Figure 5.3b**. Compared with IDTT backbone, the sp^3 hybridized sulfur was replaced with a sp^2-hybridized nitrogen in the PTBTT and PTBTP backbones. The lone pair electrons in nitrogen can move along the π molecular orbitals, thus facilitating the

delocalization of π-electron system and extending the conjugation. Along with the increased conjugation of the backbones, the maximum absorption peaks in CF red-shifted from 691 nm to 745 nm, together with enhanced extinction coefficients observed from IT-4F (2.03×10^5 M^{-1} cm^{-1}), IT-4Cl (2.11×10^5 M^{-1} cm^{-1}), PTBTT-4F (2.39×10^5 M^{-1} cm^{-1}), PTBTT-4Cl (2.45×10^5 M^{-1} cm^{-1}), PTBTP-4F (2.74×10^5 M^{-1} cm^{-1}) and PTBTP-4Cl (2.83×10^5 M^{-1} cm^{-1}). Compared with the absorption from solutions, the maximum absorption peaks of the corresponding films red-shifted to the NIR region, suggesting that stronger π-π molecular stacking formed in solid state. PTBTP-4F films exhibited broad absorption from 550 nm to 840 nm, with a maximum absorption peak at 764 nm. As validated by the EQE spectra of the blend films, PTBTT-4F exhibited complementary light absorption with PBDB-TF so that photons can be harvested sufficiently. Meanwhile, by combining chlorine substitution with TP block introduction, full absorption coverage from 700 nm to 800 nm was realized. Along with the extended molecular conjugation in IT-4F, PTBTT-4F, and PTBTP-4F, the optical bandgaps narrowed correspondingly, that were 1.55 eV, 1.48 eV, and 1.46 eV, respectively. Compared to the fluorinated acceptors, chlorinated IT-4Cl, PTBTT-4Cl, and PTBTP-4Cl exhibited more narrowed optical bandgaps of 1.48 eV, 1.45 eV, and 1.44 eV, respectively, owing to enhanced aggregations. Additionally, the molecular conformations of the potential rotamers extracted from three molecular backbones, simplified as TT-IC2F and PT-IC2F, were theoretically simulated, as depicted in **Figure 5.3d**. Noticeably, the surface potential energy of TT-IC2F and PT-IC2F were lowest at 0 degree, suggesting that the molecular conformations of PTBTT-4F and PTBTP-4F (C-shape and S-shape) were stable. Owing to steric hindrance effects induced by the alkyl chain in the pyrrole ring, S-shape conformation was achieved for PTBTP-4F/4Cl.

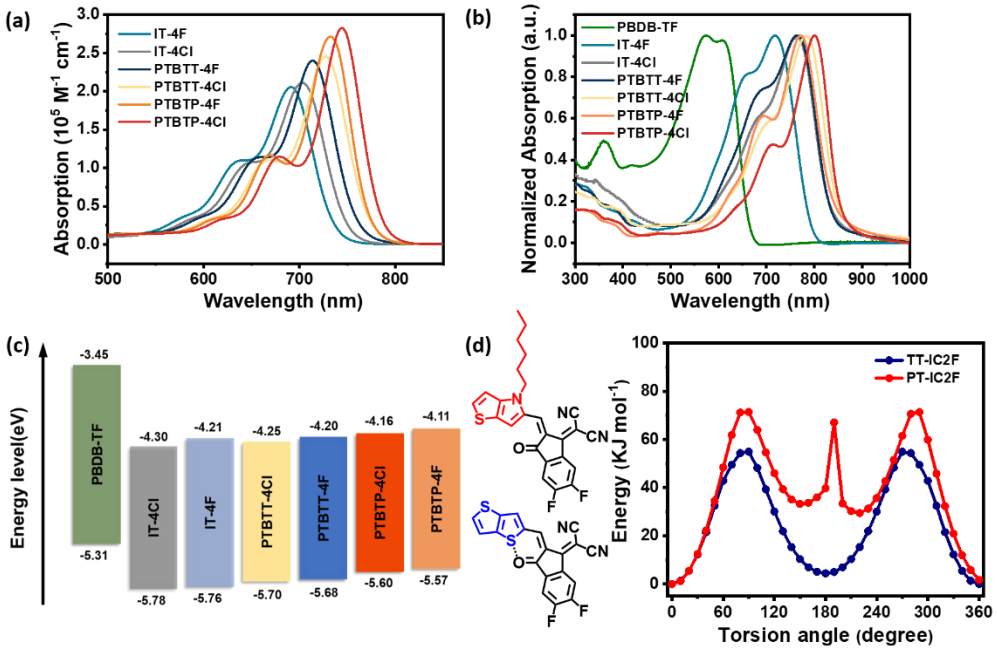

Figure 5.3 Absorption curves for IT-4F/4Cl, PTBTT-4F/4Cl and PTBTP-4F/4Cl (a) in dilute chloroform solutions (10^{-5} M) and (b) normalized absorption curves in films. (c) Energy levels diagram of the devices. (d) Surface potential energy scan of possible rotamers (TT-IC4F and PT-IC4F) extracted from IT-4F/4Cl and PTBTP-4F/4Cl, respectively.

Table 5.1 Electrochemistry and photophysical properties of IT-4F/4Cl, PTBTT-4F/4Cl and PTBTP-4F/4Cl.

Acceptors	E_{HOMO} [eV]	E_{LUMO} [eV]	$\lambda_{max}^{sol.}$ a) [nm]	λ_{max}^{film} [nm]	λ_{onset}^{film} [nm]	E_g^{opt} b) [eV]	ε_{max} a) [$M^{-1}cm^{-1}$]
IT-4F	-5.76	-4.21	691	719	799	1.55	2.03×10^5
IT-4Cl	-5.78	-4.30	703	762	839	1.48	2.11×10^5
PTBTT-4F	-5.68	-4.20	714	764	839	1.48	2.39×10^5
PTBTT-4Cl	-5.70	-4.25	727	783	855	1.45	2.45×10^5
PTBTP-4F	-5.57	-4.11	733	772	849	1.46	2.74×10^5
PTBTP-4Cl	-5.60	-4.16	745	801	861	1.44	2.83×10^5

a)In chloroform solution. b)$E_g^{opt}=1240/\lambda_{onset}^{film}$

An ionization energy measurement system (Nakano, Kaji and Tajima, 2021) was employed to detect the electrochemical properties of the acceptors under N_2 atmosphere. As depicted in **Figure 5.4**, the HOMO energy levels of IT-4F/4Cl, PTBTT-4F/4Cl, and PTBTP-4F/4Cl were measured to be -5.76 eV/-5.78 eV, -5.68 eV/-5.70 eV, and -5.57 eV/-5.60 eV, respectively. In combination with the optical bandgaps, the corresponding LUMO energy levels were calculated to be -4.21 eV/-4.30 eV, -4.20 eV/-4.25 eV, and -4.11eV/-4.16 eV, respectively. The enhanced molecular conjugation induced by the pyrrole ring upshifted energy levels gradually and narrowed optical bandgaps of the

acceptors. Compared with IT-4F/4Cl, pyrrole ring contained acceptors obtained higher LUMO energy levels, which led to higher V_{OC} and lower energy loss. Moreover, the HOMO energy levels offset between PBDB-TF and PTBTT-4F was realized to be 0.37 eV, which ensured adequate driving force for sufficient charge separation.

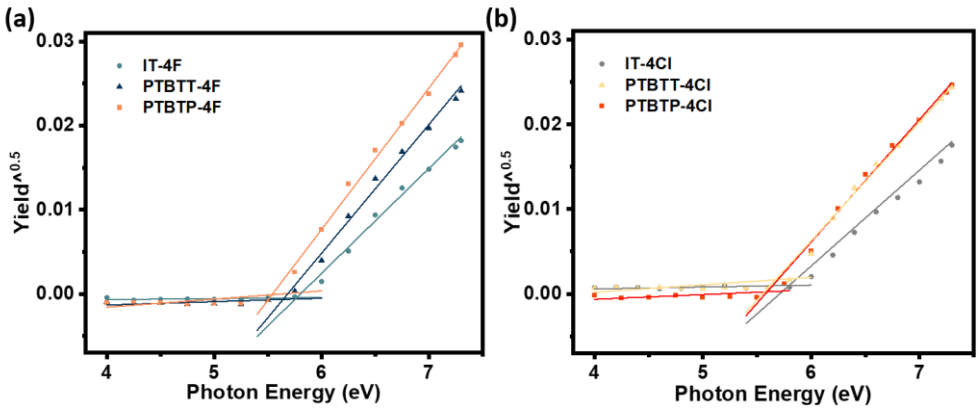

Figure 5.4 IPS curves for (a) IT-4F, PTBTT-4F, PTBTP-4F (b) IT-4Cl, PTBTT-4Cl, PTBTP-4Cl under N_2.

5.3.2 Quantum Chemical Calculations

To make quantum chemical calculations tractable, the long-chain alkyl side group was replaced by a methyl group for the three acceptors, which speeded up excited states calculation without altering the nature of frontier molecular orbitals. The molecular geometries of all three molecules were firstly optimized using DFT at the B3LYP/6-31G (d,p) level. TDDFT was employed to characterize the electronic excitations of the acceptors. The long-range corrected ωB97XD functional in conjunction with the 6-31G (d,p) basis set was employed to compute the lowest five singlet states, as this functional could capture both short- and long-range interactions and describe charge transfer states accurately. The effects of the size of the basis set and the number of electronic states on the excited states calculation results have been discussed in our recent work (Jiang, Hirst and Do, 2022). All quantum chemical calculations were performed with the Gaussian 09 program package (Frisch et al., 2009), while the electronic structure-property analysis was completed using the Multiwfn codes (Lu and Chen, 2012;Zhang and Lu, 2021). The ESP was computed to characterize conformation differences between symmetric and asymmetric structures. As shown in **Figure 5.5b & Figure 5.6a**, symmetric IT-

4F/4Cl and PTBTP-4F/4Cl exhibited centrosymmetric charge distribution (electron density isosurfaces at 0.001 au), while PTBTT-4F/4Cl displayed axisymmetric charge distribution owing to the C-shape conformation. As indicated by the dashed circle, different from S-shape molecules, more concentrated positive charges (referring to the red area) gathered in the central core of PTBTT-4F, resulting in a higher dipole moment of 3.25 Debye. Due to the enhanced dipole moment, intensified intermolecular interaction can be realized in PTBTT-4F blends, which would facilitate more efficient charge generation. To clarify the ICT difference between symmetric and asymmetric molecules and quantify charge separation, the charge density difference between the ground state (S_0) and the first excited state (S_1) was analyzed by separating the molecules into seven moieties (**Figure 5.5a & Appendix II**). Our excited states calculations showed that the HOMO-LUMO pair transition contributed over 99% to the S_0-S_1 excited states for all three acceptors. Therefore, multiple excited states were excluded to simplify the calculation process. As shown in **Figure 5.5 & Figure 5.6**, asymmetric PTBTT-4F/4Cl exhibited a distinctive ICT process compared to two symmetric acceptors. The holes (referring to the yellow grid) in PTBTT-4F/4Cl concentrated on the TP block instead of the central core, with the electrons gathering onto the end-capping groups. Such unbalanced hole-electron distribution generated nearly double charge transfer strength from moiety 5 to moiety 2, indicating a reinforced ICT effect in asymmetric PTBTT-4F/4Cl. Conversely, more dispersed hole distribution in symmetric molecules resulted in a weaker ICT effect in IT-4F/4Cl and PTBTP-4F/4Cl.

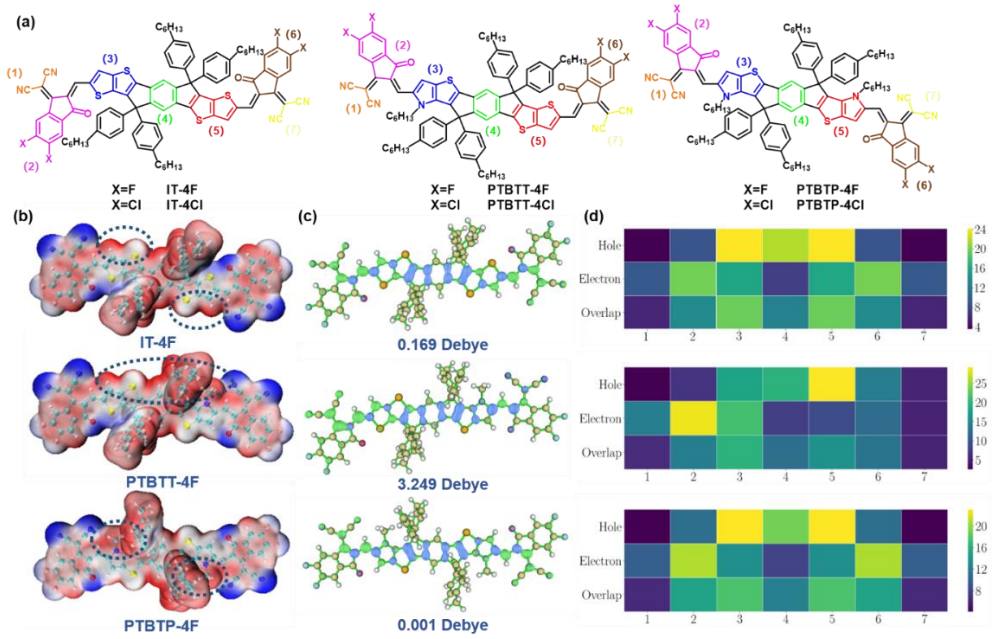

Figure 5.5 (a) Moiety classification of the hole-electron distribution heat map. (b) ESP of IT-4F, PTBTT-4F and PTBTP-4F. (c) Isosurface of hole (blue) and electron (red) distributions for the $S_0 \rightarrow S_1$ (HOMO-LUMO) transition. (d) Heat map of the fragment contributions (as a percentage) to the hole and electron distributions for the $S_0 \rightarrow S_1$ transition.

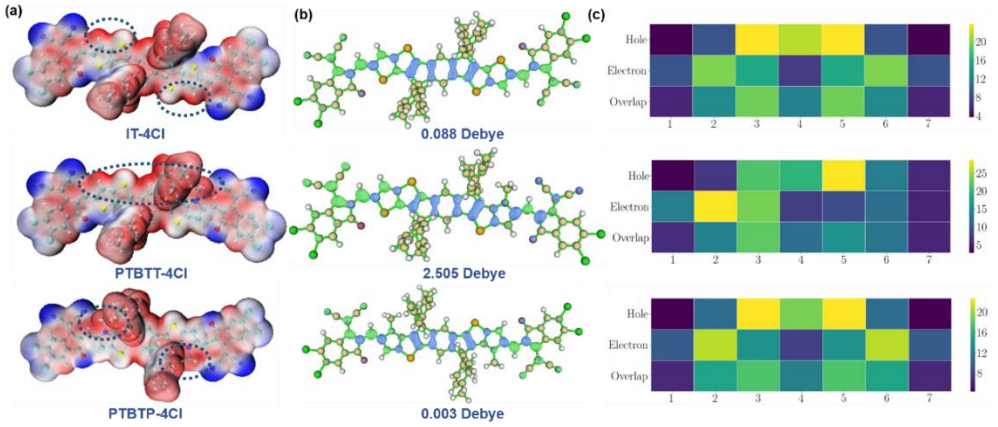

Figure 5.6 (a) ESP of IT-4Cl, PTBTT-4Cl and PTBTP-4Cl. (b) Isosurface of hole (blue) and electron (red) distributions for the $S_0 \rightarrow S_1$ (HOMO-LUMO) transition. (c) Heat map of the fragment contributions (as a percentage) to the hole and electron distributions for the lowest excited state $S_0 \rightarrow S_1$ transition.

5.3.3 Photovoltaic Properties

To characterize the photovoltaic performance of the acceptors, OSCs with conventional device configuration of ITO/PEDOT:PSS/Active Layer/PDINN/Ag were fabricated. The blend solutions of PBDB-TF: PTBTT-4F/4Cl (1:1, w/w) or PTBTP-4F/4Cl (1:0.8, w/w) in chloroform at a total concentration of 15 mg/mL were spin-coated as the active layers. Similarly, the

blend solution of PBDB-TF: IT-4F/4Cl (1:1, w/w) in chloroform at a total concentration of 16 mg/mL was prepared to fabricate control devices, as previously reported (Gao et al., 2018a). The devices' performance was optimized by manipulating donor/acceptor blend ratios, introducing various additives, and varying annealing temperature, as summarized (**Table 5.2Table 5.4)**. As a result, PTBTT-4F blend films were fabricated with 0.5% DIO as the additive at an optimized thermal annealing temperature of 100 ℃ for 3 min. The optimal PBDB-TF: PTBTP-4F/4Cl and IT-4F/IT-4Cl devices were produced under the same conditions and the detailed photovoltaic parameters are summarized in **Table 5.5**. The PBDB-TF: IT-4F based devices delivered an average *PCE* of 13.18%, with a V_{OC} of 0.86 V, a J_{SC} of 20.80 mA cm^{-2}, and an *FF* of 73.67%. By contrast, the devices based on PBDB-TF: PTBTP-4F blends obtained a lower *PCE* of 10.49%, a higher V_{OC} of 0.95 V, a J_{SC} of 18.30 mA cm^{-2}, and a lower *FF* of 60.25%. Compared with IT-4F based devices, the higher V_{OC}s of PTBTP-4F based devices can be ascribed to the reduced V_{OC} loss ($E_{loss} = E_g - qV_{OC}$) of 0.55 eV, as the pyrrole substitution narrowed optical bandgaps and elevated LUMO energy levels of PTBTP-4F. The PTBTT-4F based devices not only retained lower energy loss but also achieved a remarkable *FF* of 76.73%, thus delivering an outstanding *PCE* of 14.49%, owing to suppressed recombination and efficient photon collection efficiency, exquisite phase separation, and closer molecular packing of the blend films. Likewise, PTBTT-4Cl based devices exhibited superior performance than those of the two symmetric acceptors, which obtained a V_{OC} of 0.85 V, a J_{SC} of 22.81 mA cm^{-2}, and an *FF* of 73.82%. Compared with three fluorinated acceptors, chlorinated IT-4Cl, PTBTT-4Cl, and PTBTP-4Cl based devices obtained higher J_{SC} due to extra light harvesting but lower V_{OC} because of deeper LUMO energy levels.

Table 5.2 The optimized photovoltaic parameters of devices based on PBDB-TF: PTBTT-4F blends.

Ratio	Additive	TA [°C]	V_{OC} [V]	J_{SC} [mAcm^{-2}]	*FF* [%]	*PCE* [%]
1:0.8	-	-	0.87	22.12	64.56	12.40
1:1	-	-	0.88	21.04	70.39	13.09
1:1.2	-	-	0.88	21.01	69.39	12.82
1:1	0.5%DIO	-	0.89	21.62	70.80	13.72
1:1	0.25%DIO&0.25%CN	-	0.89	21.07	71.03	13.30
1:1	0.5%CN	-	0.87	22.88	67.54	13.46
1:1	0.5%DIO	80	0.90	21.38	71.70	13.80
1:1	0.5%DIO	100	0.88	21.43	76.73	14.49
1:1	0.5%DIO	120	0.88	23.25	67.76	13.85

Table 5.3 The optimized photovoltaic parameters of devices based on PBDB-TF: PTBTT-4Cl blends.

Ratio	Additive	TA [°C]	V_{OC} [V]	J_{SC} [mAcm^{-2}]	*FF* [%]	*PCE* [%]
1:0.8	-	-	0.91	22.50	54.77	11.15
1:1	-	-	0.89	22.63	59.99	12.12
1:1.2	-	-	0.89	22.48	56.85	11.44
1:1	0.5%DIO	-	0.88	24.33	61.34	13.19
1:1	0.25%DIO&0.25%CN	-	0.88	23.09	62.96	12.80
1:1	0.5%CN	-	0.91	22.56	63.03	12.99
1:1	0.5%DIO	80	0.85	22.25	72.53	13.73
1:1	0.5%DIO	100	0.85	22.81	73.28	14.17
1:1	0.5%DIO	120	0.84	22.10	71.22	13.27

Table 5.4 The optimized photovoltaic parameters of devices based on PBDB-TF: PTBTP-4Cl blends.

Ratio	Additive	TA [°C]	V_{OC} [V]	J_{SC} [mAcm^{-2}]	*FF* [%]	*PCE* [%]
1:0.8	-	-	0.94	17.38	59.08	9.67
1:1	-	-	0.94	17.79	60.06	10.05
1:1.2	-	-	0.92	18.43	58.03	9.88
1:1	0.5%DIO	-	0.94	18.04	62.39	10.62
1:1	0.25%DIO&0.25%CN	-	0.95	17.63	62.11	10.37
1:1	0.5%CN	-	0.95	17.46	61.59	10.19
1:1	0.5%DIO	80	0.93	18.40	64.69	11.12
1:1	0.5%DIO	100	0.92	19.58	64.14	11.58
1:1	0.5%DIO	120	0.92	19.59	61.06	11.01

Table 5.5 Photovoltaic parameters of the optimized OSCs based on six PBDB-TF: acceptor blends.

Acceptor	V_{OC} [V]	J_{SC} [mAcm^{-2}]	$J_{cal.}$[a)] [mAcm^{-2}]	*FF* [%]	*PCE*[b)] [%]
IT-4F	0.860	20.80	19.82	73.67	13.18 (12.81±0.31)
PTBTT-4F	0.881	21.43	21.32	76.73	14.49 (14.21±0.24)
PTBTP-4F	0.951	18.30	17.79	60.25	10.49 (10.28±0.21)
IT-4Cl	0.768	22.63	21.78	70.92	12.32 (12.07±0.25)
PTBTT-4Cl	0.848	22.81	21.83	73.28	14.17 (13.89±0.21)
PTBTP-4Cl	0.922	19.58	18.74	64.14	11.58 (11.31±0.22)

[a)] Integrated current densities obtained from EQE measurements. [b)]Average *PCE*s achieved from 18 devices.

The EQE spectra were measured to investigate J_{SC} difference (**Figure 5.7b**). The EQE spectra of the PBDB-TF: PTBTT-4F based devices exhibited broad and strong response (> 70%) from 450 nm to 780 nm, suggesting efficient photon harvesting would be realized. The average response intensity of PTBTP-4F/4Cl was much lower than IT-4F/4Cl and PTBTT-4F/4Cl, resulting in the decrement of J_{SC}. The wavelength response range of PTBTT-4F/4Cl was broader than IT-4F/4Cl, which was consistent with the corresponding optical bandgaps. In addition, due to the influence of halogenation on absorption, the response ranges of chlorinated IT-4Cl, PTBTT-4Cl, and PTBTP-4Cl blends

were broader than those of the fluorinated blends. As a result, the integrated J_{cal}s of PBDB-TF: IT-4F/IT-4Cl/PTBTT-4F/PTBTT-4Cl/PTBTP-4F/PTBTP-4Cl based devices were 19.82 mA cm^{-2}, 21.78 mA cm^{-2}, 21.32 mA cm^{-2}, 21.83 mA cm^{-2}, 17.79 mA cm^{-2} and 18.74 mA cm^{-2}, respectively, which were consistent with the *J-V* characterizations.

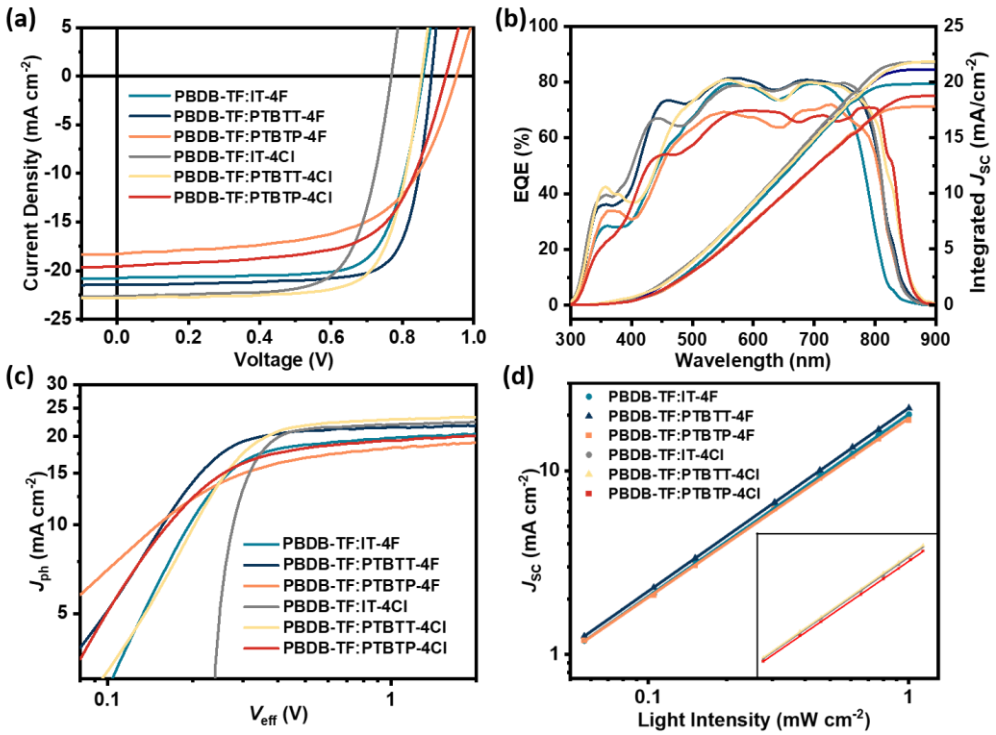

Figure 5.7 (a) *J-V* characteristics of the optimal OSCs. (b) EQE spectra and integrated J_{cal}s for the IT-4F/4Cl, PTBTT-4F/4Cl and PTBTP-4F/4Cl based OSCs. (c) J_{ph} versus V_{eff} curves. (d) J_{SC} versus light intensity of the optimized devices.

To better understand charge generation and collection efficiencies of the devices, the dependence of photocurrent (J_{ph}) on the effective voltage (V_{eff}) was investigated (**Figure 5.7c**) and summarized (**Table 5.6**). J_{ph} can be defined as $J_L - J_D$, where J_L and J_D are the currents measured under illumination and in the dark. When J_{ph} reaches saturation current (J_{sat}) at higher applied voltages (V_{eff}), charge carriers dissociated from excitons would be collected soon. Thus, the J_{ph}/J_{sat} ratio was utilized to characterize exciton dissociation efficiency (P_{diss}) and charge collection probability (P_{coll}) under short-circuit and maximum power output conditions, respectively. As a result, the P_{diss}/P_{coll} values of IT-4F, PTBTT-4F, and PTBTP-4F were calculated to be 92.3%/86.6%, 92.5%/87.1% and 91.0%/72.4%, respectively. The higher P_{diss}/P_{coll} values of PBDB-TF:

PTBTT-4F based devices implied more efficient exciton dissociation and charge collection, which contributed to higher J_{SC}. Similarly, PTBTT-4Cl obtained higher P_{diss}/P_{coll} values of 96.5%/88.2% amongst three chlorinated acceptors (IT-4Cl: 93.1%/87.4% and PTBTP-4Cl: 92.5%/76.4%). The P_{diss}/P_{coll} results coincided well with their EQE response, concerning charge collection property. Furthermore, charge recombination behaviors were studied and evaluated from the slopes (α) of linearly fitted $ln(J_{SC}) - ln(P_{light})$ curves through measuring *J-V* curves under various light intensities (P_{light}) (**Figure 5.7d**). The bimolecular recombination under short-circuit conditions was commonly described as the slopes (α) of linearly fitted $ln(J_{SC}) - ln(P_{light})$ curves. If α was closer to 1, it means the bimolecular recombination was better suppressed in the devices. The slopes (α) were determined to be 0.990/0.988, 0.996/0.993, and 0.973/0.975 for IT-4F/4Cl, PTBTT-4F/4Cl, and PTBTP-4F/4Cl, respectively. The results suggested that PTBTP-4F/4Cl based devices had suffered from severe bimolecular recombination, causing lower *FF*s.

Table 5.6 The exciton dissociation efficiencies and charge collection efficiencies.

Active layer	J_{sat} (mA/cm^2)	J_{ph}[a)] (mA/cm^2)	J_{ph}[b)] (mA/cm^2)	η_{diss}	η_{coll}
PBDB-TF:IT-4F	22.54	20.80	19.53	92.3	86.6
PBDB-TF:PTBTT-4F	23.17	21.43	20.18	92.5	87.1
PBDB-TF:PTBTP-4F	20.10	18.30	14.56	91.0	72.4
PBDB-TF:IT-4Cl	24.31	22.63	21.25	93.1	87.4
PBDB-TF:PTBTT-4Cl	23.63	22.81	20.85	96.5	88.2
PBDB-TF:PTBTP-4Cl	21.16	19.58	16.16	92.5	76.4

[a)]Under short circuit condition; [b)]Under maximal power output condition

The SCLC method was conducted to evaluate charge transport properties of six NFAs blends. As plotted in **Figure 5.8** and summarized in **Table 5.7**, the hole and electron mobilities (μ_h and μ_e) of PTBTP-4F based devices were determined to be 4.29×10^{-4} cm^2 V^{-1} s^{-1} and 2.37×10^{-4} cm^2 V^{-1} s^{-1}, relatively lower than 4.49×10^{-4} cm^2 V^{-1} s^{-1} and 2.96×10^{-4} cm^2 V^{-1} s^{-1} for IT-4F based devices. By contrast, the asymmetric acceptor PTBTT-4F presented an increased μ_h of 5.34×10^{-4} cm^2 V^{-1} s^{-1} and a higher μ_e of 4.22×10^{-4} cm^2 V^{-1} s^{-1}, indicating enhanced crystallinity in PTBTT-4F prepared films.[42] Moreover, the μ_e/μ_h ratios of PBDB-TF: IT-4F/PTBTT-4F/PTBTP-4F were calculated to

be 1.52, 1.27, and 1.81, respectively. Compared with symmetric acceptors, more balanced charge transfer property of the PTBTT-4F/4Cl blend films contributed to higher J_{SC}s and *FF*s. Additionally, chlorinated IT-4Cl/PTBTT-4Cl/PTBTP-4Cl blends obtained comparative μ_h and enhanced μ_e, thus realizing more balanced μ_e/μ_h ratios of 1.19, 1.05 and 1.59, respectively. Compared with three fluorinated acceptors, enhanced μ_e indicated chlorinated counterparts facilitated enhanced crystallinity and closer molecular packing of the corresponding blend films.

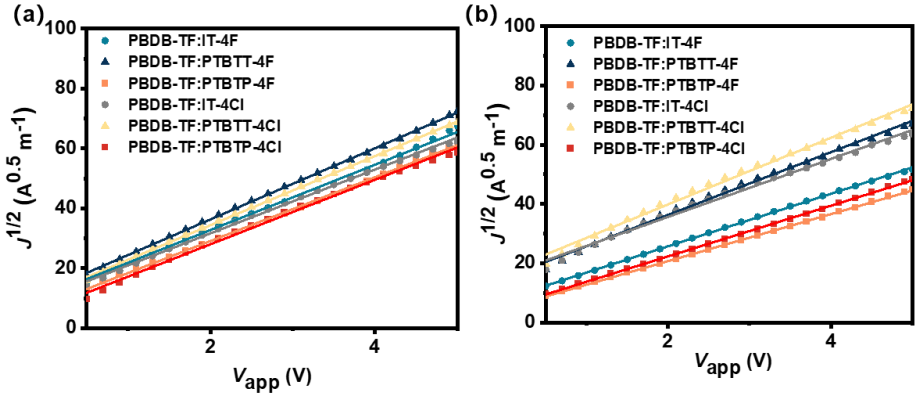

Figure 5.8 (a) Hole and (b) electron mobilities of the blend films.

Table 5.7 The hole mobilities and electron mobilities.

Active layer	μ_h (10^{-4} cm^2 V^{-1} s^{-1})	μ_e (10^{-4} cm^2 V^{-1} s^{-1})	μ_h/μ_e
PBDB-TF:IT-4F	4.49	2.96	1.52
PBDB-TF:PTBTT-4F	5.34	4.22	1.27
PBDB-TF:PTBTP-4F	4.29	2.37	1.81
PBDB-TF:IT-4Cl	4.30	3.61	1.19
PBDB-TF:PTBTT-4Cl	5.03	4.77	1.05
PBDB-TF:PTBTP-4Cl	4.39	2.76	1.59

5.3.4 Energy Loss

To investigate the effects of pyrrole substitution in the conjugated backbone on E_{Loss}, FTPS-EQE and EL spectra were measured (**Figure 5.9a**). E_g of the acceptors were obtained by determining the energies at the crossing points between the absorption and emission spectra of the corresponding films (**Figure 5.10**). Energy loss of the devices can be divided into three parts according to the following equation:

$$E_{\mathrm{Loss}} = E_{\mathrm{g}} - eV_{\mathrm{OC}} = \Delta E_{\mathrm{rad}} + \left(E_{\mathrm{g}} - E_{\mathrm{CT}}\right) + \Delta E_{\mathrm{nonrad}}$$

$$= \Delta E_{\mathrm{rad}} + \Delta E_{\mathrm{CT}} + \Delta E_{\mathrm{nonrad}} \quad (5\text{-}1)$$

where ΔE_{rad} is considered as the radiative energy loss due to absorption above the optical bandgap, ΔE_{CT} is defined as the driving force for charge transfer from the acceptor phase to the CT states, and $\Delta E_{\mathrm{nonrad}}$ arises from non-radiative recombination. Amongst of them, ΔE_{rad} is unavoidable for all kinds of OSCs. As summarized in **Table 5.8**, $\Delta E_{\mathrm{nonrad}}$ varied much between these devices, which mainly determined the total energy loss, and eventually contributing to V_{OC} difference. According to the formula: $\Delta E_{\mathrm{nonrad}} = -kT\ln(EQE_{\mathrm{EL}})$, $\Delta E_{\mathrm{nonrad}}$ can be quantified by EQE_{EL} directly. Therefore, EQE_{EL} was measured to explore non-radiative energy loss **(Figure 5.9b)**. The PBDB-TF: PTBTP-4F based devices exhibited higher EQE_{EL} of 1.01 × 10^{-4} than those of PBDB-TF: PTBTT-4F (6.43 × 10^{-6}) and PBDB-TF: IT-4F (1.34 × 10^{-6}), along with achieving lower $\Delta E_{\mathrm{nonrad}}$ of 0.238 eV. Moreover, the EQE_{EL} improved as the energy levels were elevated due to pyrrole substitution. Thereby, $\Delta E_{\mathrm{nonrad}}$ of PBDB-TF: PTBTT-4F decreased and achieved a lower value of 0.310 eV. As expected, the introduction of pyrrole ring effectively suppressed $\Delta E_{\mathrm{nonrad}}$, thus guaranteeing lower E_{Loss} and maintained V_{OC}. In addition, chlorinated PTBTT-4Cl/PTBTP-4Cl presented similar findings with reduced $\Delta E_{\mathrm{nonrad}}$ of 0.327eV and 0.274 eV. During charge separation process, the coulombic binding force between electrons and holes needs to be overcome. The energy offset between E_{g} and E_{CT} plays a decisive role in generating free charges in OSCs. FTPS-EQE measurements were conducted to investigate the driving force for charge separation in the blend films. E_{CT}s were obtained by dual fitting of the FTPS-EQE curves in **Figure 5.11**. ΔE_{CT} of PBDB-TF:IT-4F/PTBTT-4F/PTBTP-4F/IT-4Cl/PTBTT-4Cl/PTBTP-4Cl were calculated to be 0.161 eV, 0.055 eV, 0.024 eV, 0.093 eV, 0.038 eV, 0.024 eV, respectively. Although symmetric PTBTP-4F/4Cl blends obtained lower energy loss, the limited ΔE_{CT} resulted in poor charge generation efficiency, thus relatively lower J_{SC}s and *FF*s. By contrast, higher energy offsets in asymmetric PTBTT-4F/4Cl blends led to more efficient charge separation. According to previous report, more hybridized CT states and higher energy offset can be generated along with

closer intermolecular molecular stacking. Thus, we suspect that ΔE_{CT} difference might be resulted from different molecular stacking behaviors of the blend films.

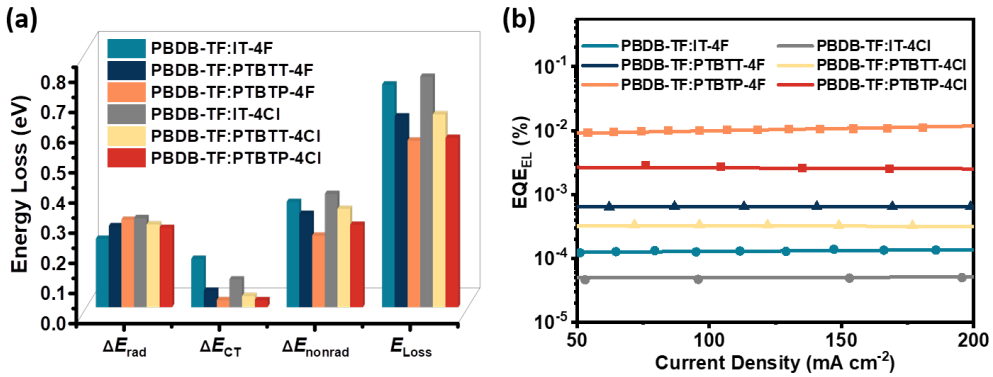

Figure 5.9 (a) Energy loss and (b) EQE_{EL} of IT-4F/4Cl, PTBTT-4F/4Cl and PTBTP-4F/4Cl based devices.

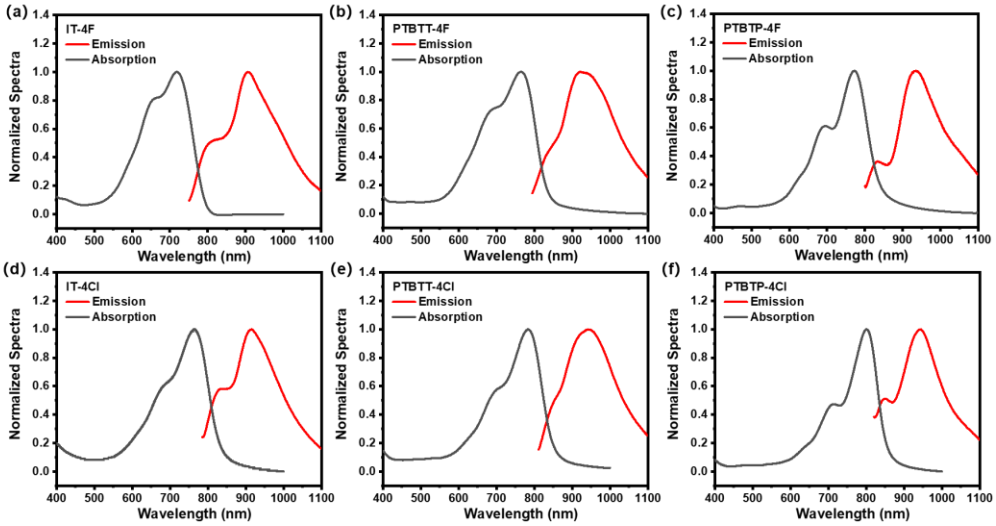

Figure 5.10 Absorption and emission curves for neat films based on six acceptors.

Table 5.8 Detailed E_{Loss} parameters of the OSCs based on PBDB-TF: acceptor blends

Acceptors	E_g [eV]	E_{CT} [eV]	ΔE_{CT} [eV]	ΔE_{rad} [eV]	EQE_{EL} [%]	ΔE_{nonrad} [eV]	E_{Loss} [eV]
IT-4F	1.601	1.44	0.161	0.228	1.34×10^{-4}	0.350	0.739
PTBTT-4F	1.515	1.46	0.055	0.269	6.43×10^{-4}	0.310	0.634
PTBTP-4F	1.504	1.48	0.024	0.291	1.01×10^{-2}	0.238	0.553
IT-4Cl	1.533	1.44	0.093	0.296	4.89×10^{-5}	0.376	0.765
PTBTT-4Cl	1.488	1.45	0.038	0.275	3.35×10^{-4}	0.327	0.640
PTBTP-4Cl	1.484	1.46	0.024	0.264	2.59×10^{-3}	0.274	0.562

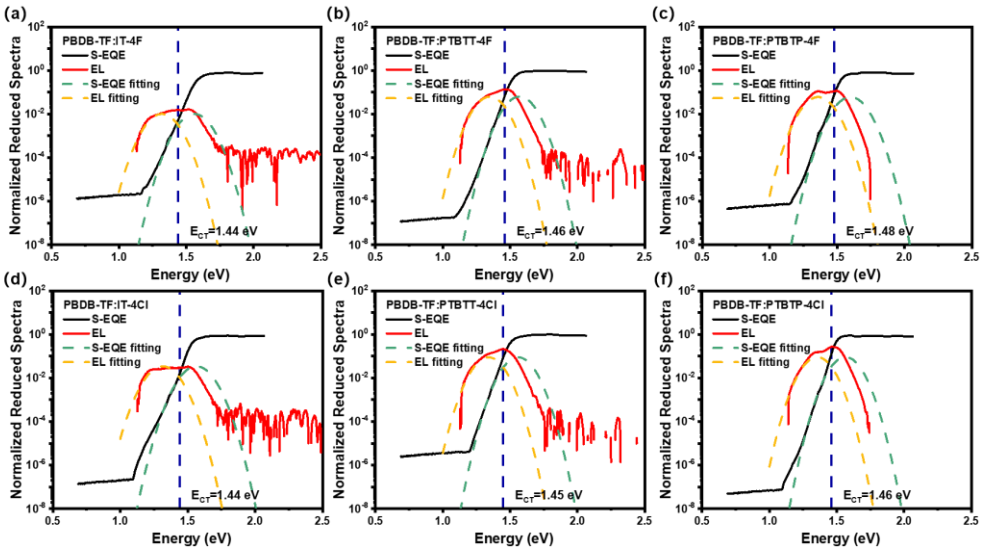

Figure 5.11 FTPS-EQE and dual-fitting curves of six binary blend films.

5.3.5 Morphology Characterizations

To explain the outstanding *FF*s of asymmetric PTBTT-4F/4Cl based devices, surface morphology of the three blend films was characterized by AFM and TEM. All the films were fabricated under the same conditions as those for preparing the optimized devices. As shown in **Figure 5.12**, all the neat films exhibited smooth surfaces with low RMS. After blending with PBDB-TF (**Figure 5.13a & Figure 5.14a**), the RMS of PBDB-TF: IT-4F/PTBTT-4F/PTBTP-4F films were measured to be 1.10 nm, 1.07 nm, and 1.18 nm, respectively, confirming that all the three blend films possessed relatively uniform surface. Moreover, the AFM phase images of PBDB-TF: IT-4F and PBDB-TF: PTBTT-4F blend films presented clearer and finer fiber-like phase separation domains than that of PBDB-TF: PTBTP-4F blend films. A larger

domain size of the phase separation was observed from the PBDB-TF: PTBTP-4F phase images, which indicates that limited interface area and thus weaker exciton dissociation was induced. The speculation can also be validated by TEM images exhibited in **Figure 5.13b**. The much more exquisite phase separation and smaller phase domain size of PBDB-TF: PTBTT-4F blend films were beneficial to generate much larger interface area between donor and acceptor, which would facilitate effective exciton dissociation and thus outstanding *FF*s of the blends. Additionally, chlorinated IT-4Cl/PTBTT-4Cl/PTBTP-4Cl films also exhibited obvious network phase separation structure but smaller surface roughness of 0.97 nm, 0.96 nm, and 1.03 nm, respectively, indicating more uniform film surface was formed. Amongst three chlorinated acceptors, asymmetric PTBTT-4Cl prepared films realized the smallest surface roughness and much more intricate nanophase separation, which contributed to the higher *FF*s compared with IT-4Cl and PTBTP-4Cl blend films.

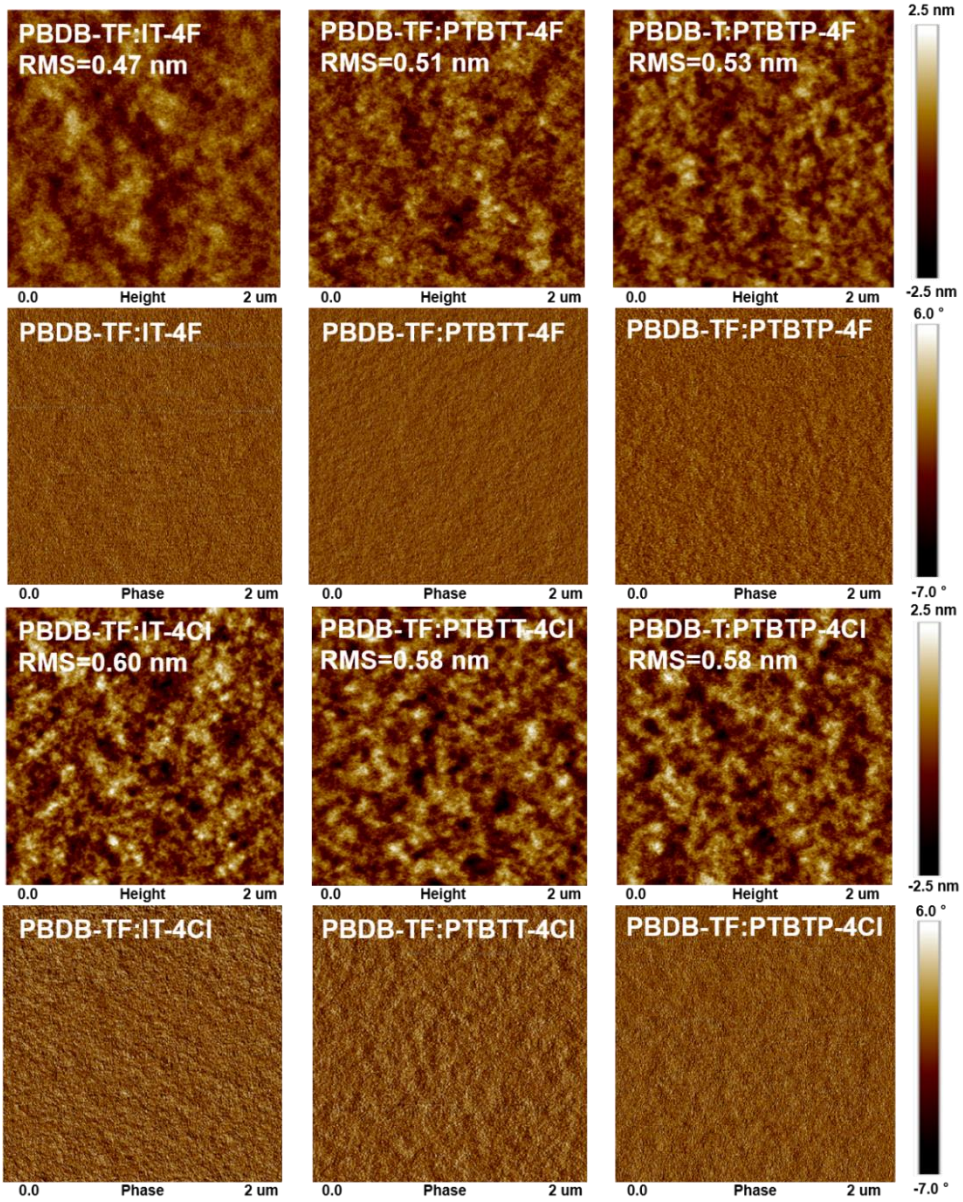

Figure 5.12 AFM images of the six neat films.

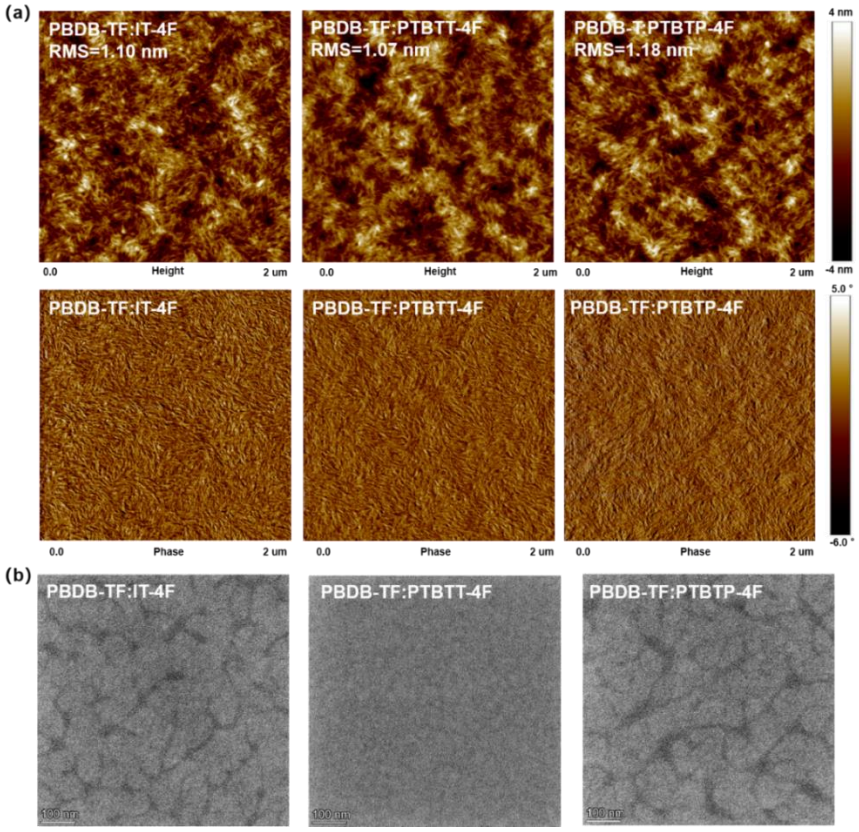

Figure 5.13 (a) AFM images and (b) TEM images of the PBDB-TF: IT-4F/PTBTT-4F/PTBTP-4F blend films.

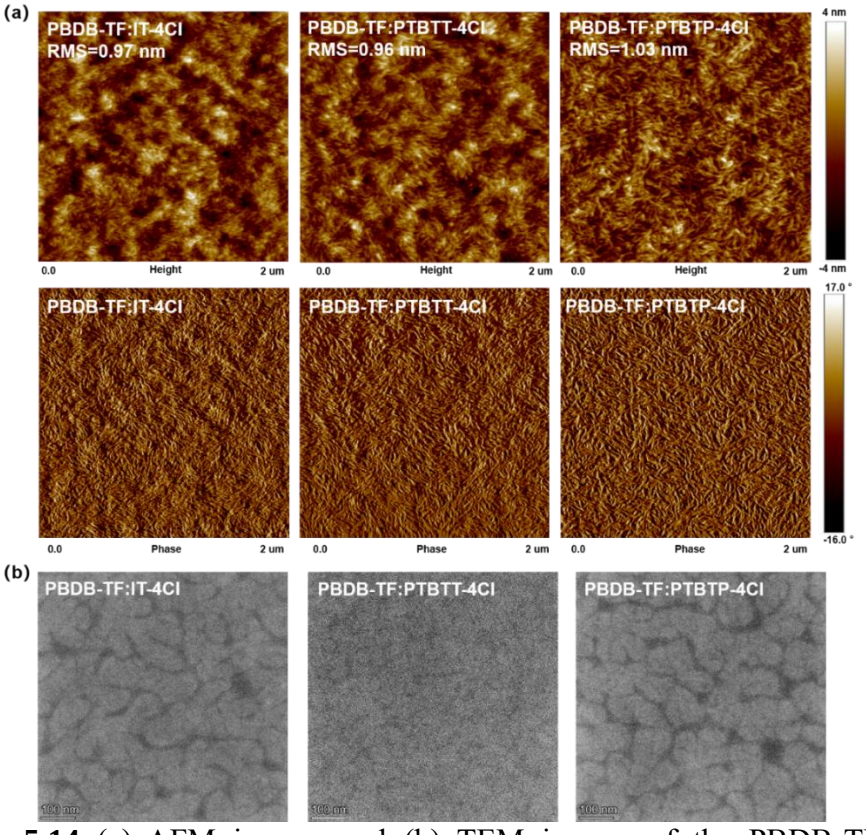

Figure 5.14 (a) AFM images and (b) TEM images of the PBDB-TF:IT-4Cl/PTBTT-4Cl/PTBTP-4Cl blend films.

Along with introducing the hexyl functionalized pyrrole, the length of the alkyl chain increased, which would affect the miscibility between donor and acceptor, thus the phase separation of the blend films. Therefore, the contact angles between neat films of PBDB-TF, IT-4F/4Cl, PTBTT-4F/4Cl, PTBTP-4F/4Cl and H_2O/glycerol (GL) were measured to investigate the miscibility thus the phase separation origins. The detailed contact angles (θ) and surface energies (γ) are depicted in **Figure 5.15** and **Table 5.9**. The miscibility can be evaluated according to the empirical equation, $\chi_{A-D} = k(\sqrt{\gamma_A} - \sqrt{\gamma_D})^2$, where χ represents the Flory-Huggins interaction parameter. In general, a smaller χ indicates better miscibility between two materials, which is favorable for forming decent phase separation in the blend films. For this reason, χ_{A-D} was calculated to be 0.53/0.77, 0.40/0.36 and 0.28/0.23, for IT-4F/4Cl, PTBTT-4F/4Cl, PTBTP-4F/4Cl respectively. As the introduction of alkyl chains in the pyrrole ring, decreased χ_{A-D} values were obtained, suggesting better miscibility between PBDB-TF and PTBTP-4F/4Cl was achieved. However, the phase separation of PTBTP-4F/4Cl blends was inferior to that of PTBTT-4F/4Cl blends. Thus, based on the above observation, we reckon that miscibility was not the determinative factor for phase separation formation, the internal molecular packing in the blend films would be the key factor that influenced phase separation and charge separation in our devices.

Table 5.9 Summarized contact angles and surface energy parameters of PBDB-TF and six acceptors.

Films	θ_{water}**[°]**	θ_{GL}**[°]**	γ**[mNm^{-1}]**	$\chi_{donor\text{-}acceptor}$**[$k$]**
PBDB-TF	107.5	94.5	20.24	-
IT-4F	94.7	79.8	27.29	0.53
PTBTT-4F	92.7	80.3	26.33	0.40
PTBTP-4F	92.1	82.0	25.25	0.28
IT-4Cl	95.6	78.6	28.92	0.77
PTBTT-4Cl	92.6	80.8	25.98	0.36
PTBTP-4Cl	90.4	83.5	24.83	0.23

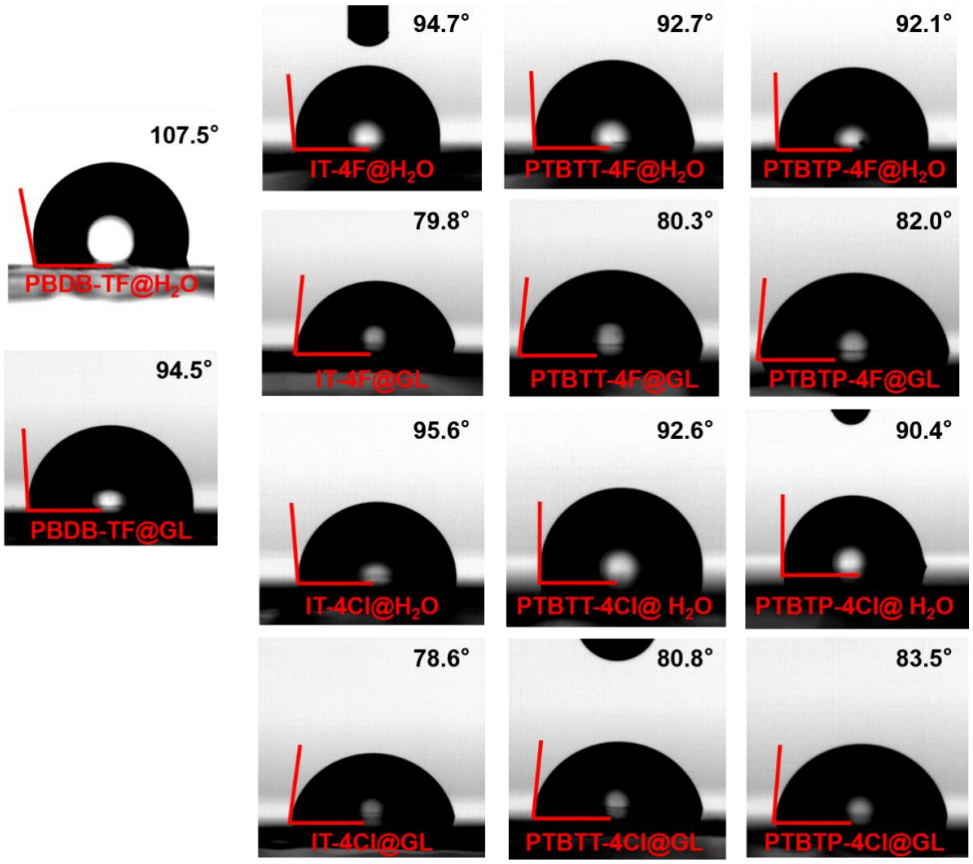

Figure 5.15 Contact angles between the neat films and H_2O/glycerol (GL).

5.3.6 Molecular Packing

Molecular optimizations were conducted to study the intermolecular stacking of three acceptors. As displayed in **Figure 5.16a & Figure 5.17a**, compared with PTBTT-4F and PTBTP-4F, better planarity was observed in IT-4F/4Cl molecules, which possess smaller torsion angles of 0.1° between the backbone and terminal groups. By contrast, PTBTT-4F/4Cl and PTBTP-4F/4Cl presented larger torsion angles (around 3.0°-3.4°) between the backbone and terminal groups, which induced enlarged steric hindrance and thus negative impact on the molecular planarity.

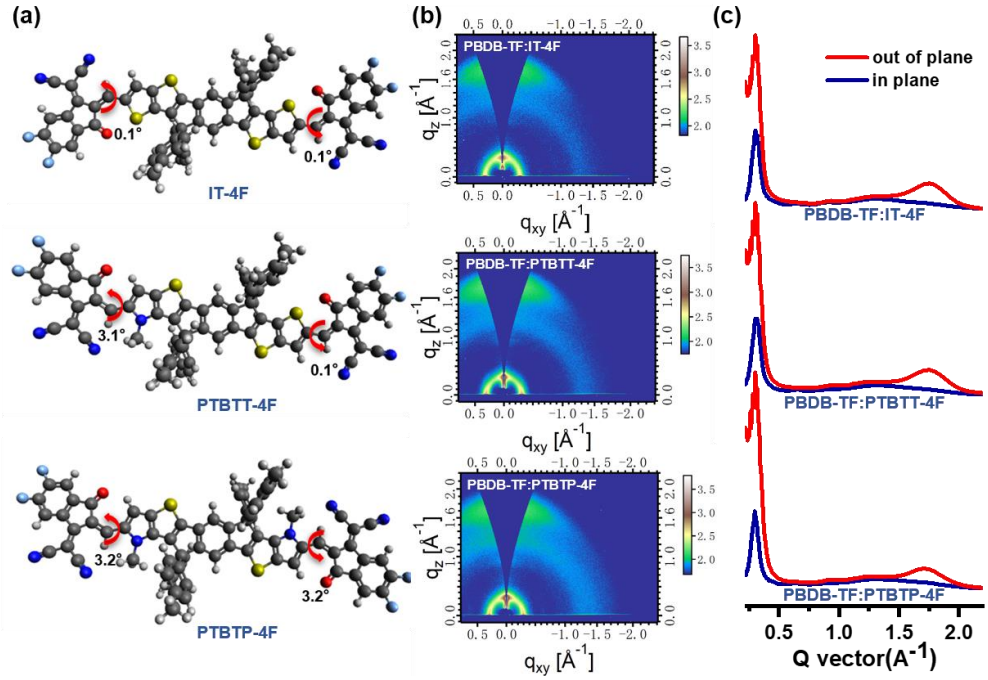

Figure 5.16 (a) The optimized 3D geometries of IT-4F/PTBTT-4F/PTBTP-4F (b) 2D GIWAXS patterns of PBDB-TF: acceptor blend films (c) The corresponding out-of-plane (red lines) and in-plane (blue lines) line cuts.

To figure out the realistic intermolecular stacking behaviors of IT-4F/4Cl, PTBTT-4F/4Cl, and PTBTP-4F/4Cl films, graze-incidence wide-angle X-ray scattering (GIWAXS) measurements were conducted. The 2D GIWAXS patterns and 1D line cuts of the binary films are exhibited in **Figure 5.16 & Figure 5.17** and summarized in **Table 5.10**. All the 2D patterns revealed a predominant (010) peak in the out-of-plane (OOP) direction, which suggested that face-on orientational molecular packing was dominant in the three blend films. At the same time, a strong (100) lamellar signal around 0.30 Å was observed in PTBTP-4F/4Cl films, which was induced by substantial side chain stacking from the hexyl-substituted pyrrole rings. Along the OOP direction, the π-π stacking appeared at 1.714 Å^{-1} for PBDB-TF: IT-4F, 1.715 Å^{-1} for PBDB-TF: PTBTT-4F and 1.669 Å^{-1} for PBDB-TF: PTBTP-4F blends, the corresponding π-π stacking distances were 3.67 Å, 3.66 Å, and 3.76 Å, respectively. In addition, chlorinated PTBTT-4Cl blend films presented closer packing (3.65 Å) than IT-4Cl (3.66 Å) and PTBTP-4Cl (3.69 Å) blends. The crystalline coherent length (CCL) was calculated to be 19.52 Å for PTBTT-4F blend films, which was higher than those of IT-4F (18.35 Å) and PTBTP-4F (17.51 Å), while the CCLs of IT-4Cl, PTBTT-4Cl, and PTBTP-4Cl blends were calculated to be 18.76 Å, 18.98 Å and 18.61 Å, respectively. As a result, PBDB-

TF: PTBTT-4F/4Cl blend films achieved closer π-π stacking, suggesting enhanced crystallinity thus higher charge mobilities generated in the blend films. Out of our initial expectation, more compact face-on packing was observed in the asymmetric PTBTT-4F/4Cl blend films, leading to higher *FF*s of the corresponding devices. At last, it is worth mentioning that all three chlorinated blend films achieved relatively closer molecular packing than their fluorinated counterparts. Nevertheless, the CCL of PTBTT-4Cl blends was smaller than that of PTBTT-4F, suggesting that intermolecular stacking in PTBTT-4F blend films was much more ordered, thus contributing to higher *FF*s.

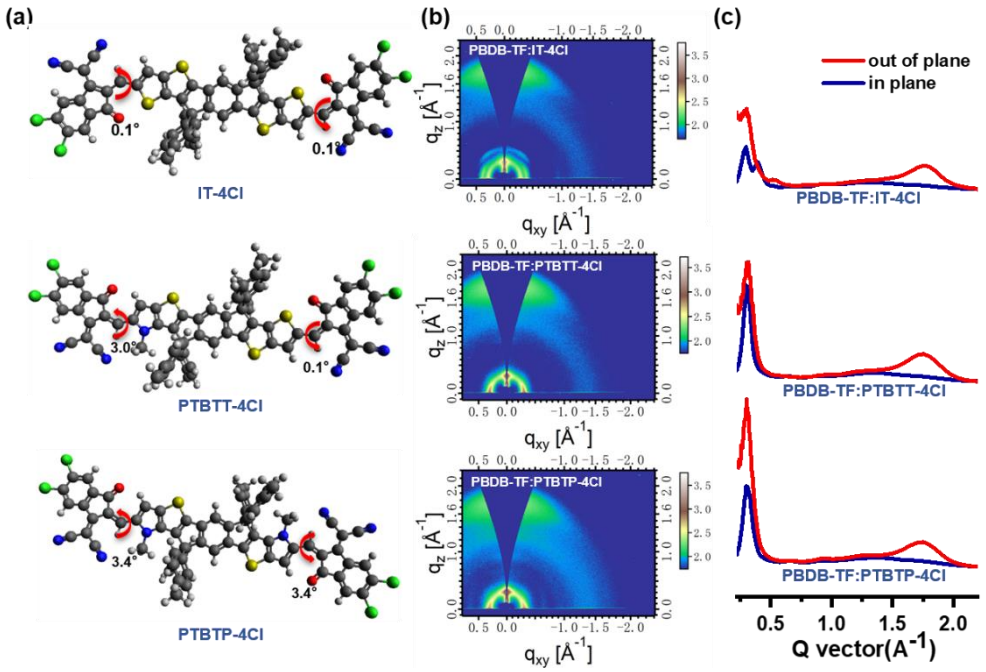

Figure 5.17 (a) The optimized 3D geometries of IT-4Cl/PTBTT-4Cl/PTBTP-4Cl (b) 2D GIWAXS patterns of PBDB-TF: acceptor blend films (c) The corresponding out-of-plane (red lines) and in-plane (blue lines) line cuts.

Table 5.10 The diffraction vector (q) values of diffraction peaks and CCLs of the binary blend films.

Active layer	Diffraction vector[Å^{-1}]		Crystal correlation length[Å]	
	OOP(010)	IP(100)	OOP(010)	IP(100)
PBDB-TF:IT-4F	1.714	0.293	18.35	69.61
PBDB-TF:PTBTT-4F	1.715	0.306	19.52	66.40
PBDB-TF:PTBTP-4F	1.669	0.309	17.51	72.65
PBDB-TF:IT-4Cl	1.719	0.309	18.76	31.37
PBDB-TF:PTBTT-4Cl	1.721	0.317	18.98	74.96
PBDB-TF:PTBTP-4Cl	1.704	0.306	18.61	62.50

5.4 Conclusion

In conclusion, this work designed and synthesized two asymmetric acceptors PTBTT-4F/4Cl, which were derived from IT-4F/4Cl and PTBTP-4F/4Cl. The photophysical and photovoltaic properties of IT-4F/4Cl, PTBTT-4F/4Cl and PTBTP-4F/4Cl were investigated to address the influence of molecular backbone engineering of acceptors on device performance of OSCs. Compared with IT-4F, PTBTT-4F exhibited red-shifted absorption, elevated LUMO energy levels, and reduced optical bandgaps. Due to the enhanced energy levels, PTBTT-4F based devices realized lower nonradiative energy loss, therefore higher V_{OC}. In addition, PTBTT-4F devices achieved higher J_{SC} and *FF*s than PTBTP-4F devices, mainly because of better miscibility between PTBTT-4F and PBDB-TF, as well as enhanced π-π stacking and improved charge transfer mobilities of the blends. Three chlorinated acceptors were synthesized and compared with fluorinated acceptors as a check experiment to verify the asymmetric design strategy in this work. Conclusively, PBDB-TF: PTBTT-4F based devices achieved a maximum *PCE* of 14.49%, a V_{OC} of 0.88 V, a J_{SC} of 21.43 mA cm^{-2}, as well as an *FF* of 76.73%. This work demonstrated that asymmetric design strategy would be a promising method for finely regulating the molecular structure and synthesizing high performance NFAs for fabricating OSCs with high *FF*s and low E_{Loss}.

Chapter 6

A-D-A type nonfullerene acceptors synthesized by core segmentation and isomerization for realizing organic solar cells with low nonradiative energy loss ‡

6.1 Synopsis

Reducing non-radiative recombination energy loss ($\Delta E_{\mathrm{nonrad}}$) in OSCs has been considered an effective method to improve the device efficiency. In this study,

‡ The work in this chapter was in preparation:

Zhu, J., Qin, Z., Lan, A., Jiang, S., Mou, J., Ren, Y., Do, H., Chen, Z., & Chen, F. (2023). "A-D-A type nonfullerene acceptors synthesized by core segmentation and isomerization for realizing organic solar cells with low nonradiative energy loss." *Small*, Under review.

the backbone of PTBTT-4F/4Cl, was divided into D1-D2-D3 segments and reconstructed. The isomerized TPBTT-4F/4Cl obtained stronger ICT, thus leading to elevated HOMO energy level and reduced E_g. According to $E_{Loss} = E_g - qV_{OC}$, the reduced E_g and enhanced V_{OC} resulted in lower E_{Loss}, indicating that E_{Loss} had been effectively suppressed in the TPBTT-4F/4Cl based devices. Furthermore, compared to PTBTT derivatives, the isomeric TPBTT derivatives exhibited more planar molecular structure and closer intermolecular stacking, thus affording higher crystallinity of the neat films. Therefore, the reduced energy disorder and corresponding lower Urbach energy (E_U) of the TPBTT-4F/4Cl blend films led to low E_{Loss} and high charge-carrier mobility of the devices. As a result, benefitting from synergetic control of molecular stacking and energetic offsets, a maximum *PCE* of 15.72% was realized from TPBTT-4F based devices, along with a reduced ΔE_{nonrad} of 0.276 eV. This work demonstrated a rational method of suppressing V_{OC} loss and improving the device performance through molecular design engineering by core segmentation and isomerization.

6.2 Introduction

The innovation of NFAs has been deemed an essential thrust for OSCs. The maximum *PCE* of single-junction solar cells has approached over 19%. (Pang et al.;Wang et al.;Jiang et al., 2022;Zhu et al., 2022c;Bi et al., 2023;Xu et al., 2023) However, compared with silicon and perovskite solar cells, the OSCs usually suffer from significant E_{Loss} and inferior charge mobility, which restrict further performance improvement. (Yoshikawa et al., 2017;Hou et al., 2018;Qian et al., 2018) Commonly, the E_{Loss} is defined as $E_g - qV_{OC}$, (Vandewal, Benduhn and Nikolis, 2018) in which the V_{OC} can be quantified as the difference between the HOMO of the donor and the LUMO of the acceptor. Thus, to maintain the LUMO energy level and compress E_g, reasonably

elevating the HOMO energy level is considered an effective strategy for designing NFAs with lower E_{Loss}. (Sun et al.;Zhou et al., 2020a)

In the old perception, many binary OSCs with incompatible HOMO energy levels suffered from insufficient charge separation and thus limited *FF*s and J_{SC}s. Hence, the HOMO E_{offset} was considered as the driving force for exciton dissociation and interfacial charge transfer. (Ran et al., 2018) However, more and more binary OSCs with low E_{offset} also exhibited sufficient exciton dissociation and impressive device performance recently. (Bakulin et al., 2012;Menke et al., 2018;Li et al., 2019b) Though it has been gradually acknowledged that E_{offset} showed limited influence on charge separation, minimizing E_{offset} is still pivotal to reducing the charge-transfer loss and improving V_{OC} on the premise of enough driving force for charge transfer and exciton dissociation. (Sun et al.;Nakano et al., 2019) In previous work, we introduced TP block into IDTT backbone and developed PTBTP derivatives with suppressed E_{Loss} owing to enhanced energy levels and compress E_{g}. While excessive molecular conjugation caused pseudo potential between HOMO energy levels of donor and PTBTP derivatives, leading to an insufficient driving force. Recently, the asymmetric strategy was conducted to optimize PTBTP-4F/4Cl and synthesize PTBTT-4F/4Cl with an asymmetric structure. (Zhu et al., 2022a) The asymmetric PTBTT-4F/4Cl exhibited sufficient driving force for exciton dissociation, leading to higher J_{SC} and *FF*. (Zhu et al.)

Given the trade-offs between E_{Loss} and E_{offset} presented above, reducing the static disorder in the photoactive films may open a new path to suppress E_{Loss}, especially E_{nonrad}. In organic photovoltaic films, molecular self-assembly mainly relies on van der Waals forces. (Chen et al., 2015) Such weak intermolecular interactions will cause severe packing dislocations and, thereby, inferior crystallinity during the fast film-formation process. (Xia et al., 2022) Owing to disordered packing, inevitable energy disorder would exist inside the active layer, exhibited as high Urbach energy (E_{U}) and large E_{nonrad}. (Liu et al., 2020b;Yuan et al., 2022;Zhang et al., 2022a;Liu et al., 2023) Therefore, reinforcing the intermolecular interactions and improving the crystallinity of the

active layer is critical for regulating disorder and thus suppressing E_{nonrad} and enhancing charge mobility simultaneously.

The electron push-pull effects on NFAs are the key to adjusting ICT and intrinsic photophysical properties to develop binary systems with low E_{Loss}. Recently, most NFAs have been designed based on the Y6 molecule, (Cui et al., 2020b;Li et al., 2021a;Zhang et al., 2022b) owing to its unique C-shape conformation and the D-A'-D central core. The underlying logic of molecular design is mainly based on the contribution of the electron-deficient core to the entire backbone. In fact, the electron push-pull effects of A-D-A'-D-A type molecules can be adapted to all A-D-A type molecules and adjust the ICT. Suppose the D cores of the A-D-A type molecules are divided into three segments named D1, D2, and D3, the weak D2 segment can be considered as an electron-withdrawing moiety compared with the stronger electron-donating moieties D1 and D3 (**Figure 6.1**). (Yuan et al., 2019b;Zheng et al., 2020a;Zhou et al., 2023) Therefore, we speculate that strengthening the contributions of D1 and D3 to the relatively electron-deficient D2 core or weakening the electron-donating ability of the D2 core would be possible ways to design highly efficient backbones similar to D-A'-D of the Y6 molecule.

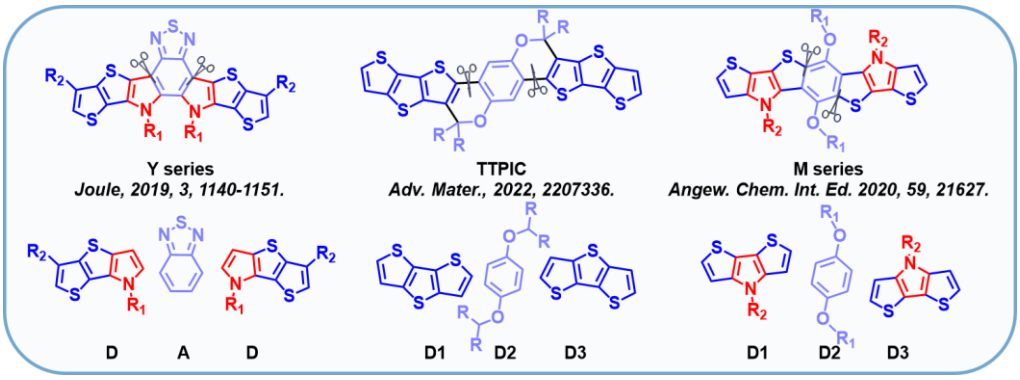

Figure 6.1 Backbone segmentation of Y series (left), TTPIC (middle) and M series (right).

Herein, to imitate the D-A'-D core, we divided the PTBTT backbone into three segments and reconstructed the TPBTT backbone (**Figure 6.2**). After isomerization of the TP block, charge transport from D1 to the D2 central core was substantially strengthened. More interestingly, charge transport from D2 central core to D3 and end-groups was also improved, owing to the inner placement of the pyrrole ring. Benefitting from the enhanced ICT, TPBTT

derivatives realized elevated HOMO energy levels and thus reduced E_{Loss}, compared to PTBTT derivatives. Different from introducing more fused-rings and heteroatoms, isomerization strategy presents a more negligible impact on the overall energy levels of the molecules to guarantee enough driving force.

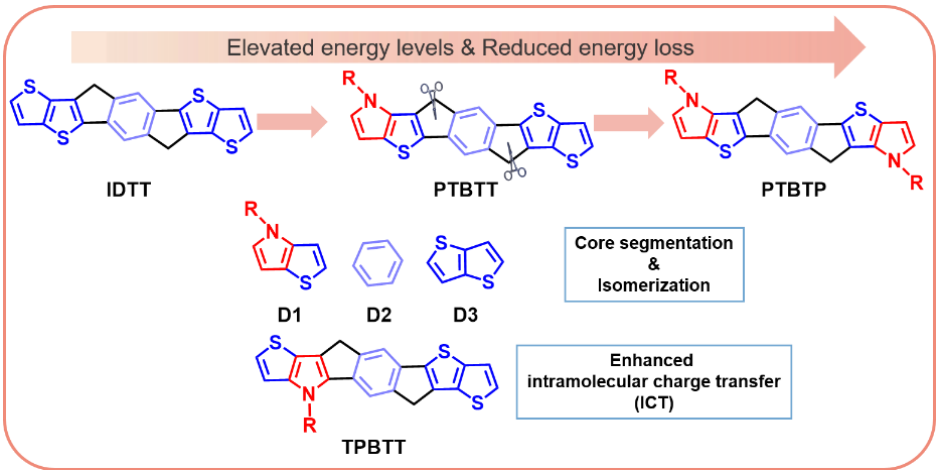

Figure 6.2 Core segmentation and isomerization based on PTBTT backbone to construct TPBTT backbone.

Additionally, the external hexyl-substituted pyrrole ring causes a larger torsion angle between the backbone and the end-capping group, which deteriorates the molecular stacking and charge mobility. By alternating the position of the pyrrole ring, the isomerized TPBTT backbone obtained enhanced molecular stacking, thus leading to higher crystallinity and amended energy disorder. Ascribed to the improved charge mobility and suppressed E_{Loss}, an impressive *PCE* of 15.72% was achieved from TPBTT-4F based devices, along with a reduced $\Delta E_{\mathrm{nonrad}}$ of 0.276 eV and a significant improvement in J_{SC}. In this work, with isomerization strategy, TPBTT derivatives with elevated HOMO energy levels and ordered molecular packing were developed, which were beneficial for suppressing ΔE_{CT} and $\Delta E_{\mathrm{nonrad}}$. We reckon that similar to the Y series, core segmentation, and isomerization strategy could be adapted to design more novel central cores with better ICT.

6.3 Results and discussion

6.3.1 Materials Synthesis and Photophysical Properties

Through core segmentation and isomerization of PTBTT-4F/4Cl, two TP-contained NFAs named TPBTT-4F/4Cl were synthesized successfully (**Figure 6.3a**). The hexyl-functionalized TP block was prepared according to the previous method. (Liu et al., 2021) The final products TPBTT-4F/4Cl were obtained with reaction routes similar to PTBTT-4F/4Cl. The corresponding molecular structures of TPBTT-4F/4Cl were identified by NMR and high-resolution mass spectrometry (see **Appendix III**). Two isomers exhibited high decomposition temperatures (Td, 5% weight loss) of 360 ℃ for TPBTT-4F, and 404 ℃ for TPBTT-4Cl, respectively (**Figure 6.4**).

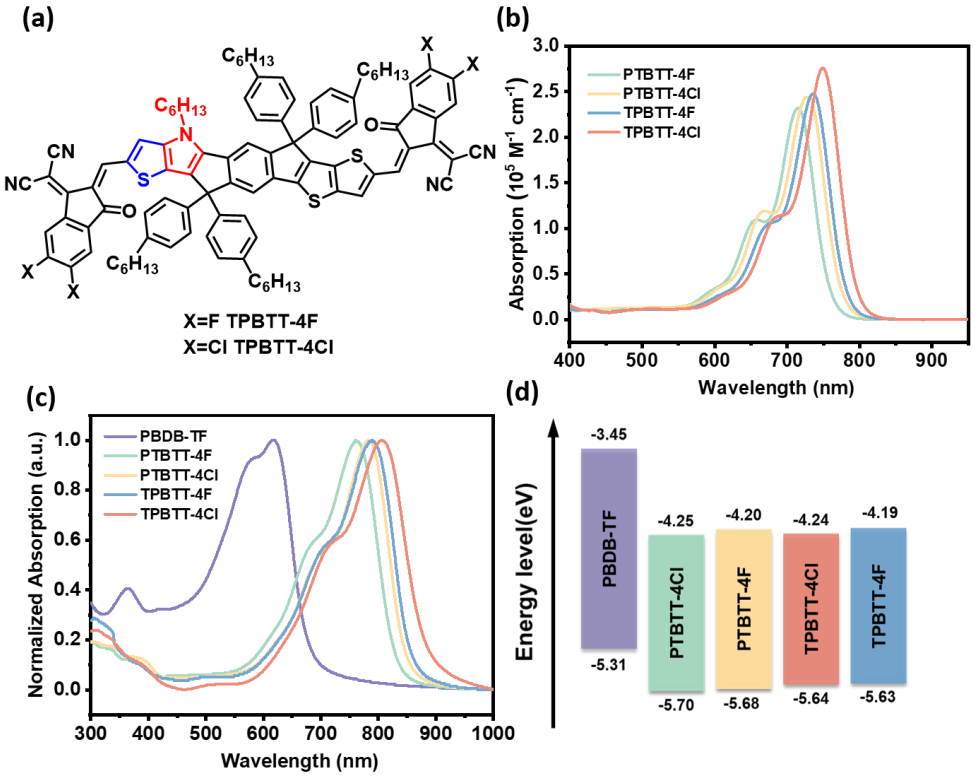

Figure 6.3 (a) Molecular structures of TPBTT-4F/4Cl. Absorption curves for PTBTT-4F/4Cl and TPBTT-4F/4Cl (b) in $CHCl_3$ solutions (10^{-5} M) and (c) normalized absorption curves of neat films. (d) Energy levels diagram of PBDB-TF and four acceptors.

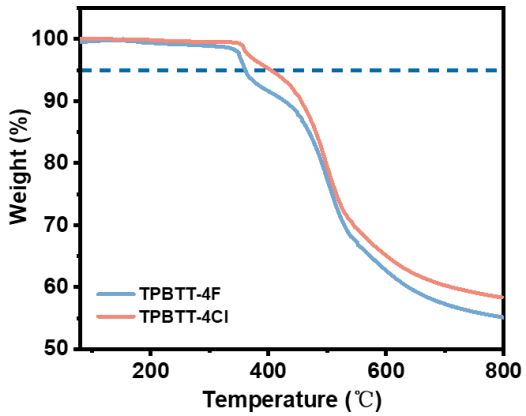

Figure 6.4 TGA curves of TPBTT-4F and TPBTT-4Cl.

The absorption spectra of the four NFAs in $CHCl_3$ solution and neat films were explored and are plotted in **Figure 6.3b and 3c**. The detailed optical parameters are summarized in **Table 6.1**. Compared with the PTBTT backbone, TPBTT obtained enhanced ICT owing to the isomerized pyrrole ring, as discussed later. Ascribed to the stronger ICT, the maximum absorption peaks in $CHCl_3$ red-shifted from 715 nm/727 nm for PTBTT-4F/4Cl to 736 nm/749 nm for TPBTT-4F/4Cl, together with increased extinction coefficients of 2.48×10^5 M^{-1} cm^{-1}/2.76×10^5 M^{-1} for TPBTT-4F/4Cl, respectively. In addition, the absorption peaks of TPBTT-4F/4Cl exhibited significant redshifts of 53 nm/57 nm from solution to solid state, compared to those of PTBTT-4F/4Cl (46 nm/56 nm), indicating stronger π-π stacking formed in TPBTT derivatives prepared films. Along with the stronger ICT, TPBTT-4F/4Cl obtained narrower optical bandgaps (E_g^{opt}) of 1.44 eV and 1.40 eV than 1.48 eV and 1.45 eV for PTBTT-4F/4Cl, respectively.

Table 6.1 Electrochemistry and photophysical properties of PTBTT-4F/4Cl and TPBTT-4F/4Cl.

Acceptors	E_{HOMO} [eV]	E_{LUMO} [eV]	$\lambda_{max}^{sol.}$ a) [nm]	λ_{max}^{film} [nm]	λ_{onset}^{film} [nm]	E_g^{opt} b) [eV]	ε_{max} a) [$M^{-1}cm^{-1}$]
PTBTT-4F	-5.68	-4.20	715	761	838	1.48	2.32×10^5
PTBTT-4Cl	-5.70	-4.25	727	783	853	1.45	2.44×10^5
TPBTT-4F	-5.63	-4.19	736	789	863	1.44	2.48×10^5
TPBTT-4Cl	-5.64	-4.24	749	806	887	1.40	2.76×10^5

a)In chloroform solution. b)$E_g^{opt}=1240/\lambda_{onset}^{film}$

IPS (Nakano, Kaji and Tajima, 2021;Liu et al., 2022b) was employed to identify the electrochemical characteristics of the acceptors under N_2 atmosphere. As plotted in **Figure 6.5**, the HOMO energy levels of TPBTT-4F and TPBTT-4Cl

were measured to be -5.63 eV and -5.64 eV. The LUMO energy levels were calculated to be -5.19 eV and -5.24 eV, in combination with the E_g^{opt}. According to the energy levels of PTBTT-4F/4Cl reported recently, (Zhu et al.) TPBTT derivatives achieved elevated HOMO energy levels and maintained LUMO energy levels. Inferred from the compressed $E_g^{opt}$and similar LUMO energy levels, isomerization prepared TPBTT derivatives would obtain suppressed E_{Loss}.

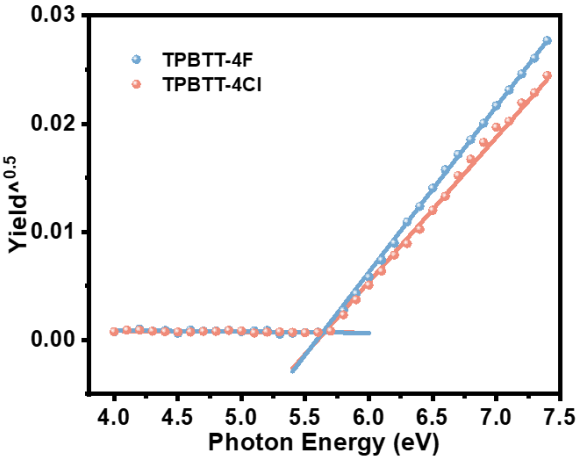

Figure 6.5 IPS curves for TPBTT-4F and TPBTT-4Cl under N_2.

6.3.2 Photovoltaic Properties

To characterize the photovoltaic performance of the acceptors, OSCs with conventional device configuration of ITO/PEDOT:PSS/Active Layer/PDINN/Ag were fabricated. The PBDB-TF: PTBTT-4F/4Cl based devices were fabricated as previously reported. The blend solutions of PBDB-TF: TPBTT-4F/4Cl (1:1, w/w) in $CHCl_3$ at a total concentration of 16 mg/mL were prepared to fabricate the active layers. As summarized in **Table 6.2Table 6.3**, the optimization process of device fabrication was conducted by manipulating donor/acceptor blend ratios, introducing various additives, and varying annealing temperature. The current density-voltage (*J*-*V*) curves for optimal devices based on four NFAs are shown in **Figure 6.6a,** and the detailed photovoltaic parameters are listed in **Table 6.4**. The PTBTT-4F/4Cl based devices attained the photovoltaic parameters in accordance with our previous results. By contrast, the isomerized PBDB-TF: TPBTT-4F based devices achieved a maximum *PCE* of 15.72%, along with a V_{OC} of 0.887 V, a J_{SC} of

23.90 mA cm^{-2}, and an *FF* of 74.15%. Likewise, the chlorinated TPBTT-4Cl based devices delivered a *PCE* of 14.84%, a V_{OC} of 0.861 V, a J_{SC} of 25.16 mA cm^{-2}, and a lower *FF* of 68.51%. Compared to PTBTT-4F/4Cl based devices, TPBTT-4F/4Cl based devices exhibited higher V_{OC}, due to reduced V_{OC} loss and suppressed ΔE_{nonrad} induced by decreased energy disorder. Meanwhile, more ordered intermolecular stacking led to enhanced crystallinity in the TPBTT-4F/4Cl photoactive blend films, thereby, superior J_{SC}s of the corresponding devices than those of the PTBTT derivatives fabricated devices. However, the *FF*s of TPBTT-4F/4Cl based devices were relatively lower than those of the PTBTT-4F/4Cl devices, which was caused by the molecular conformation change and domain size difference.

Table 6.2 The optimized photovoltaic parameters of devices based on PBDB-TF: TPBTT-4F blends.

Ratio	Additive	TA [°C]	V_{OC} [V]	J_{SC} [mA cm^{-2}]	*FF* [%]	*PCE* [%]
1:0.8	-	-	0.945	22.49	61.02	12.96
1:1	-	-	0.934	22.56	63.46	13.38
1:1.2	-	-	0.925	23.90	58.81	13.01
1:1	0.25%DIO	-	0.931	21.78	62.91	12.76
1:1	0.5%DIO	-	0.917	22.28	65.70	13.42
1:1	0.25%DIO&0.25%CN	-	0.915	22.39	62.98	12.91
1:1	0.5%DIO	60	0.887	23.88	74.15	15.72
1:1	0.5%DIO	80	0.883	24.33	69.95	15.02
1:1	0.5%DIO	100	0.883	24.30	68.93	14.79

Table 6.3 The optimized photovoltaic parameters of devices based on PBDB-TF: TPBTT-4Cl blends.

Ratio	Additive	TA [°C]	V_{OC} [V]	J_{SC} [mA cm^{-2}]	*FF* [%]	*PCE* [%]
1:0.8	-	-	0.901	22.62	53.56	10.92
1:1	-	-	0.898	22.30	55.49	11.12
1:1.2	-	-	0.891	22.67	59.64	12.04
1:1.2	0.5%DIO	-	0.884	24.33	63.61	13.68
1:1.2	0.25%DIO&0.25%CN	-	0.881	23.32	61.54	12.64
1:1.2	0.5%CN	-	0.910	22.64	63.19	13.02
1:1.2	0.5%DIO	60	0.868	23.35	67.03	13.59
1:1.2	0.5%DIO	80	0.861	25.16	68.51	14.85
1:1.2	0.5%DIO	100	0.848	24.75	68.20	14.31

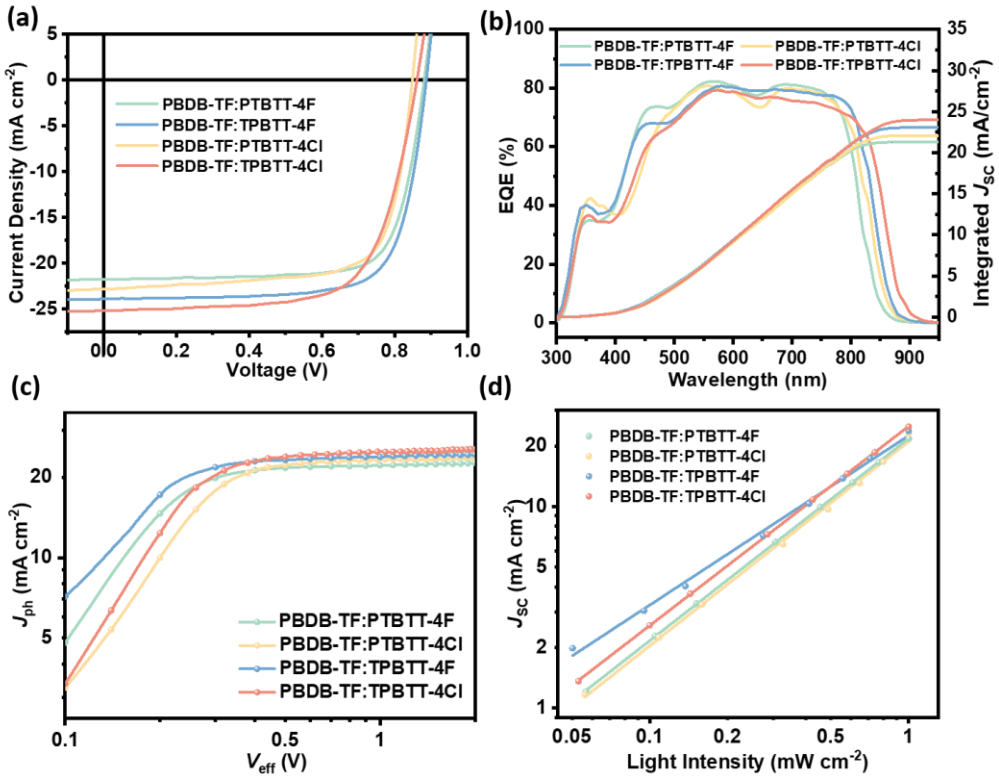

Figure 6.6 (a) *J-V* characteristics of the optimal OSCs. (b) EQE spectra and integrated J_{cal}s for the PTBTT-4F/4Cl and TPBTT-4F/4Cl based OSCs. (c) J_{ph} versus V_{eff} curves (d) J_{SC} versus light intensity of the optimized devices.

Table 6.4 Photovoltaic parameters of the optimized OSCs based on four PBDB-TF: acceptor blends.

Acceptor	V_{OC} [V]	J_{SC} [mAcm^{-2}]	$J_{cal.}$[a)] [mAcm^{-2}]	*FF* [%]	*PCE*[b)] [%]
PTBTT-4F	0.881	21.78	21.30	75.57	14.50 (14.16±0.24)
PTBTT-4Cl	0.849	22.80	22.09	72.53	14.03 (13.89±0.21)
TPBTT-4F	0.887	23.90	23.06	74.15	15.72 (15.34±0.37)
TPBTT-4Cl	0.861	25.16	23.97	68.51	14.85 (14.41±0.31)

[a)]Integrated current densities obtained from EQE measurements. [b)]Average *PCE*s achieved from 18 devices.

The EQE spectra were measured to investigate the J_{SC} difference (**Figure 6.6b**). The TPBTT-4F/4Cl based devices exhibited strong light response from 450 nm to 800 nm in EQE spectra, indicating efficient photon harvesting in both devices. The apparent photon response difference between PTBTT-4F/4Cl and TPBTT-4F/4Cl lay in the 800 nm to 900 nm range. The wavelength response range of

TPBTT-4F/4Cl was broader than PTBTT-4F/4Cl, consistent with the red-shifted absorption edges. In addition, owing to the influence of halogenation on absorption, the response ranges of chlorinated PTBTT-4Cl and TPBTT-4Cl blends were broader than those of the fluorinated blends, leading to enhanced J_{SC}s. As a result, the integrated J_{cal}s were 21.30 mA cm^{-2}, 22.09 mA cm^{-2}, 23.06 mA cm^{-2}, and 23.97 mA cm^{-2} for PTBTT-4F/PTBTT-4Cl/TPBTT-4F/TPBTT-4Cl based devices, respectively, which were consistent with the *J-V* measurements.

To learn the charge generation and collection differences of these OSCs, the photocurrent density (J_{ph}) versus effective voltage (V_{eff}) curves were investigated (**Figure 6.6c**). J_{ph} can be defined as $J_L - J_D$, where J_L and J_D are the currents measured under illumination and in the dark. Charge carriers are dissociated from excitons and collected, as J_{ph} reaches saturation current (J_{sat}) at higher applied voltages (V_{eff}). To assess the exciton dissociation efficiency (P_{diss}) and charge collection efficiency (P_{coll}) under short-circuit and maximum power output conditions, respectively, the J_{ph}/J_{sat} values were calculated. As summarized in **Table 6.5**, the P_{diss}/P_{coll} values of PTBTT-4F, PTBTT-4Cl, TPBTT-4F and TPBTT-4Cl were calculated to be 94.3%/85.0%, 94.5%/82.4%, 96.8%/86.3%, and 96.2%/83.8%, respectively. The P_{diss}/P_{coll} values correlated well with the corresponding EQE response. Compared to PTBTT-4F/4Cl based devices, TPBTT-4F/4Cl based devices presented better exciton dissociation and charge collection characteristics. In addition, the bimolecular recombination behavior under short-circuit conditions was evaluated from the slopes (α) of linearly fitted $ln(J_{SC}) - ln(P_{light})$ curves by measuring *J-V* curves under various light intensities (P_{light}) (**Figure 6.6d**). If the slope (α) was closer to 1, the bimolecular recombination was more suppressed in the devices. α were achieved as 1.002/1.012 and 0.840/0.988 for the PTBTT-4F/4Cl and TPBTT-4F/4Cl devices, respectively. The unexpected results suggested that TPBTT-4F based devices suffered from severe bimolecular recombination, causing lower *FF*s than those of PTBTT-4F based devices.

Table 6.5 The parameters of exciton dissociation efficiency and charge collection efficiency.

Active layer	J_{sat} (mA/cm^2)	J_{ph}[a)] (mA/cm^2)	J_{ph}[b)] (mA/cm^2)	η_{diss}	η_{coll}
PBDB-TF:PTBTT-4F	23.10	21.78	19.64	94.3	85.0
PBDB-TF:PTBTT-4Cl	24.13	22.80	19.89	94.5	82.4
PBDB-TF:TPBTT-4F	24.67	23.88	21.28	96.8	86.3
PBDB-TF:TPBTT-4Cl	26.13	25.15	21.90	96.2	83.8

6.3.3 Quantum Chemical Calculations and Energy Loss

The long-chain alkyl side group of the three acceptors was replaced by a methyl group to speed up the calculation of excited states without changing the nature of the frontier molecular orbitals. (Shi et al., 2022) Firstly, the molecular geometries of four NFAs were optimized at the B3LYP/6-31G (d,p) level with DFT. After that, TDDFT was conducted to describe the electronic excitations of the acceptors. The long-range corrected wB97XD functional could capture both short- and long-range interactions and accurately evaluate the charge transfer states; therefore, it was used to calculate the lowest five singlet states together with the 6-31G(d,p) basis set. The influence of the size of the basis set and the number of electronic states on the excited states calculation has been discussed in our previous work. (Jiang, Hirst and Do, 2022) All quantum chemical calculations were performed with the Gaussian 09 program package, (Frisch et al., 2009) and the electronic structure-property analysis was obtained using the Multiwfn codes. (Lu and Chen, 2012;Zhang and Lu, 2021) To explore the ICT change after isomerization and accurately quantify the charge separation, the difference between the ground state (S_0) and the first excited state (S_1) was analyzed by dividing the NFAs into five segments (**Figure 6.7a**). The excited states' calculation showed that the HOMO-LUMO pair transition contributed over 99% to the S_0-S_1 excited states for all NFAs. The multiple excited states were excluded to make the calculation process tractable. As shown in **Figure 6.7c**, TPBTT-4F/4Cl realized a stronger ICT process than that of PTBTT derivatives. Although the net charge transfer strength from moiety 1 to moiety 2-3 weakened, charge transfer from moiety 2 to moiety 3-5 was much more sufficient after isomerization. Owing to the contribution of the inner

pyrrole ring, the charge transfer from moiety 3 to moiety 4 and 5 also improved significantly. As we speculated above, when the contribution from D1 (moiety 2) to D2 core (moiety 3) was strengthened, a highly efficient backbone similar to D-A'-D was formed with enhanced ICT. By contrast, the external pyrrole ring in PTBTT-4F/4Cl caused less charge concentrated central core and thus weaker ICT effect.

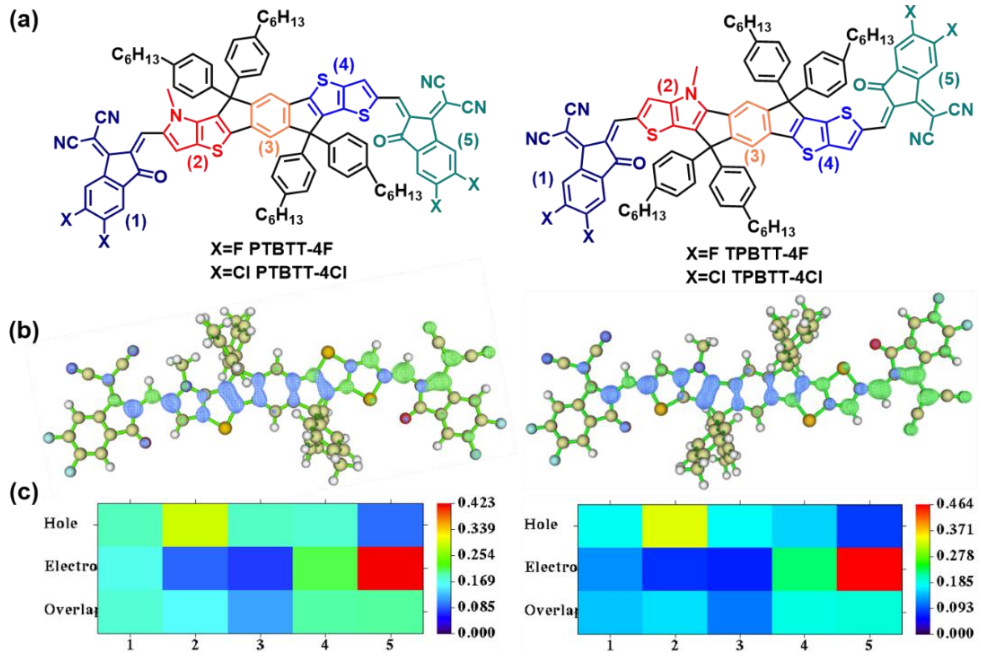

Figure 6.7 (a) Moiety classification of the hole-electron distribution heat map. (b) Isosurface of hole (blue) and electron (red) distributions for the S_0 → S_1 (HOMO-LUMO) transition in PTBTT-4F and TPBTT-4F. (c) Heat map of the fragment contributions (as a percentage) to the hole and electron distributions for the S_0 → S_1 transition in PTBTT-4F and TPBTT-4F.

Ascribed to enhanced ICT and elevated HOMO energy levels, isomerized TPBTT derivatives were expected to obtain lower E_{Loss}. To investigate the effect of pyrrole ring position on E_{Loss}, FTPS-EQE and EL spectra were measured (**Figure 6.8**). The bandgaps (E_{g}) of the acceptors were calculated by the crossing points between the absorption and emission spectra of the corresponding neat films (**Figure 6.8a**). (Liu et al., 2016;Wu et al., 2023) Commonly, the energy loss of the devices can be divided into three parts according to the following equation (Wang et al., 2020;Zeng et al., 2021):

$$E_{\mathrm{Loss}} = E_{\mathrm{g}} - eV_{\mathrm{OC}} = \Delta E_{\mathrm{rad}} + \left(E_{\mathrm{g}} - E_{\mathrm{CT}}\right) + \Delta E_{\mathrm{nonrad}}$$

$$= \Delta E_{\mathrm{rad}} + \Delta E_{\mathrm{CT}} + \Delta E_{\mathrm{nonrad}} \quad (6\text{-}1)$$

where ΔE_{rad} is regarded as the radiative energy loss due to absorption above the optical bandgap, ΔE_{CT} is defined as the driving force for charge transfer from the singlet excited state (also named as local exciton (LE) state) to the CT states, and $\Delta E_{\mathrm{nonrad}}$ arises from non-radiative recombination. Among the three sections, ΔE_{rad} is unavoidable for all kinds of OSCs. As summarized in **Table 6.6**, these devices have similar ΔE_{rad} values, suggesting comparable radiative recombination loss (0.24-0.26 eV) below the CT state. ΔE_{CT} is essential for the exciton separation, which would lead to unwanted voltage loss. This term, also known as the E_{offset} between E_{g} and E_{CT}, offers a driving force for exciton separation and charge generation in OSCs. (Deibel, Strobel and Dyakonov, 2010) To determine E_{CT} accurately, dual fitting of the corresponding FTPS-EQE and EL spectra were carried out in **Figure 6.8b**. As a result, the E_{CT} values of OSCs based on PBDB-TF: PTBTT-4F/PTBTT-4Cl/TPBTT-4F/TPBTT-4Cl were determined to be 1.448, 1.422, 1.426 and 1.407 eV, respectively. The E_{offset} between E_{g} and E_{CT} plays a decisive role in overcoming the CT state for exciton separation and charge generation in OSCs. The corresponding ΔE_{CT} of PBDB-TF: PTBTT-4F/PTBTT-4Cl/TPBTT-4F/TPBTT-4Cl were calculated to be 0.067 eV, 0.066 eV, 0.057 eV, 0.052 eV, respectively. Although ΔE_{CT} reduced in TPBTT-4F/4Cl binary systems, the devices still attained impressive J_{SC} s and *FF*s, indicating sufficient charge generation had been realized. Eventually, on the premise of enough driving force, the squeezed ΔE_{CT} also contributed to the minimized E_{Loss}. At the same time, all PBDB-TF: acceptors blend films exhibited efficient PL quenching, particularly for the PBDB-TF: TPBTT-4F/4Cl blend films (**Figure 6.8d)**. The stronger quenching of the PL spectra implied an efficient transition from LE state to CT state, associated with sufficient E_{offset} in PBDB-TF: TPBTT-4F/4Cl blend films. As summarized in **Table 6.6**, $\Delta E_{\mathrm{nonrad}}$ varied much between these devices, which mainly determined the total E_{Loss} . According to the formula: $\Delta E_{\mathrm{nonrad}} = -kT\ln(EQE_{\mathrm{EL}})$, $\Delta E_{\mathrm{nonrad}}$ can be determined from EQE_{EL} intensity directly. Therefore, EQE_{EL} was measured to evaluate $\Delta E_{\mathrm{nonrad}}$ (**Figure 6.8c**). The

PBDB-TF: TPBTT-4F based devices obtained higher EQE_{EL} of 2.33 × 10^{-5} than that of PBDB-TF: PTBTT-4F (6.44 × 10^{-6}), along with achieving lower ΔE_{nonrad} of 0.276 eV. In addition, chlorinated PTBTT-4Cl/TPBTT-4Cl presented similar findings with reduced ΔE_{nonrad} of 0.328eV and 0.285 eV. Similarly, the chlorinated derivatives exhibited a similar trend. As expected, isomerization of the TP block effectively suppressed ΔE_{nonrad}, thus leading to suppressed E_{Loss} and improved V_{OC}.

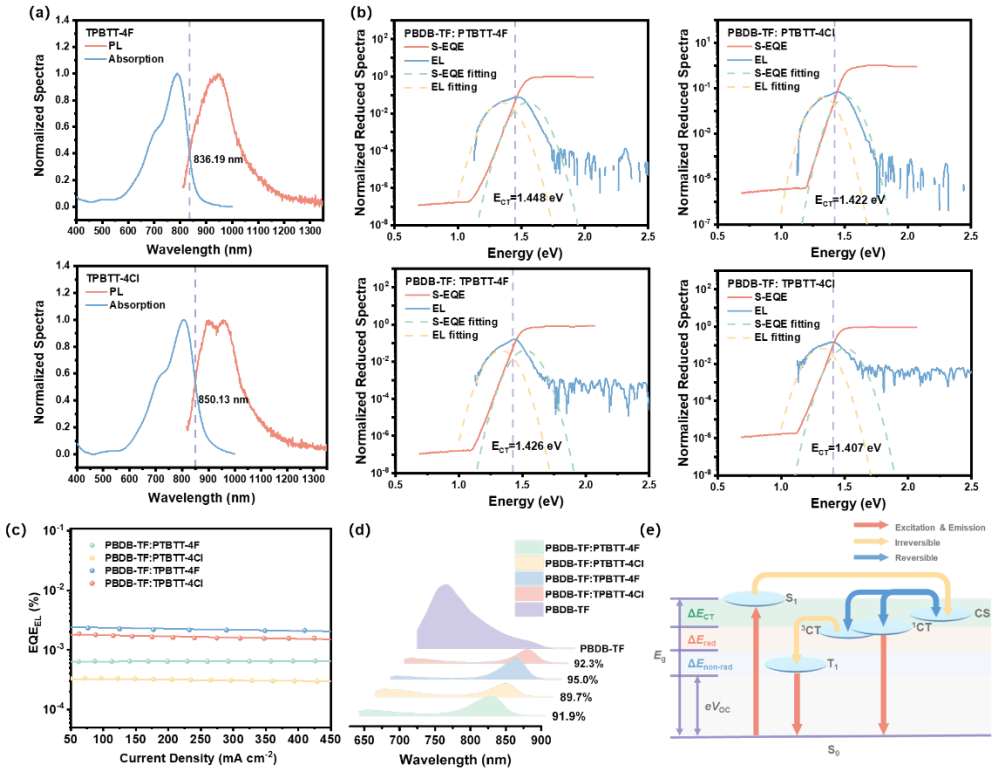

Figure 6.8 (a) Absorption and emission curves for neat films based on TPBTT-4F and TPBTT-4Cl. (b) FTPS-EQE and dual-fitting curves and (c) EQE_{EL} of PBDB-TF: acceptors based devices. (d) Emission spectra for the four blend films. (e) Illustration of excited-state dynamics in OSCs.

Table 6.6 Detailed E_{Loss} parameters of the OSCs based on PBDB-TF: acceptor blends

Acceptors	E_g [eV]	E_{CT} [eV]	ΔE_{CT} [eV]	ΔE_{rad} [eV]	EQE_{EL} [%]	ΔE_{nonrad} [eV]	E_{Loss} [eV]
PTBTT-4F	1.515	1.448	0.067	0.257	6.44 × 10^{-4}	0.310	0.634
PTBTT-4Cl	1.488	1.422	0.066	0.245	3.13 × 10^{-4}	0.328	0.639
TPBTT-4F	1.483	1.426	0.057	0.263	2.33 × 10^{-3}	0.276	0.596
TPBTT-4Cl	1.459	1.407	0.052	0.261	1.68 × 10^{-3}	0.285	0.598

6.3.4 Molecular Packing and Reduced Energy Disorder

Given the trade-offs between E_{Loss} and E_{offset} presented before, reducing the energetic disorder by regulating the microscopic properties was expected to suppress the total E_{Loss}. According to a previous report, the $\Delta E_{\mathrm{nonrad}}$ is correlated to the energetic disorder of the blend films. (Venkateshvaran et al., 2014;Kaiser et al., 2021;Feng et al., 2022) Generally, the exponential tail along the absorption coefficient curve and near the optical band edge is defined as the Urbach tail. And the Urbach tail states below the band edge are interpreted as an indicator of the degree of disorder for low crystalline materials. For the blend films with ordered stacking and thus high crystallinity, narrowed LE states in the band gap would be realized, leading to smaller degree of energetic disorder and $\Delta E_{\mathrm{nonrad}}$ in OSCs. According to the formula below, the Urbach energy (E_{U}) can be calculated from the slope of the fitting curve by plotting ln (α) against the incident photon energy (E),

$$ln\alpha(E) = ln\alpha_0 + \frac{E}{E_{\mathrm{U}}} - \frac{E_{\mathrm{g}}}{E_{\mathrm{U}}} \tag{6-2}$$

In **Figure 6.9a**, derived from the exponential fitting to the sub-bandgap s-EQE spectra, the PBDB-TF: TPBTT-4F/4Cl blend films exhibited lower energetic disorder with E_{U}s of 24.6 meV and 25.5 meV, compared to E_{U}s of 25.9 meV and 26.1 meV for PTBTT-4F/4Cl blend films, respectively. The higher E_{U}s of PTBTT-4F/4Cl based films suffered from severe $\Delta E_{\mathrm{nonrad}}$, causing larger E_{Loss}. Conversely, the lowest E_{U} of TPBTT-4F based films contributed to more suppressed $\Delta E_{\mathrm{nonrad}}$ and thus increased V_{OC}. The reason for the reduced energetic disorder can be inferred to more favorable π-π stacking of the blend films, as the external thiophene ring led to more planar molecular structure.

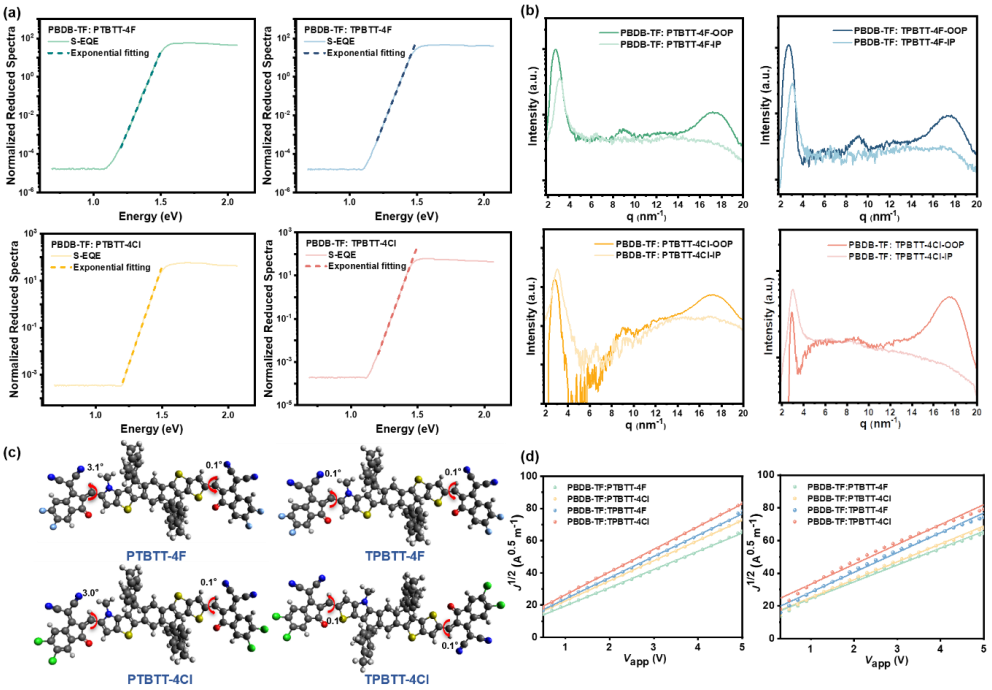

Figure 6.9 (a) Exponential fitting to the sub-bandgap s-EQE spectra of the blend films. (b) 1D line-cuts in the IP and OOP directions of PBDB-TF: PTBTT-4F/TPBTT-4F/PTBTT-4Cl/TPBTT-4Cl blend films. (c) The optimized 3D geometries of four acceptors. (d) Hole (left) and electron (right) mobilities of the blend films.

Molecular optimizations were conducted to estimate the intermolecular stacking of three acceptors. As displayed in **Figure 6.9c**, after isomerization, TPBTT-4F/4Cl obtained better planarity with smaller torsion angles of 0.1° between the backbone and end groups. Other than the small torsion angles induced from S-O non-covalent interaction in TPBTT-4F/4Cl, PTBTT-4F/4Cl presented larger torsion angles of 3.0°-3.1°, owing to strong steric hindrance.

Furthermore, to explore the realistic intermolecular interaction behaviours of four blend films, GIWAXS measurements were conducted. (Muller-Buschbaum, 2014;Li et al., 2022a) The 1D line cuts of the binary films are exhibited in **Figure 6.9b** and summarized in **Table 6.7**. Along the OOP direction, obvious π-π stacking appeared at 1.719 $Å^{-1}$/1.726 $Å^{-1}$ for PTBTT-4F/4Cl blend films and 1.740 $Å^{-1}$/1.746 $Å^{-1}$ for TPBTT-4F/4Cl blends. The more prominent peak intensities indicated a closer packing distance and stronger intermolecular interaction. The corresponding π-π stacking distances were calculated to be 3.66 Å, 3.64 Å, 3.61 Å, and 3.60 Å, for PTBTT-4F/4Cl, TPBTT-4F/4Cl, respectively. At the same time, the chlorinated PTBTT-4Cl and

TPBTT-4Cl blends exhibited closer packing, owing to the enhanced overlap of π electrons of the Cl atom. The CCLs were calculated to be 25.36 Å/21.42 Å and 25.02 Å/18.85 Å for TPBTT-4F/4Cl and PTBTT-4F/4Cl blend films, respectively. After isomerization, the external thiophene ring in the TPBTT backbone was beneficial for closer as well as more ordered π-π stacking, leading to enhanced crystallinity and lower energetic disorder in the blend films. The optimized stacking properties not only suppressed the energetic disorder and thus lowered $\Delta E_{\mathrm{nonrad}}$, but also facilitated higher electron mobilities.

Table 6.7 The diffraction vector (q) values of diffraction peaks and crystal correlation lengths (CCLs) of the binary blend films.

Active layer	Diffraction vector[Å^{-1}]		Crystal correlation length[Å]	
	OOP(010)	IP(100)	OOP(010)	IP(100)
PBDB-TF:PTBTT-4F	1.719	0.309	25.02	71.58
PBDB-TF:PTBTT-4Cl	1.726	0.301	18.85	88.36
PBDB-TF:TPBTT-4F	1.740	0.305	25.36	85.68
PBDB-TF:TPBTT-4Cl	1.746	0.301	21.42	68.46

The SCLC method (Duijnstee et al., 2020;Sivula, 2022) was conducted to evaluate the charge transport properties of these NFAs blends. As is shown in **Figure 6.9d**, the hole and electron mobilities (μ_{h} and μ_{e}) of four blend films were derived and summarized in **Table 6.8**. The μ_{h} and μ_{e} of PTBTT-4F based devices were calculated to be 4.28 × 10^{-4} cm^2 V^{-1} s^{-1} and 3.57 × 10^{-4} cm^2 V^{-1} s^{-1}.

Table 6.8 The parameters of hole mobilities and electron mobilities.

Active layer	μ_{h} (10^{-4} cm^2 V^{-1} s^{-1})	μ_e (10^{-4} cm^2 V^{-1} s^{-1})	μ_h/μ_e
PBDB-TF:PTBTT-4F	4.28	3.57	1.20
PBDB-TF:PTBTT-4Cl	5.25	4.01	1.31
PBDB-TF:TPBTT-4F	6.31	4.92	1.28
PBDB-TF:TPBTT-4Cl	6.70	4.96	1.35

Owing to the closer stacking observed in chlorinated blends, higher μ_{h} and μ_{e} of 5.25 × 10^{-4} cm^2 V^{-1} s^{-1} and 4.01 × 10^{-4} cm^2 V^{-1} s^{-1} were obtained for PTBTT-

4Cl based devices. After isomerization, TPBTT-4F and TPBTT-4Cl presented increased μ_e of 4.92 × 10^{-4} cm^2 V^{-1} s^{-1} and 4.96 × 10^{-4} cm^2 V^{-1} s^{-1}, respectively, indicating enhanced crystallinity in TPBTT derivatives. In addition, the μ_h/μ_e ratios of PBDB-TF: PTBTT-4F/4Cl and TPBTT-4F/4Cl were calculated to be 1.20/1.31 and 1.28/1.35, respectively. A more balanced charge transfer property of PTBTT-4F/4Cl blend films may account for the higher *FF*s. By contrast, TPBTT-4F/4Cl exhibited enhanced crystallinity and closer molecular packing, leading to enhanced μ_e and higher J_{SC}s.

6.4 Conclusion

In conclusion, the A-D-A type molecules PTBTT-4F/Cl were segmented into the A-D1-D2-D3-A type. To maximize the ICT effect, strengthening the contributions of D1 and D3 to the D2 core or weakening the electron-donating ability of the D2 core was considered as an effective method. After isomerization of the TP block in the PTBTT backbone, the charge transfer from D1 to D2 was enhanced, which induced stronger ICT in the TPBTT backbone. Compared with PTBTT-4F/4Cl, TPBTT-4F/4Cl exhibited red-shifted absorption, elevated HOMO energy levels, and compressed E_g, which resulted in suppressed E_{Loss}. Three parts of E_{Loss} were investigated to address the significance of the isomerization strategy in lowering E_{Loss} and further improving the device performance of the binary systems. Benefitting from the minimized driving force and reduced energetic disorder, both ΔE_{CT} and ΔE_{nonrad} were suppressed, therefore, higher V_{OC} was achieved. The enhanced π-π stacking of the blends not only contributed to reduced energetic disorder, but also improved charge transfer mobilities, thus resulting in higher J_{SC}. As a result, PBDB-TF: TPBTT-4F based devices achieved a maximum *PCE* of 15.72%, a V_{OC} of 0.887 V, a J_{SC} of 23.90 mA cm^{-2}, as well as an *FF* of 74.15%. This work demonstrated that the isomerization design strategy would be an effective method for constructing novel central cores of A-D-A'-D-A type high-performance NFAs for fabricating OSCs with suppressed both ΔE_{CT} and ΔE_{nonrad}.

Chapter 7

Conclusions and Future Work

7.1 Conclusions

The thesis firstly introduced the TP block into the backbones to construct new NFAs and investigate the design rules of highly efficient binary OSCs. The TP-substituted NFAs exhibited red-shifted absorption region, compressed energy band, and elevated energy levels. After blending with appropriate polymer donors, the devices realized suppressed energy loss, especially non-radiative energy loss. The core segmentation work introduced a new idea to design NFAs instead of solely modifying the exciting molecules. There are also many interesting findings that were not shown in the main body of the thesis, which would guide future work and new ideas of material optimization.

In the first work, the TP unit was introduced as a building block to construct pyrrole-containing conjugated backbones for preparing NFAs. Two novel acceptors, namely, PTBTP-2F and PTBTP-4F, were designed and synthesized successfully. The photophysical and electrochemical properties, device performance, energy loss, and morphology of the blend films have been investigated to evaluate the performance of the novel acceptors. Eventually, our work demonstrated thiophene[3,2-b] pyrrole (TP) building block, had shown its potential for constructing highly efficient NFAs.

In the second work, two asymmetric acceptors PTBTT-4F/4Cl, derived from IT-4F/4Cl and PTBTP-4F/4Cl, were designed and synthesized. The photophysical and photovoltaic properties of IT-4F/4Cl, PTBTT-4F/4Cl and PTBTP-4F/4Cl were investigated to address the influence of molecular backbone engineering of acceptors on device performance of OSCs. Compared with IT-4F, PTBTT-4F exhibited red-shifted absorption, elevated LUMO energy levels and reduced optical bandgaps. Due to the enhanced energy levels, PTBTT-4F based devices realized lower nonradiative energy loss therefore higher V_{OC}. In addition, PTBTT-4F devices achieved higher J_{SC} and *FF*s than PTBTP-4F devices, mainly because of better miscibility between PTBTT-4F and PBDB-TF, as well as enhanced π-π stacking and improved charge transfer mobilities of the blends. Three chlorinated acceptors were synthesized and compared with fluorinated acceptors as a check experiment to verify the asymmetric design strategy in this work.

In the third work, the A-D-A type molecules were segmented into A-D1-D2-D3-A type. To optimize the ICT, strengthening the contributions of D1 and D3 to the D2 core or weakening the electron-donating ability of the D2 core is considered as an effective method. After isomerization, TPBTT-4F/4Cl were designed and synthesized based on PTBTT-4F/4Cl. The TPBTT-4F/4Cl devices realized impressive performance, owing to enhanced ICT and suppressed ΔE_{CT} and $\Delta E_{\mathrm{nonrad}}$. This work would demonstrate that isomerization design strategy would be an effective method for constructing a novel central core and exploring high-performance NFAs for fabricating OSCs with suppressed energy loss.

7.2 Major Contributions

The major contribution of this thesis is the development of TP-based NFAs in OSCs.

- Thiophene[3,2-b] pyrrole (TP) was introduced to construct two novel fused-ring conjugated NFAs, named as PTBTP-2F and PTBTP-4F. By fusing two pyrrole rings on both sides of an IDT unit, a brand-new central

core based on TP block (denoted as PTBTP) was achieved to serve as the D core to construct an A-D-A type NFA together with two accepting units (IC-F and IC-2F). Benefitting from the nitrogen atom in the pyrrole ring, both PTBTP-2F and PTBTP-4F exhibited great film forming property as well as high LUMO energy levels of -4.09 eV and -4.11 eV for PTBTP-2F and PTBTP-4F, respectively. Since IC-2F presents stronger electron-withdrawing capability than IC-F, PTBTP-4F demonstrated red-shifted absorptions in solution/film in comparison with PTBTP-2F. When blending with donor PBDB-T, the PTBTP-2F fabricated devices achieved an average *PCE* of 11.14% with a V_{OC} of 0.91 V, a J_{SC} of 17.89 mA cm^{-2} and an *FF* of 68.66%, while the PTBTP-4F fabricated devices afforded a *PCE* of 12.33% with a V_{OC} of 0.86 V, a J_{SC} of 20.74 mA cm^{-2} and an *FF* of 69.02%.

- Two novel asymmetric TP based NFAs with flipped molecular conformation, named as PTBTT-4F/4Cl, were designed and synthesized. The introduction of the pyrrole ring in the novel NFAs would not only afford extra reaction sites for side chain modification, but also induce substantial ICT, thus leading to elevated energy levels of the NFAs and thereby lower energy loss of the OSCs. Benefitting from effective molecular stacking and optimized phase separation induced by molecular conformation variation, asymmetric PTBTT-4F fabricated OSCs exhibited much higher J_{SC}s and *FF*s than the symmetrical PTBTP-4F devices. Due to the enhanced energy levels, PTBTT-4F based devices realized lower nonradiative energy loss therefore higher V_{OC}. In addition, PTBTT-4F devices achieved higher J_{SC} and *FF*s than PTBTP-4F devices, mainly because of better miscibility between PTBTT-4F and PBDB-TF, as well as enhanced π-π stacking and improved charge transfer mobilities of the blends. Conclusively, PBDB-TF: PTBTT-4F based devices achieved a maximum *PCE* of 14.49%, a V_{OC} of 0.88 V, a J_{SC} of 21.43 mA cm^{-2}, as well as an *FF* of 76.73%. This work demonstrated that asymmetric design strategy would be a promising method for finely regulating the molecular structure and synthesizing high performance NFAs for fabricating OSCs with high *FF*s and low E_{Loss}.

- Two novel NFAs named as TPBTT-4F/4Cl were synthesized after isomerisation based on PTBTT-4F/4Cl. Benefitting from the minimized driving force and reduced energetic disorder, both ΔE_{CT} and $\Delta E_{\mathrm{nonrad}}$ were suppressed, therefore, higher V_{OC} was achieved. The enhanced π-π stacking of the blends not only contributed to reduced energetic disorder, but also improved charge transfer mobilities, and thus higher J_{SC}. As a result, the PBDB-TF: TPBTT-4F based devices achieved a maximum *PCE* of 15.72%, a V_{OC} of 0.887 V, a J_{SC} of 23.90 mA cm^{-2}, as well as an *FF* of 74.15%. This work demonstrated that isomerization design strategy would be an effective method for constructing a novel central core and exploring high-performance NFAs for fabricating OSCs with both suppressed ΔE_{CT} and $\Delta E_{\mathrm{nonrad}}$.

7.3 Future Work

- There are only three pyrrole-contained building blocks, including DTP, TP, carbazole groups. In the future, more pyrrole-contained building blocks can be explored to construct NFAs, and enrich the types of building blocks. Moreover, the length and type of *N*-alkyl chain in the TP block can be altered to modify the NFAs as a side-chain engineering work.
- In Chapter 5, the hexyl-substituted pyrrole ring in the TP based backbone was calculated to realize a conformation lock, which was more rigid than S-O non-covalent bond in TT based backbone. Hence, the conformation lock can be applied to other NFAs to fix the conformation and to improve the stability.
- In Chapter 6, dual emission peaks were observed from TPBTT-4Cl. We suppose the appearance of dual emission is caused by the conformation difference of TPBTT-4Cl. A part of single bridged bonds on the TP side of TPBTT-4Cl were rotated during thermal annealing. Therefore, the conformation lock is expected to be applied in this molecule, to fix the conformation and optimize the NFA.
- The study of stability is a hot spot in OSCs. To improve the stability of NFAs, we are trying to conduct deuteration at key positions of NFAs. We

are coming on this work, the performance of the deuterated devices exhibited improved performance, which was supposed to be induced by the enhanced crystallinity after deuteration. We are perfecting this work currently.

Appendix I

I.a Materials and Synthesis

All commercially available chemicals and solvents were purchased from Energy-Chemical, Sigma-Aldrich, or J&K Chemical Co., and used without further purification. In addition, 2-(5,6-difluoro-3-oxo-2,3-dihydro-1H-inden-1-ylidene) malononitrile, polymer donor PBDB-T were purchased from Solarmer Materials Inc.. Ethyl 2-bromo-4H-thieno[3,2-b]pyrrole-5-carboxylate was synthesized according to literature. Anhydrous THF and toluene were freshly distilled over sodium wire prior to use. Detailed synthetic processes of PTBTP-2F and PTBTP-4F are described in the following.

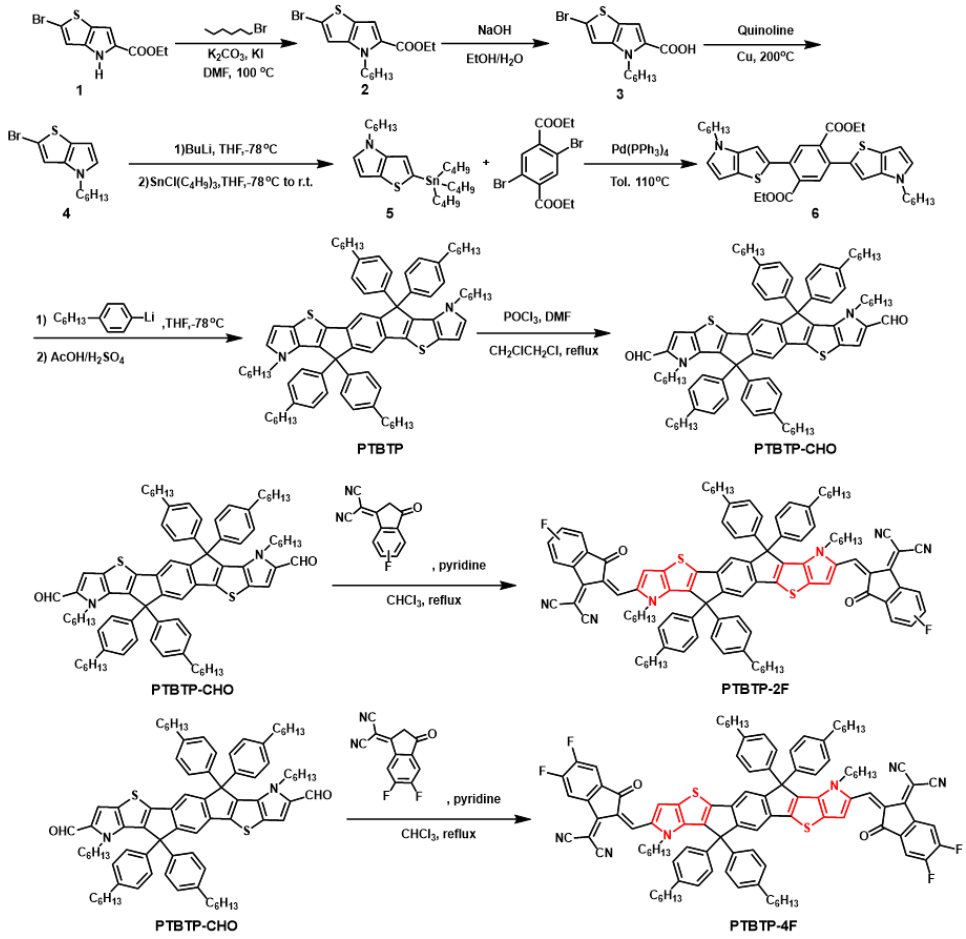

Scheme S1. Synthesis routes of PTBTP-2F and PTBTP-4F

*ethyl 2-bromo-4H-thieno[3,2-b]pyrrole-5-carboxylate (**1**)*

A solution of sodium (2.4 g, 0.10 mol) in absolute ethanol (100 mL) was cooled to 0°C, and then a mixture of 5-bromothiophene-2-carbaldehyde (10 g, 52.34 mmol) and ethyl 2-azidoacetate (8.11 g, 62.81 mmol) was added dropwise among 30 minutes and the final solution was stirred for 1 hour at 0°C. The reaction was quenched by adding a cold solution of NH_4Cl. While the pH approached 7, the resulting solution was extracted with dichloromethane for three times. The combined organic layers were concentrated and purified by silica gel column chromatography with an eluent of pure petroleum ether to afford ethyl-2-azido-3-(5-bromothiophen-2-yl)acrylate. Then the acrylate was refluxed in toluene for 30 minutes to give **1** (5.8 g, 21.16 mmol, 40.4%) as a white solid. ^{1}H NMR (600 MHz, $CDCl_3$): δ 9.19 (s, 1H), 7.15-6.90 (m, 2H), 4.37 (q, *J* = 7.1 Hz, 2H), 1.39 (t, *J* = 7.1 Hz, 3H). ^{13}C NMR (150 MHz, $CDCl_3$): δ 161.77, 139.30, 126.23, 124.79, 116.19, 114.45, 107.34, 60.88, 14.43.

*ethyl 2-bromo-4-hexyl-4H-thieno[3,2-b]pyrrole-5-carboxylate (**2**)*

The mixture of compound **1** (5.8 g, 21.16 mmol), 1-bromohexane (10.48 g, 63.47 mmol), potassium carbonate (8.77 g, 63.47 mmol), potassium iodide (351 mg, 2.12 mmol) were dissolved in N, N-dimethylformamide (30 mL) and stirred at 100 °C for 2 hours. Then the reaction solution was extracted with ethyl acetate (100 mL) for twice and washed with brine. After removing the solvent, silica gel column chromatography was used to purify the product with a mixture of petroleum ether and dichloromethane (5:1, v/v) as the eluent, yielding **2** finally (6.7 g, 18.70 mmol, 88.4%) as a white oil. ^{1}H NMR (600 MHz, $CDCl_3$): δ 7.08 (s, 1H), 6.99 (s, 1H), 4.46 – 4.36 (m, 2H), 4.31 (q, *J* = 7.1 Hz, 2H), 1.84 – 1.70 (m, 2H), 1.37 (t, *J* = 7.1 Hz, 3H), 1.29 (s, 6H), 0.90 – 0.84 (m, 3H). ^{13}C NMR (150 MHz, $CDCl_3$): δ 161.39, 142.79, 125.42, 121.96, 115.76, 113.74, 108.98, 60.17, 47.69, 31.47, 31.06, 26.50, 22.56, 14.41, 14.00.

*2-bromo-4-hexyl-4H-thieno[3,2-b]pyrrole-5-carboxylic acid (**3**)*

Compound **2** (6.7 g, 18.70 mmol) in EtOH (150 mL) was added with NaOH (11.22 g, 280.50 mmol) in water (75 mL) and the reaction mixture was refluxed for 2 hours. Then the mixture was cooled to 25°C, and subsequently acidified

with HCl. The precipitate was filtered and washed with water to give **3** (4.5 g, 13.63 mmol, 72.9%) as a white solid. ^{1}H NMR (600 MHz, $CDCl_3$): δ 7.24 – 7.20 (m, 1H), 7.04 – 6.97 (m, 1H), 4.56 – 4.26 (m, 2H), 1.93 – 1.65 (m, 2H), 1.30 (s, 6H), 1.01 – 0.68 (m, 3H). ^{13}C NMR (150 MHz, $CDCl_3$): δ 166.26, 143.93, 124.22, 122.33, 117.35, 113.73, 111.05, 47.81, 31.41, 30.97, 26.42, 22.51, 14.00.

*2-bromo-4-hexyl-4H-thieno[3,2-b]pyrrole (**4**)*

To a solution of compound **3** (4.5 g, 13.63 mmol) in quinoline (40 mL) was added with Cu (865.9 mg, 13.63 mmol) powder, and the solution was then heated at 200 °C for 2 hours. The final mixture was filtered through a silica plug with petroleum ether and washed with 1 M HCl (120 mL) and water. The organic layer was concentrated and purified by column chromatography (flash silica gel, petroleum ether/dichloromethane 5:1). Compound **4** (2.10 g, 7.34 mmol, 53.8%) was obtained as a white oil.

*4-hexyl-2-(tributylstannyl)-4H-thieno[3,2-b]pyrrole (**5**)*

Compound **4** (1.05 g, 3.67 mmol) in THF (10 mL) at -78 °C was added with *n*-BuLi (1.47 mL, 2.5 M in hexane, 3.67 mmol) and the mixture was kept at -78 °C for 1 hour. Then a solution of tributylchlorostannane (1.43 g) in THF (10 mL) was added dropwise and stirred at -78 °C for 1 h. The reaction mixture was slowly warmed up to room temperature (RT). Saturated sodium bicarbonate solution (150 mL) was then added and the mixture was extracted with dichloromethane for three times (100 mL × 3), and dried over magnesium sulfate until the solvents evaporated. Compound **5** was concentrated as a white oil and used without further purification.

*diethyl 2,5-bis(4-hexyl-4H-thieno[3,2-b]pyrrol-2-yl)terephthalate (**6**)*

Stannyl **5** and diethyl 2,5-dibromoterephthalate (557 mg, 1.47 mmol) were dissolved in degassed and dry toluene (20 mL) and tetrakis(triphenylphosphine)palladium(0) (370 mg, 0.32 mmol) were added. The reaction mixture was heated up to 110 °C and stirred for 12 h. Water (150 mL) was added and the mixture was extracted with dichloromethane for three times (100 mL × 3), and dried over magnesium sulfate, the solvents were

removed and the residue was purified by column chromatography (flash silica gel, petroleum ether/dichloromethane 1:1). Compound **6** (730 mg, 1.15 mmol, 74.9%) was obtained as a yellow solid. ^{1}H NMR (600 MHz, $CDCl_3$): δ 7.79 (s, 2H), 6.98 (s, 2H), 6.85 (d, *J* = 2.7 Hz, 2H), 6.36 (d, *J* = 2.5 Hz, 2H), 4.24 (q, *J* = 7.1 Hz, 4H), 4.02 (t, *J* = 7.1 Hz, 4H), 1.82 (t, *J* = 7.1 Hz, 4H), 1.30 (s, 12H), 1.14 (t, *J* = 7.1 Hz, 6H), 0.91 – 0.84 (m, 6H). ^{13}C NMR (150 MHz, $CDCl_3$): δ 167.48, 138.51, 136.80, 132.78, 132.72, 130.23, 124.73, 123.12, 109.09, 99.13, 60.58, 47.62, 30.37, 29.72, 25.48, 21.50, 12.98, 12.85. HRMS (ESI) *m/z*: $[M+H]^+$ calculated for $C_{36}H_{44}N_2O_4S_2$+, 672.8780; found, 672.8264.

Synthesis of ***PTBTP***

To a solution of 4-hexyl-1-bromobenzene (915 mg, 3.79 mmol) in THF (10 mL) at -78 ℃ was added with *n*-BuLi (1.53 mL, 2.5 M in hexane, 3.82 mmol) and the reaction mixture was stirred at -78 ℃ for 1 h. A solution of compound **6** (400 mg, 0.63 mmol) in THF (20 mL) was then added slowly during a period of 10 minutes. The mixture was stirred for 2 hours at -78 ℃, and then treated with a silica plug to quench the reaction. The organic eluent was concentrated and dissolved in PE (200 mL) and acetic acid (20 mL), followed by adding concentrated H_2SO_4 (1.5 mL) dropwise, the mixture was stirred at RT for 5 minutes and quenched with water. The organic layer was washed with water and extracted with ethyl acetate for three times (100 mL×3). The combined organic layers were dried over anhydrous $MgSO_4$. After removing the solvents, the residue was purified by column chromatography (flash silica gel, petroleum ether/ dichloromethane 5:1). **PTBTP** (363 mg, 0.31 mmol, 49.8%) was obtained as a yellow solid. ^{1}H NMR (600 MHz, $CDCl_3$): δ 7.28 – 7.23 (m, 10H), 7.07 – 6.98 (m, 8H), 6.69 (d, *J* = 2.9 Hz, 2H), 6.39 (d, *J* = 2.8 Hz, 2H), 3.53 (t, *J* = 7.8 Hz, 4H), 2.54 (t, *J* = 7.9 Hz, 8H), 1.60 – 1.52 (m, 6H), 1.37 – 1.21 (m, 26H), 1.15 (h, *J* = 7.3 Hz, 4H), 1.07 (q, *J* = 7.8 Hz, 4H), 0.99 (p, *J* = 7.2 Hz, 4H), 0.93 – 0.84 (m, 16H), 0.81 (t, *J* = 7.3 Hz, 6H). ^{13}C NMR (150 MHz, $CDCl_3$): δ 155.63, 141.43, 140.59, 139.23, 139.16, 135.77, 134.77, 128.82, 128.13, 125.91, 124.48, 114.54, 101.83, 62.16, 58.86, 53.96, 49.14, 35.53, 31.71, 31.58, 31.43, 31.30, 31.16, 29.24, 29.16, 26.34, 24.20, 22.59, 22.54, 20.83, 19.77, 14.13, 14.09, 14.03, 13.74. HRMS (ESI) *m/z*: $[M+H]^+$ calculated for $C_{80}H_{100}N_2S_2$+, 1153.8140; found, 1153.7546.

*Synthesis of **PTBTP-CHO***

To a solution of **PTBTP** (363 mg, 0.31 mmol) in dry 1,2-dichloroethane (20 mL) and DMF (5 mL) was added with phosphorus oxychloride (0.5 mL) at 0 °C, then kept and reacted under N_2 for 12 hours. The reaction mixture was neutralized with Na_2CO_3 solution and stirred for 30 minutes. The solution was then extracted with dichloromethane for twice (100 mL × 2) and washed with brine for twice (50 mL × 2). The organic layer was concentrated to give the crude product. Eventually, the product was purified by column chromatography (flash silica gel, petroleum ether/ dichloromethane 3:1) to afford **PTBTP-CHO** (335 mg, 0.28 mmol, 88.0%) as a yellow solid. ^{1}H NMR (600 MHz, $CDCl_3$) δ 9.47 (s, 2H), 7.36 (s, 2H), 7.25 (d, *J* = 8.3 Hz, 8H), 7.12 (s, 2H), 7.08 (d, *J* = 8.1 Hz, 8H), 3.92 (t, *J* = 8.1 Hz, 4H), 2.56 (t, *J* = 7.9 Hz, 8H), 1.55 (d, *J* = 3.2 Hz, 4H), 1.35 – 1.25 (m, 26H), 1.13 (p, *J* = 7.4 Hz, 4H), 0.94 (h, *J* = 7.7 Hz, 6H), 0.86 (t, *J* = 6.7 Hz, 16H), 0.80 (dt, *J* = 14.0, 7.5 Hz, 10H). ^{13}C NMR (150 MHz, $CDCl_3$) δ 177.83, 141.07, 140.71, 137.56, 136.69, 135.01, 133.95, 127.56, 127.41, 125.95, 114.66, 61.51, 47.71, 34.50, 30.66, 30.42, 30.35, 30.17, 28.15, 25.30, 21.66, 21.55, 13.05, 13.04. HRMS (ESI) *m/z*: $[M+H]^+$ calculated for $C_{82}H_{100}N_2O_2S_2$+, 1209.8340; found, 1209.7477.

*Compound **PTBTP-2F***

The mixture of **PTBTP-CHO** (160 mg, 0.13 mmol), 2-(6-fluoro-3-oxo-2,3-dihydro-1H-inden-1-ylidene)malononitrile (140 mg, 0.66 mmol) and pyridine (0.2 mL) were dissolved in dry $CHCl_3$ (20 mL). The mixture was stirred and refluxed for 8 h. The mixture was poured into methanol (150 mL) and filtered to get the residue. Then the residue was purified by column chromatography on silica gel using petroleum ether/dichloromethane (1:2, v/v) as the eluent. Compound **PTBTP-2F** (141 mg, 65.2%) was obtained as a dark-green solid. ^{1}H NMR (600 MHz, $CDCl_3$) δ 9.04 (d, J = 8.7 Hz, 2H), 8.62 (d, J = 11.1 Hz, 1H), 8.34 (s, 2H), 8.31 (d, J = 9.0 Hz, 1H), 7.83 – 7.45 (m, 2H), 7.42 (s, 2H), 7.32 (t, J = 8.1 Hz, 2H), 7.25 (s, 6H), 7.13 (d, J = 7.7 Hz, 8H), 3.94 – 3.83 (m, 4H), 2.58 (t, J = 7.7 Hz, 8H), 1.66 – 1.58 (m, 8H), 1.40 – 1.23 (m, 26H), 1.13 (q, J = 7.3 Hz, 4H), 0.99 (s, 4H), 0.95 – 0.89 (m, 4H), 0.89 – 0.77 (m, 22H). ^{13}C NMR (150 MHz, $CDCl_3$) δ 186.22, 161.48, 158.72, 155.61, 145.71, 142.83, 138.44, 136.94,

136.89, 134.94, 133.01, 128.94, 128.90, 128.53, 125.35, 125.29, 121.54, 121.37, 119.83, 116.70, 115.86, 115.27, 112.53, 112.35, 66.21, 62.67, 47.37, 35.66, 32.55, 31.81, 31.54, 31.29, 29.36, 26.34, 22.73, 22.71, 14.22, 14.18. HRMS (ESI) *m/z*: $[M+H]^+$ calcd for $C_{106}H_{106}F_2N_6O_2S_2+$, 1598.1708; found, 1598.7897.

*Compound **PTBTP-4F***

The mixture of **PTBTP-CHO** (160 mg, 0.13 mmol), 2-(5,6-difluoro-3-oxo-2,3-dihydro-1H-inden-1-ylidene)malononitrile (152 mg, 0.66 mmol) and pyridine (0.2 mL) were dissolved in dry $CHCl_3$ (20 mL). The mixture was stirred and refluxed for 8 h. The mixture was poured into methanol (150 mL) and filtered to get the residue. Then the residue was purified by column chromatography on silica gel using petroleum ether/dichloromethane (1:2, v/v) as the eluent. Compound **PTBTP-4F** (152 mg, 70.3%) was obtained as a dark-green solid. ^{1}H NMR (600 MHz, $CDCl_3$) δ 9.02 (s, 2H), 8.47 (dd, *J* = 9.9, 6.5 Hz, 2H), 8.33 (s, 2H), 7.60 (t, *J* = 7.5 Hz, 2H), 7.41 (s, 2H), 7.18 (dd, *J* = 73.9, 8.2 Hz, 14H), 3.93 – 3.83 (m, 4H), 3.49 (s, 6H), 2.66 – 2.49 (m, 8H), 1.60 (dt, *J* = 15.5, 7.6 Hz, 8H), 1.39 – 1.23 (m, 24H), 1.12 (dt, *J* = 14.9, 7.5 Hz, 4H), 0.97 (d, *J* = 5.6 Hz, 4H), 0.91 (dd, *J* = 15.3, 7.5 Hz, 4H), 0.87 (t, *J* = 6.7 Hz, 10H), 0.81 (q, *J* = 10.0, 8.7 Hz, 8H). ^{13}C NMR (150 MHz, $CDCl_3$) δ 185.02, 160.13, 158.69, 156.01, 145.93, 142.75, 138.31, 136.86, 136.68, 134.90, 133.09, 128.79, 128.69, 128.39, 121.55, 118.92, 116.66, 115.55, 115.14, 114.56, 114.41, 112.22, 65.92, 62.56, 47.26, 35.53, 32.43, 31.68, 31.41, 31.16, 29.22, 26.20, 22.60, 22.58, 14.09, 14.05. HRMS (ESI) *m/z*: $[M+H]^+$ calcd for $C_{106}H_{106}F_2N_6O_2S_2+$, 1634.1516; found, 1634.7709.

I.b NMR spectra

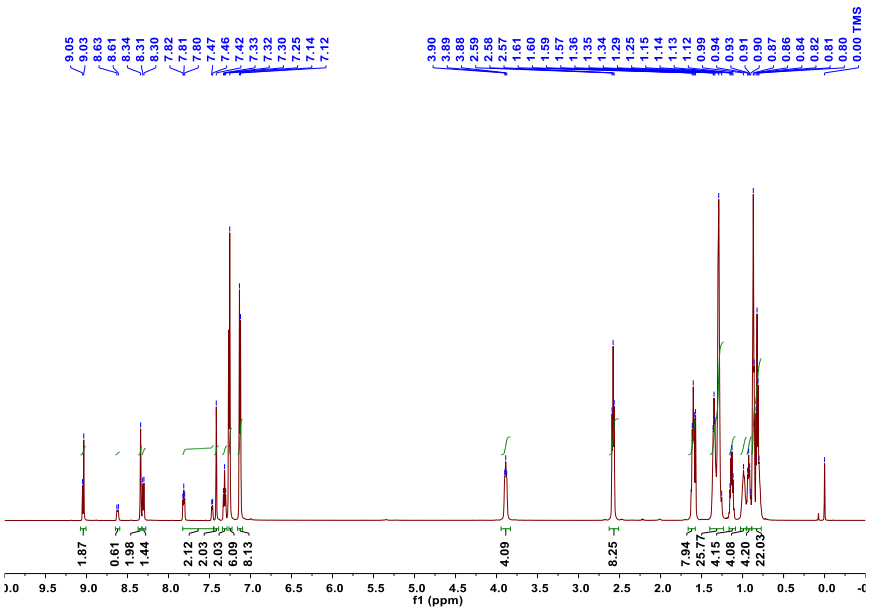

Figure S1 ^{1}H NMR of **PTBTP-2F**

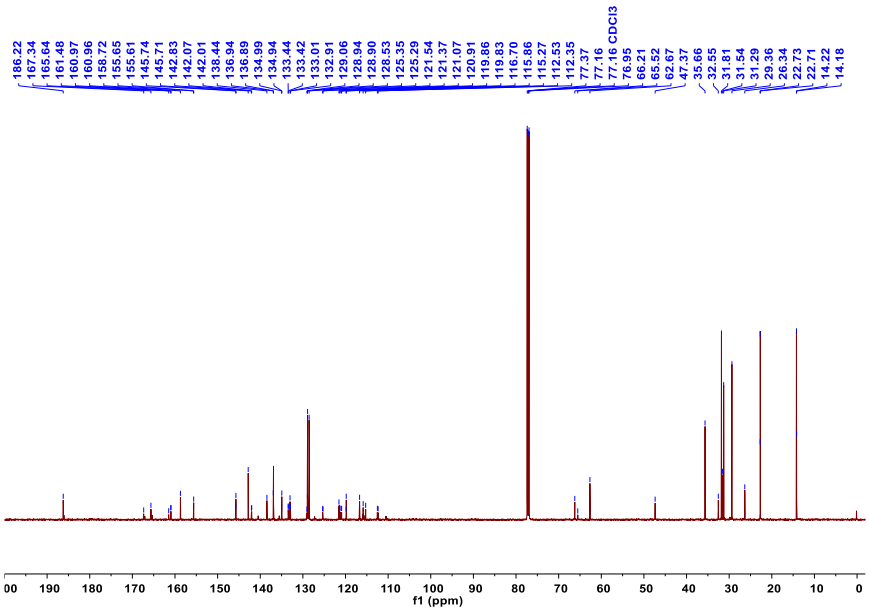

Figure S2 ^{13}C NMR of **PTBTP-2F**

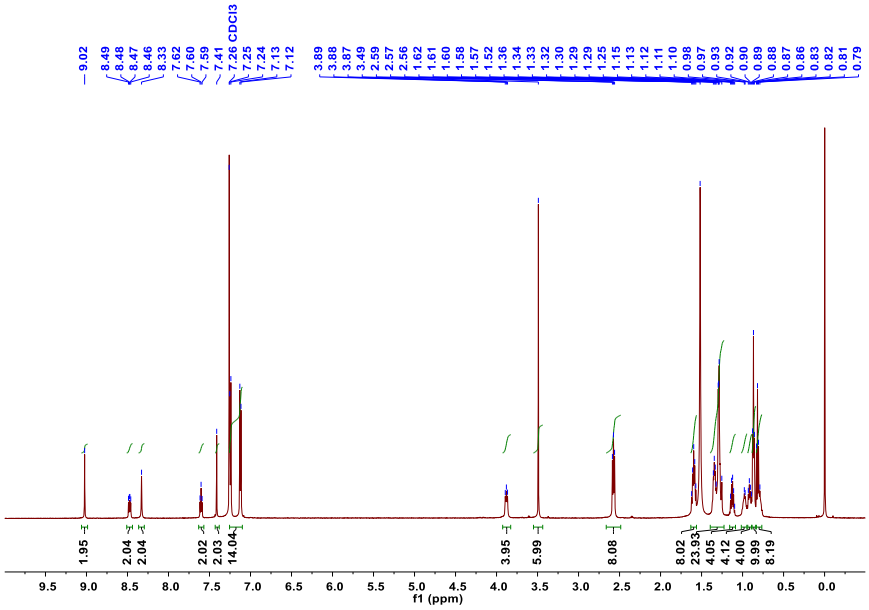

Figure S3 ^{1}H NMR of **PTBTP-4F**

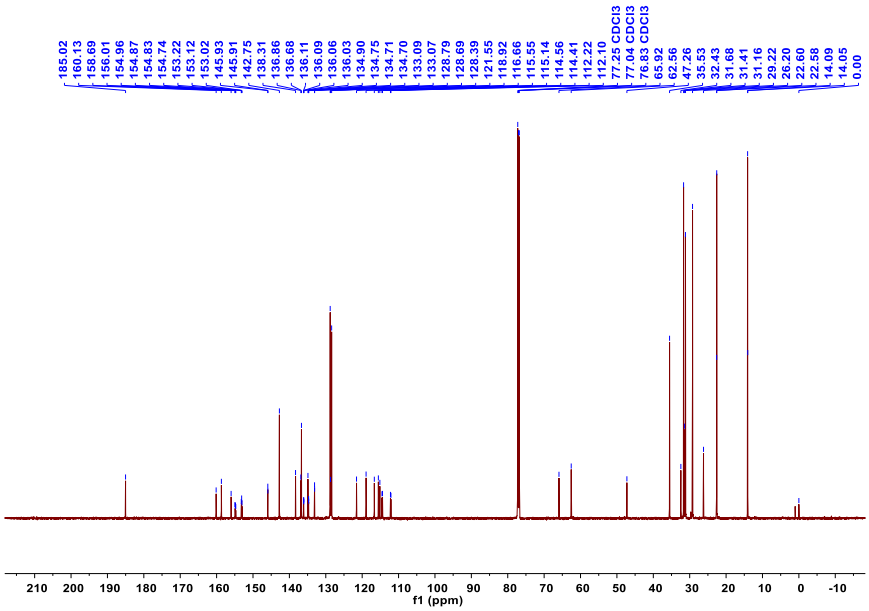

Figure S4 ^{13}C NMR of **PTBTP-4F**.

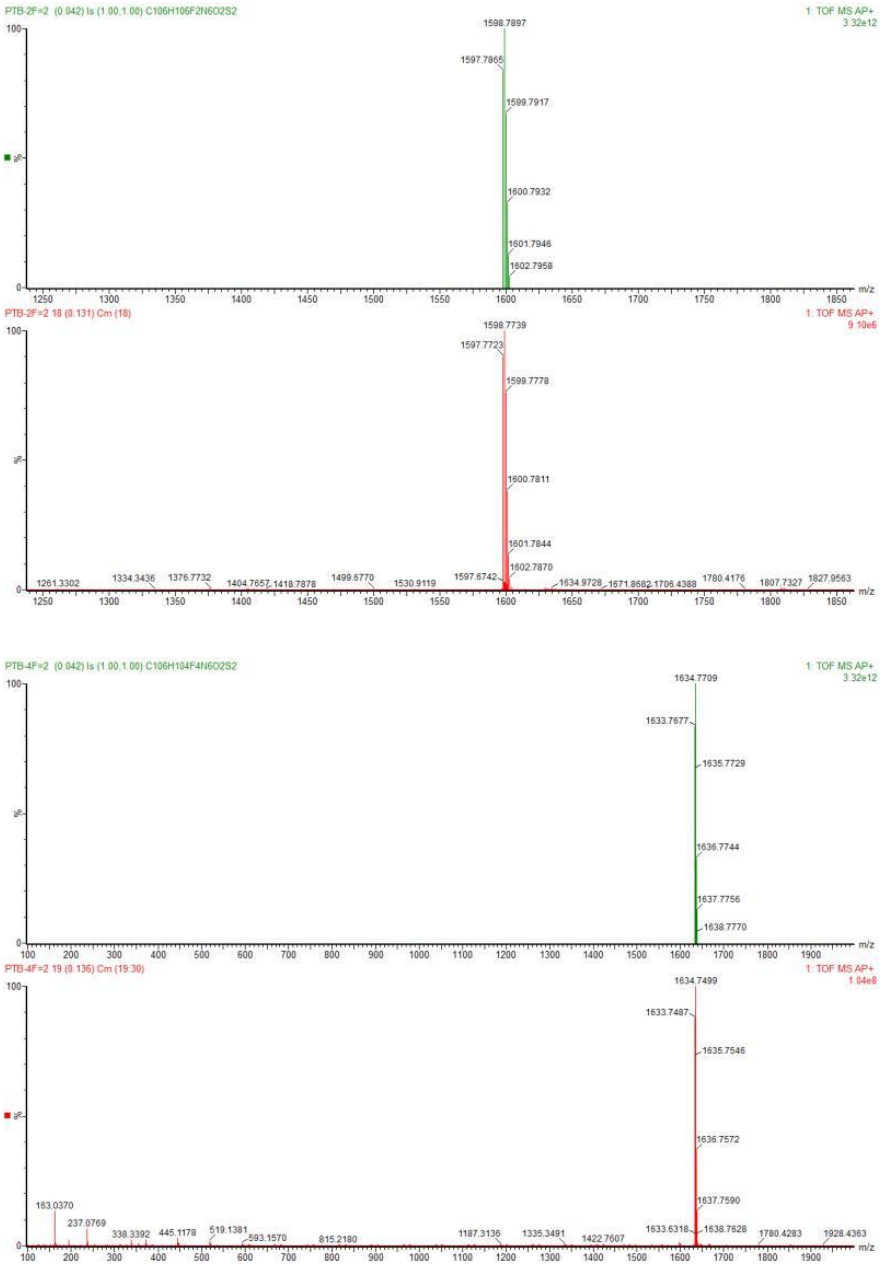

Figure S5 Mass spectra of **PTBTP-2F** and **PTBTP-4F**

Appendix II

I.a Materials and Synthesis

All commercially available chemicals and solvents were purchased from Energy-Chemical, Sigma-Aldrich, or J&K Chemical Co., and used without further purification, 2-(5,6-difluoro-3-oxo-2,3-dihydro-1H-inden-1-ylidene) malononitrile and IT-4F/4Cl were purchased from Nanjing Zhiyan Technology Co. Ltd., polymer donor PBDB-TF was purchased from Solarmer Materials Inc.. Compound **1**, PTBTP-CHO and PTBTP-4F were synthesized according to our previous work. Anhydrous THF and toluene were freshly distilled over sodium wire prior to use. The detailed synthetic processes of PTBTT-4F, PTBTT-4Cl, and PTBTP-4Cl are described in the following.

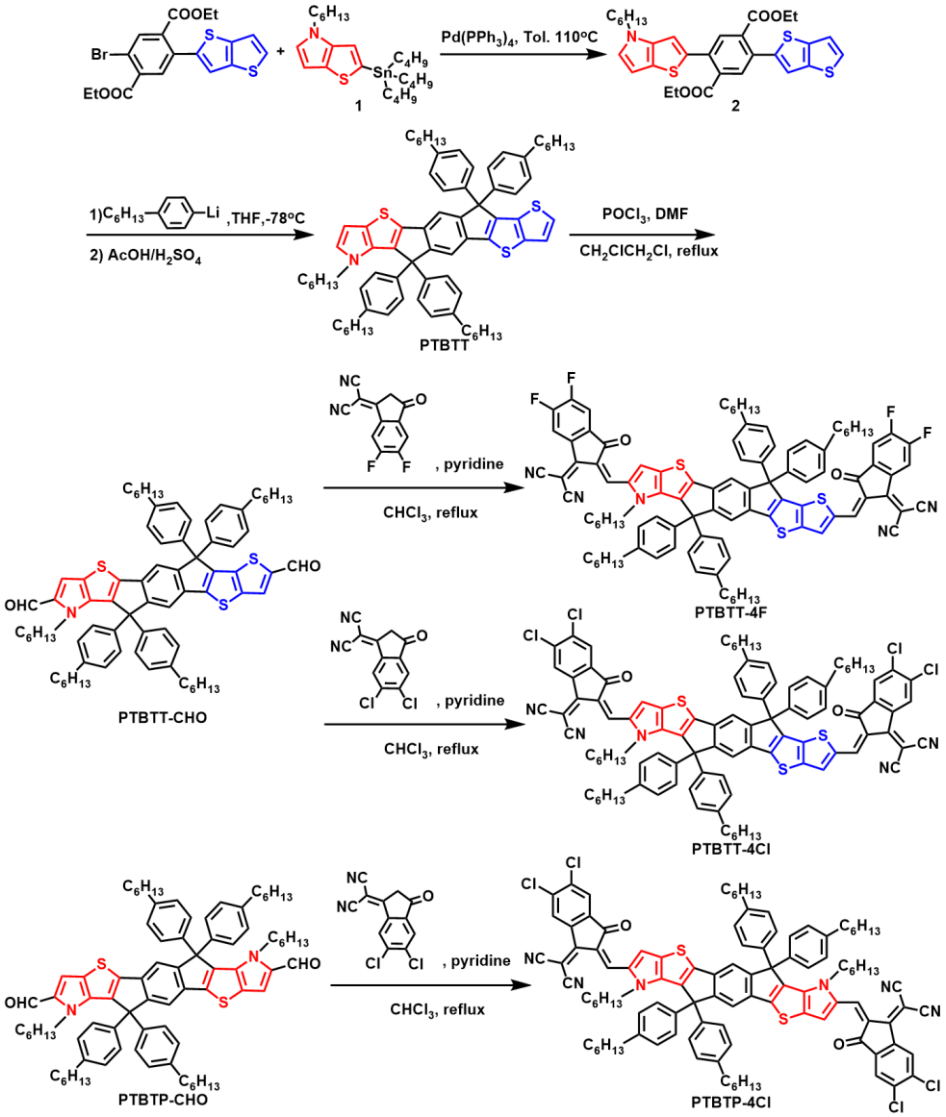

Scheme S1. Synthesis routes of PTBTT-4F and PTBTT-4Cl

*4-hexyl-2-(tributylstannyl)-4H-thieno[3,2-b]pyrrole (**1**)*

2-bromo-4-hexyl-4H-thieno[3,2-b]pyrrole (1.00 g, 3.49 mmol) in THF (10 mL) was added dropwise with *n*-BuLi (1.60 mL, 2.4 M in hexane, 3.84 mmol) and the mixture was kept at -78 °C for 2 hours. Then a solution of tributylchlorostannane (1.36 g, 4.19 mmol) in THF (10 mL) was added and stirred at -78 °C for 1 hour. The reaction mixture was slowly warmed up to room temperature (RT). Saturated sodium bicarbonate solution (100 mL) was then added and the mixture was extracted with dichloromethane for three times (100 mL × 3), and dried over magnesium sulfate until the solvents evaporated. Compound **1** was finally concentrated as a white oil and used without further purification.

*Diethyl-2-(4-hexyl-4H-thieno[3,2-b]pyrrol-2-yl)-5-(thieno[3,2-b]thiophen-2-yl)terephthalate (**2**)*

Compound **1** and diethyl 2-bromo-5-(thieno[3,2-b]thiophen-2-yl)terephthalate (612 mg, 1.39 mmol) were dissolved in degassed and dry toluene (20 mL), tetrakis(triphenylphosphine)palladium(0) (161 mg, 0.139 mmol) were added. The reaction mixture was heated up to 110 ℃ and stirred for 12 hours. Water (150 mL) was then added and the mixture was extracted with dichloromethane for three times (100 mL×3), and dried over magnesium sulfate. The organic layers were combined and evaporated under vacuum. The residue was purified by column chromatography (flash silica gel, petroleum ether/dichloromethane 1:1). Compound **2** (510 mg, 0.90 mmol, 64.7%) was obtained as a yellow solid. ^{1}H NMR (600 MHz, $CDCl_3$): δ 7.90 (s, 1H), 7.78 (s, 1H), 7.39 (d, *J* = 5.4 Hz, 1H), 7.27 (d, *J* = 5.4 Hz, 2H), 7.00 (s, 1H), 6.86 (d, *J* = 3.0 Hz, 1H), 6.37 (d, *J* = 3.0 Hz, 1H), 4.24 (p, *J* = 7.2 Hz, 4H), 4.02 (t, *J* = 7.2 Hz, 2H), 1.85-1.79 (m, 2H), 1.33-1.27 (m, *J* = 4.8, 4.5 Hz, 6H), 1.15 (t, *J* = 7.2 Hz, 3H), 1.12 (t, *J* = 7.2 Hz, 3H), 0.90-0.85 (m, 3H). ^{13}C NMR (150 MHz, $CDCl_3$): δ 168.29, 167.67, 142.38, 139.78, 139.55, 139.33, 137.48, 134.76, 134.03, 133.82, 132.74, 131.71, 131.62, 127.18, 125.93, 124.35, 119.42, 119.09, 110.32, 100.19, 61.72, 61.69, 48.67, 31.40, 30.74, 26.51, 22.52, 14.01, 13.88, 13.83. HRMS (ESI) *m/z*: $[M+H]^+$ calculated for $C_{31}H_{31}NO_4S_3^+$, 565.7610; found, 566.1220.

*Synthesis of **PTBTT***

To a solution of 4-hexyl-1-bromobenzene (1.15 g, 4.77 mmol) in THF (10 mL) at -78 ℃ was added with *n*-BuLi (2.02 mL, 2.4 M in hexane, 4.85 mmol) and the reaction mixture was stirred at -78 ℃ for 1 hour. A solution of compound **2** (450 mg, 0.80 mmol) in THF (20 mL) was then added slowly for a period of 10 min. The mixture was stirred for 2 hours at -78 ℃, then treated with a silica plug to quench the reaction. The organic eluent was concentrated and dissolved in petroleum ether (200 mL) and acetic acid (20 mL), followed by adding concentrated H_2SO_4 (1.5 mL) dropwise, the mixture was then stirred at RT for 5 min and quenched with water. Afterward, the mixture was washed with water and extracted with dichloromethane for three times (100 mL×3).

The organic layer was dried over anhydrous $MgSO_4$. After removing the solvents, the residue was purified by column chromatography (flash silica gel, petroleum ether/dichloromethane 5:1). **PTBTT** (460 mg, 0.42 mmol, 53.2%) was obtained as a yellow solid. ^{1}H NMR (600 MHz, $CDCl_3$): δ 7.38 (d, *J* = 9.6 Hz, 2H), 7.29 (d, *J* = 8.4 Hz, 4H), 7.24 (d, *J* = 5.4 Hz, 1H), 7.22 (d, *J* = 5.4 Hz, 1H), 7.16-7.12 (m, 4H), 7.10-7.03 (m, 8H), 6.73 (d, *J* = 3.0 Hz, 1H), 6.41 (d, *J* = 3.0 Hz, 1H), 3.55 (t, *J* = 7.8 Hz, 2H), 2.58-2.51 (m, 8H), 1.35-1.25 (m, 30H), 1.16 (q, *J* = 7.2 Hz, 2H), 1.09 (q, *J* = 7.8 Hz, 2H), 1.00 (p, *J* = 7.2 Hz, 2H), 0.94-0.84 (m, 16H), 0.82 (t, *J* = 7.2 Hz, 3H). ^{13}C NMR (150 MHz, $CDCl_3$): δ 155.98, 152.82, 145.35, 143.55, 141.60, 141.55, 141.10, 140.49, 140.27, 139.72, 139.06, 136.65, 135.21, 134.71, 133.84, 128.82, 128.34, 128.21, 128.09, 126.48, 125.87, 124.84, 120.27, 115.82, 115.60, 101.94, 62.84, 62.26, 49.17, 35.59, 35.54, 31.71, 31.44, 31.30, 31.26, 31.17, 29.17, 26.35, 22.59, 22.55, 14.09, 14.03. HRMS (ESI) *m/z*: $[M+H]^+$ calculated for $C_{74}H_{87}NS_3^+$, 1086.6970; found, 1086.9132.

*Synthesis of **PTBTT-CHO***

To a solution of **PTBTT** (200 mg, 0.18 mmol) in dry 1,2-dichloroethane (10 mL) and DMF (2 mL) was introduced with phosphorus oxychloride (0.3 mL) and stirred at 0 °C. The mixture reacted under N_2 for 12 hours and was subsequently neutralized with Na_2CO_3 solution, followed by stirring for 30 min. The solution was then extracted with dichloromethane twice (100 mL × 2) and washed with brine twice (50 mL × 2). The organic layer was concentrated to yield the crude product. Finally, the product was purified by column chromatography (flash silica gel, petroleum ether/ dichloromethane 2:1) to afford **PTBTT-CHO** (188 mg, 0.16 mmol, 89.4%) as a yellow solid. ^{1}H NMR (600 MHz, $CDCl_3$) δ 9.86 (s, 1H), 9.51 (s, 1H), 7.91 (s, 1H), 7.49 (s, 2H), 7.28 (d, *J* = 8.4 Hz, 4H), 7.15 (s, 1H), 7.1-7.00 (m, 12H), 3.98-3.92 (m, 2H), 2.60-2.52 (m, 8H), 1.61-1.56 (m, 8H), 1.34-1.25 (m, 28H), 1.14 (p, *J* = 7.2 Hz, 2H), 0.98-0.93 (m, 2H), 0.88-0.84 (m, 12H), 0.82 (t, *J* = 7.2 Hz, 3H). ^{13}C NMR (150 MHz, $CDCl_3$) δ 182.79, 179.00, 157.67, 154.18, 149.82, 148.82, 146.17, 144.11, 142.22, 142.21, 141.64, 141.40, 140.31, 139.34, 139.07, 137.58, 136.56, 135.99, 135.13, 129.80, 128.66, 128.59, 128.50, 128.40, 128.21, 127.85, 127.30, 116.92,

116.77, 62.98, 62.65, 48.77, 36.00, 35.57, 35.53, 31.69, 31.47, 31.38, 31.25, 31.20, 29.71, 29.18, 29.13, 26.33, 22.69, 22.57, 14.08. HRMS (ESI) *m/z*: $[M+H]^+$ calculated for $C_{76}H_{87}NO_2S_3^+$, 1142.7170; found, 1142.3416.

*Compound **PTBTT-4F***

The mixture of **PTBTT-CHO** (150 mg, 0.13 mmol), 2-(5,6-difluoro-3-oxo-2,3-dihydro-1H-inden-1-ylidene)malononitrile (150 mg, 0.65 mmol) and pyridine (0.2 mL) were dissolved in dry $CHCl_3$ (20 mL). The mixture was stirred and refluxed for 8 hours, and then poured into methanol (150 mL) and filtered to obtain the residue. The residue was purified by column chromatography on silica gel using petroleum ether/dichloromethane (1:2, v/v) as the eluent. Compound **PTBTT-4F** (161 mg, 0.1 mmol, 78.3%) was obtained as a dark blue solid. ^{1}H NMR (600 MHz, $CDCl_3$) δ 9.05 (s, 1H), 8.83 (s, 1H), 8.53 (dd, *J* = 9.6, 6.0 Hz, 1H), 8.48 (dd, *J* = 10.2, 6.6 Hz, 1H), 8.35 (s, 1H), 8.21 (s, 1H), 7.67 (t, *J* = 7.2 Hz, 1H), 7.61 (t, *J* = 7.2 Hz, 1H), 7.53 (d, *J* = 4.8 Hz, 2H), 7.29 (d, *J* = 7.8 Hz, 4H), 7.18-7.12 (m, 12H), 3.94-3.88 (m, 2H), 2.57 (dt, *J* = 15.0, 7.8 Hz, 8H), 1.63-1.56 (m, 8H), 1.36-1.22 (m, 24H), 1.14 (h, *J* = 7.2 Hz, 3H), 1.03-0.98 (m, 2H), 0.93 (p, *J* = 7.8 Hz, 3H), 0.88-0.76 (m, 15H). ^{13}C NMR (150 MHz, $CDCl_3$) δ 185.75, 185.06, 160.20, 158.97, 158.21, 155.84, 155.50, 155.38, 155.29, 154.87, 153.69, 153.57, 153.27, 153.16, 153.07, 147.67, 147.58, 145.86, 143.80, 142.79, 142.56, 139.39, 138.78, 138.48, 138.38, 137.39, 137.22, 136.70, 136.68, 136.13, 136.08, 134.88, 134.77, 134.45, 133.13, 128.86, 128.81, 128.40, 127.83, 121.70, 121.54, 119.07, 117.79, 117.53, 115.55, 115.13, 115.05, 114.90, 114.59, 114.45, 114.23, 114.12, 112.72, 112.59, 112.28, 112.16, 69.80, 66.04, 63.14, 62.66, 47.29, 35.59, 35.53, 32.46, 31.69, 31.68, 31.41, 31.25, 31.16, 29.21, 29.17, 26.21, 22.60, 22.58, 14.08, 14.05. HRMS (ESI) *m/z*: $[M+H]^+$ calcd for $C_{100}H_{91}F_4N_5O_2S_3^+$, 1567.0346; found, 1566.6272.

*Compound **PTBTT-4Cl***

The mixture of **PTBTT-CHO** (100 mg, 0.09 mmol), 2-(5,6-dichloro-3-oxo-2,3-dihydro-1H-inden-1-ylidene)malononitrile (100 mg, 0.38 mmol) and pyridine (0.2 mL) were dissolved in dry $CHCl_3$ (20 mL). The mixture was stirred and refluxed for 8 hours. The mixture was poured into methanol (120

mL) and filtered to get the residue. The residue was purified by column chromatography on silica gel using petroleum ether/dichloromethane (1:2, v/v) as the eluent. Compound **PTBTT-4Cl** (106 mg, 0.06 mmol, 74.2%) was obtained as a dark blue solid. ^{1}H NMR (500 MHz, $CDCl_3$) δ 9.08 (s, 1H), 8.83 (s, 1H), 8.74 (s, 1H), 8.69 (s, 1H), 8.36 (s, 1H), 8.21 (s, 1H), 7.87 (d, *J* = 39.5 Hz, 2H), 7.57 (d, *J* = 6.5 Hz, 2H), 7.31 (d, *J* = 8.0 Hz, 4H), 7.17 (m, 12H), 3.93 (t, *J* = 8.5 Hz, 2H), 2.59 (dt, *J* = 12.0, 7.8 Hz, 8H), 1.65-1.56 (m, 8H), 1.38-1.26 (m, 24H), 1.16 (q, *J* = 7.5 Hz, 2H), 1.07-1.01 (m, 2H), 0.95 (q, *J* = 7.5 Hz, 2H), 0.89-0.80 (m, 17H). ^{13}C NMR (125 MHz, $CDCl_3$) δ 185.89, 160.11, 148.13, 147.84, 142.97, 142.72, 139.89, 139.84, 139.57, 139.00, 138.88, 138.81, 138.76, 137.62, 136.85, 136.80, 135.46, 129.25, 129.02, 128.97, 128.55, 127.97, 127.06, 126.53, 125.31, 124.79, 122.05, 121.83, 118.03, 117.73, 114.31, 63.32, 62.85, 47.45, 35.73, 35.66, 32.58, 31.82, 31.81, 31.54, 31.35, 31.27, 29.34, 29.29, 26.34, 22.73, 22.70, 14.20, 14.17. HRMS (ESI) *m/z*: $[M+H]^+$ calcd for $C_{100}H_{91}Cl_4N_5O_2S_3^+$, 1632.8410; found, 1633.5231.

*Compound **PTBTP-4Cl***

The mixture of **PTBTP-CHO** (90 mg, 0.07 mmol), 2-(5,6-dichloro-3-oxo-2,3-dihydro-1H-inden-1-ylidene)malononitrile (90 mg, 0.34 mmol) and pyridine (0.2 mL) were dissolved in dry $CHCl_3$ (15 mL). The mixture was stirred and refluxed for 5 hours. The mixture was poured into methanol (100 mL) and filtered to get the residue. Then the residue was purified by column chromatography on silica gel using petroleum ether/dichloromethane (1:3, v/v) as the eluent. Compound **PTBTP-4Cl** (94 mg, 0.06 mmol, 74.3%) was obtained as a dark blue solid. ^{1}H NMR (500 MHz, $CDCl_3$) δ 9.04 (s, 2H), 8.68 (s, 2H), 8.33 (s, 2H), 7.83 (s, 2H), 7.42 (s, 2H), 7.25 (d, *J* = 3.5 Hz, 8H), 7.13 (d, *J* = 8.5 Hz, 8H), 3.88 (s, 4H), 2.62-2.53 (m, 8H), 1.60 (p, *J* = 7.5 Hz, 8H), 1.39-1.32 (m, 8H), 1.31-1.24 (m, 16H), 1.13 (h, *J* = 7.5 Hz, 4H), 1.03-0.91 (m, 8H), 0.87 (t, *J* = 7.0 Hz, 12H), 0.83-0.79 (m, 10H). ^{13}C NMR (125 MHz, $CDCl_3$) δ 158.92, 146.36, 142.94, 138.80, 138.68, 138.53, 136.78, 135.45, 133.48, 129.22, 128.95, 128.53, 126.54, 124.78, 122.03, 116.87, 62.74, 47.42, 35.67, 32.55, 31.81, 31.53, 31.28, 29.35, 26.34, 22.72, 22.71, 14.21, 14.17. HRMS (ESI) *m/z*: $[M+H]^+$ calcd for $C_{106}H_{104}Cl_4N_6O_2S_2^+$, 1699.9580; found, 1699.6781.

I.b NMR spectra and Mass spectra

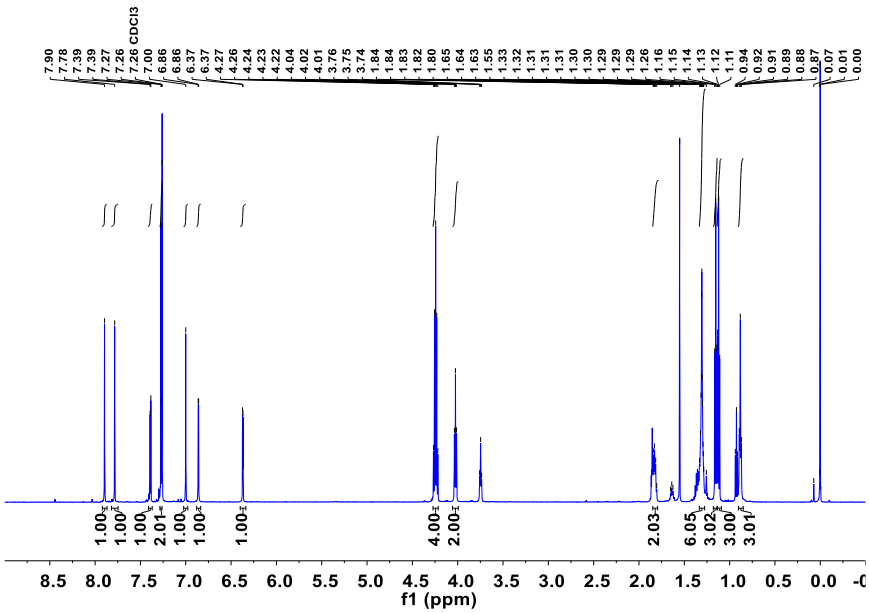

Figure S1. ^{1}H NMR of Compound **2**

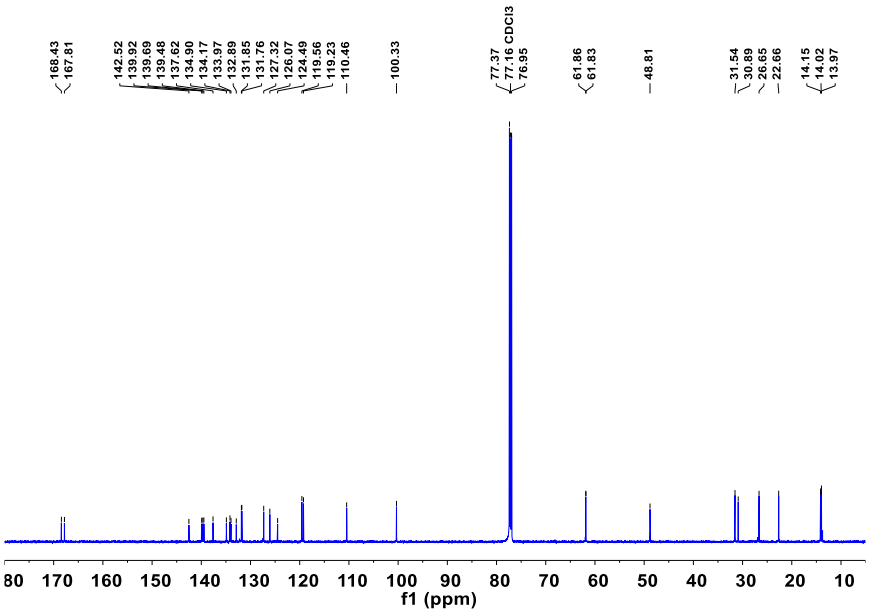

Figure S2. ^{13}C NMR of Compound **2**

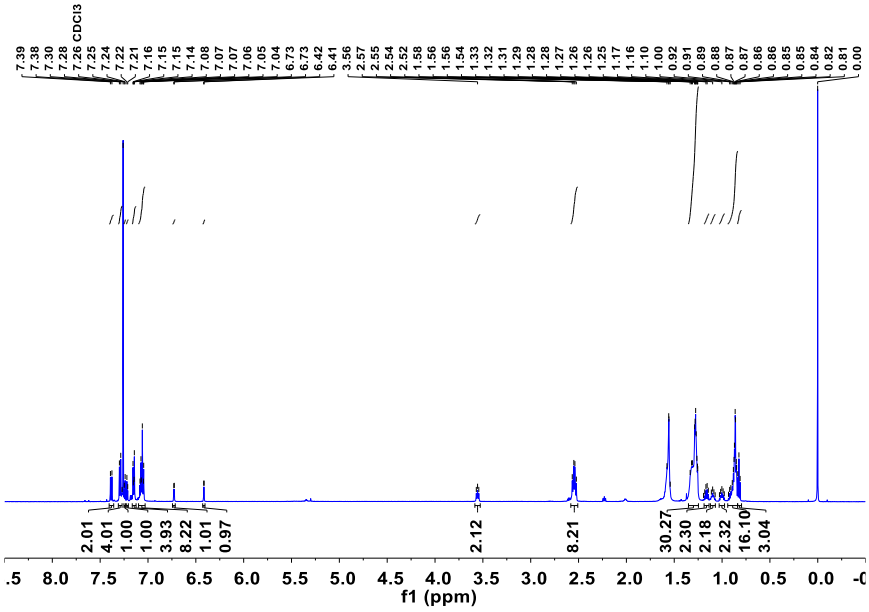

Figure S3. ^{1}H NMR of **PTBTT**

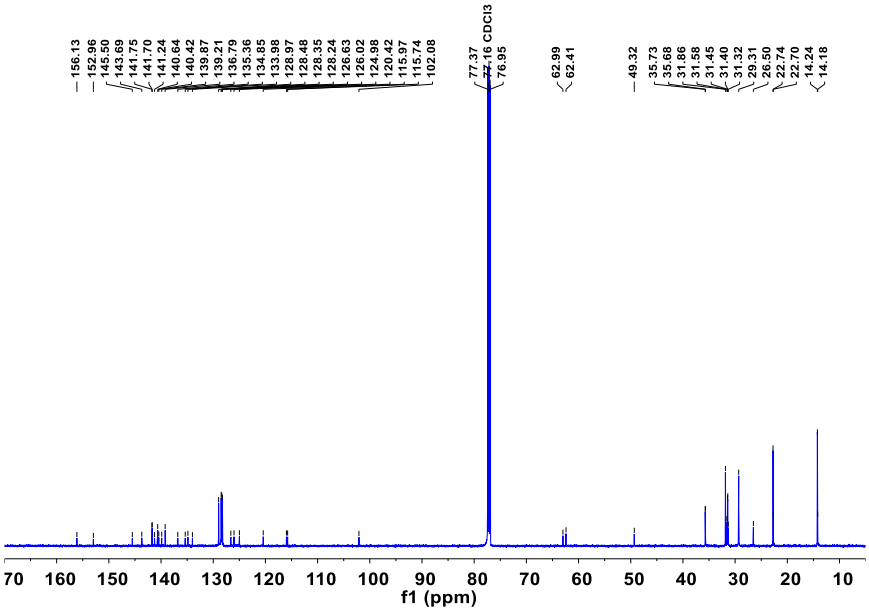

Figure S4. ^{13}C NMR of **PTBTT**

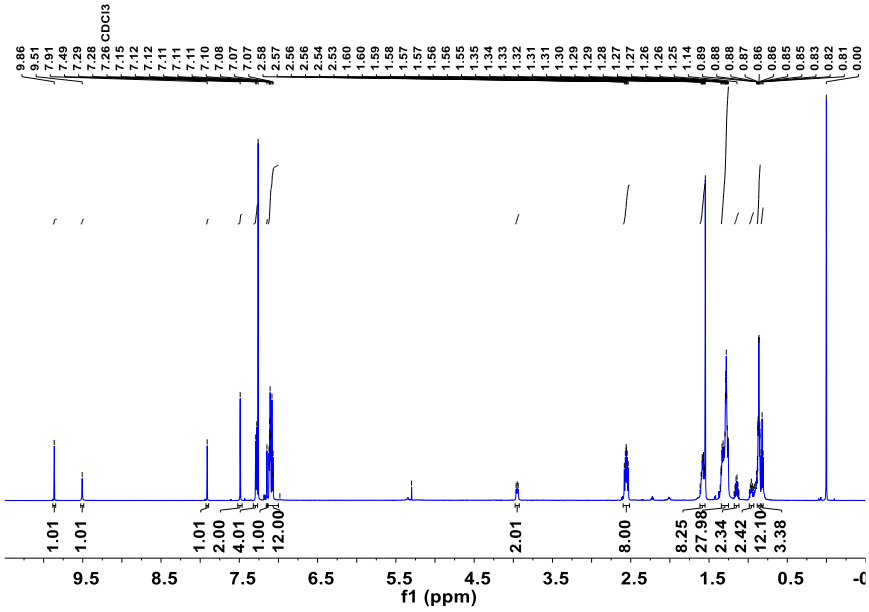

Figure S5. ^{1}H NMR of **PTBTT-CHO**

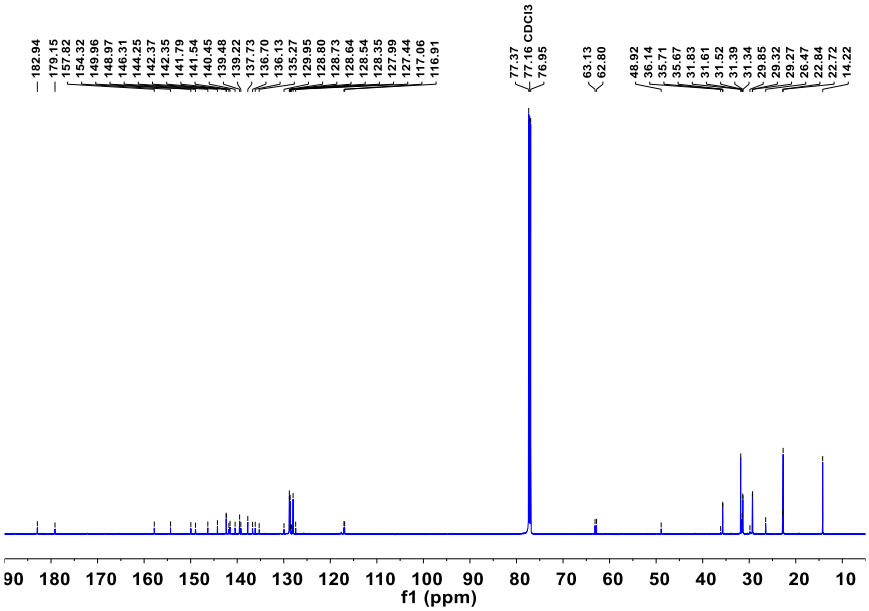

Figure S6. ^{13}C NMR of **PTBTT-CHO**

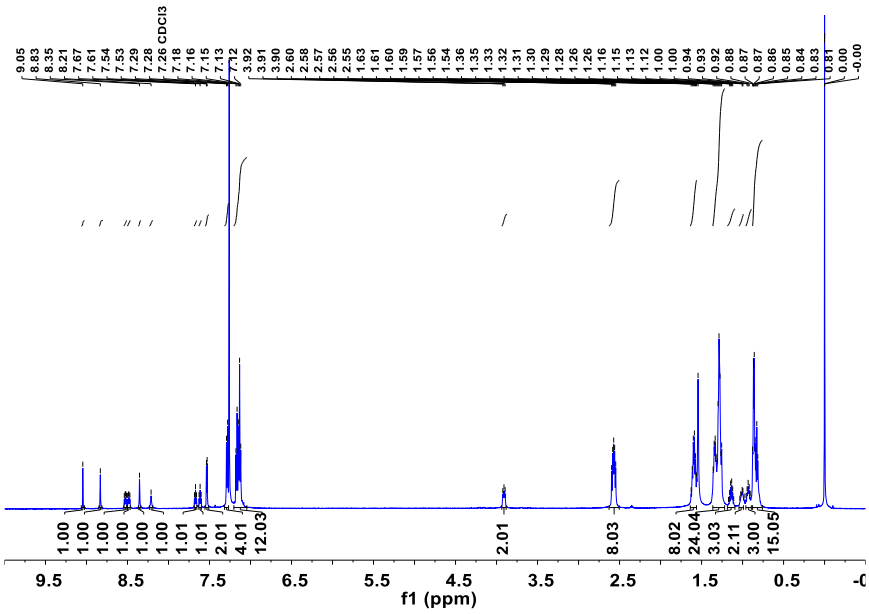

Figure S7a. ^{1}H NMR of **PTBTT-4F**

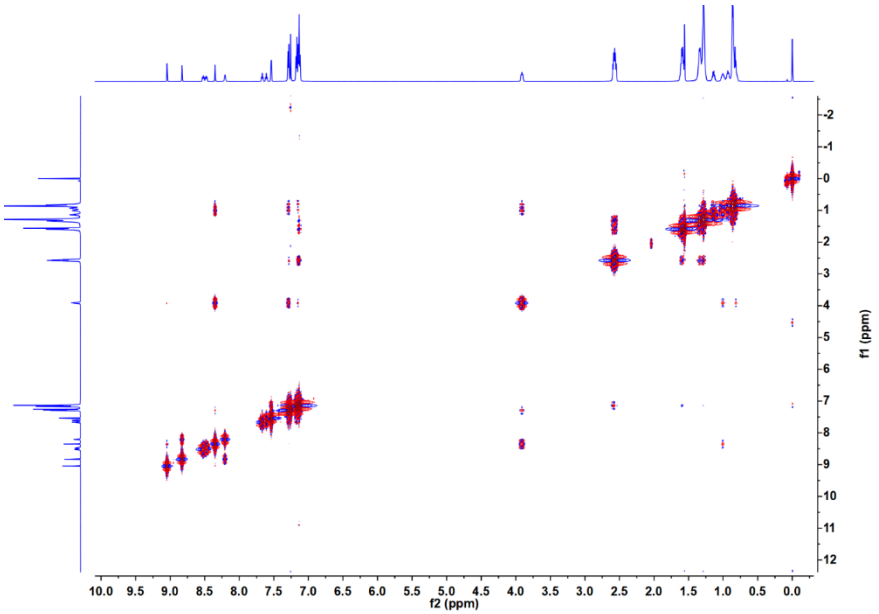

Figure S7b. COSEY NMR of **PTBTT-4F**

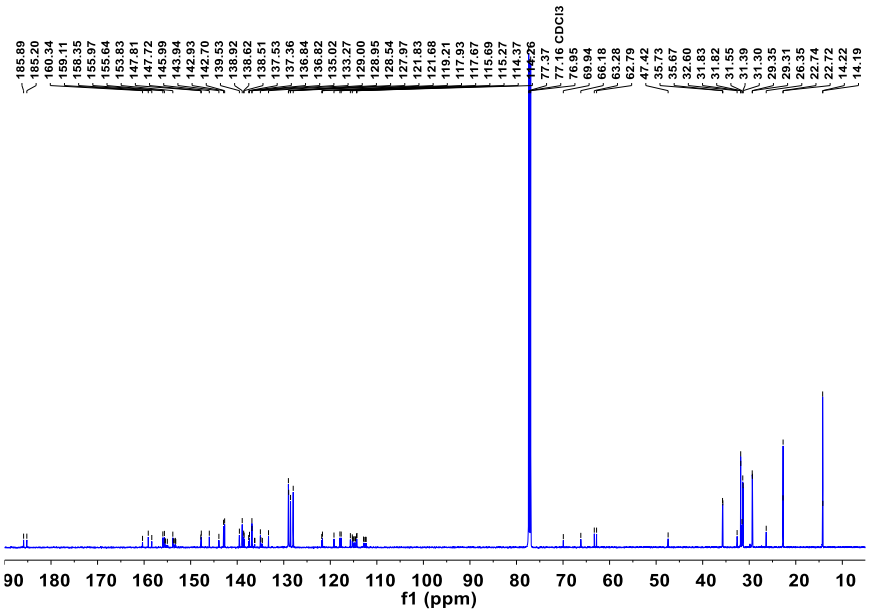

Figure S8. ^{13}C NMR of **PTBTT-4F**

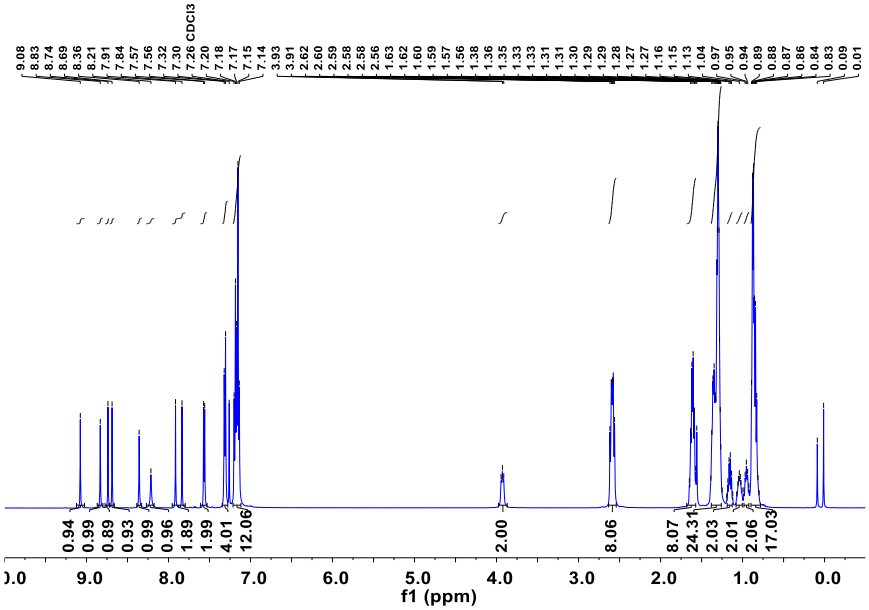

Figure S9a. ^{1}H NMR of **PTBTT-4Cl**

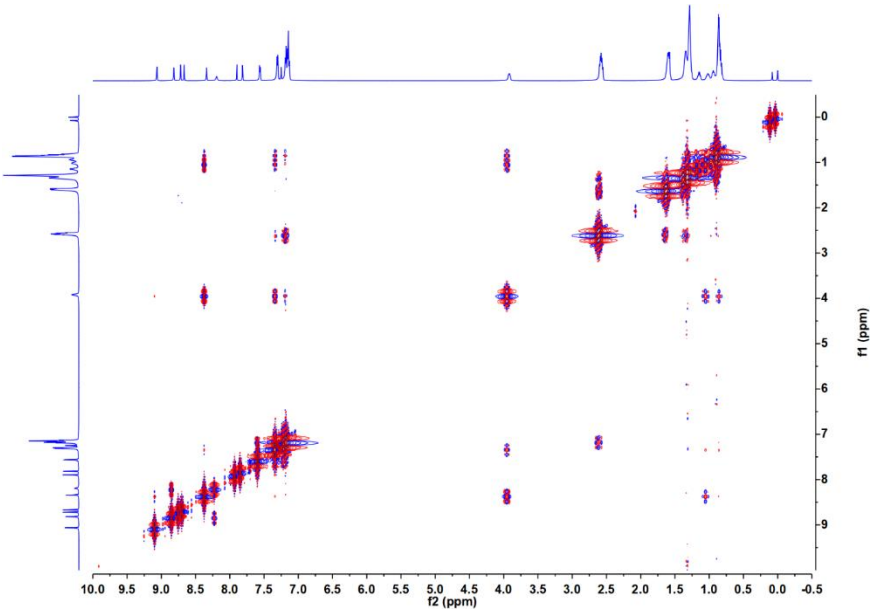

Figure S9b. COSEY NMR of **PTBTT-4Cl**

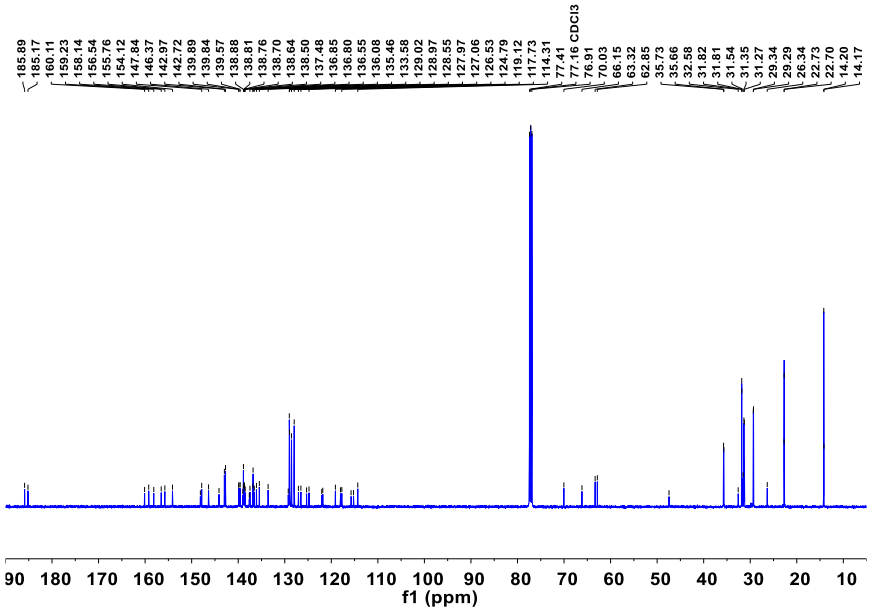

Figure S10. ^{13}C NMR of **PTBTT-4Cl**

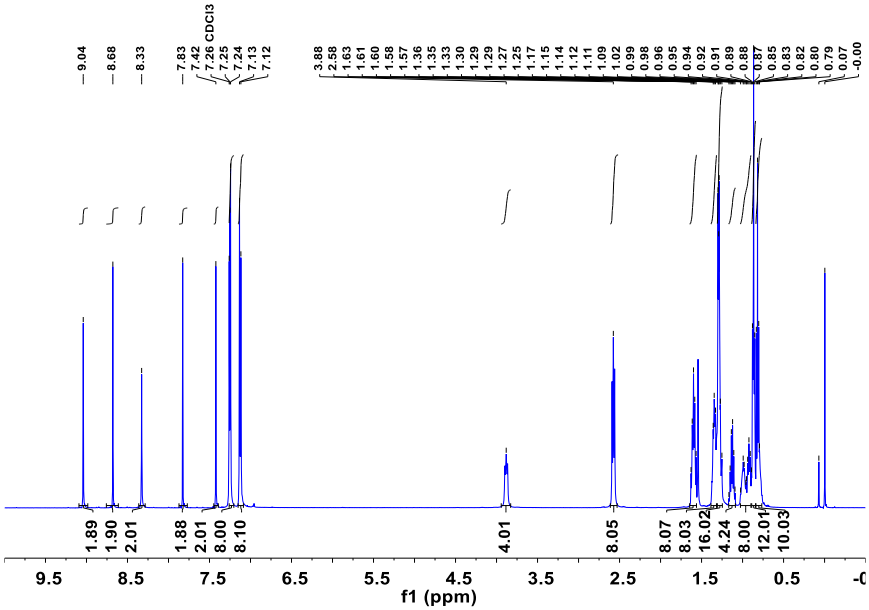

Figure S11a. ^{1}H NMR of **PTBTP-4Cl**

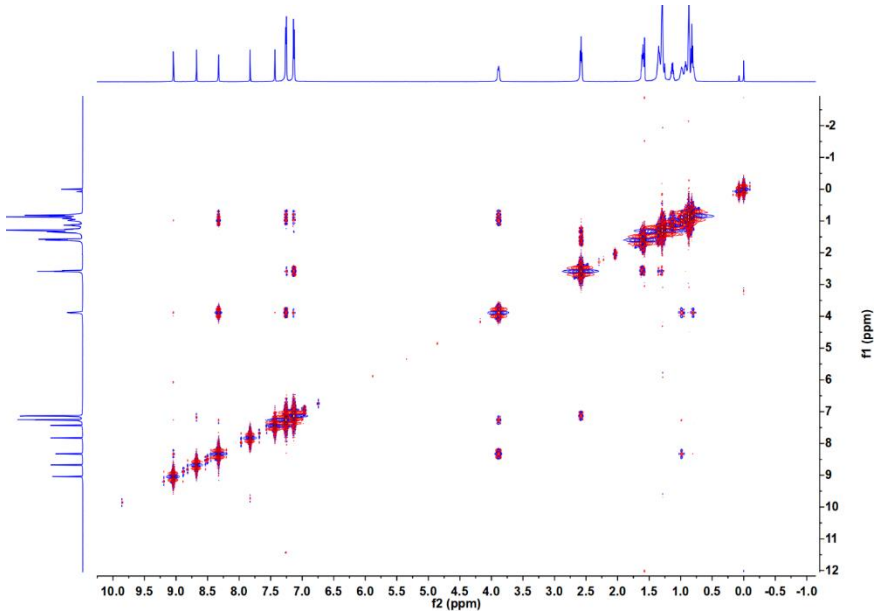

Figure S11b. COSEY NMR of **PTBTP-4Cl**.

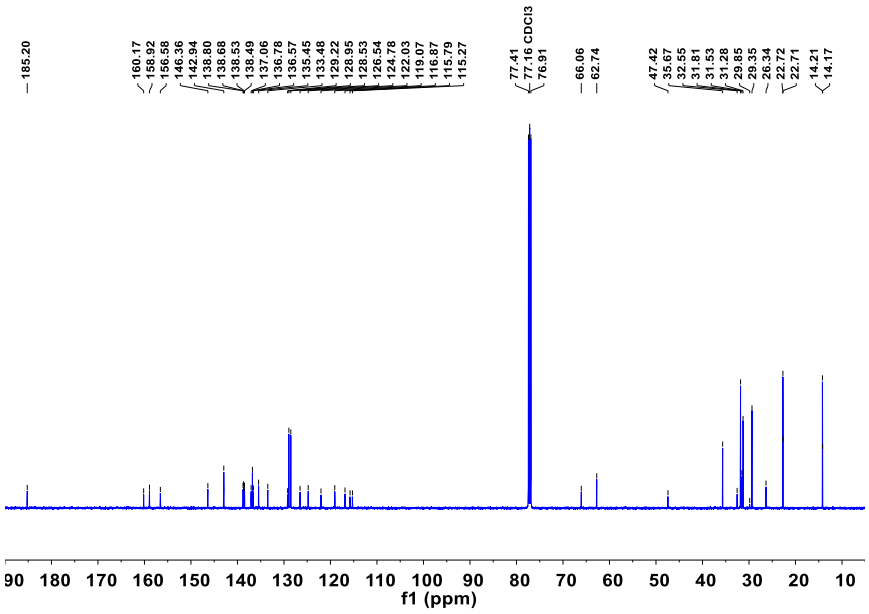

Figure S12. ^{13}C NMR of **PTBTP-4Cl**

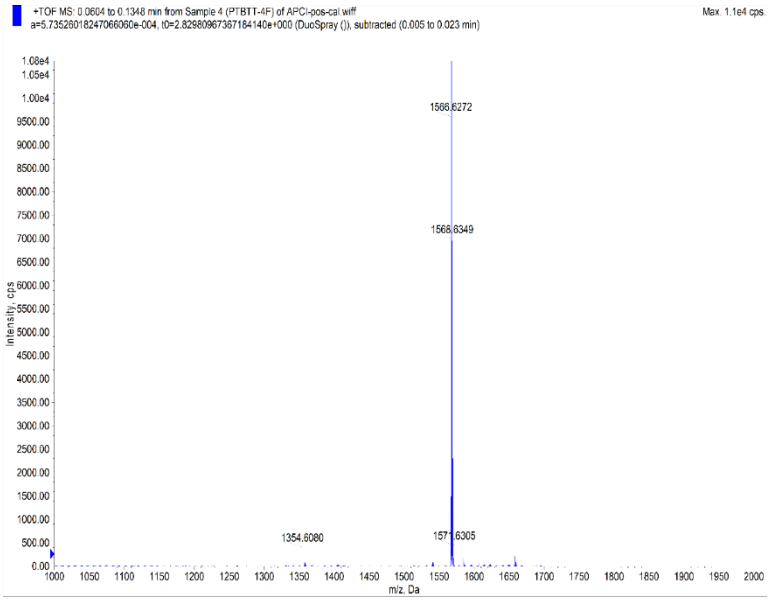

Figure S13. Mass spectra of **PTBTT-4F**

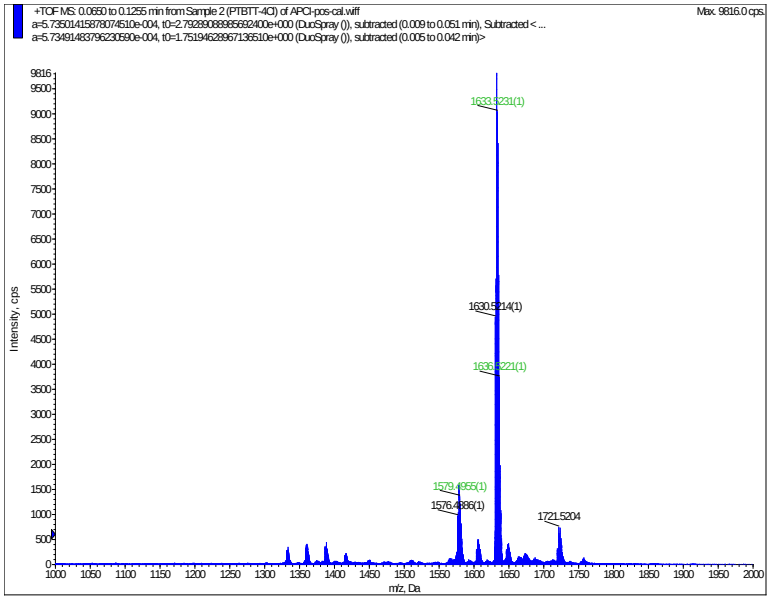

Figure S14. Mass spectra of **PTBTT-4Cl**

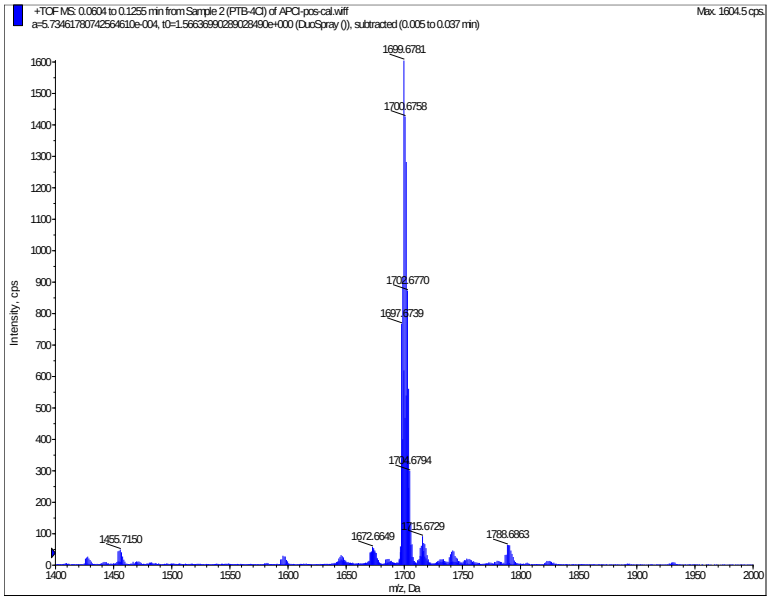

Figure S15. Mass spectra of **PTBTP-4Cl**.

I.c Calculation details

1 -> 2: 0.00692	1 <- 2: 0.00829	Net 1 -> 2: -0.00136
1 -> 3: 0.00551	1 <- 3: 0.02232	Net 1 -> 3: -0.01681
1 -> 4: 0.00256	1 <- 4: 0.02014	Net 1 -> 4: -0.01758
1 -> 5: 0.00553	1 <- 5: 0.02234	Net 1 -> 5: -0.01682
1 -> 6: 0.00695	1 <- 6: 0.00829	Net 1 -> 6: -0.00134
1 -> 7: 0.00324	1 <- 7: 0.00324	Net 1 -> 7: 0.00001
2 -> 3: 0.01411	2 <- 3: 0.04777	Net 2 -> 3: -0.03366
2 -> 4: 0.00655	2 <- 4: 0.04311	Net 2 -> 4: -0.03656
2 -> 5: 0.01416	2 <- 5: 0.04783	Net 2 -> 5: -0.03367
2 -> 6: 0.01781	2 <- 6: 0.01775	Net 2 -> 6: 0.00006
2 -> 7: 0.00832	2 <- 7: 0.00694	Net 2 -> 7: 0.00138
3 -> 4: 0.01763	3 <- 4: 0.03428	Net 3 -> 4: -0.01665
3 -> 5: 0.03812	3 <- 5: 0.03803	Net 3 -> 5: 0.00009
3 -> 6: 0.04796	3 <- 6: 0.01412	Net 3 -> 6: 0.03384
3 -> 7: 0.02239	3 <- 7: 0.00551	Net 3 -> 7: 0.01687
4 -> 5: 0.03440	4 <- 5: 0.01765	Net 4 -> 5: 0.01675
4 -> 6: 0.04328	4 <- 6: 0.00655	Net 4 -> 6: 0.03673
4 -> 7: 0.02020	4 <- 7: 0.00256	Net 4 -> 7: 0.01764
5 -> 6: 0.04802	5 <- 6: 0.01417	Net 5 -> 6: 0.03385
5 -> 7: 0.02241	5 <- 7: 0.00553	Net 5 -> 7: 0.01688
6 -> 7: 0.00832	6 <- 7: 0.00696	Net 6 -> 7: 0.00136

Table S1. Charge transfer between fragments of IT-4F

1 -> 2: 0.00728	1 <- 2: 0.00926	Net 1 -> 2: -0.00198
1 -> 3: 0.00543	1 <- 3: 0.02497	Net 1 -> 3: -0.01954
1 -> 4: 0.00191	1 <- 4: 0.02719	Net 1 -> 4: -0.02529
1 -> 5: 0.00223	1 <- 5: 0.04027	Net 1 -> 5: -0.03804
1 -> 6: 0.00302	1 <- 6: 0.01895	Net 1 -> 6: -0.01592
1 -> 7: 0.00130	1 <- 7: 0.00724	Net 1 -> 7: -0.00594
2 -> 3: 0.01427	2 <- 3: 0.05161	Net 2 -> 3: -0.03734
2 -> 4: 0.00501	2 <- 4: 0.05620	Net 2 -> 4: -0.05119
2 -> 5: 0.00587	2 <- 5: 0.08324	Net 2 -> 5: -0.07737
2 -> 6: 0.00795	2 <- 6: 0.03916	Net 2 -> 6: -0.03121
2 -> 7: 0.00342	2 <- 7: 0.01497	Net 2 -> 7: -0.01155
3 -> 4: 0.01351	3 <- 4: 0.04190	Net 3 -> 4: -0.02839
3 -> 5: 0.01582	3 <- 5: 0.06205	Net 3 -> 5: -0.04623
3 -> 6: 0.02143	3 <- 6: 0.02919	Net 3 -> 6: -0.00777
3 -> 7: 0.00922	3 <- 7: 0.01116	Net 3 -> 7: -0.00194
4 -> 5: 0.01723	4 <- 5: 0.02179	Net 4 -> 5: -0.00455
4 -> 6: 0.02333	4 <- 6: 0.01025	Net 4 -> 6: 0.01308
4 -> 7: 0.01005	4 <- 7: 0.00392	Net 4 -> 7: 0.00613
5 -> 6: 0.03456	5 <- 6: 0.01201	Net 5 -> 6: 0.02255
5 -> 7: 0.01488	5 <- 7: 0.00459	Net 5 -> 7: 0.01029
6 -> 7: 0.00700	6 <- 7: 0.00622	Net 6 -> 7: 0.00078

Table S2. Charge transfer between fragments of PTBTT-4F

1 -> 2:	0.00855	1 <- 2:	0.01072	Net 1 -> 2:	-0.00217
1 -> 3:	0.00557	1 <- 3:	0.02257	Net 1 -> 3:	-0.01700
1 -> 4:	0.00327	1 <- 4:	0.01862	Net 1 -> 4:	-0.01534
1 -> 5:	0.00557	1 <- 5:	0.02260	Net 1 -> 5:	-0.01703
1 -> 6:	0.00852	1 <- 6:	0.01073	Net 1 -> 6:	-0.00221
1 -> 7:	0.00402	1 <- 7:	0.00404	Net 1 -> 7:	-0.00002
2 -> 3:	0.01481	2 <- 3:	0.04783	Net 2 -> 3:	-0.03302
2 -> 4:	0.00870	2 <- 4:	0.03944	Net 2 -> 4:	-0.03075
2 -> 5:	0.01479	2 <- 5:	0.04787	Net 2 -> 5:	-0.03309
2 -> 6:	0.02265	2 <- 6:	0.02274	Net 2 -> 6:	-0.00009
2 -> 7:	0.01068	2 <- 7:	0.00856	Net 2 -> 7:	0.00212
3 -> 4:	0.01832	3 <- 4:	0.02573	Net 3 -> 4:	-0.00741
3 -> 5:	0.03115	3 <- 5:	0.03123	Net 3 -> 5:	-0.00008
3 -> 6:	0.04770	3 <- 6:	0.01483	Net 3 -> 6:	0.03287
3 -> 7:	0.02249	3 <- 7:	0.00558	Net 3 -> 7:	0.01691
4 -> 5:	0.02569	4 <- 5:	0.01834	Net 4 -> 5:	0.00735
4 -> 6:	0.03934	4 <- 6:	0.00871	Net 4 -> 6:	0.03063
4 -> 7:	0.01855	4 <- 7:	0.00328	Net 4 -> 7:	0.01527
5 -> 6:	0.04774	5 <- 6:	0.01481	Net 5 -> 6:	0.03294
5 -> 7:	0.02251	5 <- 7:	0.00557	Net 5 -> 7:	0.01694
6 -> 7:	0.01069	6 <- 7:	0.00854	Net 6 -> 7:	0.00216

Table S3. Charge transfer between fragments of PTBTP-4F

1 -> 2: 0.00739	1 <- 2: 0.00819	Net 1 -> 2: -0.00080
1 -> 3: 0.00589	1 <- 3: 0.02159	Net 1 -> 3: -0.01569
1 -> 4: 0.00270	1 <- 4: 0.01960	Net 1 -> 4: -0.01690
1 -> 5: 0.00589	1 <- 5: 0.02159	Net 1 -> 5: -0.01569
1 -> 6: 0.00739	1 <- 6: 0.00819	Net 1 -> 6: -0.00080
1 -> 7: 0.00336	1 <- 7: 0.00336	Net 1 -> 7: -0.00000
2 -> 3: 0.01436	2 <- 3: 0.04750	Net 2 -> 3: -0.03313
2 -> 4: 0.00657	2 <- 4: 0.04312	Net 2 -> 4: -0.03655
2 -> 5: 0.01436	2 <- 5: 0.04750	Net 2 -> 5: -0.03314
2 -> 6: 0.01801	2 <- 6: 0.01802	Net 2 -> 6: -0.00000
2 -> 7: 0.00819	2 <- 7: 0.00739	Net 2 -> 7: 0.00079
3 -> 4: 0.01732	3 <- 4: 0.03438	Net 3 -> 4: -0.01706
3 -> 5: 0.03787	3 <- 5: 0.03787	Net 3 -> 5: -0.00000
3 -> 6: 0.04750	3 <- 6: 0.01436	Net 3 -> 6: 0.03313
3 -> 7: 0.02158	3 <- 7: 0.00589	Net 3 -> 7: 0.01569
4 -> 5: 0.03438	4 <- 5: 0.01733	Net 4 -> 5: 0.01705
4 -> 6: 0.04312	4 <- 6: 0.00657	Net 4 -> 6: 0.03655
4 -> 7: 0.01960	4 <- 7: 0.00270	Net 4 -> 7: 0.01690
5 -> 6: 0.04750	5 <- 6: 0.01436	Net 5 -> 6: 0.03313
5 -> 7: 0.02158	5 <- 7: 0.00589	Net 5 -> 7: 0.01569
6 -> 7: 0.00819	6 <- 7: 0.00739	Net 6 -> 7: 0.00079

Table S4. Charge transfer between fragments of IT-4Cl

1 -> 2:	0.00773	1 <- 2:	0.00935	Net 1 -> 2:	-0.00162
1 -> 3:	0.00627	1 <- 3:	0.02917	Net 1 -> 3:	-0.02291
1 -> 4:	0.00198	1 <- 4:	0.02682	Net 1 -> 4:	-0.02484
1 -> 5:	0.00238	1 <- 5:	0.03914	Net 1 -> 5:	-0.03676
1 -> 6:	0.00326	1 <- 6:	0.01884	Net 1 -> 6:	-0.01558
1 -> 7:	0.00140	1 <- 7:	0.00769	Net 1 -> 7:	-0.00629
2 -> 3:	0.01583	2 <- 3:	0.06095	Net 2 -> 3:	-0.04511
2 -> 4:	0.00501	2 <- 4:	0.05602	Net 2 -> 4:	-0.05102
2 -> 5:	0.00601	2 <- 5:	0.08177	Net 2 -> 5:	-0.07576
2 -> 6:	0.00824	2 <- 6:	0.03936	Net 2 -> 6:	-0.03112
2 -> 7:	0.00354	2 <- 7:	0.01607	Net 2 -> 7:	-0.01252
3 -> 4:	0.01562	3 <- 4:	0.04544	Net 3 -> 4:	-0.02981
3 -> 5:	0.01877	3 <- 5:	0.06632	Net 3 -> 5:	-0.04754
3 -> 6:	0.02572	3 <- 6:	0.03192	Net 3 -> 6:	-0.00620
3 -> 7:	0.01106	3 <- 7:	0.01303	Net 3 -> 7:	-0.00197
4 -> 5:	0.01726	4 <- 5:	0.02096	Net 4 -> 5:	-0.00371
4 -> 6:	0.02364	4 <- 6:	0.01009	Net 4 -> 6:	0.01355
4 -> 7:	0.01017	4 <- 7:	0.00412	Net 4 -> 7:	0.00605
5 -> 6:	0.03450	5 <- 6:	0.01212	Net 5 -> 6:	0.02238
5 -> 7:	0.01484	5 <- 7:	0.00495	Net 5 -> 7:	0.00989
6 -> 7:	0.00714	6 <- 7:	0.00678	Net 6 -> 7:	0.00036

Table S5. Charge transfer between fragments of PTBTT-4Cl

1 -> 2:	0.00914	1 <- 2:	0.01051	Net 1 -> 2:	-0.00137
1 -> 3:	0.00600	1 <- 3:	0.02188	Net 1 -> 3:	-0.01588
1 -> 4:	0.00347	1 <- 4:	0.01836	Net 1 -> 4:	-0.01489
1 -> 5:	0.00600	1 <- 5:	0.02188	Net 1 -> 5:	-0.01587
1 -> 6:	0.00914	1 <- 6:	0.01050	Net 1 -> 6:	-0.00136
1 -> 7:	0.00424	1 <- 7:	0.00424	Net 1 -> 7:	0.00000
2 -> 3:	0.01488	2 <- 3:	0.04718	Net 2 -> 3:	-0.03230
2 -> 4:	0.00860	2 <- 4:	0.03958	Net 2 -> 4:	-0.03099
2 -> 5:	0.01488	2 <- 5:	0.04717	Net 2 -> 5:	-0.03228
2 -> 6:	0.02266	2 <- 6:	0.02264	Net 2 -> 6:	0.00002
2 -> 7:	0.01051	2 <- 7:	0.00914	Net 2 -> 7:	0.00138
3 -> 4:	0.01791	3 <- 4:	0.02600	Net 3 -> 4:	-0.00810
3 -> 5:	0.03100	3 <- 5:	0.03099	Net 3 -> 5:	0.00001
3 -> 6:	0.04720	3 <- 6:	0.01488	Net 3 -> 6:	0.03233
3 -> 7:	0.02189	3 <- 7:	0.00600	Net 3 -> 7:	0.01589
4 -> 5:	0.02601	4 <- 5:	0.01790	Net 4 -> 5:	0.00811
4 -> 6:	0.03961	4 <- 6:	0.00859	Net 4 -> 6:	0.03101
4 -> 7:	0.01837	4 <- 7:	0.00347	Net 4 -> 7:	0.01490
5 -> 6:	0.04719	5 <- 6:	0.01488	Net 5 -> 6:	0.03231
5 -> 7:	0.02189	5 <- 7:	0.00600	Net 5 -> 7:	0.01589
6 -> 7:	0.01051	6 <- 7:	0.00914	Net 6 -> 7:	0.00137

Table S6. Charge transfer between fragments of PTBTP-4Cl

Appendix III

I.a Materials and Synthesis

All commercially available chemicals and solvents were purchased from Energy-Chemical, Sigma-Aldrich, or J&K Chemical Co., and used without further purification. Moreover, polymer donor PBDB-TF, 2-(5,6-difluoro-3-oxo-2,3-dihydro-1H-inden-1-ylidene) malononitrile and 2-(5,6-dichloro-3-oxo-2,3-dihydro-1H-inden-1-ylidene) malononitrile were purchased from Nanjing Zhiyan Technology Co. Ltd.. In addition, PDINN was purchased from SunaTech Inc.. PTBTT-4F/4Cl were synthesized according to previous work. The detailed synthetic processes of TPBTT-4F and TPBTT-4Cl are described in the following.

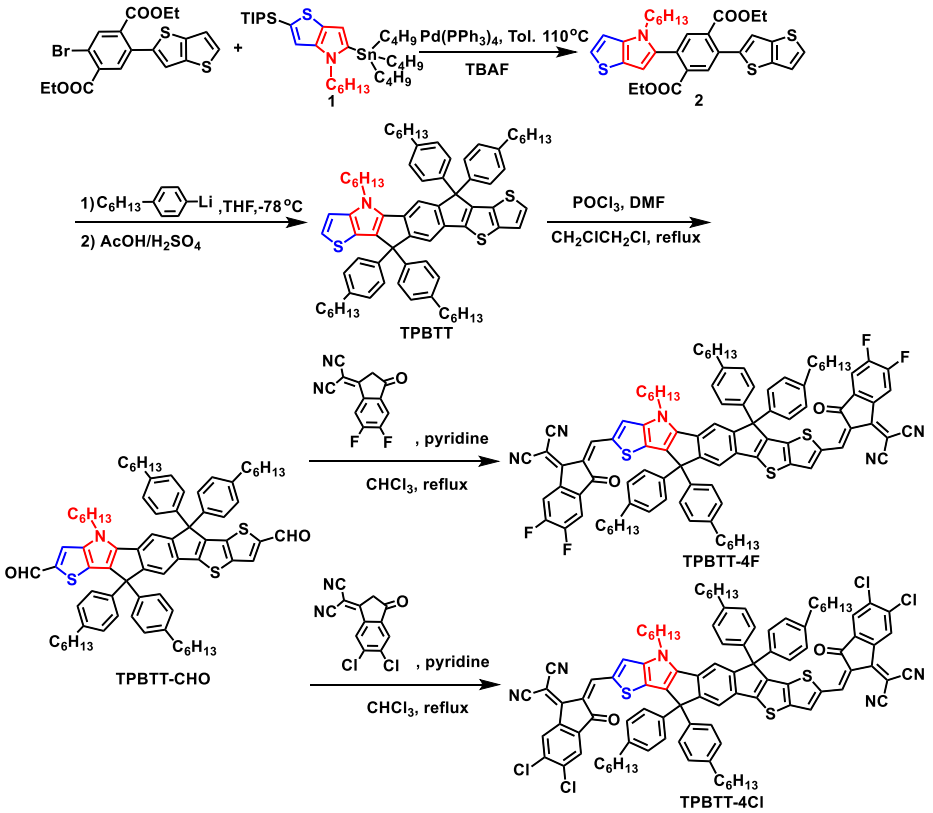

Scheme S1. Synthesis routes of TPBTT-4F and TPBTT-4Cl

*Synthesis of **TPBTT-CHO***

To a solution of **TPBTT** (260 mg, 0.24 mmol) in dry 1,2-dichloroethane (15 mL) and DMF (2 mL) was stirred and introduced with phosphorus oxychloride (0.3 mL) at 0 °C. Then the mixture reacted under N_2 for 12 hours and was subsequently neutralized with Na_2CO_3 solution, followed by stirring for 30 mins. The solution was then extracted with dichloromethane twice (100 mL × 2) and washed with brine twice (50 mL × 2). The organic layer was concentrated to yield the crude product. Finally, the product was purified by column chromatography (flash silica gel, petroleum ether/ dichloromethane 2:1) to afford **TPBTT-CHO** (241 mg, 0.21 mmol, 88.2%) as an orange solid. ^{1}H NMR (500 MHz, $CDCl_3$) δ 9.85 (s, 1H), 9.80 (s, 1H), 7.63 (s, 1H), 7.54 (d, *J* = 16.5 Hz, 2H), 7.45 (s, 1H), 7.31 (d, *J* = 8.5 Hz, 4H), 7.20 – 7.03 (m, 12H), 3.82 – 3.71 (m, 2H), 2.66 – 2.50 (m, 8H), 1.63 – 1.56 (m, 8H), 1.30 (dqd, *J* = 10.5, 7.0, 4.5, 3.5 Hz, 24H), 1.17 (q, *J* = 7.5 Hz, 2H), 1.03 (ddd, *J* = 30.5, 15.5, 7.5 Hz, 4H), 0.93 – 0.80 (m, 17H). ^{13}C NMR (125 MHz, $CDCl_3$) δ 182.84, 182.76, 142.31, 142.03, 140.83, 137.58, 132.19, 128.55, 128.54, 127.70, 117.77, 116.74, 77.27, 76.77, 48.35, 35.54, 35.50, 31.70, 31.68, 31.41, 31.33, 31.26, 30.38, 29.14, 29.11, 26.48, 22.59, 22.57, 14.11, 14.09, 14.05. HRMS (ESI) *m/z*: $[M+H]^+$ calculated for $C_{76}H_{87}NO_2S_3^+$, 1142.7170; found, 1142.6049.

*Compound **TPBTT-4F***

The mixture of **TPBTT-CHO** (120 mg, 0.11 mmol), 2-(5,6-difluoro-3-oxo-2,3-dihydro-1H-inden-1-ylidene)malononitrile (120 mg, 0.52 mmol) and pyridine (0.2 mL) were dissolved in dry $CHCl_3$ (20 mL). The mixture was stirred and refluxed for 8 hours. The mixture was poured into methanol (150 mL) and filtered to obtain the residue. The residue was then purified by column chromatography on silica gel using petroleum ether/dichloromethane (1:2, v/v) as the eluent. Compound **TPBTT-4F** (113 mg, 0.07 mmol, 68.7%) was obtained as a dark blue solid. ^{1}H NMR (500 MHz, $CDCl_3$) δ 8.86 (s, 2H), 8.51 (ddd, *J* = 19.0, 10.0, 6.5 Hz, 2H), 7.68 (s, 2H), 7.64 (dt, *J* = 10.0, 7.5 Hz, 3H), 7.50 (s, 1H), 7.30 (d, *J* = 8.5 Hz, 4H), 7.18 – 7.08 (m, 12H), 3.81 – 3.74 (m, 2H), 2.59 (q, *J* = 7.0 Hz, 8H), 1.59 (dq, *J* = 10.5, 4.5, 3.0 Hz, 8H), 1.38 – 1.26 (m, 24H), 1.19 (q, *J* = 7.5 Hz, 2H), 1.14 – 1.08 (m, 2H), 1.04 – 0.98 (m, 2H), 0.87 (td, *J* = 8.5, 7.5, 5.5 Hz, 17H). ^{13}C NMR (125 MHz, $CDCl_3$) δ 186.07, 185.88, 160.84,

158.44, 157.82, 156.52, 150.51, 147.32, 146.73, 142.77, 142.39, 140.65, 140.55, 140.28, 140.07, 138.70, 138.63, 138.45, 136.97, 135.36, 128.78, 128.76, 128.47, 127.73, 120.87, 120.25, 118.80, 117.53, 114.99, 114.88, 114.31, 114.22, 112.25, 67.32, 62.96, 62.65, 48.57, 35.57, 31.71, 31.69, 31.38, 31.30, 31.24, 30.37, 29.14, 29.11, 26.44, 22.63, 22.59, 22.58, 14.09, 14.07, 14.02. HRMS (ESI) *m/z*: $[M+H]^+$ calcd for $C_{100}H_{91}F_4N_5O_2S_3^+$, 1567.0346; found, 1566.6397.

*Compound **TPBTT-4Cl***

The mixture of **TPBTT-CHO** (100 mg, 0.09 mmol), 2-(5,6-dichloro-3-oxo-2,3-dihydro-1H-inden-1-ylidene)malononitrile (100 mg, 0.38 mmol) and pyridine (0.2 mL) were dissolved in dry $CHCl_3$ (20 mL). The mixture was stirred and refluxed for 8 hours. The mixture was poured into methanol (120 mL) and filtered to get the residue. Then the residue was purified by column chromatography on silica gel using petroleum ether/dichloromethane (1:2, v/v) as the eluent. Compound **TPBTT-4Cl** (102 mg, 0.06 mmol, 71.4%) was obtained as a dark-blue solid. ^{1}H NMR (500 MHz, $CDCl_3$) δ 8.87 (s, 1H), 8.82 (s, 1H), 8.75 (s, 1H), 8.65 (s, 1H), 7.89 (s, 1H), 7.84 (s, 1H), 7.70 (d, *J* = 5.0 Hz, 2H), 7.51 (s, 1H), 7.32 (d, *J* = 8.5 Hz, 4H), 7.26 (s, 1H), 7.14 (dd, *J* = 13.5, 7.5 Hz, 12H), 3.78 (s, 2H), 2.59 (q, *J* = 8.0 Hz, 8H), 1.65 – 1.57 (m, 8H), 1.40 – 1.27 (m, 24H), 1.22 – 1.17 (m, 2H), 1.13 (dt, *J* = 16.0, 7.5 Hz, 2H), 1.06 – 0.99 (m, 2H), 0.87 (td, *J* = 6.5, 3.6 Hz, 17H). ^{13}C NMR (125 MHz, $CDCl_3$) δ 161.45, 158.64, 158.55, 158.12, 156.77, 151.10, 142.93, 142.54, 141.10, 140.71, 140.36, 139.29, 139.08, 138.93, 138.86, 138.80, 138.76, 137.05, 136.89, 136.16, 135.57, 128.93, 128.90, 128.61, 127.86, 127.10, 126.73, 125.22, 124.89, 120.98, 119.03, 117.75, 114.43, 69.56, 67.43, 63.09, 62.80, 48.73, 35.70, 35.67, 31.84, 31.82, 31.50, 31.43, 31.38, 30.49, 29.28, 29.23, 26.58, 22.77, 22.72, 22.71, 14.22, 14.21, 14.16. HRMS (ESI) *m/z*: $[M+H]^+$ calcd for $C_{100}H_{91}Cl_4N_5O_2S_3^+$, 1632.8410; found, 1634.5220.

I.b NMR data

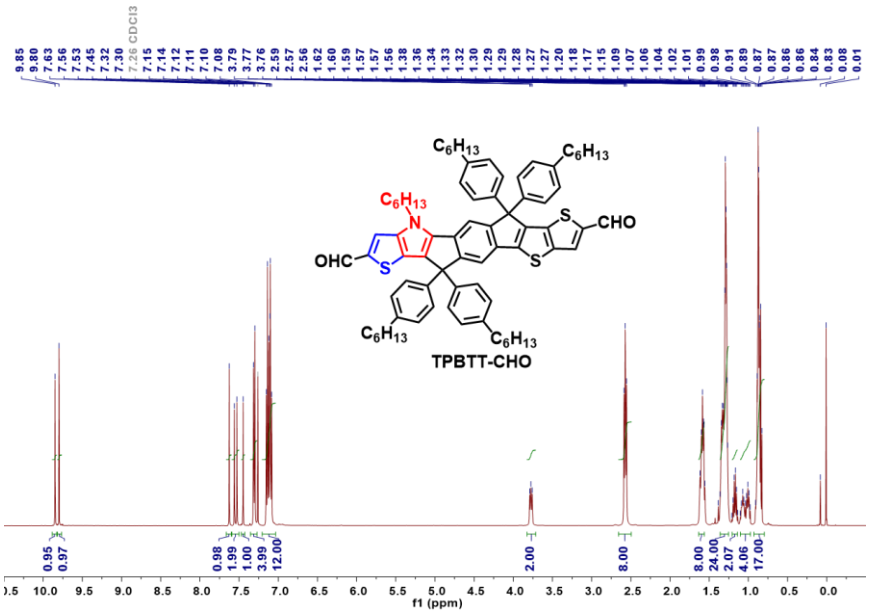

Figure S1. ^{1}H NMR of **TPBTT-CHO**

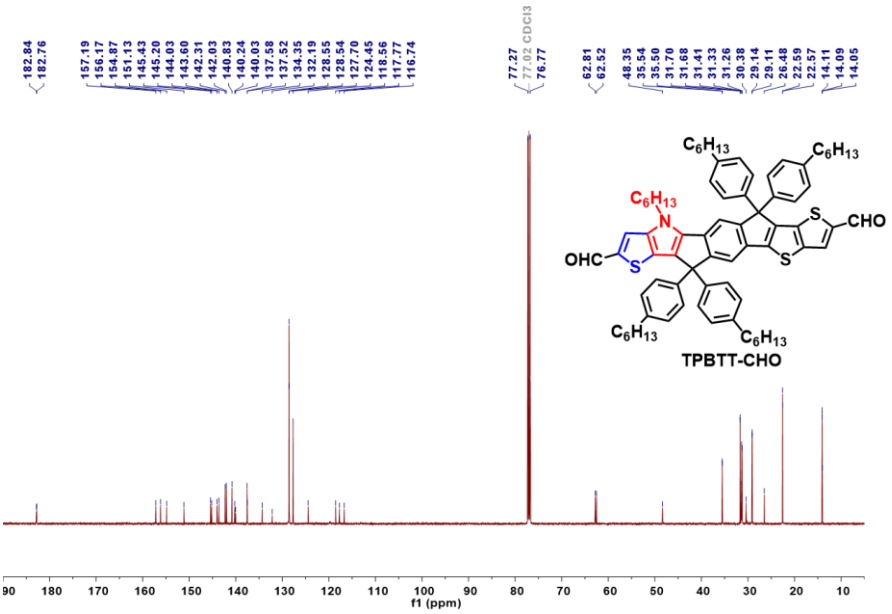

Figure S2. ^{13}C NMR of **TPBTT-CHO**

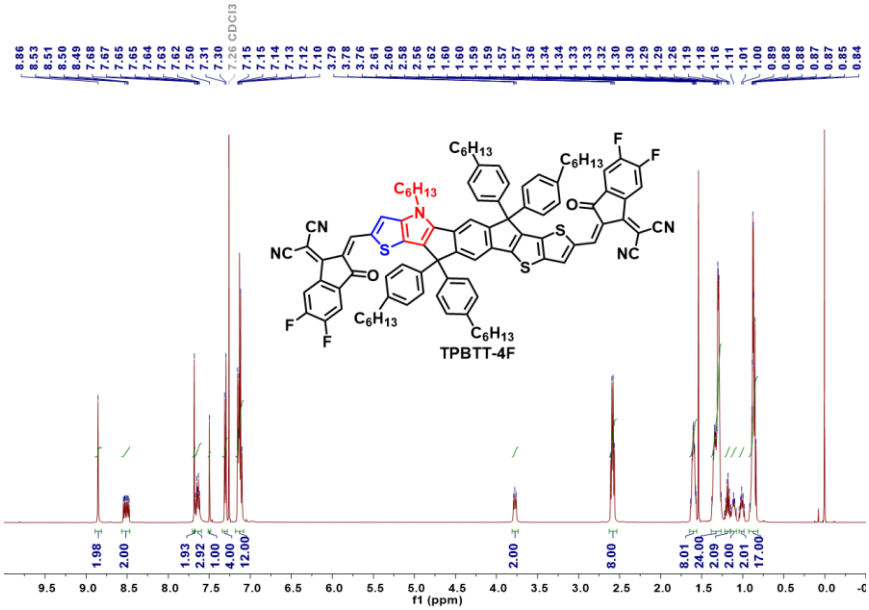

Figure S3. ^{1}H NMR of **TPBTT-4F**

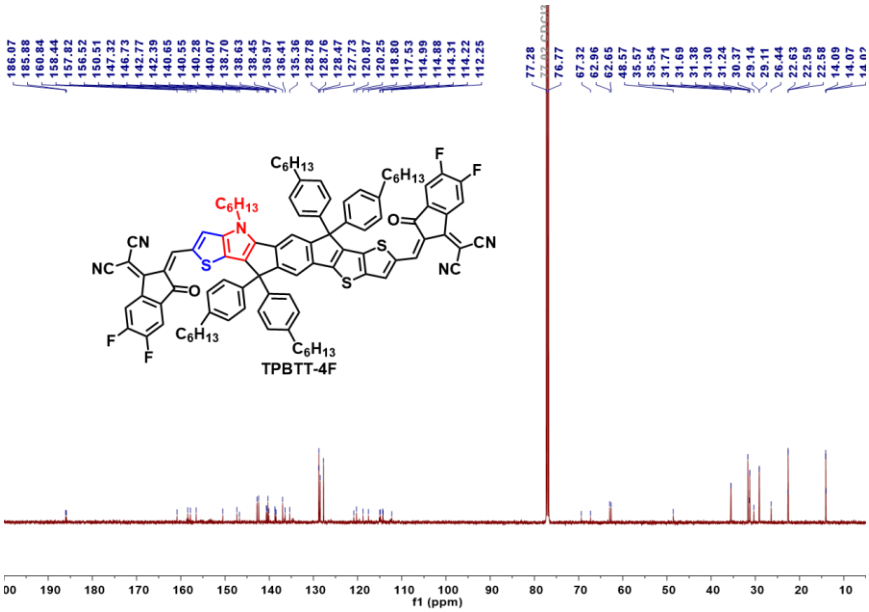

Figure S4. ^{13}C NMR of **TPBTT-4F**

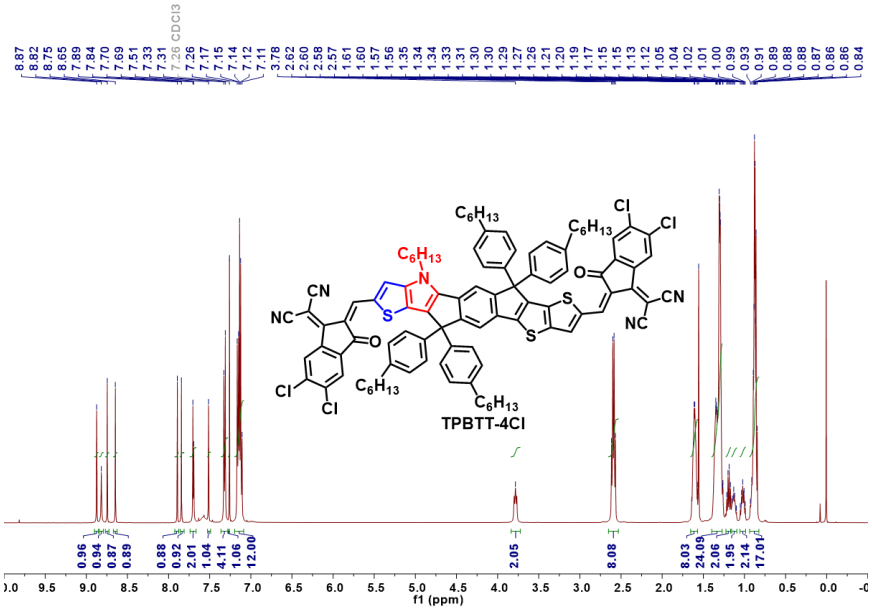

Figure S5. ^{1}H NMR of **TPBTT-4Cl**

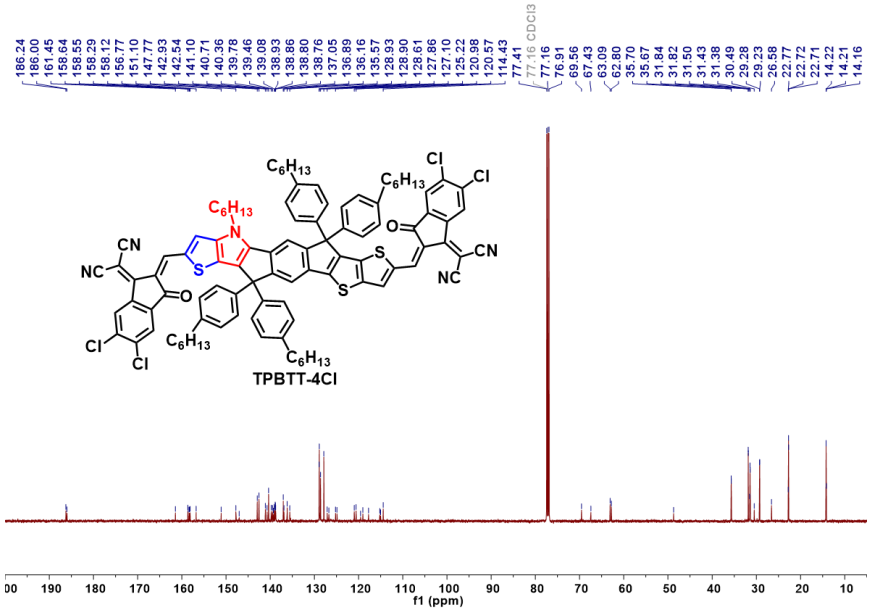

Figure S6. ^{13}C NMR of **TPBTT-4Cl**

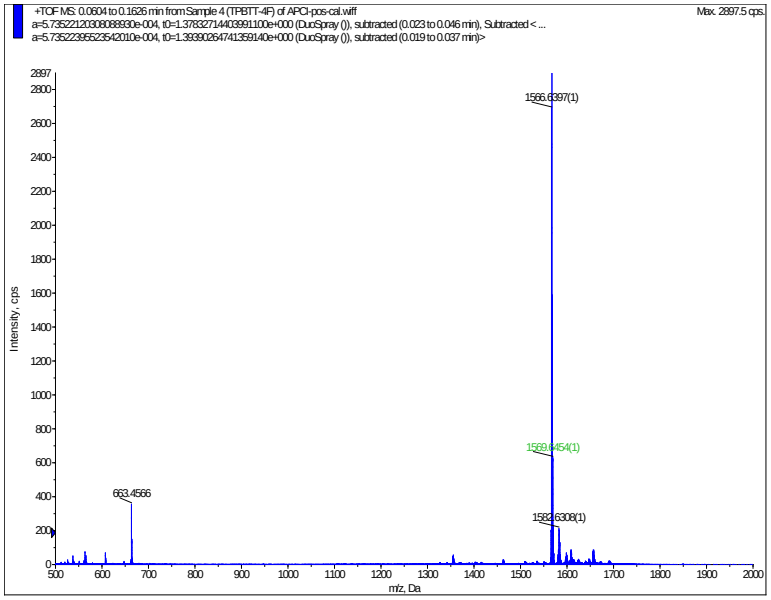

Figure S7. Mass spectra of **TPBTT-4F**

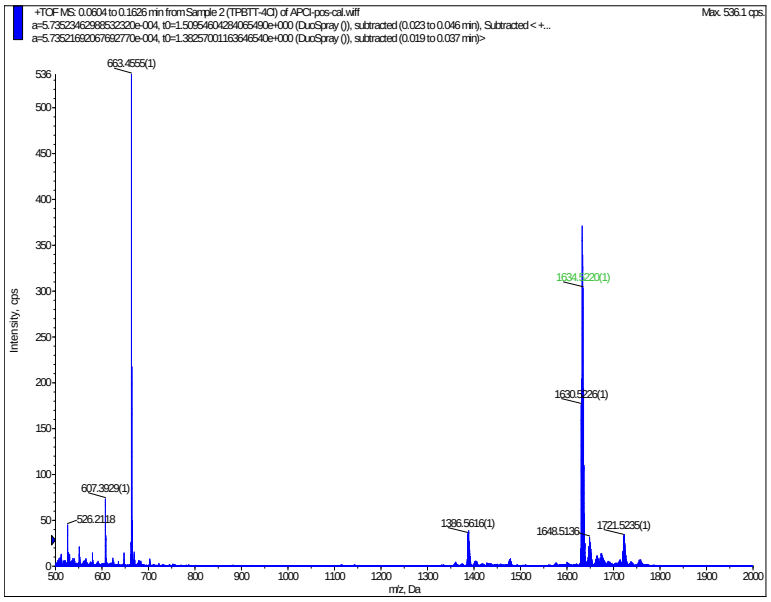

Figure S8. Mass spectra of **TPBTT-4Cl**

References

Amorim, C.A. *et al.* (2012) 'Determination of carrier mobility in MEH-PPV thin-films by stationary and transient current techniques'. *Journal of Non-Crystalline Solids,* 358 (3), pp. 484-491.

Bakulin, A.A. *et al.* (2012) 'The Role of Driving Energy and Delocalized States for Charge Separation in Organic Semiconductors'. *Science,* 335 (6074), pp. 1340-1344.

Bi, P. *et al.* (2023) 'Enhancing Photon Utilization Efficiency for High-Performance Organic Photovoltaic Cells via Regulating Phase-Transition Kinetics'. *Advanced Materials,* 35 (16), pp. 2210865.

Bi, P. *et al.* (2021) 'Reduced non-radiative charge recombination enables organic photovoltaic cell approaching 19% efficiency'. *Joule,* 5 (9), pp. 2408-2419.

Bin, H. *et al.* (2016a) '11.4% Efficiency non-fullerene polymer solar cells with trialkylsilyl substituted 2D-conjugated polymer as donor'. *Nature Communications,* 7 (1), pp. 13651.

Bin, H. *et al.* (2016b) 'Non-Fullerene Polymer Solar Cells Based on Alkylthio and Fluorine Substituted 2D-Conjugated Polymers Reach 9.5% Efficiency'. *Journal of the American Chemical Society,* 138 (13), pp. 4657-4664.

Cai, G. *et al.* (2019) 'High-Performance Mid-Bandgap Fused-Pyrene Electron Acceptor'. *Chemistry of Materials,* 31 (17), pp. 6484-6490.

Cai, J. *et al.* (2021) 'Asymmetric and Halogenated Fused-Ring Electron Acceptor for Efficient Organic Solar Cells'. *Advanced Functional Materials,* pp. 2102189.

Cao, J. *et al.* (2020) 'An asymmetric acceptor enabling 77.51% fill factor in organic solar cells'. *Science Bulletin,* pp. 65.

Cao, T. *et al.* (2017) 'Towards a full understanding of regioisomer effects of indene-C60 bisadduct acceptors in bulk heterojunction polymer solar cells'. *Journal of Materials Chemistry A,* 5 (21), pp. 10206-10219.

Chatterjee, S., Jinnai, S. and Ie, Y. (2021) 'Nonfullerene acceptors for P3HT-based organic solar cells'. *Journal of Materials Chemistry A,* 9 (35), pp. 18857-18886.

Chen, L. *et al.* (2019) 'Polyoxometalates in dye-sensitized solar cells'. *Chemical Society Reviews,* 48 (1), pp. 260-284.

Chen, S. *et al.* (2015) 'Self-Assembly of Perylene Imide Molecules into 1D Nanostructures: Methods, Morphologies, and Applications'. *Chemical Reviews,* 115 (21), pp. 11967-11998.

Chen, T.-W. *et al.* (2020a) 'A chlorinated nonacyclic carbazole-based acceptor affords over 15% efficiency in organic solar cells'. *Journal of Materials Chemistry A,* 8 (3), pp. 1131-1137.

Chen, Y. *et al.* (2020b) 'Asymmetric Alkoxy and Alkyl Substitution on Nonfullerene Acceptors Enabling High-Performance Organic Solar Cells'. *Advanced Energy Materials,* 11 (3), pp. 2003141.

Cui, C. and Li, Y. (2019) 'High-performance conjugated polymer donor materials for polymer solar cells with narrow-bandgap nonfullerene acceptors'. *Energy & Environmental Science,* 12 (11), pp. 3225-3246.
Cui, Y. *et al.* (2020a) 'Organic photovoltaic cell with 17% efficiency and superior processability'. *National Science Review,* 7 (7), pp. 1239-1246.
Cui, Y. *et al.* (2020b) 'Single-Junction Organic Photovoltaic Cells with Approaching 18% Efficiency'. *Adv Mater,* 32 (19), pp. e1908205.
Dai, S. *et al.* (2018a) 'Enhancing the Performance of Polymer Solar Cells via Core Engineering of NIR-Absorbing Electron Acceptors'. *Advanced Materials,* 30 (15), pp. 1706571.
Dai, S. *et al.* (2018b) 'Effect of Core Size on Performance of Fused-Ring Electron Acceptors'. *Chemistry of Materials,* 30 (15), pp. 5390-5396.
Dai, S. and Zhan, X. (2018) 'Nonfullerene Acceptors for Semitransparent Organic Solar Cells'. *Advanced Energy Materials,* 8 (21), pp. 1800002.
Deibel, C., Strobel, T. and Dyakonov, V. (2010) 'Role of the Charge Transfer State in Organic Donor-Acceptor Solar Cells'. *Adv Mater,* 22 (37), pp. 4097-4111.
Dou, L. *et al.* (2013) '25th Anniversary Article: A Decade of Organic/Polymeric Photovoltaic Research'. *Adv Mater,* 25 (46), pp. 6642-6671.
Duijnstee, E.A. *et al.* (2020) 'Toward Understanding Space-Charge Limited Current Measurements on Metal Halide Perovskites'. *ACS Energy Letters,* 5 (2), pp. 376-384.
Eisner, F.D. *et al.* (2019) 'Hybridization of Local Exciton and Charge-Transfer States Reduces Nonradiative Voltage Losses in Organic Solar Cells'. *J Am Chem Soc,* 141 (15), pp. 6362-6374.
Elumalai, N.K. and Uddin, A. (2016) 'Open circuit voltage of organic solar cells: an in-depth review'. *Energy & Environmental Science,* 9 (2), pp. 391-410.
Faist, M.A. *et al.* (2012) 'Competition between the charge transfer state and the singlet states of donor or acceptor limiting the efficiency in polymer:fullerene solar cells'. *J Am Chem Soc,* 134 (1), pp. 685-692.
Fei, Z. *et al.* (2018) 'An Alkylated Indacenodithieno[3,2-b]thiophene-Based Nonfullerene Acceptor with High Crystallinity Exhibiting Single Junction Solar Cell Efficiencies Greater than 13% with Low Voltage Losses'. *Adv Mater,* 30 (8), pp. 1705209.
Feng, W. *et al.* (2022) 'Tuning Morphology of Active Layer by using a Wide Bandgap Oligomer-Like Donor Enables Organic Solar Cells with Over 18% Efficiency'. *Advanced Energy Materials,* 12 (16), pp. 2104060.
Frisch, M.J. *et al.* (2009) 'Gaussian 09 Revision A.1. Gaussian Inc'.
Gao, B. *et al.* (2018a) 'Multi-component non-fullerene acceptors with tunable bandgap structures for efficient organic solar cells'. *Journal of Materials Chemistry A,* 6 (46), pp. 23644-23649.
Gao, W. *et al.* (2020) 'Asymmetric Acceptors Enabling Organic Solar Cells to Achieve an over 17% Efficiency: Conformation Effects on Regulating Molecular Properties and Suppressing Nonradiative Energy Loss'. *Advanced Energy Materials,* 11 (4), pp. 2003177.
Gao, W. *et al.* (2018b) 'Asymmetrical Small Molecule Acceptor Enabling Nonfullerene Polymer Solar Cell with Fill Factor Approaching 79%'. *ACS Energy Letters,* 3 (7), pp. 1760-1768.
Gao, W. *et al.* (2018c) 'Asymmetrical Ladder-Type Donor-Induced Polar Small Molecule Acceptor to Promote Fill Factors Approaching 77% for High-

Performance Nonfullerene Polymer Solar Cells'. *Advanced Materials,* 30 (26), pp. 1800052.
Goh, C. *et al.* (2005) 'Molecular-weight-dependent mobilities in regioregular poly(3-hexyl-thiophene) diodes'. *Applied Physics Letters,* 86 (12), pp. 122110.
Guillemoles, J.-F. *et al.* (2019) 'Guide for the perplexed to the Shockley–Queisser model for solar cells'. *Nature Photonics,* 13 (8), pp. 501-505.
Guo, J. *et al.* 'Miscibility Regulation and Thermal Annealing Induced Hierarchical Morphology Enables High-Efficiency All-Small-Molecule Organic Solar Cells Over 17%'. *Advanced Energy Materials,* 13 (25), pp. 2300481.
Hao, M. *et al.* (2019) 'Achieving Balanced Charge Transport and Favorable Blend Morphology in Non-Fullerene Solar Cells via Acceptor End Group Modification'. *Chemistry of Materials,* 31 (5), pp. 1752-1760.
Haugeneder, A. *et al.* (1999) 'Exciton diffusion and dissociation in conjugated polymer/fullerene blends and heterostructures'. *Physical Review B,* 59 (23), pp. 15346-15351.
He, C. *et al.* (2022) 'Manipulating the D:A interfacial energetics and intermolecular packing for 19.2% efficiency organic photovoltaics'. *Energy & Environmental Science,* 15 (6), pp. 2537-2544.
Heeger, A.J. (2014) '25th Anniversary Article: Bulk Heterojunction Solar Cells: Understanding the Mechanism of Operation'. *Advanced Materials,* 26 (1), pp. 10-28.
Hodgkiss, J.M. (2021) 'No free lunch for non-fullerene acceptors'. *Nat Mater,* 20 (3), pp. 289-290.
Hong, L. *et al.* (2019) 'Eco-Compatible Solvent-Processed Organic Photovoltaic Cells with Over 16% Efficiency'. *Adv Mater,* 31 (39), pp. e1903441.
Hou, J. *et al.* (2018) 'Organic solar cells based on non-fullerene acceptors'. *Nature Materials,* 17 (2), pp. 119-128.
Hu, Z. *et al.* (2020) 'A critical review on semitransparent organic solar cells'. *Nano Energy,* 78, pp. 105376.
Huang, C. *et al.* (2018) 'Highly Efficient Organic Solar Cells Based on S,N-Heteroacene Non-Fullerene Acceptors'. *Chemistry of Materials,* 30 (15), pp. 5429-5434.
Huang, F. *et al.* (2023) 'Atomic Optimization on Pyran-Fused Nonfullerene Acceptor Enables Organic Solar Cells With an Efficiency Approaching 16% and Reduced Energy Loss'. *Advanced Functional Materials,* 33 (4), pp. 2211140.
Huang, Y. *et al.* (2014) 'Bulk Heterojunction Solar Cells: Morphology and Performance Relationships'. *Chemical Reviews,* 114 (14), pp. 7006-7043.
Humphrey, W., Dalke, A. and Schulten, K. (1996) 'VMD: Visual molecular dynamics'. *Journal of Molecular Graphics,* 14 (1), pp. 33-38.
Jeon, I. *et al.* (2016) 'Room temperature-processed inverted organic solar cells using high working-pressure-sputtered ZnO films'. *Journal of Materials Chemistry A,* 4 (48), pp. 18763-18768.
Ji, L. *et al.* (2020) 'Air-Stable Organic Radicals: New-Generation Materials for Flexible Electronics?'. *Adv Mater,* 32 (32), pp. e1908015.
Jiang, K. *et al.* (2019) 'Alkyl Chain Tuning of Small Molecule Acceptors for Efficient Organic Solar Cells'. *Joule,* 3 (12), pp. 3020-3033.

Jiang, K. *et al.* (2022) 'Suppressed recombination loss in organic photovoltaics adopting a planar-mixed heterojunction architecture'. *Nature Energy,* 7 (11), pp. 1076-1086.
Jiang, L., Hirst, J.D. and Do, H. (2022) 'Structure-Property Relationships in Amorphous Thieno[3,2-b]thiophene-Diketopyrrolopyrrole-Thiophene-Containing Polymers'. *The Journal of Physical Chemistry C,* 126 (26), pp. 10842-10854.
Kaiser, C. *et al.* (2021) 'A universal Urbach rule for disordered organic semiconductors'. *Nature Communications,* 12 (1), pp. 3988.
Kan, B. *et al.* (2017) 'Small-Molecule Acceptor Based on the Heptacyclic Benzodi(cyclopentadithiophene) Unit for Highly Efficient Nonfullerene Organic Solar Cells'. *Journal of the American Chemical Society,* 139 (13), pp. 4929-4934.
Kim, K.-H. *et al.* (2012) 'Effects of Solubilizing Group Modification in Fullerene Bis-Adducts on Normal and Inverted Type Polymer Solar Cells'. *Chemistry of Materials,* 24 (12), pp. 2373-2381.
Kim, Y. *et al.* (2006) 'A strong regioregularity effect in self-organizing conjugated polymer films and high-efficiency polythiophene:fullerene solar cells'. *Nature Materials,* 5 (3), pp. 197-203.
Koo, D. *et al.* (2020) 'Flexible Organic Solar Cells Over 15% Efficiency with Polyimide-Integrated Graphene Electrodes'. *Joule,* 4 (5), pp. 1021-1034.
Kubota, Y. *et al.* (2019) 'Synthesis of near-infrared absorbing and fluorescing thiophene-fused BODIPY dyes with strong electron-donating groups and their application in dye-sensitised solar cells'. *New Journal of Chemistry,* 43 (3), pp. 1156-1165.
Lagalante, A.F. and Greenbacker, P.W. (2007) 'Flow injection analysis of imidacloprid in natural waters and agricultural matrixes by photochemical dissociation, chemical reduction, and nitric oxide chemiluminescence detection'. *Analytica Chimica Acta,* 590 (2), pp. 151-158.
Li, C. *et al.* (2019a) 'Asymmetric Nonfullerene Small Molecule Acceptors for Organic Solar Cells'. *Advanced Energy Materials,* 9 (25), pp. 1900999.
Li, C. *et al.* (2021a) 'Non-fullerene acceptors with branched side chains and improved molecular packing to exceed 18% efficiency in organic solar cells'. *Nature Energy,* 6 (6), pp. 605-613.
Li, G. *et al.* (2005) 'High-efficiency solution processable polymer photovoltaic cells by self-organization of polymer blends'. *Nature Materials,* 4 (11), pp. 864-868.
Li, G. *et al.* (2020) 'Novel Nitrogen-Containing Heterocyclic Non-Fullerene Acceptors for Organic PhotovoltaicCells: Different End-Capping Groups Leading to a Big Difference of Power Conversion Efficiencies'. *ACS Appl Mater Interfaces,* 12 (11), pp. 13068-13076.
Li, G. *et al.* (2021b) 'Systematic Merging of Nonfullerene Acceptor π-Extension and Tetrafluorination Strategies Affords Polymer Solar Cells with >16% Efficiency'. *Journal of the American Chemical Society,* 143 (16), pp. 6123-6139.
Li, N. *et al.* (2022a) 'Mapping structure heterogeneities and visualizing moisture degradation of perovskite films with nano-focus WAXS'. *Nature Communications,* 13 (1), pp. 6701.
Li, S. *et al.* (2017a) 'Efficient Organic Solar Cells with Non-Fullerene Acceptors'. *Small,* 13 (37), pp. 1701120.

Li, S. *et al.* (2016) 'Energy-Level Modulation of Small-Molecule Electron Acceptors to Achieve over 12% Efficiency in Polymer Solar Cells'. *Advanced Functional Materials,* 28 (42), pp. 9423-9429.
Li, S. *et al.* (2019b) 'Highly Efficient Fullerene-Free Organic Solar Cells Operate at Near Zero Highest Occupied Molecular Orbital Offsets'. *Journal of the American Chemical Society,* 141 (7), pp. 3073-3082.
Li, W. *et al.* (2018) 'A High-Efficiency Organic Solar Cell Enabled by the Strong Intramolecular Electron Push–Pull Effect of the Nonfullerene Acceptor'. 30 (16), pp. 1707170.
Li, X. *et al.* (2019c) 'Effects of Short‐Axis Alkoxy Substituents on Molecular Self‐Assembly and Photovoltaic Performance of Indacenodithiophene‐Based Acceptors'. *Advanced Functional Materials,* 30 (3), pp. 1906855.
Li, X. *et al.* (2022b) 'Additive-Induced Vertical Component Distribution Enables High-Performance Sequentially Cast Organic Solar Cells'. *ACS Applied Materials & Interfaces,* 14 (22), pp. 25842-25850.
Li, Y. *et al.* (2017b) 'High Efficiency Near-Infrared and Semitransparent Non-Fullerene Acceptor Organic Photovoltaic Cells'. *J Am Chem Soc,* 139 (47), pp. 17114-17119.
Liang, Y. *et al.* (2009) 'Development of New Semiconducting Polymers for High Performance Solar Cells'. *Journal of the American Chemical Society,* 131 (1), pp. 56-57.
Liang, Y. *et al.* (2022) 'Organic solar cells using oligomer acceptors for improved stability and efficiency'. *Nature Energy,* 7 (12), pp. 1180-1190.
Lin, F. *et al.* (2020) 'A Non-fullerene Acceptor with Enhanced Intermolecular π-Core Interaction for High-Performance Organic Solar Cells'. *Journal of the American Chemical Society,* 142 (36), pp. 15246-15251.
Lin, Y. *et al.* (2016a) 'Structure Evolution of Oligomer Fused-Ring Electron Acceptors toward High Efficiency of As-Cast Polymer Solar Cells'. *Advanced Energy Materials,* 6 (18), pp. 1600854.
Lin, Y. *et al.* (2015) 'An Electron Acceptor Challenging Fullerenes for Efficient Polymer Solar Cells'. *Advanced Materials,* 27 (7), pp. 1170-1174.
Lin, Y. and Zhan, X. (2015) 'Designing Efficient Non-Fullerene Acceptors by Tailoring Extended Fused-Rings with Electron-Deficient Groups'. *Advanced Energy Materials,* 5 (20), pp. 1501063.
Lin, Y. *et al.* (2016b) 'High-Performance Electron Acceptor with Thienyl Side Chains for Organic Photovoltaics'. *Journal of the American Chemical Society,* 138 (14), pp. 4955-4961.
Liu, D. *et al.* (2015) 'Highly Efficient Photovoltaic Polymers Based on Benzodithiophene and Quinoxaline with Deeper HOMO Levels'. *Macromolecules,* 48 (15), pp. 5172-5178.
Liu, J. *et al.* (2016) 'Fast charge separation in a non-fullerene organic solar cell with a small driving force'. *Nature Energy,* 1 (7), pp. 16089.
Liu, M. *et al.* (2017a) 'Quinoxaline-based conjugated polymers for polymer solar cells'. *Polymer Chemistry,* 8 (32), pp. 4613-4636.
Liu, Q. *et al.* (2020a) '18% Efficiency organic solar cells'. *Science Bulletin,* 65 (4), pp. 272-275.
Liu, Q. *et al.* (2017b) 'High open-circuit voltage and short-circuit current flexible polymer solar cells using ternary blends and ultrathin Ag-based transparent electrodes'. *Journal of Materials Chemistry A,* 5 (48), pp. 25476-25484.

Liu, S. *et al.* (2020b) 'High-efficiency organic solar cells with low non-radiative recombination loss and low energetic disorder'. *Nature Photonics,* 14 (5), pp. 300-305.
Liu, W. *et al.* (2021) 'Design of Near-Infrared Nonfullerene Acceptor with Ultralow Nonradiative Voltage Loss for High-Performance Semitransparent Ternary Organic Solar Cells'. *Angew Chem Int Ed Engl,* 61 (19), pp. e202116111.
Liu, Y. *et al.* (2023) 'The Electronic Disorder Landscape of Mixed Halide Perovskites'. *ACS Energy Letters,* 8 (1), pp. 250-258.
Liu, Y. *et al.* (2022a) 'Recent progress in organic solar cells (Part I material science)'. *Science China Chemistry,* 65 (2), pp. 224-268.
Liu, Y. *et al.* (2022b) 'Recent progress in organic solar cells (Part II device engineering)'. *Science China Chemistry,* 65 (8), pp. 1457-1497.
Liu, Y. *et al.* (2014) 'Aggregation and morphology control enables multiple cases of high-efficiency polymer solar cells'. *Nature Communications,* 5 (1), pp. 5293.
Lu, L. and Yu, L. (2014) 'Understanding Low Bandgap Polymer PTB7 and Optimizing Polymer Solar Cells Based on It'. *Advanced Materials,* 26 (26), pp. 4413-4430.
Lu, T. and Chen, F. (2012) 'Multiwfn: a multifunctional wavefunction analyzer'. *J Comput Chem,* 33 (5), pp. 580-592.
Luo, Z. *et al.* (2018) 'Fine-Tuning of Molecular Packing and Energy Level through Methyl Substitution Enabling Excellent Small Molecule Acceptors for Nonfullerene Polymer Solar Cells with Efficiency up to 12.54%'. *Advanced Materials,* 30 (9), pp. 1706124.
Luo, Z. *et al.* (2020) 'Isomerization Strategy of Nonfullerene Small-Molecule Acceptors for Organic Solar Cells'. *Advanced Functional Materials,* 30 (46), pp. 2004477.
Ma, W. *et al.* (2005) 'Thermally Stable, Efficient Polymer Solar Cells with Nanoscale Control of the Interpenetrating Network Morphology'. *Advanced Functional Materials,* 15 (10), pp. 1617-1622.
Mahesh, S. *et al.* (2020) 'Revealing the origin of voltage loss in mixed-halide perovskite solar cells'. *Energy & Environmental Science,* 13 (1), pp. 258-267.
Meng, D. *et al.* (2022) 'Near-Infrared Materials: The Turning Point of Organic Photovoltaics'. *Advanced Materials,* 34 (10), pp. 2107330.
Menke, S.M. *et al.* (2018) 'Order enables efficient electron-hole separation at an organic heterojunction with a small energy loss'. *Nature Communications,* 9 (1), pp. 277.
Muller-Buschbaum, P. (2014) 'The active layer morphology of organic solar cells probed with grazing incidence scattering techniques'. *Adv Mater,* 26 (46), pp. 7692-7709.
Nakano, K. *et al.* (2019) 'Anatomy of the energetic driving force for charge generation in organic solar cells'. *Nature Communications,* 10 (1), pp. 2520.
Nakano, K., Kaji, Y. and Tajima, K. (2021) 'Highly Sensitive Evaluation of Density of States in Molecular Semiconductors by Photoelectron Yield Spectroscopy in Air'. *ACS Applied Materials & Interfaces,* 13 (24), pp. 28574-28582.
Pan, L. *et al.* (2020) 'Efficient Organic Ternary Solar Cells Employing Narrow Band Gap Diketopyrrolopyrrole Polymers and Nonfullerene Acceptors'. *Chemistry of Materials,* 32 (17), pp. 7309-7317.

Pang, B. *et al.* 'Benzo[d]thiazole Based Wide Bandgap Donor Polymers Enable 19.54% Efficiency Organic Solar Cells Along with Desirable Batch-to-Batch Reproducibility and General Applicability'. *Advanced Materials,* 35 (21), pp. 2300631.
Patil, Y. and Misra, R. (2019) 'Rational molecular design towards NIR absorption: efficient diketopyrrolopyrrole derivatives for organic solar cells and photothermal therapy'. *Journal of Materials Chemistry C,* 7 (42), pp. 13020-13031.
Peng, X. *et al.* (2017) 'Perovskite and Organic Solar Cells Fabricated by Inkjet Printing: Progress and Prospects'. *Advanced Functional Materials,* 27 (41), pp. 1703704.
Potscavage, W.J., Jr., Sharma, A. and Kippelen, B. (2009) 'Critical Interfaces in Organic Solar Cells and Their Influence on the Open-Circuit Voltage'. *Accounts of Chemical Research,* 42 (11), pp. 1758-1767.
Price, S.C. *et al.* (2011) 'Fluorine Substituted Conjugated Polymer of Medium Band Gap Yields 7% Efficiency in Polymer−Fullerene Solar Cells'. *Journal of the American Chemical Society,* 133 (12), pp. 4625-4631.
Qian, D. *et al.* (2012) 'Design, Application, and Morphology Study of a New Photovoltaic Polymer with Strong Aggregation in Solution State'. *Macromolecules,* 45 (24), pp. 9611-9617.
Qian, D. *et al.* (2018) 'Design rules for minimizing voltage losses in high-efficiency organic solar cells'. *Nature Materials,* 17 (8), pp. 703-709.
Ran, N.A. *et al.* (2018) 'Charge Generation and Recombination in an Organic Solar Cell with Low Energetic Offsets'. *Advanced Energy Materials,* 8 (5), pp. 1701073.
Rao, A. and Friend, R.H. (2017) 'Harnessing singlet exciton fission to break the Shockley-Queisser limit'. *Nature Reviews Materials,* 2 (11), pp. 17063.
Ren, J. *et al.* (2021) 'Molecular design revitalizes the low-cost PTV-polymer for highly efficient organic solar cells'. *National Science Review,* 8 (8), pp. 17063.
Rong, Y. *et al.* (2018) 'Challenges for commercializing perovskite solar cells'. *Science,* 361 (6408), pp. eaat8235.
Shen, Y.-F. *et al.* (2023) 'In Situ Absorption Characterization Guided Slot-Die-Coated High-Performance Large-Area Flexible Organic Solar Cells and Modules'. *Advanced Materials,* 35 (10), pp. 2209030.
Shi, X. *et al.* (2018) 'Terthieno[3,2-b]Thiophene (6T) Based Low Bandgap Fused-Ring Electron Acceptor for Highly Efficient Solar Cells with a High Short-Circuit Current Density and Low Open-Circuit Voltage Loss'. *Advanced Energy Materials,* 8 (12), pp. 1702831.
Shi, Y. *et al.* (2022) 'Small reorganization energy acceptors enable low energy losses in non-fullerene organic solar cells'. *Nature Communications,* 13 (1), pp. 3256.
Sivula, K. (2022) 'Improving Charge Carrier Mobility Estimations When Using Space-Charge-Limited Current Measurements'. *ACS Energy Letters,* 7 (6), pp. 2102-2104.
Song, J. *et al.* (2018) 'Extension of Indacenodithiophene Backbone Conjugation Enables Efficient Asymmetric A-D-A Type Non-Fullerene Acceptors'. *Journal of Materials Chemistry A,* 6, pp. 18847-18852.
Song, J. *et al.* (2019a) 'Ternary Organic Solar Cells with Efficiency >16.5% Based on Two Compatible Nonfullerene Acceptors'. *Adv Mater,* 31 (52), pp. e1905645.

Song, X. *et al.* (2019b) 'Efficient DPP Donor and Nonfullerene Acceptor Organic Solar Cells with High Photon-to-Current Ratio and Low Energetic Loss'. *Advanced Functional Materials,* 29 (34), pp. 1902441.
Sun, B. *et al.* 'Toward More Efficient Organic Solar Cells: A Detailed Study of Loss Pathway and Its Impact on Overall Device Performance in Low-Offset Organic Solar Cells'. *Advanced Energy Materials,* 13, pp. 2300980.
Sun, C. *et al.* (2018a) 'A low cost and high performance polymer donor material for polymer solar cells'. *Nature Communications,* 9 (1), pp. 743.
Sun, C. *et al.* (2020) 'High Efficiency Polymer Solar Cells with Efficient Hole Transfer at Zero Highest Occupied Molecular Orbital Offset between Methylated Polymer Donor and Brominated Acceptor'. *Journal of the American Chemical Society,* 142 (3), pp. 1465-1474.
Sun, H., Chen, F. and Chen, Z.-K. (2019) 'Recent progress on non-fullerene acceptors for organic photovoltaics'. *Materials Today,* 24, 94-118.
Sun, J. *et al.* (2018b) 'Dithieno[3,2-b:2',3'-d]pyrrol Fused Nonfullerene Acceptors Enabling Over 13% Efficiency for Organic Solar Cells'. *Adv Mater,* 30 (16), pp. e1707150.
Sun, J. *et al.* (2018c) 'High performance non-fullerene polymer solar cells based on PTB7-Th as the electron donor with 10.42% efficiency'. *Journal of Materials Chemistry A,* 6 (6), pp. 2549-2554.
Sun, Y. *et al.* (2018d) 'Asymmetric Selenophene-Based Non-Fullerene Acceptors for High-Performance Organic Solar Cells'. *Journal of Materials Chemistry A,* 7, pp. 1435-1441.
Vandewal, K., Benduhn, J. and Nikolis, V.C. (2018) 'How to determine optical gaps and voltage losses in organic photovoltaic materials'. *Sustainable Energy & Fuels,* 2 (3), pp. 538-544.
Venkateshvaran, D. *et al.* (2014) 'Approaching disorder-free transport in high-mobility conjugated polymers'. *Nature,* 515 (7527), pp. 384-388.
Wang, J. *et al.* (2016) 'Triarylamine: Versatile Platform for Organic, Dye-Sensitized, and Perovskite Solar Cells'. *Chemical Reviews,* 116 (23), pp. 14675-14725.
Wang, J. *et al.* 'Binary Organic Solar Cells with 19.2% Efficiency Enabled by Solid Additive'. *Adv Mater,* 35 (25), pp. 2301583.
Wang, Y. *et al.* (2020) 'A novel wide-bandgap small molecule donor for high efficiency all-small-molecule organic solar cells with small non-radiative energy losses'. *Energy & Environmental Science,* 13 (5), pp. 1309-1317.
Wang, Y. and Zhan, X. (2016) 'Layer-by-Layer Processed Organic Solar Cells'. *Advanced Energy Materials,* 6 (17), pp. 1600414.
Watley, R.L. *et al.* (2015) 'Dual Functioning Thieno-Pyrrole Fused BODIPY Dyes for NIR Optical Imaging and Photodynamic Therapy: Singlet Oxygen Generation without Heavy Halogen Atom Assistance'. *Chem Asian J,* 10 (6), pp. 1335-1343.
Wetzel, C. *et al.* (2015) 'Fused thiophene-pyrrole-containing ring systems up to a heterodecacene'. *Angew Chem Int Ed Engl,* 54 (42), pp. 12334-12338.
Wu, H. *et al.* (2023) 'Impact of donor halogenation on reorganization energies and voltage losses in bulk-heterojunction solar cells'. *Energy & Environmental Science,* 16 (3), pp. 1277-1290.
Wu, Y. and Zhu, W. (2013) 'Organic sensitizers from D-pi-A to D-A-pi-A: effect of the internal electron-withdrawing units on molecular absorption,

energy levels and photovoltaic performances'. *Chem Soc Rev,* 42 (5), pp. 2039-2058.
Xia, H. *et al.* (2022) 'Novel Oligomer Enables Green Solvent Processed 17.5% Ternary Organic Solar Cells: Synergistic Energy Loss Reduction and Morphology Fine-Tuning'. *Advanced Materials,* 34 (10), pp. 2107659.
Xia, Z. *et al.* (2021) 'Fine-Tuning the Dipole Moment of Asymmetric Non-Fullerene Acceptors Enabling Efficient and Stable Organic Solar Cells'. *ACS Appl Mater Interfaces,* 13 (20), pp. 23983-23992.
Xiao, Z. *et al.* (2017) '26 mA cm^{-2} J_{SC} from organic solar cells with a low-bandgap nonfullerene acceptor'. *Science Bulletin,* 62 (22), pp. 1494-1496.
Xu, X. *et al.* (2023) 'Sequential Deposition of Multicomponent Bulk Heterojunctions Increases Efficiency of Organic Solar Cells'. *Advanced Materials,* 35 (12), pp. 2208997.
Xu, X. *et al.* (2016) '10.20% Efficiency polymer solar cells via employing bilaterally hole-cascade diazaphenanthrobisthiadiazole polymer donors and electron-cascade indene-C70 bisadduct acceptor'. *Nano Energy,* 25, 170-183.
Yan, C. *et al.* (2018a) 'Non-fullerene acceptors for organic solar cells'. *Nature Reviews Materials,* 3 (3), pp. 18003.
Yan, D. *et al.* (2021) 'Polysilicon passivated junctions: The next technology for silicon solar cells?'. *Joule,* 5 (4), pp. 811-828.
Yan, D. *et al.* (2018b) 'Fused-Ring Nonfullerene Acceptor Forming Interpenetrating J-Architecture for Fullerene-Free Polymer Solar Cells'. *Advanced Energy Materials,* 8 (31), pp. 1800204.
Yang, F. *et al.* (2017) 'Halogenated conjugated molecules for ambipolar field-effect transistors and non-fullerene organic solar cells'. *Materials Chemistry Frontiers,* 1 (7), pp. 1389-1395.
Yang, L. *et al.* (2020) 'Molecular engineering of acceptors to control aggregation for optimized nonfullerene solar cells'. *Journal of Materials Chemistry A,* 8 (11), pp. 5458-5466.
Yang, L. *et al.* (2019) 'Tuning of the conformation of asymmetric nonfullerene acceptors for efficient organic solar cells'. *Journal of Materials Chemistry A,* 7 (39), pp. 22279-22286.
Yang, Y. *et al.* (2016) 'Side-Chain Isomerization on an n-type Organic Semiconductor ITIC Acceptor Makes 11.77% High Efficiency Polymer Solar Cells'. *Journal of the American Chemical Society,* 138 (45), pp. 15011-15018.
Yao, H. *et al.* (2016) 'Molecular Design of Benzodithiophene-Based Organic Photovoltaic Materials'. *Chemical Reviews,* 116 (12), pp. 7397-7457.
Yin, P. *et al.* (2020) 'Improving the charge transport of the ternary blend active layer for efficient semitransparent organic solar cells'. *Energy & Environmental Science,* 13 (12), pp. 5177-5185.
Yoshikawa, K. *et al.* (2017) 'Silicon heterojunction solar cell with interdigitated back contacts for a photoconversion efficiency over 26%'. *Nature Energy,* 2 (5), pp. 17032.
Yu, G. *et al.* (1995) 'Polymer Photovoltaic Cells: Enhanced Efficiencies via a Network of Internal Donor-Acceptor Heterojunctions'. *Science,* 270 (5243), pp. 1789-1791.
Yu, H. *et al.* (2020) 'Tailoring non-fullerene acceptors using selenium-incorporated heterocycles for organic solar cells with over 16% efficiency'. *Journal of Materials Chemistry A,* 8 (45), pp. 23756-23765.

Yu, T. *et al.* (2022) '3D Nanoscale Morphology Characterization of Ternary Organic Solar Cells'. *Small Methods,* 6 (1), pp. e2100916.
Yuan, J. *et al.* (2022) 'Effects of energetic disorder in bulk heterojunction organic solar cells'. *Energy & Environmental Science,* 15 (7), pp. 2806-2818.
Yuan, J. *et al.* (2019a) 'Fused Benzothiadiazole: A Building Block for n-Type Organic Acceptor to Achieve High-Performance Organic Solar Cells'. *Advanced Materials,* 31 (17), pp. 1807577.
Yuan, J. *et al.* (2019b) 'Single-Junction Organic Solar Cell with over 15% Efficiency Using Fused-Ring Acceptor with Electron-Deficient Core'. *Joule,* 3 (4), pp. 1140-1151.
Zeng, Y. *et al.* (2021) 'Exploring the Charge Dynamics and Energy Loss in Ternary Organic Solar Cells with a Fill Factor Exceeding 80%'. *Advanced Energy Materials,* 11 (31), pp. 2101338.
Zhan, L. *et al.* (2020) 'Over 17% efficiency ternary organic solar cells enabled by two non-fullerene acceptors working in an alloy-like model'. *Energy & Environmental Science,* 13 (2), pp. 635-645.
Zhang, C. *et al.* (2022a) 'Unraveling Urbach Tail Effects in High-Performance Organic Photovoltaics: Dynamic vs Static Disorder'. *ACS Energy Letters,* 7 (6), pp. 1971-1979.
Zhang, G. *et al.* (2020a) 'Delocalization of exciton and electron wavefunction in non-fullerene acceptor molecules enables efficient organic solar cells'. *Nat Commun,* 11 (1), pp. 3943.
Zhang, G. *et al.* (2022b) 'Renewed Prospects for Organic Photovoltaics'. *Chemical Reviews,* 122 (18), pp. 14180-14274.
Zhang, H. *et al.* (2018a) 'Over 14% Efficiency in Organic Solar Cells Enabled by Chlorinated Nonfullerene Small-Molecule Acceptors'. *Advanced Materials,* 30 (28), pp. 1800613.
Zhang, J. and Lu, T. (2021) 'Efficient evaluation of electrostatic potential with computerized optimized code'. *Phys Chem Chem Phys,* 23 (36), pp. 20323-20328.
Zhang, M. *et al.* (2014) 'A Polythiophene Derivative with Superior Properties for Practical Application in Polymer Solar Cells'. *Advanced Materials,* 26 (33), pp. 5880-5885.
Zhang, S. *et al.* (2016) 'Fullerene Adducts Bearing Cyano Moiety for Both High Dielectric Constant and Good Active Layer Morphology of Organic Photovoltaics'. *Advanced Functional Materials,* 26 (33), pp. 6107-6113.
Zhang, T. *et al.* (2021) 'A Thiadiazole-Based Conjugated Polymer with Ultradeep HOMO Level and Strong Electroluminescence Enables 18.6% Efficiency in Organic Solar Cell'. *Advanced Energy Materials,* 11 (35), pp. 2101705.
Zhang, W. *et al.* (2019) 'Graphene:silver nanowire composite transparent electrode based flexible organic solar cells with 13.4% efficiency'. *Journal of Materials Chemistry A,* 7 (38), pp. 22021-22028.
Zhang, Y. *et al.* (2022c) 'Recent Progress of Y6-Derived Asymmetric Fused Ring Electron Acceptors'. *Advanced Functional Materials,* 32 (35), pp. 2205115.
Zhang, Z. *et al.* (2017) 'Achieving over 10% efficiency in a new acceptor ITTC and its blends with hexafluoroquinoxaline based polymers'. *Journal of Materials Chemistry A,* 5 (22), pp. 11286-11293.

Zhang, Z. *et al.* (2020b) 'Over 15.5% efficiency organic solar cells with triple sidechain engineered ITIC'. *Science Bulletin,* 65 (18), pp. 1533-1536.
Zhang, Z. *et al.* (2020c) 'Selenium Heterocyclic Electron Acceptor with Small Urbach Energy for As-Cast High-Performance Organic Solar Cells'. *Journal of the American Chemical Society,* 142 (44), pp. 18741-18745.
Zhang, Z. *et al.* (2020d) 'Modification on the Indacenodithieno[3,2-b]thiophene Core to Achieve Higher Current and Reduced Energy Loss for Nonfullerene Solar Cells'. *Chemistry of Materials,* 32 (3), pp. 1297-1307.
Zhang, Z. *et al.* (2018b) 'Conformation Locking on Fused-Ring Electron Acceptor for High-Performance Nonfullerene Organic Solar Cells'. *Advanced Functional Materials,* 28 (11), pp. 1705095.
Zhao, F., Wang, C. and Zhan, X. (2018) 'Morphology Control in Organic Solar Cells'. *Advanced Energy Materials,* 8 (28), pp. 1703147.
Zhao, F. *et al.* (2020) 'Emerging Approaches in Enhancing the Efficiency and Stability in Non-Fullerene Organic Solar Cells'. *Advanced Energy Materials,* 10 (47), pp. 2002746.
Zhao, J. *et al.* (2016a) 'Efficient organic solar cells processed from hydrocarbon solvents'. *Nature Energy,* 1 (2), pp. 15027.
Zhao, W. *et al.* (2017) 'Molecular Optimization Enables over 13% Efficiency in Organic Solar Cells'. *Journal of the American Chemical Society,* 139 (21), pp. 7148-7151.
Zhao, W. *et al.* (2016b) 'Fullerene-Free Polymer Solar Cells with over 11% Efficiency and Excellent Thermal Stability'. *Adv Mater,* 28 (23), pp. 4734-4739.
Zhao, X. *et al.* (2023) 'High-speed printing of a bulk-heterojunction architecture in organic solar cells films'. *Energy & Environmental Science,* 16 (4), pp. 1711-1720.
Zheng, Q. *et al.* (2020a) 'Ladder-Type Heteroheptacenes with Different Heterocycles for Nonfullerene Acceptors'. *Angew Chem Int Ed Engl,* 59 (48), pp. 21627-21633.
Zheng, Z. *et al.* (2018) 'A Highly Efficient Non-Fullerene Organic Solar Cell with a Fill Factor over 0.80 Enabled by a Fine-Tuned Hole-Transporting Layer'. *Adv Mater,* 30 (34), pp. 1801801.
Zheng, Z. *et al.* (2020b) 'PBDB-T and its derivatives: A family of polymer donors enables over 17% efficiency in organic photovoltaics'. *Materials Today,* 35, pp. 115-130.
Zhou, J. *et al.* (2023) 'Reducing Trap Density in Organic Solar Cells via Extending the Fused Ring Donor Unit of an A-D-A-Type Nonfullerene Acceptor for Over 17% Efficiency'. *Adv Mater,* 35 (3), pp. 2207336.
Zhou, K. *et al.* (2020a) 'Molecular and Energetic Order Dominate the Photocurrent Generation Process in Organic Solar Cells with Small Energetic Offsets'. *ACS Energy Letters,* 5 (2), pp. 589-596.
Zhou, Z. *et al.* (2020b) 'Subtle Molecular Tailoring Induces Significant Morphology Optimization Enabling over 16% Efficiency Organic Solar Cells with Efficient Charge Generation'. *Adv Mater,* 32 (4), pp. 1906324.
Zhu, C. *et al.* (2020) 'Tuning the electron-deficient core of a non-fullerene acceptor to achieve over 17% efficiency in a single-junction organic solar cell'. *Energy & Environmental Science,* 13 (8), pp. 2459-2466.
Zhu, J. *et al.* (2017) 'Subtle side-chain tuning on terminal groups of small molecule electron acceptors for efficient fullerene-free polymer solar cells'. *Journal of Materials Chemistry A,* 5 (29), pp. 15175-15182.

Zhu, J. *et al.* 'Conformation Flipping of Asymmetric Nonfullerene Acceptors Enabling High-Performance Organic Solar Cells with 77% Fill Factors'. *Solar RRL,* 7 (13), pp. 2300171.
Zhu, J. *et al.* (2022a) 'Organic solar cells based on non-fullerene acceptors containing thiophene [3,2-b] pyrrole'. *Organic Electronics,* 103, pp. 106461.
Zhu, L. *et al.* (2022b) 'Single-junction organic solar cells with over 19% efficiency enabled by a refined double-fibril network morphology'. *Nature Materials,* 21 (6), pp. 656-663.
Zhu, L. *et al.* (2022c) 'Single-junction organic solar cells with over 19% efficiency enabled by a refined double-fibril network morphology'. *Nat Mater,* 21 (6), pp. 656-663.
Zou, Y. *et al.* (2022) 'Peripheral halogenation engineering controls molecular stacking to enable highly efficient organic solar cells'. *Energy & Environmental Science,* 15 (8), pp. 3519-3533.